Temporal Diffusion MRI of Post-Exercise Human Calf Muscles

TEMPORAL DIFFUSION MRI OF POST-EXERCISE HUMAN CALF MUSCLES

BY

CONRAD PETER ROCKEL, B.A.

A THESIS
SUBMITTED TO THE SCHOOL OF BIOMEDICAL ENGINEERING
AND THE SCHOOL OF GRADUATE STUDIES
OF MCMASTER UNIVERSITY
IN PARTIAL FULFILMENT OF THE REQUIREMENTS
FOR THE DEGREE OF
DOCTOR OF PHILOSOPHY

Doctor of Philosophy (2016)	McMaster University
(School of Biomedical Engineering)	Hamilton, Ontario, Canada

TITLE:	Temporal Diffusion MRI of Post-Exercise Human Calf Muscles
AUTHOR:	Conrad Peter Rockel B.A., (Hons. Psychology) McMaster University, Hamilton, ON , Canada
SUPERVISOR:	Dr. Michael D Noseworthy
NUMBER OF PAGES:	xxxi, 219

Abstract

Diffusion tensor imaging (DTI) is a magnetic resonance imaging (MRI) method that resolves structures by three-dimensional measurement of water movement, and has shown to benefit studies of anisotropic tissues such as brain and skeletal muscle. While many studies have used DTI to non-invasively study static tissue architecture, little attempt has been made to use this technique to temporally characterize muscle during post-exercise recovery. Thus, the goal of this work was to use DTI to study the timecourse of changes in skeletal muscle following exercise.

The first study was performed to test stability of DTI eigenvectors (ε_1 ε_2 ε_3), and to determine how time-expensive parameters such as increased number of diffusion directions (NDD) or signal averages (NSA) improve vector stability. The ε_2 vector was found to have more directional variability than ε_1, and showed less improvement than ε_1 with increased NDD or NSA. Furthermore, decreasing directional variability of ε_1 was correlated with increasing NDD, not NSA ($p<0.0008$), while decreased variability of ε_2 was correlated with increasing NSA, not NDD ($p<0.0005$). The variation in ε_2 indicated that combining the corresponding minor eigenvalues into a measure of Radial Diffusivity is more robust than analyzing λ_2 and λ_3 eigenvalues separately.

The second study tested the use of DTI to characterize temporal calf muscle changes following a mild in-bore dorsiflexion-eversion exercise. DTI volumes were acquired before and immediately after exercise. Anterior tibialis (ATIB), extensor digitorum longus (EDL), and peroneus longus (PER) showed significantly-elevated mean diffusivity (MD) post-exercise, while soleus (SOL) and lateral gastrocnemius (LG) did not (p<0.0001). The EDL showed greater initial MD increase and remained significantly elevated across more time points than ATIB or PER (p<0.05 to p=7.41x10^{-10}). Significant signal increases were observed in post-exercise EDL b=0s/mm^2 volumes (S_0) relative to other muscles across the majority of timepoints (p<0.01 to p<0.001). The notable differences of EDL temporal MD and S_0 relative to ATIB and PER may be related to the physiology of the increased Type-II fiber content in this muscle.

The third and final study investigated the feasibility of a 'sliding window' multiple-timescale temporal DTI approach, intended to acquire data with high temporal resolution and ongoing structural representation. Continuous diffusion data was acquired in the calf before and after four plantarflexion tasks, which varied by number of flexions (10 or 60), and weight load (10% or 40% of individual max). Apparent diffusion coefficient (ADC) and S_0 were calculated from 3-direction subunits, while 15-direction subunits produced DTI measures such as mean diffusivity (MD). Four different post-exercise temporal patterns were observed for ADC, S_0, and MD amongst the measured muscles: 'elevated-decline', 'latent peak', 'sub-to-peak', and 'horizontal'. The 10-flex 10% condition elicited 'elevated-decline' in active muscles, particularly SOLlat. Exercise of greater intensity produced 'latent peak' and 'sub-to-peak' patterns, with peak height related to greater workload. The 10-flex 40% trial produced a 'sub-to-peak' pattern across all subjects only in the LG and MG, but 'latent-peak' in these muscles 60-flex 40%. The specificity of temporal diffusion patterns according to muscle and task indicate that this technique could be beneficial to future studies of muscle function.

These experiments have demonstrated the limits of DTI in the study of skeletal muscle, yet established a basis for future investigation of muscle dynamics using temporal diffusion methods.

Acknowledgements

There are many people I would like to thank for their support during my journey through graduate school:

First and foremost, I would like to thank my supervisor, Dr. Michael Noseworthy, for welcoming my foot into the door of MR engineering, taking me places I would not have gone otherwise, and for providing funding clout, statistical advice, tireless editing, musical opportunities, and friendship. I also thank my committee members, Dr Dinesh Kumbhare, Dr Nick Bock, Dr Greg Wohl, and Dr Greg Wells for their input and for expanding my critical awareness.

I would also like to thank the IRC MR technologists for all of their teachings about the practical side of MRI acquisition. Kudos to Janet Burr for forgiveness about the tape measure incident, Cheryl Contant for playing the Desi to my post-tape-measure Lucy (not to mention her coaching and wisdom at the MR console), Julie Lecomte for her perspective (and for putting up with the cowboys), and Carol Awde, the Jedi of sass who knows a cyst when she sees one. While I am at it, I guess I should begrudgingly thank Norm Konyer for his MR guru-ness, dry wit, and putting up with me and us the last few years.

A large thank you to Natalie Illingsworth for making the majority of my grad school official stuff go smoothly, as well as the welcome face of commiseration and gossip during my TA-ship of BME 701. Your absence was widely felt by myself and the department when you decided to move on.

A big shout out to Dr Alireza Akbari: friend, colleague, Woody master, bow-legged koskesh. Thanks for being on the road with me for the long haul, for the encouragement and advice, and for being an example of an inquisitive and dedicated engineer. I would also like to thank IRC students past and present for their technical advice, comradeship, and scannable anatomy over the years: Jen Stoneburgh, Kirsten Zernask, Superstar Andrew Davis, Dr Alex Weber, Dr Mohammed Warsi, Arv Jegatheesan, Ben Garety, Dr Oilei Wong, Dr Alyaa Elzibak, Dr Raghda Hasswa, Robin Engels, Jeff Thompson, Dr Amy Harrison, Evan McNabb, Olga Dona Lemus, Alejandro Santos, Catalina Charles, Dave Stillo, Saurabh Shaw, and Michael Behr.

My PhD life would have been much bleaker without the friends I made in Hamilton. Thank-youuuu to Dr Heidi Daxberger for having a weirdly parallel life to my own, and for your perspective, wisdom, and encouragement. Kugelshrieber!! A big thank-you to the rest of Team Awesome for the good food, good climbing, good tunes, dumb conversations, good times (and occasional Kentucky Sunrise): Richard Wolff, Kris Raab, Josh Hill, Dr Ray Comeau, Hank Raab, Brad Moore, Paula Penton, Jeff Higgins, Kat Hill, Brooke McKrae, and Robert Koszegi.

OG winks to Andrew Hase, Sabrina Dias, Mark Aylward, Nicole Cvetkovic, Jo Skocic, Salim Haniff, Jolynn Dickson, Dr Nadia Scantlebury, Dr Trish Domi, Dr Garland Jones, Dr Don Mabbott, Cam Hood and Dwayne Harkness (....and John McNabb for laughing hysterically *with* me when I mentioned I was going back to school yet again.)

Finally, a heartfelt thank you to my mother, Trudy-Lee Rockel, for buoying me, listening to my rants in my darkest moments, and reminding me to eat. Queen Pizza thanks you for my support of their business. I also want to thank Duncan, Trish, Mars and Pangaea Rockel for being awesome, reminding me about family, and making me feel cool when I needed it the most. I would also like to thank the Norman, Hermant, and extended Rockel clans for their ongoing encouragement and support.

Notation and abbreviations

ADC	- Apparent Diffusion Coefficient (DW and DWI)
ADP	- Adenosine Diphosphate
ANOVA	- Analysis of Variance
ATIB	- Anterior Tibialis muscle (calf)
ATP	- Adenosine Triphosphate
b	- Amount of diffusion weighting applied during acquisition
CPMG	- Carr-Purcell-Meiboom-Gill (MRI sequence)
CO_2	- Carbon Dioxide
dir	- Directions, pertaining to number of diffusion gradient vectors
DTI	- Diffusion Tensor Imaging
DW	- Diffusion weighted
DWI	- Diffusion Weighted Imaging
EDL	- Extensor Digitorum Longus muscle (calf)
EMG	- Electromyography
EPI	- Echo Planar Image
ε_1	- First eigenvector (Diffusion Tensor Imaging)
ε_2	- Second eigenvector (Diffusion Tensor Imaging)
ε_3	- Third eigenvector (Diffusion Tensor Imaging)
FA	- Fractional Anisotropy (Diffusion Tensor Imaging)
FOV	- Field of View
Hz	- Hertz. Cycles or repetitions per second
λ_1	- First eigenvalue (Diffusion Tensor Imaging)
λ_2	- Second eigenvalue (Diffusion Tensor Imaging)
λ_3	- Third eigenvalue (Diffusion Tensor Imaging)

LG	- Lateral Gastrocnemius muscle (calf)
MD	- Mean Diffusivity (Diffusion Tensor Imaging)
MG	- Medial Gastrocnemius muscle (calf)
MRI	- Magnetic Resonance Imaging
MWSF	- Maximum (Woody) Weight Single Flex
n	- Number of subjects
N	- Number of diffusion directions
NDD	- Number of diffusion directions
NMR	- Nuclear Magnetic Resonance
NSA	- Number of Signal Averages
PCr	- Phosphocreatine
PD-FatSat	- Proton Density Fat-Saturation (anatomical MRI sequence)
PER	- Peroneus Longus muscle (calf)
PGSE	- Pulsed Gradient Spin Echo (MRI sequence)
P_i	- Inorganic Phosphate ion
RD	- Radial Diffusivity - mean of second and third eigenvalues ($(\lambda_2 + \lambda_3)/2$)
RF	- Radiofrequency
ROI	- Region of Interest
RPBM	- Random Permeable Barrier Model (Sigmund *et al.*, NMR Biomed 2014.)
S_0	- Signal intensity of the b=0 s/mm^2 image (DTI)
SD	- Standard Deviation
SE	- Spin Echo
SEM	- Standard Error of the Mean
SNR	- Signal-to-noise Ratio
SOL	- Soleus muscle (calf)
SOLlat	- Soleus muscle (calf; lateral compartment)
STE	- Standard Time Equivalency
T	- Tesla (MRI static field strength)
T_1	- Longitudinal relaxation time (67% of longitudinal magnetization recovery (MRI)
T_2	- Transverse relaxation time (67% of transverse magnetization loss (MRI)
TE	- Echo Time (MRI)
TR	- Repetition Time (MRI)

Contents

List of Figures

Chapter 1

Introduction

The following dissertation pertains to the assessment of post-exercise skeletal muscle response as measured by Diffusion Tensor Imaging (DTI), a magnetic resonance approach. A particular focus is the use of repeated DTI acquisition for the creation of temporal patterns representative of individual muscle recovery dynamics.

Chapter 2 contains a review of skeletal muscle, metabolism, and exercise, as well as a description of the human calf.

Chapter 3 contains a review of magnetic resonance imaging (MRI) techniques that are used or referenced within this body of work.

Chapter 4 describes a pilot study of weighted plantarflexion that inspired further investigation into using DTI in a temporal manner to study skeletal muscle dynamics. Details of how this pilot study determined the direction of this thesis projects are provided, as well as the Study Objectives.

Chapter 5 presents a published paper regarding the stability of individual DTI output measures, with particular focus on the tensor eigenvectors. This paper also discusses the gains in eigenvector stability at the cost of temporal resolution.

Chapter 6 presents a published paper that expands on the pilot study work. A timecourse DTI analysis is used to study diffusion changes invoked within individual calf muscles by dorsiflexion-eversion exercise with minimal workload. Furthermore, a theory that post-exercise skeletal muscle temporal diffusion patterns are related to tissue composition is proposed.

Chapter 7 describes the development and testing of a novel 'sliding window' diffusion acquisition technique intended to produce data at a higher temporal resolution, but capable of recombination to achieve the structural representation provided by DTI. This technique is then used to investigate human calf muscle function following four plantarflexion exercises of differing intensity.

Finally, *Chapter 8* contains a summary and conclusion of this body of work, as well as suggestions for future directions.

Chapter 2

Skeletal Muscle

NOTE: The following chapter largely contains material from two textbooks (<Guyton and Hall, 2006> and <Marieb and Hoehn, 2010>) unless specifically referenced.

2.1 The structure of skeletal muscle

Skeletal muscle makes up approximately 40% of the mass of the human body. This tissue is responsible both for the support of the skeleton, as well as the majority of voluntary movement, due to its attachment to bone via collagenous tendons and capability for contraction. Skeletal muscle also has elastic properties, which allow for elongation in muscles counter to contraction. There are at least 640 different skeletal muscles within the human body, each responsible for a specific motion, although muscles often act as group, with agonists (”prime movers”) and synergists (secondary muscles which support the ”prime movers”).

Skeletal muscle is comprised of progressively smaller sub-units, each sheathed by fascia, a tough connective tissue that maintains muscle shape and integrity during

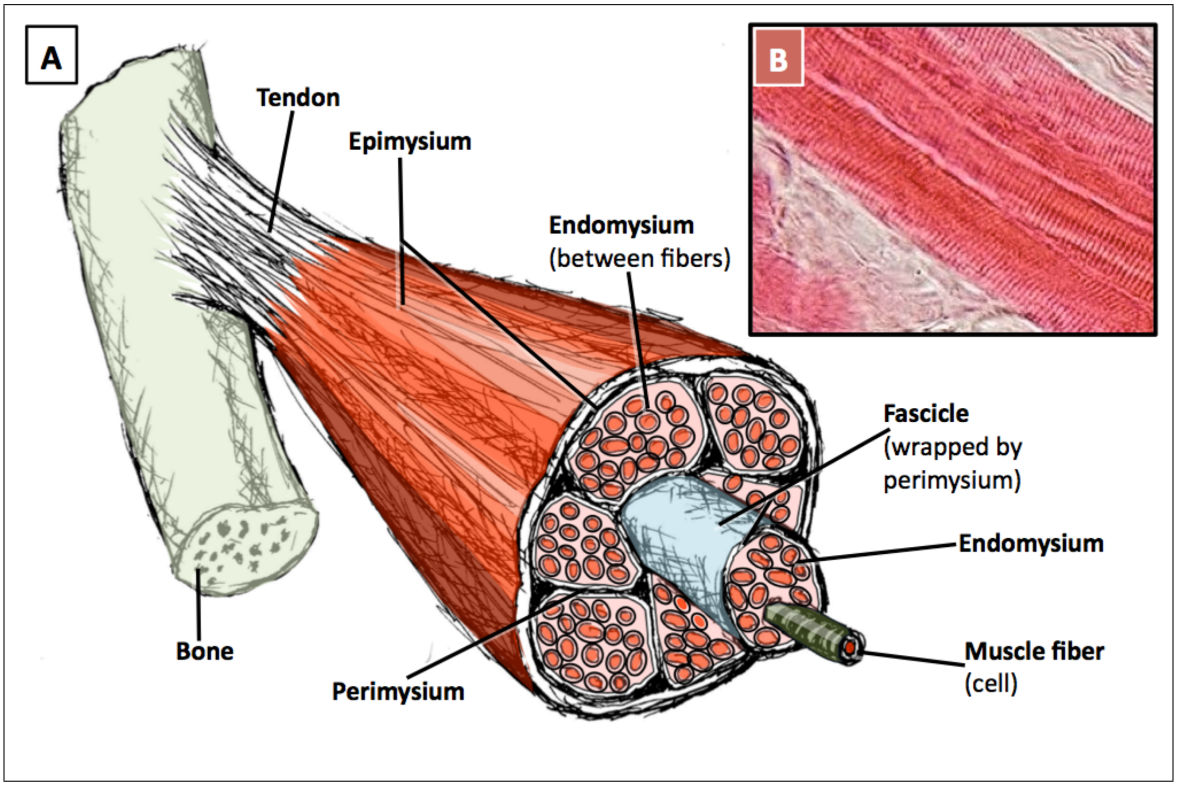

Figure 2.1: Architecture of skeletal muscle. **(A)** Illustration of concentric muscle subunits. **(B)** Micrograph depicting longitudinal axis of skeletal muscle fiber. Visible are the parallel arrangement of fibers, as well as striations (banding) along the fiber length. (Credits: Figure 2.1a based on an illustration from *studyblue.com*; Figure 2.1b from *commons.wikimedia.org*.)

contractions **(Fig. 2.1)**.

2.1.1 Micro-anatomy

At the cellular level, skeletal muscles consist of multinucleate cylindrical fibers 10-40mm in length and 10-80 μm in diameter <Bonny and Renou, 2002>, and arranged in a parallel fashion within the tissue. A single skeletal muscle fiber contains several hundred to several thousand large polymerized protein molecules known as myofibrils.

Each myofibril is composed of roughly 1500 myosin (”thick”) filaments and 3000 actin (”thin”) filaments. One end of an actin filament is attached to a *z-disc*, a strip of filamentous protein connected to fascia that passes through and between the myofibrils **(Fig. 2.2)**. The other end of the actin filament is overlapped by a myosin filament, which extends a series of protrusions known as *cross-bridges*. The opposite end of the myosin filament is overlapped by another actin filament, which is in turn connected to a second z-disc. The configuration of actin and myosin filaments lying between two z-discs is collectively known as a *sarcomere*. Each sarcomere is roughly 2μm in length, and multiple sarcomeres are connected end-to-end in a chain to form the myofibril.

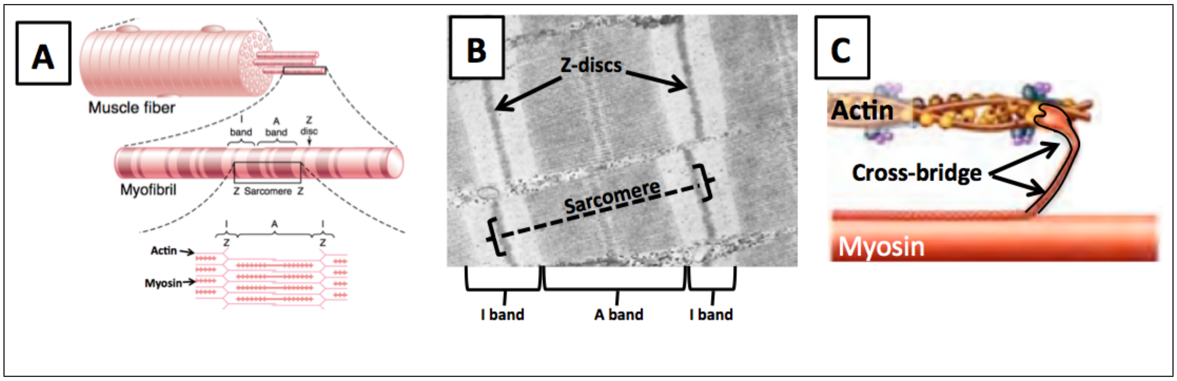

Figure 2.2: The muscle fiber. **(A)** Illustration of a muscle fiber showing overlap of actin and myosin within A-bands, as well as I-bands (myosin only), and the banding of Z-discs. **(B)** Electron micrograph indicating bands within striated muscle fibers. The dashed line depicts the range of one sarcomere, and is oriented to fiber direction. **(C)** Depiction of a myosin cross-bridge bound to actin. (Credits: Figures 2.2a and 2.2b used with permission from <Guyton and Hall, 2006>, see Appendix C; Figure 2.2c adapted from *open.umich.edu*)

Muscle fibers are wrapped with a membranous structure known as the *sarcolemma*. This membrane coating serves to house the nuclei of the muscle cell, as well as maintain an ionic gradient important in the transmission of action potentials along the muscle fiber. Within the sarcolemma, the myofibrils are bathed in a fluid known as *sarcoplasm*, which is dense with organelles, dissolved proteins, macromolecules, and ions necessary for cellular function. Throughout this cellular matrix is a membraneous network known as the *sarcoplasmic reticulum*, which serves to store calcium ions, needed for the process of muscle contraction.

The muscle fibers are in turn surrounded by interstitial fluid, which also contains proteins and ions, although at a density far less than the sarcoplasm within the fiber. The interstitial fluid serves to transport nutrients from the bloodstream to the fiber, as well as removal of waste products from the fiber back to the bloodstream.

2.2 Contraction of Skeletal Muscle

Muscle contraction is initiated by a neural impulse which travels down the nerve and elicits secretion of the neurotransmitter acetylcholine, which in turn acts upon local areas of the muscle fiber at the neuromuscular junction. This signal is then carried along the sarcolemma via sodium-potassium channels and a wave of membrane depolarization (the ”action potential”) into the center of the myofibril via membrane invaginations known as *T-tubules*.

This action potential triggers the release of calcium ions from the sarcoplasmic reticulum <Allen *et al.*, 2008>, which in turn initiates attractive forces between actin and myosin filaments by activating binding sites for cross-bridges. The cross-bridges, fueled by the energy produced by hydrolysis of adenosine triphosphate (ATP), go through a cycle involving extension of the cross-bridge, attachment to actin, bending of the cross-bridge (the ”power stroke”), and then detachment from actin **(Fig. 2.3a)**. If the binding sites are still activated, the cycle will begin again. This produces a ratchet-like motion which causes the actin and myosin filaments to slide into one another **(Fig. 2.3b)**. As a result, the sarcomeres shorten and pull on the z-discs, thus shortening the muscle fibers which collectively contract the muscle.

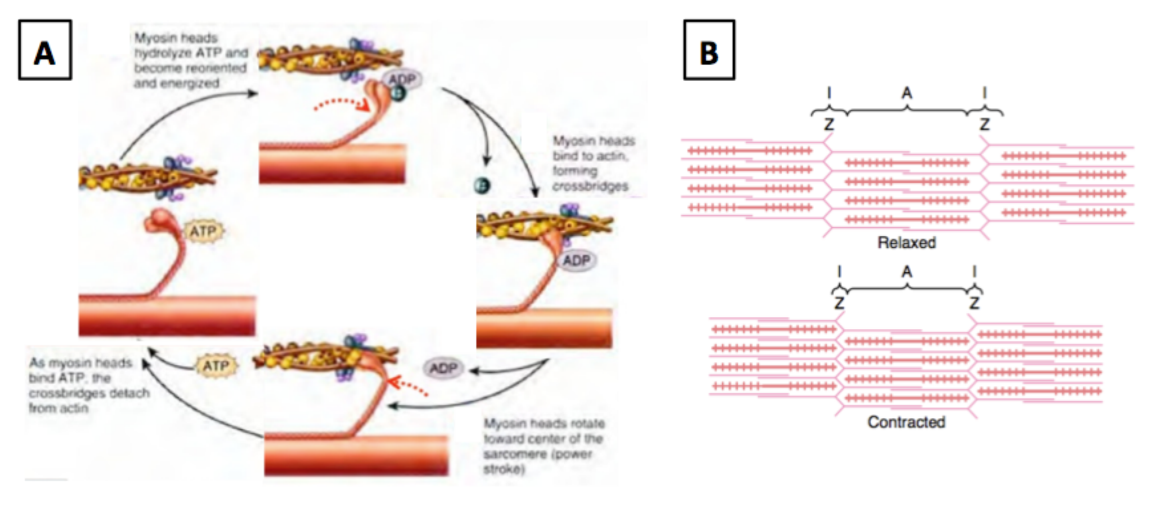

Figure 2.3: Contraction of skeletal muscle. **(A)** Cycle of myosin cross-bridge shape change, attachment to actin, power stroke, and detachment. **(B)** Depiction of actin sliding within myosin filaments as the sarcomere contracts. 'Z': Z-discs, 'I': I-band (myosin only), 'A': A-band (overlap of actin and myosin). (Credits: Figure 2.3a from *open.umich.edu*; Figure 2.3b used with permission from <Guyton and Hall, 2006>, see Appendix C.)

2.2.1 Types of Contraction

Muscle contraction can be broken down into 2 main categories: an increase of muscle tension while length remains static (*isometric*), and an increase in muscle tension with changes in its length (*isotonic*). Isometric contractions are "holding" contractions, such as standing on tiptoe or pushing against a wall. Isotonic contractions consist of 2 types: *concentric* contractions, which involve increased tension and the shortening and fattening of the muscle (e.g. a bicep curl); and *eccentric* contractions, which involve increased tension yet elongation of the muscle (e.g. lowering the weight after a bicep curl).

2.2.2 Physiology of Contraction

Adenosine triphosphate (ATP) is the primary source of energy of skeletal muscle. Energy is released when ATP interacts with enzymatic proteins within the muscle, which break the high-energy chemical bonds (7300 calories/mol), thus producing adenosine diphosphate (ADP) and a free phosphate radical (P_i). The energy released by the cleaving of the phosphate bond is transferred to the muscular system, activating changes in the shape of muscle proteins in order to induce contraction or activate membrane-based ion pumps.

However, the ATP immediately available for use by the muscle lasts only for approximately 3 seconds, and thus must be continuously regenerated. Therefore, ATP is reconstituted from ADP by the muscle cells via three pathways: direct phosphorylation, anaerobic glycolysis, and aerobic respiration **(Fig. 2.4)**.

During *direct phosphorylation*, phosphocreatine (PCr) stored in the muscle transfers a phosphate group to ADP to reform ATP. This is an immediate and efficient reaction, such that the level of ATP available for use changes very little. A muscle stores 2-3 times as much PCr as ATP, and with the phosphorylation of PCr, muscle can sustain maximal power (work x time) for about 8-10 seconds **(Fig. 2.4a)**.

As muscle stores of ATP and PCr become exhausted, ATP is then obtained from glucose found in the bloodstream or released from glycogen stores within the muscle. Initially, glucose is broken down to pyruvic acid, producing some ATP in the process. The pyruvic acid is in turn broken down by two different metabolic pathways.

If oxygen is not present, the pyruvic acid regenerates ATP by *anaerobic glycolysis*

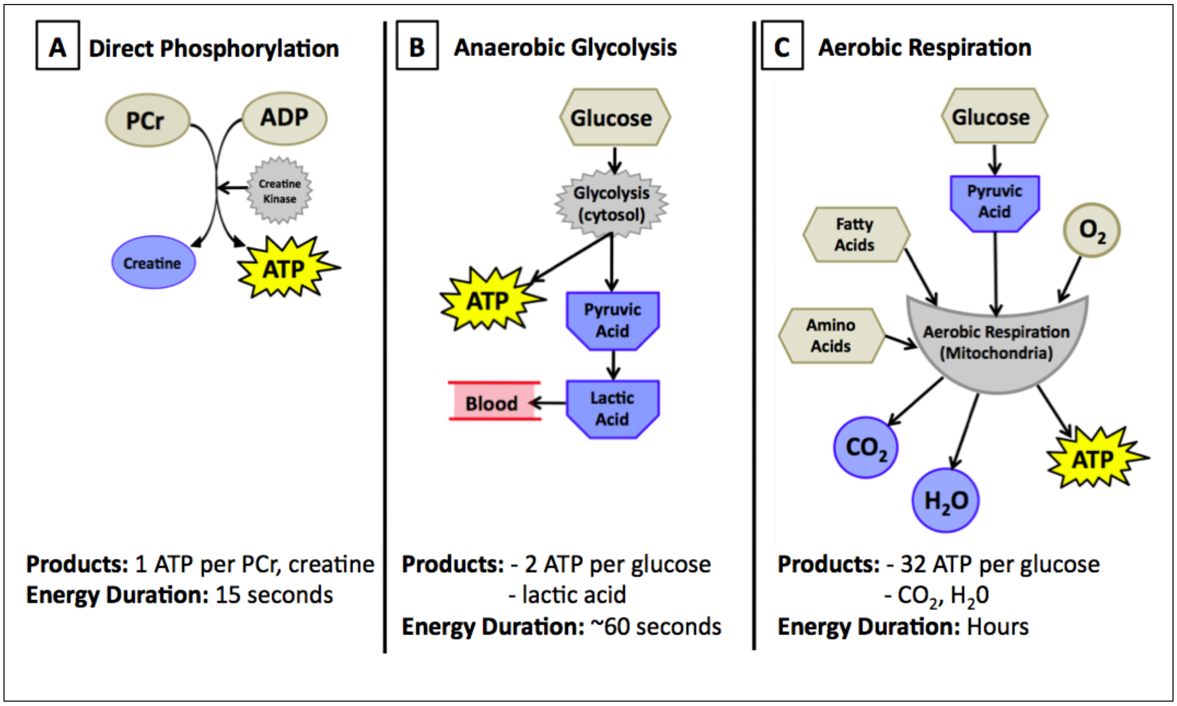

Figure 2.4: Metabolic pathways for regeneration of ATP during muscle activity. **(A)** Direct phosphorylation. **(B)** Anaerobic glycolysis. **(C)** Aerobic respiration. PCr: Phosphocreatine, ADP: Adenosine Diphosphate, ATP: Adenosine Triphosphate. (Credit: based on <Marieb and Hoehn, 2010>)

(Fig. 2.4b). This reaction can sustain maximal muscle power for about a minute, but produces lactic acid as a by-product.

Should oxygen be available, pyruvic acid enters the mitochondria and undergoes *aerobic respiration* **(Fig. 2.4c)**. The body contains approximately 2 litres of oxygen available for aerobic (oxidative) reactions without the need for additional breathing, consisting of that contained in the lungs, dissolved in body fluids, and combined with hemoglobin in the blood or myoglobin in the muscle. The mitochondria regenerate large amounts of ATP while producing only CO_2 and water. Aerobic respiration can continue to supply ATP indefinitely for light to moderate muscle demands as long as the requisite oxygen supply is available. Aerobic respiration produces 19-times more

ATP per molecule of glucose than does anaerobic glycolysis (i.e. 38 ATP vs 2 ATP), yet at a production rate that is 2.5-times slower.

Typically, for short bursts of power such as a sprint, the muscle collectively uses direct phosphorylation to maintain ATP. For longer periods of on-and-off bursts, such as a soccer match, the muscle relies on anaerobic glycolysis, while for daily activities or endurance exercise, ATP is regenerated using aerobic respiration.

2.3 Fiber Type

Skeletal muscles in the human body are comprised of two broad classes of muscle fibers: slow-twitch (Type I) and fast-twitch (Type II). Slow-twitch fibers enable prolonged activity, though they react much slower than fast-twitch fibers. They rely on aerobic processes for the production of energy, with their small diameter allowing for efficient diffusion of oxygen and nutrients <Guyton and Hall, 2006; Polgar *et al.*, 1973>. Furthermore, they have extensive blood vessel and capillary systems to enable the supply of oxygen, and contain high concentrations of mitochondria for oxidative (aerobic) metabolism <Andersen and Kroese, 1978>. Slow-twitch fibers also contain large amounts of myoglobin, a protein complex similar to hemoglobin, the role of which is to store and shuttle oxygen throughout the muscle cell.

Fast-twitch (Type II) fibers have a greater diameter than slow-twitch fibers <Guyton and Hall, 2006; Polgar *et al.*, 1973>, and have great strength and speed of contraction, though only for short durations. They have an extensive sarcoplasmic reticulum, which allows for the rapid release of contraction-inducing calcium ions, and a large amount of glycolytic enzymes that enable fast production of energy. Fast-twitch fibers are primarily anaerobic (Type IIb), and due to the decreased reliance on oxygen, they have less extensive blood supply and fewer mitochondria than slow-twitch fibers. However, there exists a hybrid form of fast-twitch fiber (Type IIb) that utilizes oxidative metabolism (Type IIa), as well as an additional form that is only found in non-human animals (Type IIx) <Fitts and Widrick, 1995>.

All human skeletal muscles have varying percentages of fast- and slow-twitch fibers, depending on the function of the muscle <Johnson *et al.*, 1973>. Muscles that typically require fast and forceful contractions contain a large percentage of fast-twitch fibers, while supportive and stabilizing muscles tend to contain higher percentages of slow-twitch fibers.

2.4 Exercise

Exercise is a dynamic activity that increases demand on skeletal muscle function beyond the typical levels required for mobility and skeletal support. As such, exercise can range from quick bursts of maximal muscle power (e.g. shot putting), to short periods of repetitive contraction (e.g. sprints in soccer or hockey), or to prolonged periods of repetitive contraction (e.g. endurance sports such as marathon running). As described in Section 2.2.2, the metabolic mechanism utilized by these exercise conditions ranges from direct phosphorylation, to anaerobic glycolysis, to aerobic respiration, respectively <Guyton and Hall, 2006; Marieb and Hoehn, 2010>.

As the duration of exercise progresses, the demand on the muscle to maintain PCr and ATP levels exceeds its availability, and thus numerous changes take place within the human body regarding water and blood distribution, and respiratory functions in order to increase the amount of oxygen available to muscle tissue. As contractile muscle tissues become oxygen-deprived, local arterioles dilate in order to increase the flow of oxygenated blood, while blood vessels within resting muscles undergo vasoconstriction in order to redirect blood to the active tissues. This is followed by heavier breathing and increased heart rate and stroke volume, all of which contribute to a greater rate of blood perfusion through the lungs and skeletal muscle tissue, and thus availability of oxygen and nutrients such as glucose <Guyton and Hall, 2006>. Furthermore, the venous system undergoes vasoconstriction, serving to increase the rate at which oxygen-depleted blood returns to the heart and lungs.

However, there are elements of exercise that complicate the presence of water and nutrients during exertion. First, the expanded diameter of contractile muscles in contraction compresses local blood vessels and capillaries, impairing the flow of oxygen-rich blood to the muscle fibers <Guyton and Hall, 2006; Marieb and Hoehn, 2010>. Secondly, 60% of the energy released by cleaving the phosphate bonds of ATP produces heat, requiring mechanisms such as thermal radiation from the skin surface and sweating in order to maintain internal body temperature and homeostasis <Marieb and Hoehn, 2010>. Unless rehydration occurs, especially during intense exercise, the loss of water due to sweating impacts both the amount of blood and global interstitial fluid volumes, leading to loss of muscle performance or even death <Guyton and Hall, 2006>. Finally, prolonged or intense exercise can result in micro-tearing of myocytic membranes, thus impairing the ability of tissues to maintain excitatory ion gradients or otherwise perform optimally <Duner and Penrow, 1958>.

As exercise continues, the ability of the muscles to produce force begins to decline, a condition known as *fatigue*. There are a multitude of contributory causes of muscle fatigue that have been investigated, such as the ability of the sarcoplasmic reticulum to release calcium ions <Allen and Westerblad, 2001>, the ability of the sarcolemma to carry an action potential <Allen *et al.*, 2008>, the availability of nutrients such as oxygen, glucose, glycogen or ATP <Guyton and Hall, 2006; Marieb and Hoehn, 2010; Bergstrom *et al.*, 1967>, or an accumulation of waste products such as lactic acid <Westerblad *et al.*, 2002; McKenna and Hargreaves, 2008>. In short, muscle fatigue is due to a temporary chemical imbalance within the tissue caused when demand exceeds availability, thus requiring a subsequent period of lesser demand and return to equilibrium before the muscles can regain their maximum force.

2.4.1 Recovery

In the minutes following the conclusion of strenuous exercise, the flow of blood to active tissues slowly decreases due to slowing of the heart rate and relaxation of sympathetic vasoconstriction. The rate at which these changes occur is dependent on the severity of *oxygen debt* acquired within the tissue during exercise. Additionally, an individual continues to breathe heavily following exercise in order to supply the blood with oxygen. During this ”repayment” of oxygen debt, homeostatic levels of dissolved oxygen are restored, ATP and PCr are aerobically constituted, and lactic acid is converted back into pyruvic acid. The liver is key in the process of oxidative conversion of lactic acid and free glucose into substances to be readily available for consumption for future intense contractions, although reconstitution of glycogen may take days following a session of intensive exercise <Guyton and Hall, 2006; Marieb and Hoehn, 2010>.

2.5 Muscles of the Human Calf

The muscles within the lower leg which are distal to the knee but proximal to the ankle are collectively known as the *calf* **(Fig. 2.5)**. This set of muscles, which surround the medial, lateral, and anterolateral sides of the tibia bone, are responsible for support and stabilization of the body while standing, as well as movement of the foot about the ankle, aiding in balance as well as propulsion **(Fig. 2.6)** .

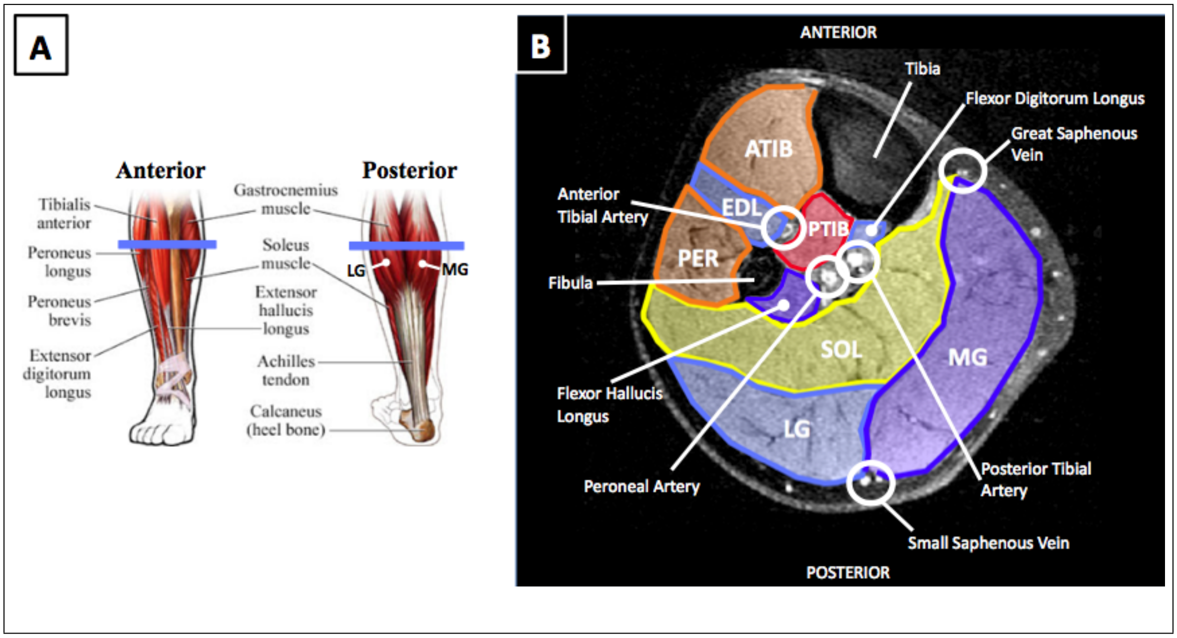

Figure 2.5: The human calf. **(A)** Anterior and posterior views depicting muscles in the calf. Blue line represents approximate location of axial slice. **(B)** Axial T1-weighted MR image at widest cross-section of calf, showing key muscles, blood vessels, and bones of the lower leg. ATIB: Anterior Tibialis; EDL: Extensor Digitorum Longus; PER: Peroneus Longus; PTIB: Posterior Tibialis; SOL: Soleus; LG: Lateral Gastrocnemius; MG: Medial Gastrocnemius. (Credit: Figure 2.5a adapted from *bodybuilding-mauritius.blogspot.ca*)

The human calf serves as a convenient model with which to study the effects of exercise upon skeletal muscle, as this limb is easily isolated, and controlled movements of the foot can induce contraction in specific sets of muscles depending on the particular movement, body center of gravity, or angle of the knee joint <Basmajian and de Luca, 1985; Miaki *et al.*, 1999>. Furthermore, individual muscles which make up the calf are known to differ in terms of their typical fiber distribution <Johnson *et al.*, 1973; Edgarton *et al.*, 1975>, fiber angle <Okamoto *et al.*, 2012>, and blood supply <Andersen and Kroese, 1978>.

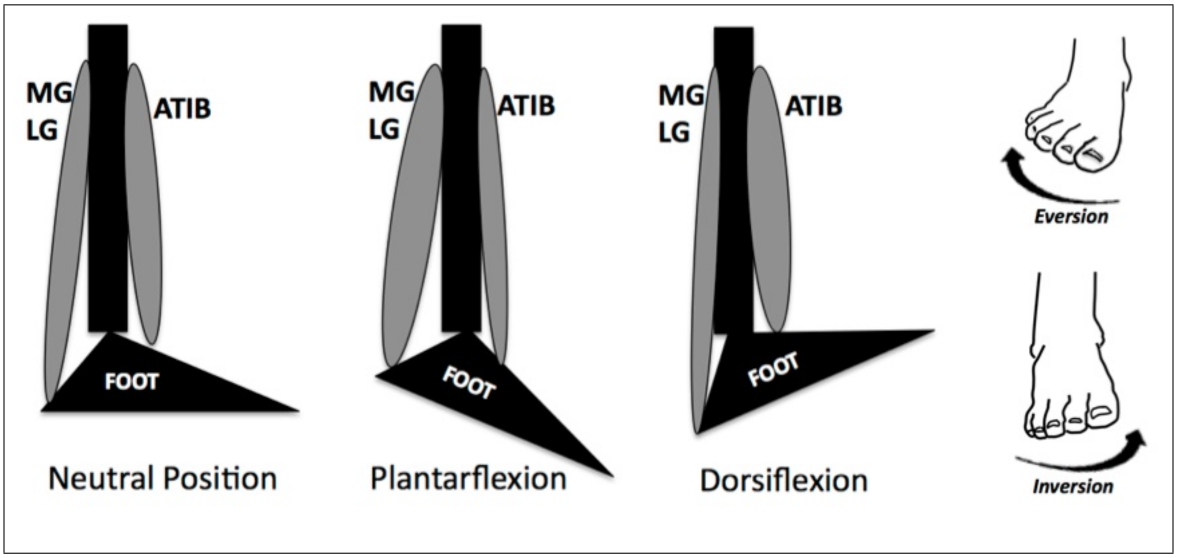

Figure 2.6: Movements of the foot around the ankle. MG: Medial Gastrocnemius, LG: Lateral Gastrocnemius, ATIB: Anterior Tibialis. (Credit: Partially adapted from <Okamoto *et al.*, 2010>.)

There are several key muscles that make up the majority of muscle volume within the calf. The first is the gastrocnemius, which is made up of lateral and medial compartments (MG and LG), and is found in the posterior portion of the calf (Fig. 2.5). Contraction of the gastrocnemius pulls the end of the foot and toe downward, known as plantarflexion <Basmajian and de Luca, 1985> **(Fig. 2.6)**. Both compartments of this muscle have been found to contain approximately equal amounts of fast-twitch and slow-twitch fibers <Johnson *et al.*, 1973; Edgarton *et al.*, 1975>, and thus this muscle serves to contract rapidly to provide fast limb movement for running and jumping.

The second muscle is the soleus (SOL), found in the central portion of the calf, posterior to the tibia and fibula (Fig. 2.5). The soleus provides long-term plantarflexion to support the body's weight when standing <Basmajian and de Luca, 1985>, propulsion during walking <Snell, 2012>, and is particularly active in plantarflexion when the the knee is bent <Miaki *et al.*, 1999> **(Fig. 2.6)**. The soleus contains a large percentage of slow-twitch fibers (about 70-87% <Johnson *et al.*, 1973; Edgarton *et al.*, 1975>), as well as a high density of capillarization, allowing for a greater supply of oxygen via the blood.

The third considerable calf muscle is the anterior tibialis (ATIB), found anterolateral to the tibia **(Fig. 2.5)**. Contraction of this muscle pulls the end of the foot and toes upwards (dorsiflexion) **(Fig. 2.6)**, and also assists in supporting the arch of the foot. The ATIB has been found to have a greater percentage of slow-twitch fibers (73.1%) than fast-twitch <Johnson *et al.*, 1973>.

In addition to these muscles, there are numerous smaller muscles within the calf such as the peroneus longus, posterior tibialis, extensor digitorum longus (EDL), and extensor hallucis longus. These muscles assist the three main muscles in foot stabilization against body weight, and are responsible for fine movements of the foot, such as eversion and inversion **(Fig. 2.6)**.

2.5.1 Blood Supply to Calf Muscles

(**NOTE:** This summary is based on <Guyton and Hall, 2006> and <Snell, 2012>).

Blood flow to the calf is supplied by the popliteal artery, which is an extension of the femoral artery. Distal to the patella, this artery splits into two main branches:

the anterior tibial artery and the posterior tibial artery. A further branch of the posterior tibial artery produces the peroneal artery. In the region of calf, all three of these arteries are located deep within the leg **(Fig. 2.5)**. The anterior tibial artery supplies blood to muscles such as the anterior tibialis and extensor digitorum longus, while the peroneal artery supplies the peroneus longus and other lateral muscles. The posterior tibial artery remains the largest of these three arteries, and supplies muscles such as gastrocnemius and soleus.

Small branches extend from these arteries, reducing in diameter to a network of capillaries that penetrate the muscle. After blood has passed through the muscle, these capillaries empty into venules and then larger veins. Veins in the calf contain valves that allow only unidirectional blood flow, an anti-gravity adaptation that directs blood back up to the heart. Furthermore, these perforative veins are arranged in a manner whereby any contraction of a muscle squeezes blood out of the tissue, providing additional pressure to venous blood movement, a construct known as the "venous pump".

Ultimately, these smaller veins empty into either the great saphenous or small saphenous veins, which travel under the surface of the skin and deep fascia along the medial aspect of the calf or between the heads of the gastrocnemius, respectively **(Fig. 2.5)**.

Chapter 3

Magnetic Resonance Imaging

Magnetic resonance imaging (MRI) is a diagnostic imaging modality that allows for non-invasive assessment and measurement of soft tissues *in vivo.* MRI uses radiofrequency (RF) pulses and magnetic field gradients within a strong static magnetic field to excite nuclei within tissue, and uses RF coils (i.e. antennae) to monitor the return of these nuclei to equilibrium. The nucleus typically targeted by MRI is that of hydrogen, the most abundant atom in the human body, and can occur in the form of free water, fats, and as bound to macromolecules. MRI is routinely used clinically for the evaluation of diseases, injuries, and vascular insufficiency. This chapter describes the primary MRI scan used in this thesis (diffusion imaging) and also T_2 mapping due to its use in the MRI exercise literature.

3.1 Diffusion Imaging

Diffusion imaging is based on a nuclear magnetic resonance (NMR) technique, first proposed by Stejkal & Tanner <Stejkal and Tanner, 1965>, that allows the measurement of free water mobility through the use of direction-specific magnetic field gradients and refocusing RF pulses <McRobbie *et al.*, 2006>.

Within a liquid medium, individual particles (in this case, hydrogen nuclei within free water molecules) are propelled by thermal energy throughout the medium, yet collide with other particles to produce a random and erratic three-dimensional trajectory, a process known as Brownian motion. However, within tissue, membranous barriers inhibit the spatial range of Brownian motion, allowing the structure of the tissue to be probed according to this restriction of free water. By measuring the net movement of water for a given location, diffusion MRI can provide valuable insight into tissue structure and dynamic behaviour.

3.1.1 Acquiring diffusion images using MRI

Diffusion MRI relies upon the spin-echo (SE) phenomenon. To generate a spin echo, a 90 degree RF pulse tips proton magnetization into the transverse plane, upon which the magnetization begins to dephase. A subsequent 180 degree RF pulse then inverts the magnetization and causes the dephasing protons to now rephase, eventually producing an echo which is measured by the RF coil of the MRI (at time TE).

Diffusion imaging involves a further manipulation to the typical SE-MRI acquisition strategy by employing two identical gradients on either side of the 180-degree RF pulse, known as the Pulsed Gradient Spin Echo (PGSE) **(Fig. 3.1)**. These gradients can be oriented along any three-dimensional direction, as they are comprised of a combination of X-, Y-, and Z-axis components from separate MR gradient coils. Once a diffusion gradient is applied, the precession speed of the hydrogen protons is linearly increased or decreased along the length of the gradient.

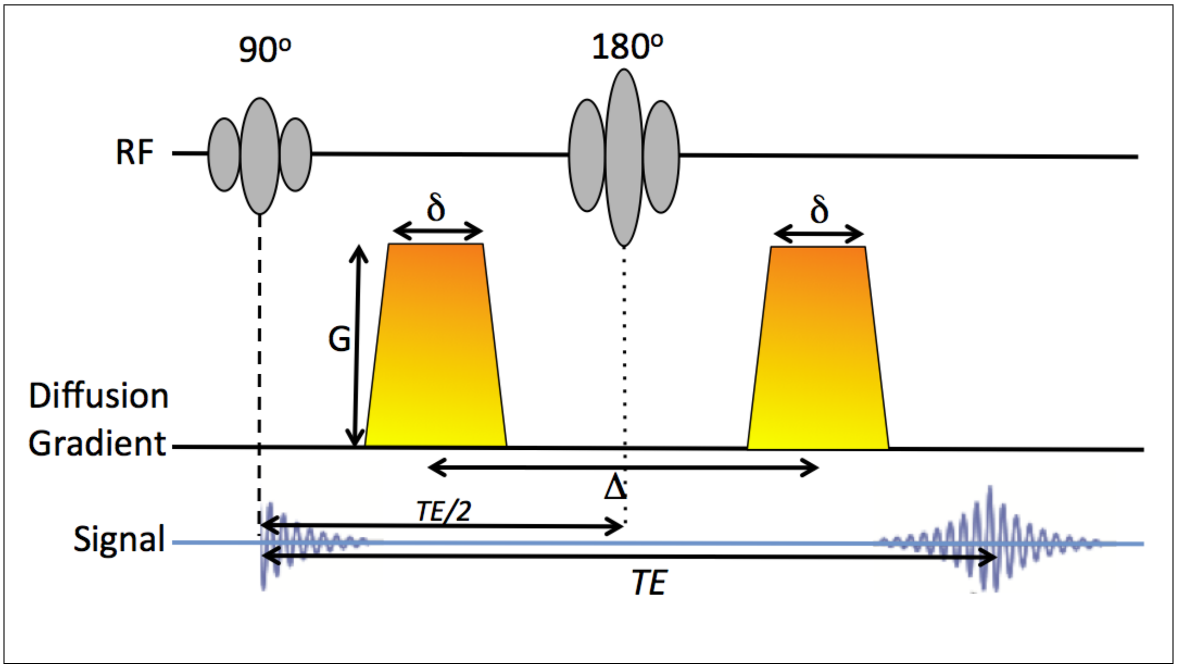

Figure 3.1: Simplified pulse sequence diagram of diffusion acquisition. The timing of the radiofrequency pulses (RF), diffusion gradients, and resulting signal are depicted. TE is the time between initial 90^o pulse and echo (signal acquisition), G is gradient magnitude, δ is the gradient pulse width, and Δ is the center-to-center time between the two diffusion gradients.

The first diffusion gradient serves to impose a phase shift on protons dependent upon where along the gradient the proton is located **(Fig. 3.1)**. Following the SE 180-degree pulse, the second diffusion gradient is applied, after which the echo occurs and detected by the RF coil. Theoretically, if protons have not moved during time Δ there is full recovery of the spin echo, and thus a large signal is induced in the RF coil. However, if a proton has moved along the particular gradient, the spins are incompletely refocussed. The greater the net movement along the gradient, the less the rephasing, and thus the echo magnitude is reduced.

The amount of diffusion to which the MRI is sensitized (the "diffusion weighting") is achieved by adjusting the timing and amplitude of the gradients. The parameters are combined to produce a "b-value" (measured in units of seconds/mm^2) according to the following equation:

$$b = \gamma^2 G^2 \delta^2 \left(\Delta - \frac{\delta}{3} \right) \tag{3.1}$$

where γ is the gyromagnetic ratio of hydrogen nuclei, G is gradient magnitude, δ is the gradient pulse width, and Δ is the center-to-center time between the two diffusion gradients (see **Fig 3.1**).

Diffusion imaging with a small b-value (e.g. b=50 s/mm^2) will thus use small gradients with minimal inter-gradient time, and be sensitive only to fast-moving protons, such as blood flow or perfusion <LeBihan *et al.*, 1986>. Conversely, the use of a high b-value (e.g. b>2000 s/mm^2) can probe the slow movements of protons attached to macromolecules. Typical b-values used in the brain are b=900-1200 s/mm^2 (e.g. <Mabbott *et al.*, 2006>), while studies of muscle tend to use b=400-500 s/mm^2 (e.g. <Damon, 2008; Lansdown *et al.*, 2007>).

3.1.2 Quantification of Diffusion Imaging

In order to measure the effect of diffusion weighting on signal loss, acquisition of a baseline image must accompany collection of diffusion-weighted images. The baseline image is acquired with the same MR parameters as the diffusion-weighted images, but without diffusion gradients (therefore b=0 s/mm^2). The loss of signal in the diffusion-weighted image is then compared against the b=0 image to provide an estimate of diffusion along the gradient direction for each location in the image, according to the following equation:

$$D = \frac{-1}{b} ln \left(\frac{S(b)}{S(0)} \right) \tag{3.2}$$

where *b* is the diffusion weighting, *S(b)* is the signal intensity of the diffusion-weighted image, and *S(0)* is the signal intensity of the baseline image. The value obtained (D) is referred to as the Apparent Diffusion Coefficient or ADC (”apparent” being added to account for the potential media heterogeneity represented for each location, or voxel, as a net value), and is measured in units of mm^2/second.

3.1.3 Diffusion within tissue

Within tissue, the self-diffusion of hydrogen protons (as free water) is restricted by physical barriers, such as cell membranes, organelles or other large structures, and further governed by factors such as viscosity, temperature, and the presence of blood perfusion <LeBihan *et al.*, 1986, 2001>. Acquisition of diffusion measures along multiple gradient directions therefore allows a three-dimensional representation of net fluid mobility to be estimated, and thus provides insight into the local tissue microstructure.

For example, the acquisition of diffusion measurements from three orthogonal gradient directions has been shown to have great clinical value, as it can detect alterations in tissue structure not apparent on routine anatomical MRI scans <Moseley *et al.*, 1990>. Furthermore, this method is often used in assessment of acute stroke, where diffusion images aid in distinguishing necrotic from affected yet viable tissue, known as *diffusion-perfusion mismatch* <Neumann-Haefelin *et al.*, 1999>. However, while this 3-gradient strategy has shown to be suitable in qualitatively contrasting the

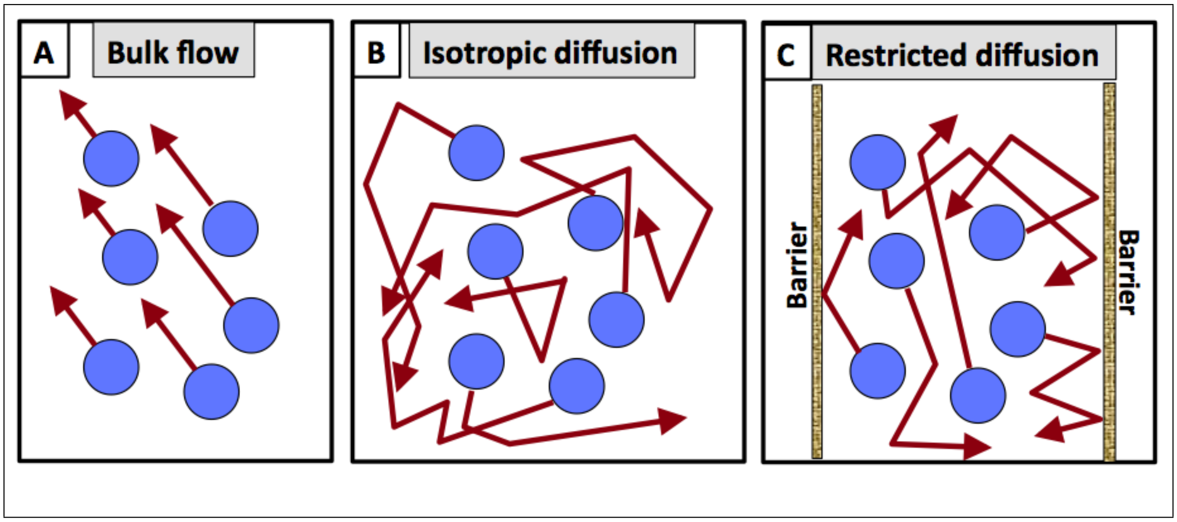

Figure 3.2: Representation of hydrogen proton mobility through tissue. **(A)** Directional flow, such as within blood vessels. **(B)** Isotropic diffusion (unhindered Brownian motion). **(C)** Restricted diffusion (Brownian motion confined within barriers).

overall diffusion between tissue states, it is less than adequate for quantitative representation of anisotropic tissue. Elongated tissues, as found in the brain or skeletal muscle, provide substantial barriers to diffusion along the cross-section of the fibers, with less inhibition along the long axis of the fiber.

Individual measurements of diffusion along each orthogonal gradient direction have been shown to reflect anisotropy in cerebral tissues <Moseley *et al.*, 1990>. This implies that quantitative measurements are affected by the angle between fiber orientation and diffusion gradient directions (i.e. *rotational variance*). In short, ADC calculations of the three axes would differ if the relationship between fiber orientation and gradient direction were to change, as in being parallel to one particular gradient direction rather than being oblique to all three directions, the latter preventing the true long axis from being accurately measured. This issue has been addressed by the development of a technique that better quantifies the orientation of fibers within three dimensional space: Diffusion Tensor Imaging.

3.1.4 Diffusion Tensor Imaging (DTI)

Diffusion Tensor Imaging (DTI) is a rotationally-invariant form of diffusion imaging that calculates a three-dimensional ellipsoidal representation of diffusion within MRI space, regardless of the orientation of tissue relative to diffusion gradients (and thus *rotational invariance*). Based on the work of Basser *et al* <Basser *et al.*, 1994; Basser and Pierpaoli, 1996>, this method utilizes diffusion volumes from at least six non-collinear gradient directions, which are in turn combined by multivariate linear regression to calculate the tensor ellipsoid **(Fig. 3.3)**.

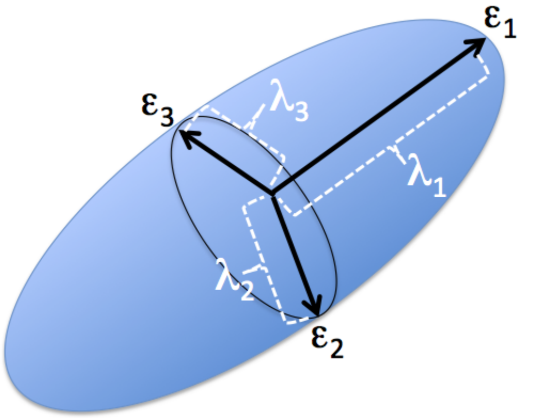

Figure 3.3: The diffusion tensor ellipsoid. The eigenvectors $(\varepsilon_1, \varepsilon_2, \varepsilon_3)$ represent the vector orientation of the three main ellipsoidal axes, while the eigenvalues $(\lambda_1, \lambda_2, \lambda_3)$ represent the length of each of these vectors.

A number of software tools for diffusion tensor calculation and image analysis have been made freely available for academic research purposes. Examples of such tools are *FDT* (part of the FMRIB Software Library (FSL) <Jenkinson *et al.*, 2012>), *DTIStudio* <Jiang *et al.*, 2006>, and *Diffusion Toolkit* (www.trackvis.org).

The length of the 3 major orthogonal axes of the ellipsoid, sorted from longest to shortest, are referred to as the *eigenvalues* $(\lambda_1, \lambda_2, \lambda_3)$, while the directional orientation of these axes within three-dimensional space are referred to as the *eigenvectors* $(\varepsilon_1, \varepsilon_2, \varepsilon_3)$.

The potential utility of DTI was demonstrated with evidence that the orientation of the principal eigenvector (ε_1) corresponded with the fiber orientation of targeted tissue <Basser *et al.*, 1994>. These findings imply that measures of the tensor ellipsoid can be used as indicators of tissue structure. This is most commonly performed by using the three eigenvalues to calculate scalar indices representing the size (mean diffusivity) and shape (fractional anisotropy) of the tensor ellipsoid.

Mean Diffusivity (MD) represents the overall amount of diffusion for a given location, based upon the long axis of the ellipsoid, and is measured in units of mm^2/second:

$$\mathbf{MD} = \left(\frac{\lambda_1 + \lambda_2 + \lambda_3}{3}\right) \tag{3.3}$$

The shape of the ellipsoid is represented by the measure of Fractional Anisotropy (FA), calculated as follows:

$$\mathbf{FA} = \sqrt{\frac{3}{2}}\sqrt{\frac{(\lambda_1 - MD)^2 + (\lambda_2 - MD)^2 + (\lambda_3 - MD)^2}{\lambda_1^2 + \lambda_2^2 + \lambda_3^2}} \tag{3.4}$$

Measures of FA are unitless and range from 0 to 1 **(Fig. 3.4)**. A value of 0 indicates that all three eigenvalues are equal, and indicate diffusion within a medium that is unhindered, or hindered equally in all directions. On the other hand, an FA value of 1 indicates a line with no three-dimensional cross area, with the ideal example being the first eigenvalue (λ_1) having infinite length, while the two minor eigenvalues $(\lambda_2$, $\lambda_3)$ having a length of zero.

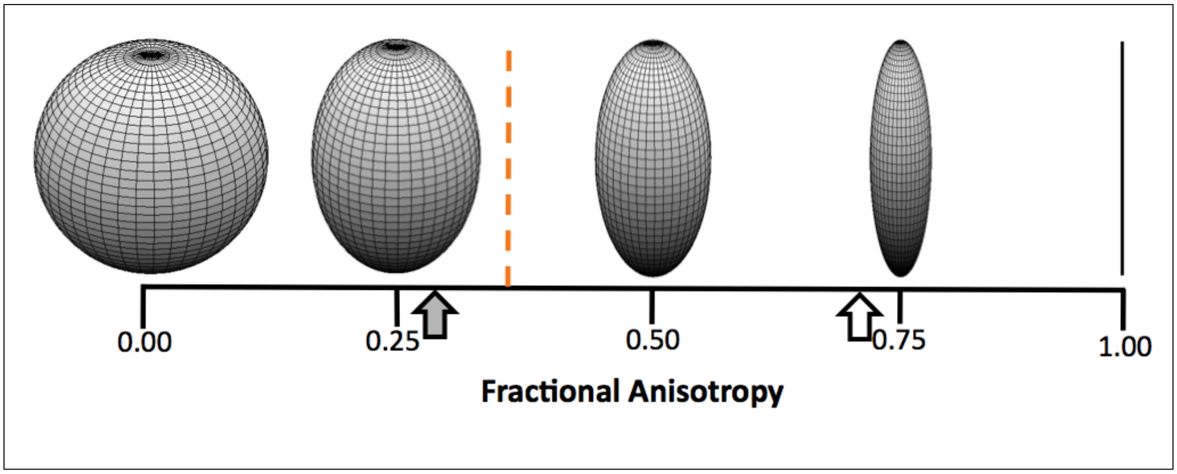

Figure 3.4: Visualization of FA range. White arrow represents approximate FA values for major white matter tracts in the brain, gray arrow represents approximate FA of skeletal muscle. Dashed orange line represents typical FA cutoff used in fibertracking algorithms within the brain.

Within the scientific literature, FA measures are often used as an index to quantify the integrity of anisotropic tissue. For example, within the brain, a decrease in FA for white matter tracts indicates greater freedom of water movement perpendicular to the fiber, and thus could indicate decreased fiber packing and/or neuronal myelination <Beaulieu, 2002>. Additionally, FA measures of white matter have been found to correspond with both age and neuropsychological assessments <Mabbott *et al.*, 2006>.

Radial Diffusivity (RD) represents the mean of the two minor eigenvalues (λ_2, λ_3), and is measured in units of mm^2/second:

$$\mathbf{RD} = \left(\frac{\lambda_2 + \lambda_3}{2}\right) \tag{3.5}$$

Measures of RD are used to represent diffusion perpendicular to the long axis of the ellipsoid in DTI studies where indices of the individual minor eigenvalues are of less concern (e.g. cylindrical neural fibers) or directionally uncertain.

A further use of DTI is to perform fiber tracking of anisotropic tissue based on the connectivity of ε_1 between adjacent voxels. While fiber-tracking has served to further popularize the use of DTI in both brain <Mori *et al.*, 1999> and muscle <Heemskirk *et al.*, 2005> to represent tissue architecture, not to mention production of impressive computer renderings, this technique is difficult to quantify and as such not utilized in this thesis.

3.1.5 Diffusion Imaging, DTI, and Skeletal Muscle

It has been shown that the anisotropy of mammalian *ex vivo* skeletal muscle can be detected using the 3-gradient DWI method <Cleveland *et al.*, 1966>, and further, that DTI measures of ε_1 correspond with fiber orientation <van Doorn *et al.*, 1996; van Donkelaar *et al.*, 1999; Damon *et al.*, 2002b>. However, diffusion imaging of *in vivo* human muscle presents more challenges than *ex vivo* tissue samples, as the magnetic field strength of clinical MRI machines is lower than research NMR units, and assessment of diffusion is complicated by factors such as fluidics within the living tissue, subject movement, and the potential for signal-to-noise (SNR) differences with distance from the RF coil.

Nonetheless, DTI has been used been used to investigate the structure of skeletal muscle in many regions of the human body, such as jaw <Liu *et al.*, 2016>, forearm <Froeling *et al.*, 2012>, lower back <Jones *et al.*, 2013>, female pelvic floor <Zijta *et al.*, 2013>, thigh <Budzik *et al.*, 2002; Kermarrec *et al.*, 2010>, calf <Galban *et al.*, 2004; Sinha *et al.*, 2006; Karampinos *et al.*, 2009>, and foot <Elzibak *et al.*, 2014>. Furthermore, it has been demonstrated that tractography is feasible within human skeletal muscle despite lower FA values than observed in the brain (see **Fig. 3.4**), and the fiber tracking appears to correspond with fiber orientation <Deux *et al.*, 2008; Heemskirk *et al.*, 2010; Lansdown *et al.*, 2007; Zaraiskaya *et al.*, 2006>.

It has been further observed that the cross-section of ellipsoids (i.e. λ_2 and λ_3) calculated from human calf muscle tend to be themselves anisotropic (i.e. λ_2>λ_3 rather than λ_2=λ_3), prompting one study to suggest that λ_2 represents movement across a sheet or layer of muscle, while λ_3 is indicative of cross-fiber diffusion <Galban *et al.*, 2004>. This theory appears to correspond with reports that the cross-sectional shape of the underlying muscle fibers is more elliptical rather than circular <Campos *et al.*, 2002; Karampinos *et al.*, 2009>. However, little work has been performed to substantiate this theory of eigenvalue meaning within human skeletal muscle. Furthermore, simulation studies have reported that the individual eigenvalues can also be affected by MR acquisition conditions, such as low values of signal-to-noise ratio (SNR) contributing to over-estimation of λ_1 and underestimation of λ_3 <Damon, 2008>.

An additional consideration in the study of skeletal muscle using diffusion imaging is that this tissue is pliable rather than rigid. DTI measures have shown to be sensitive to changes in muscle shape and body positioning. For example, calf muscles that are contracted either passively or without weighting demonstrate decreases in λ_1 and increases in λ_2 and λ_3, attributed to fattening of the sarcomere and the bulbous nature of the overall muscle <Deux *et al.*, 2008; Hatakenaka *et al.*, 2008, 2010>. Elongation of the opposing muscles appear to have the opposite effect. The changes in eigenvalues in turn play into calculations of FA, which thus decreases in contracted muscle, and increases in elongated muscle <Deux *et al.*, 2008; Hatakenaka *et al.*, 2008, 2010>. Furthermore, external compression on resting muscle has been shown to affect results by decreasing λ_3 and increasing FA <Hata *et al.*, 2012>. Finally, DTI measures in the calf have been shown to be affected by changes in body positioning from standing to lying supine, thought to represent a redistribution of body water <Elzibak and Noseworthy, 2014>.

Pathological skeletal muscle tissue has also been investigated using DTI. Within animal models, increases in MD and decreases in FA have been observed at points of injury, associated with loss of muscle force, and shown to disrupt fiber tracking <McMillan *et al.*, 2011>. Similar DTI results have been found in studies of human subjects with muscle injury <Zaraiskaya *et al.*, 2006>. DTI has also been used to investigate muscle features of more chronic conditions, such as pennation angle and force modelling in patients with lateral patellar dislocation <Kan *et al.*, 2009>, elevations in the MD of affected muscles in inflammatory conditions such as polymyositis and dermatomyositis <Ai *et al.*, 2014>, and comparisons of ADC (MD) and FA with gradations of fatty infiltration in patients with Duchenne Muscular Dystrophy <Li *et al.*, 2016>.

3.1.6 Diffusion Imaging, DTI, Muscle, and Exercise

Skeletal muscle under the influence of exercise is different from resting muscle due to increased blood flow, increased cross-sectional area, increased temperature, metabolic changes, potential membrane damage, and the gradual onset of fatigue <Guyton and Hall, 2006; McKenna and Hargreaves, 2008>. Therefore, observation of the functional behaviour of this tissue in response to a task can provide complementary information to static assessments regarding muscle dynamics or health. Acquisition of diffusion imaging during exercise is currently not possible due to motion artifacts, although some studies have investigated the changes in muscle using DTI during resistive isometric contraction <Okamoto *et al.*, 2010>. However, once the exercise is complete and the exercised region returned to a motionless position, MRI can then be used to investigate the effects of exercise upon diffusion within skeletal muscle tissues.

A number of groups have used diffusion MRI techniques to evaluate the acute changes occurring within human skeletal muscles following a bout of exercise. Early studies observed that diffusion in muscle would increase from baseline following exercise <Morvan, 1995; Nygren and Kaijser, 2002; Ababneh *et al.*, 2008>. Moreover, by acquiring a series of consecutive scans, these studies observed that post-exercise diffusion then gradually decreased from this initial elevation over the course of 10-20 minutes <Morvan, 1995; Nygren and Kaijser, 2002; Ababneh *et al.*, 2008>. Furthermore, greater work loads during exercise were found to induce greater diffusion increases <Nygren and Kaijser, 2002>. While these studies were able to demonstrate an acute timecourse of diffusion changes within the muscle, the directional resolution of diffusion-encoding gradients was minimal, due to both temporal constraints and MRI hardware and gradient limitations.

With the advent of DTI, research into post-exercise muscle changes shifted towards using static assessment of tissue structure. The fractional anisotropy (FA) was found to decrease following exercise, indicating that water movement throughout the tissue became more isotropic <Okamoto *et al.*, 2008>. Strenuous eccentric exercise was found to demonstrate reduced FA and increased mean diffusivity (MD) for several days after the exercise, the levels of which correlated with soreness and histological evidence <Yangisawa *et al.*, 2011; Cermak *et al.*, 2012>. Longer exercise tasks, such as a marathon, have been found to show elevated MD in thigh muscles up to three weeks post-event while no detectable changes were observed in corresponding anatomical scans <Froeling *et al.*, 2015>.

While the forementioned DTI studies have assessed a longer time period in response to damaging exercise, little literature exists using consecutive DTI acquisition to assess acute temporal muscle changes.

3.2 T_2 measurements of skeletal muscle

Within the fields of NMR and MRI, the term "T_2" represents the loss of transverse magnetization in hydrogen protons within a medium due to interactions with other protons, and thus is also known as *spin-spin relaxation*.

Strictly speaking, the T_2 of a medium is the time needed for the signal to exponentially decay from the maximum level (immediately after RF excitation) to 37 % of the original signal, and is essentially independent of magnetic field strength <McRobbie *et al.*, 2006; Stanisz *et al.*, 2005>. Pure water has a long T_2, as the free hydrogen protons are able to influence the magnetization of one another, but protons bound to macromolecules and other tissue structures have shorter T_2, as their binding inhibits their ability to maintain transverse magnetization.

Therefore, should adjacent tissue regions have differing water compartmentalization, this may produce differing relaxation rates of transverse magnetization. MRI can exploit this phenomenon by acquiring data at times that accentuate differences in remaining transverse magnetization, thus providing contrast between tissues. As an example, Stanisz *et al.* found that within the bovine brain, white matter has a T_2 of 69 ms at 3 Tesla, and thus appears darker than gray matter, which has a T_2 of 99 ms <Stanisz *et al.*, 2005>. In comparison, the same study found that T_2 of musine skeletal muscle is shorter than cerebral tissue, with a T_2 of 50 ms, while human blood has a long T_2 of 275 ms <Stanisz *et al.*, 2005>.

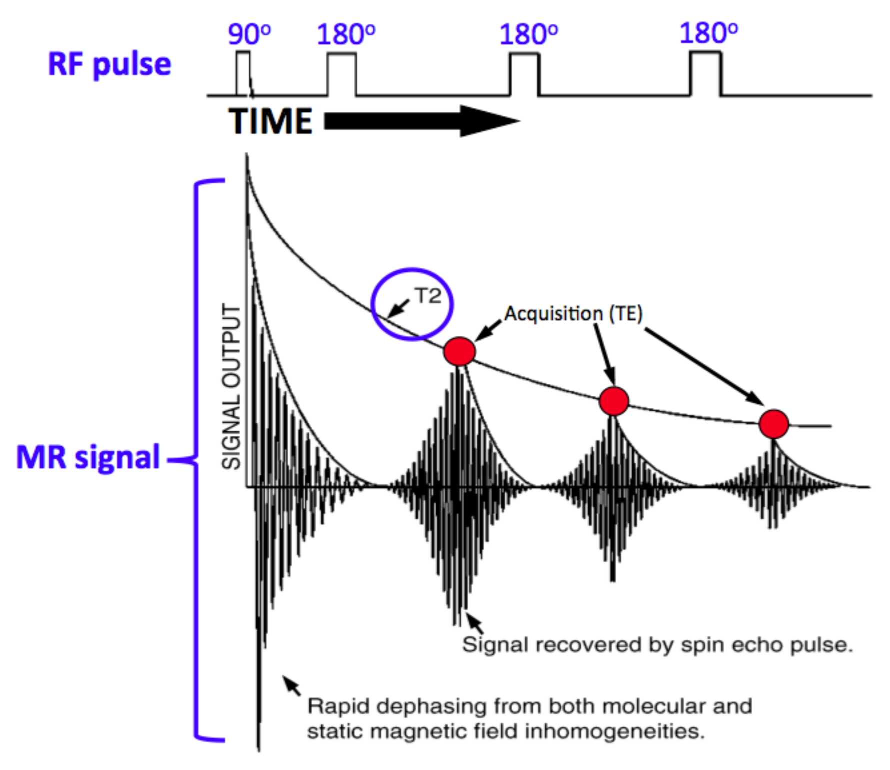

Figure 3.5: Depiction of T_2 measurement using the CPMG sequence. A 90° RF pulse is initially administered to induce transverse magnetization, followed by a series of 180° RF pulses which produce a chain of spin echoes. MR signal is acquired at each echo time (TE, red dots), and a curve is fitted to these signal measurements (T2, blue oval). Although this diagram depicts three echoes, the number of echoes is typically much higher, and results in a multi-exponential curve fit. (Credit: courtesy of *Dr. MD Noseworthy*)

The precise T_2 decay curve for a given tissue is quantified using the Carr-Purcell-Meiboom-Gill (CPMG) sequence, which acquires a chain of MR images with increasing signal acquisition echo times <Carr and Purcell, 1954; Meiboom and Gill, 1958>

(**Fig. 3.5**). This technique allows the detailed modelling of T_2 relaxation within tissues, and it has been shown that skeletal muscle has a multi-exponential T_2 relaxation rate with up to 4 components. These components are believed to belong to (in order of increasing T_2): macromolecules, intracellular (2 components), and extracellular water <Saab *et al.*, 1999>. There is some debate as to whether these compartments represent differing rates of hydrogen proton exchange, exchange of magnetization, or true anatomical compartmentalization <Fung and Puon, 1981; Saab *et al.*, 1999; Noseworthy *et al.*, 1999>. Blood oxygenation has also been shown to have influence longer T_2 components in this multi-exponential analysis <Noseworthy *et al.*, 1999>. Nonetheless, the acquisition of a single T_2-weighted image of skeletal muscle will have contributions of each of these components, dependent on the time of acquisition.

3.2.1 T_2, muscle, and exercise

Numerous studies have investigated the relationship between T_2 and activation within skeletal muscle. T_2 relaxation does not change when human calf muscles are passively contracted or elongated <Hatakenaka *et al.*, 2008>, yet there are marked increases in T_2 within active muscles following exercise <Fleckenstein *et al.*, 1988; Fisher *et al.*, 1990; Ploutz-Snyder *et al.*, 1997; Saab *et al.*, 2000; Ababneh *et al.*, 2008>. Furthermore, studies have used these T_2 increases to identify recruited muscles for a particular exercise task <Fleckenstein *et al.*, 1988; Green and Wilson, 2000>. Correlations have also been found between the level of exertion during exercise and subsequent increases in T_2 signal <Fisher *et al.*, 1990; Adams *et al.*, 1992; Nygren and Kaijser, 2002>. However, some debate exists as to how accurately T_2 change represent the full range of exercise intensity, as only conditions of greater exercise intensity seem to induce these T_2 increases <Fleckenstein *et al.*, 1988; Nygren and Kaijser, 2002>.

There have many explanations proposed for this post-exercise increase in T_2, such as an increase in extra-cellular water or exercise-related edema <Fleckenstein *et al.*, 1988>. However the T2 change of edema is different than that seen following exercise <Ploutz-Snyder *et al.*, 1997> or venous occlusion of passive muscle <Fisher *et al.*, 1990>. Additionally, T2 increases are seen even in the absence of arterial blood flow <Fleckenstein *et al.*, 1988>. Other suggestions have been that the T2 increase is related to a reorganization of tissue water, such as the release of bound intracellular water to free compartments <Saab *et al.*, 2000; Nygren and Kaijser, 2002; Ababneh *et al.*, 2008>, or osmotic water shifts induced by the accumulation of acidic metabolic byproducts of anaerobic glycolytic metabolism <Fung and Puon, 1981; Fisher *et al.*, 1990; Prior *et al.*, 2001; Damon *et al.*, 2002a>.

Chapter 4

Problem Statement and Objectives

4.1 Preliminary Study and Inspiration for Thesis

Early in the project that evolved into this dissertation, an exploratory experiment was undertaken to study the effect of caffeine on DTI measures following exercise. The present chapter briefly describes the rationale, methods, and results of this initial experiment, and then delves into how the research direction drastically shifted based on this preliminary study.

Based on the literature described in the previous chapter, it seemed that post-exercise increases in ADC or MD reflected workload experienced by the muscles during exercise. Caffeine (trimethylxanthine) is a substance known to have stimulatory, vasodilatory, and calcium-release moderating properties, and thus its performance-enhancing attributes have been the focus of many exercise studies (as reviewed in <Graham, 2001>). The initial experiment proposed that the presence of caffeine prior to exercise would reduce the diffusion increases observed in skeletal muscle following exercise.

4.1.1 Methods (Analysis v1.0)

Muscles in the human calf were chosen for this study, with weighted plantarflexion of the ankle used as an exercise model to initiate dynamic changes within the active muscles, specifically the gastrocnemius and soleus <Snell, 2012>. The widest cross-section of the calf in 6 volunteers (4 males, mean age 29.8 yrs) was scanned prior to and immediately following a session of plantarflexion. Two trials were performed in random order on separate days, one trial with 200mg caffeine consumed an hour prior to exercise, and a second trial performed without caffeine.

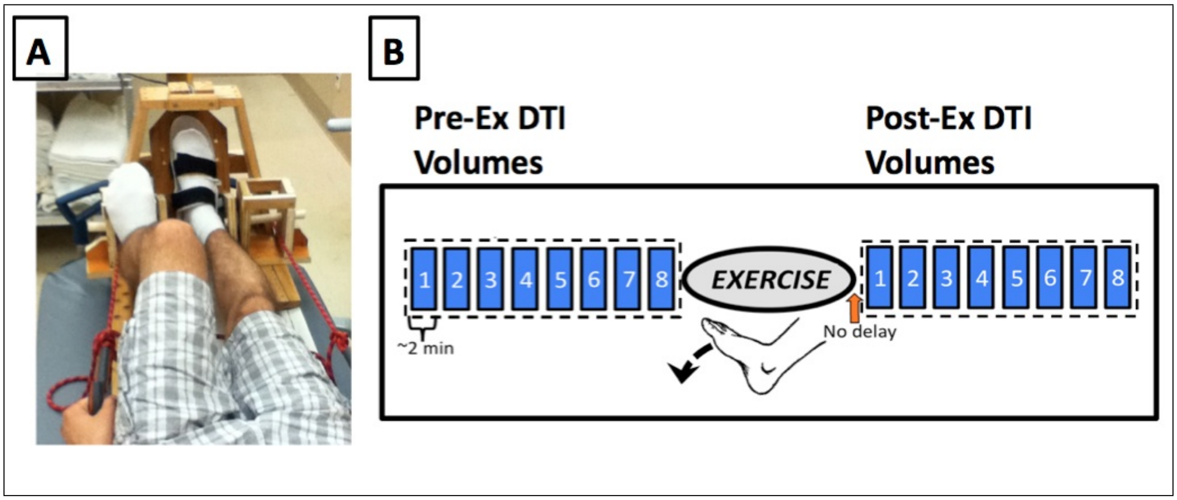

Figure 4.1: Experimental Setup. **(A)** Example of subject positioning within wooden MRI-compatible ergometer used for plantarflexion experiments. **(B)** Temporal layout of DTI acquisition with exercise. Eight 15-direction DTI volumes were acquired in succession prior to exercise (Pre-Ex), plantarflexion was performed for 2.5 minutes, and then another eight 15-direction volumes (Post-Ex) were acquired immediately after cessation of exercise.

Prior to scanning, a custom-built MRI-compatible ergometer (”Woody”) was used to estimate the ”maximum weight, single flex” (MWSF) of each subject for plantarflexion using this equipment **(Fig. 4.1a)**.

The exercise protocol during the experiment consisted of in-bore plantarflexion using "Woody" at 50% MWSF at a rate of 0.5 Hz for 2.5 minutes. DTI data sets were acquired before and immediately after the exercise, with each set consisting of eight consecutive 15-direction DTI volumes (108 seconds/volume) **(Fig. 4.1b)**. The multiple volumes of each set were acquired with the intention of combining them into a single volume during post-processing in order to increase the signal-to-noise ratio (SNR).

4.1.2 Results and Conclusions (v1.0)

The results of this study indicated that the plantarflexion induced a large increase in the gastrocnemius MD from baseline, while the soleus showed minimal change. Furthermore, the similarity of MD between caffeinated and non-caffeinated trials suggested that the presence of caffeine did not affect post-exercise diffusion (**Fig. 4.2**).

The Inspiration (aka Change in Project Direction)

A curious result was observed when examining the diffusion volumes in the consecutive order in which they were acquired, rather than the combined volume as was originally intended. The gastrocnemius was found to have negligible change from baseline at the first post-exercise DTI volume (108 seconds post-exercise), but was followed by a substantial increase in MD at the second volume ($\sim$216 seconds post-exercise), and then a decline towards baseline **(Fig. 4.3a)**. In contrast, the soleus revealed a slight increase from baseline after the first DTI volume, after which it decreased to baseline levels.

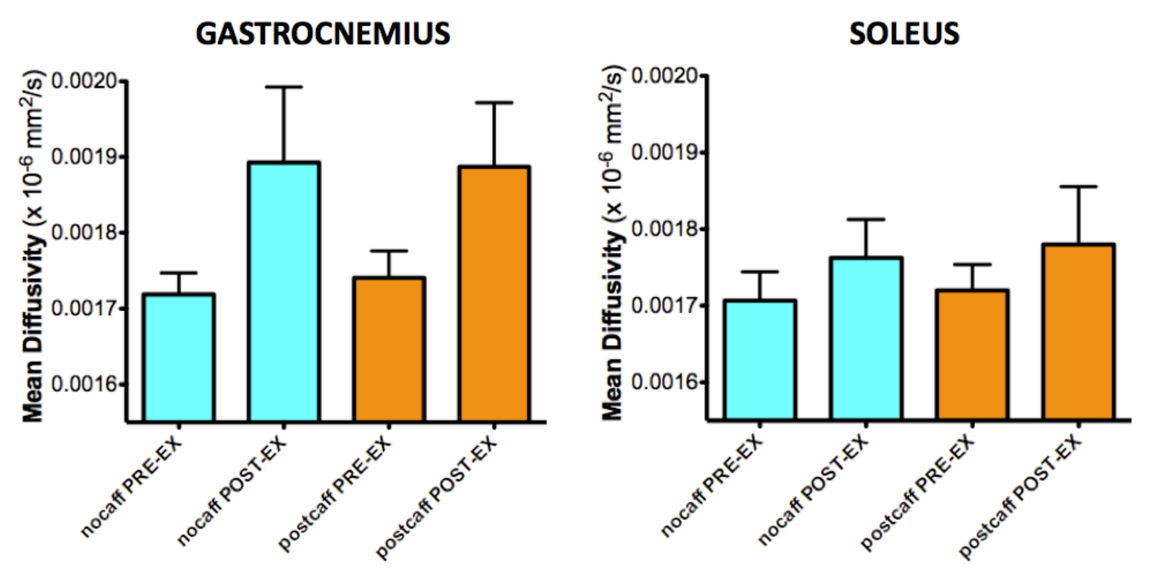

Figure 4.2: Comparison of DTI mean diffusivity (MD) measures within gastrocnemius and soleus with (orange bars) and without (cyan bars) the presence of caffeine. Graph represents MD measures prior to (PRE-EX) and following (POST-EX) a session of plantarflexion. The presence of caffeine did not have a significant effect on either pre- or post-exercise MD measures. Graphs indicate mean MD ± SD.

These results indicated that by collecting several DTI volumes in a row immediately following exercise, dynamic changes in the muscles could be observed, and furthermore, that individual muscles displayed differing patterns of diffusion change. It was therefore decided that the original investigation of caffeine would be abandoned due to its negligible effects on DTI in post-exercise calf muscle, and instead temporal DTI as a tool to study exercise would be pursued.

4.1.3 Methods (Analysis v2.0 - Timecourse)

The non-caffeine DTI data was thus re-analyzed to assess the timecourse of muscles beyond the gastrocnemius and soleus in reaction to the exercise protocol, namely

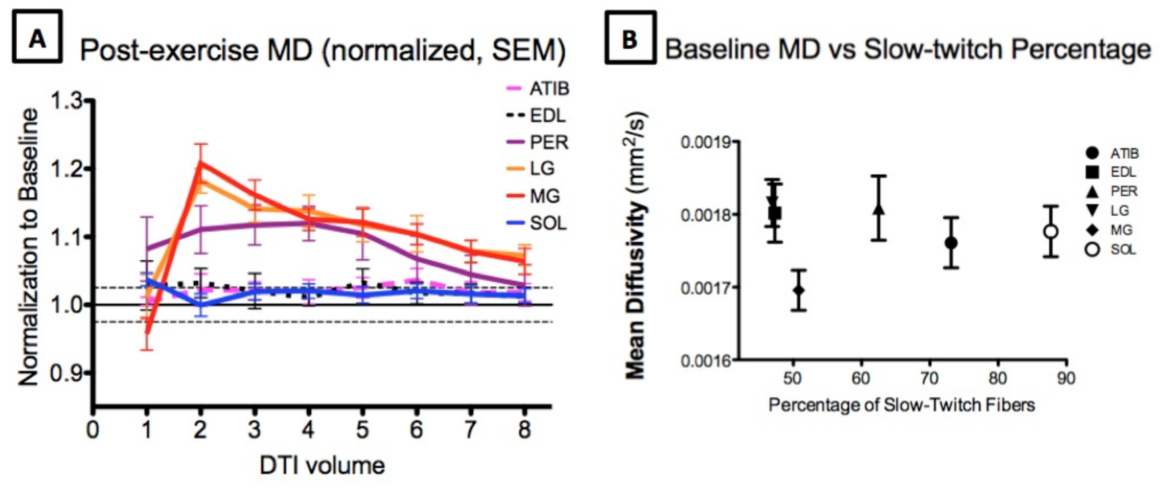

Figure 4.3: Results of exploratory DTI study into calf muscle with plantarflexion. **(A)** Timecourse assessment of individual muscles following exercise. Normalization values for each muscle were calculated using the post-exercise MD value per timepoint divided by the mean of 8 pre-exercise baseline values. Dashed horizontal lines represent mean variation of baseline values across timepoints. **(B)** Baseline mean diffusivity (MD) values of each muscle according to published measures of fiber percentage <Johnson *et al.*, 1973>.

the anterior tibialis (ATIB), the extensor digitorum longus (EDL), and the peroneus longus (PER). Additionally, the two heads of the gastrocnemius (lateral (LG) and medial (MG)) were analyzed separately rather than combined. Post-exercise values were assessed according to the percentage change from baseline.

4.1.4 Results and Conclusions (v2.0)

This timecourse analysis of the DTI data revealed at least three differing patterns of diffusion change following exercise **(Fig. 4.3a)**. First, the two heads of the gastrocnemius (LG and MG) behaved remarkably alike, in that they showed similarity to baseline after the first DTI volume (the first timepoint), a large increase after the second volume (the second timepoint), and subsequent decline. The second pattern was that of PER, which showed a moderate increase at the first timepoint, continuing a gradual increase which peaked at the fourth timepoint, and then subsequently decreasing. The third pattern was minimal departure from baseline, observed in muscles not expected to be active in plantarflexion (ATIB and EDL). The SOL produced a temporal diffusion pattern which was akin to that of uninvolved muscles, which was initially surprising. However, after further background research, it became apparent that the soleus results were likely due to the minimal activation of this muscle during supine straight-legged plantarflexion <Miaki *et al.*, 1999; Price *et al.*, 2003; Yangisawa *et al.*, 2003>.

In seeking a possible explanation for the differing temporal diffusion patterns between gastrocnemius and peroneus (and at the time, soleus), it was found that published studies of muscle fiber content had shown greater percentages of slow-twitch muscle fibers in the soleus and peroneus than in the gastrocnemius <Johnson *et al.*, 1973>, differences that were not apparent during routine scans nor static diffusion imaging **(Fig. 4.3b)**. The results of this study initiated a new line of inquiry into the potential of timecourse DTI to investigate functionality differences between individual muscles.

4.2 Thesis Objectives:

The overall purpose of this body of work was to further explore how DTI, a modality commonly used for assessment of static tissue structure, can be utilized in a functional timecourse manner to characterize dynamic changes within skeletal muscle following exercise.

The notable change in gastrocnemius observed in the preliminary study (**Section 4.1**) was governed by a time resolution of 108 seconds/volume. By increasing the time resolution, it was felt that muscle behaviour of individual muscles following a particular session of exertion could be better quantified and perhaps interpreted. Therefore, by reducing the number of directions used, and acquisition parameters such as *repetition time* (TR), temporal resolution could be increased.

However, the use of MRI requires trade-offs between scan acquisition time and subsequent image quality. The less time spent on scan acquisition, whether in terms of individual volumes or number of gradient directions, the greater the likelihood of reduced scan quality in terms of SNR, spatial resolution, or in the case of DTI, directional resolution.

Furthermore, to assess the utility of a temporal DTI approach in the study of post-exercise skeletal muscle, this technique would need to be tested in other experimental situations beyond that of the preliminary study. Examples of this would be measurement of post-exercise change in other muscle groups, or comparison of different levels of exercise within one set of muscles.

Therefore, the **objectives** of this thesis were:

(1) - to develop temporally-optimized DTI acquisition strategies for assessment of dynamic muscle changes

(2) - to determine the stability of the three eigenvectors expected from a single DTI volume, as well as assess the benefits of time-expensive image improvement strategies (e.g. increased directions or signal averages) upon eigenvector stability. Assessments of eigenvector stability would indicate the capability of the corresponding individual eigenvalues to represent actual tissue structure.

(3) - to investigate the post-exercise diffusion patterns within multiple muscle groups, with attention paid to the patterns of individual muscles, as well as published values of their fiber content

(4) - to assess the sensitivity of a temporal DTI method to changes of individual muscles following exercises of different intensity

The following chapters describe projects collectively undertaken to achieve these objectives. *Chapter 5* addresses the issue of eigenvector stability within the human calf using a range of diffusion tensor acquisition parameters. *Chapter 6* discusses the use of a temporally-optimized DTI strategy to assess diffusion changes in the antero-lateral muscles of the calf following a session of mild dorsiflexion-eversion exercise. *Chapter 7* discusses the development of a novel 'sliding window' DTI acquisition strategy intended to provide even finer temporal resolution in diffusion measures while producing viable ongoing DTI representation of dynamic tissue structure. This chapter also discusses the initial results of a human *in vivo* experiment using the 'sliding window' DTI strategy to assess post-exercise temporal diffusion patterns within individual muscles following four intensities of plantarflexion exercise.

Chapter 5

An Exploration of Diffusion Tensor Eigenvector Variability Within Human Calf Muscles

Conrad P Rockel, B.A., Michael D. Noseworthy, Ph.D., P.Eng.

5.1 Context of Paper

The goal of this project was to generate a timecourse of diffusion from consecutive DTI volumes, and thus it was important to get an estimate of how a single timepoint volume would be able to represent underlying tissue structure.

Previous studies using diffusion tensor imaging (DTI) to study skeletal muscle have attributed meaning to each individual eigenvalue ($\lambda_1, \lambda_2, \lambda_3$), namely that these measures represent diffusion along the muscle fiber, across a sheet or layer of fibers, and across the fiber, respectively <Galban *et al.*, 2004>. However, only the first eigenvector (ε_1) has been addressed regarding directional stability and validity in representing muscle fibers, whereas the vector directions of the minor eigenvectors have not undergone such scrutiny.

The following experiment was performed to assess the stability of the second and third eigenvectors (ε_2 and ε_3) in a volume of resting human calf muscle, with the expectation that future studies involving exercise would demonstrate dynamic changes in these measures. Furthermore, acquisition parameters expected to increase eigenvector stability, such as more signal averages or number of diffusion directions, were explored as to their actual impact on stability within *in vivo* human subjects in comparison to the temporal cost of their implementation.

5.2 Declaration

Conrad Rockel provided the concept for this study, generated data, performed statistics, and wrote the initial manuscript draft. Michael D Noseworthy (corresponding author) provided funding, statistical analysis using Matlab, contributed substantial editing, and completed the online submission.

This paper was published in the *Journal of Magnetic Resonance Imaging (JMRI)*: Rockel C, Noseworthy MD. An exploration of diffusion tensor eigenvector variability within human muscles. J Magn Reson Imaging 2016; 43(1):190-202. doi: 10.1002/jmri.24957

5.3 Paper

An Exploration of Diffusion Tensor Eigenvector Variability Within Human Calf Muscles

Conrad Rockel[1,2] and *Michael D. Noseworthy[1,2,3,4,5]

[1] *McMaster School of Biomedical Engineering, McMaster University, Hamilton, Ontario, Canada.*

[2] *Imaging Research Centre, St. Josephs Healthcare, Hamilton, Ontario, Canada.*

[3] *Department of Radiology, McMaster University, Hamilton, Ontario, Canada.*

[4] *Department of Electrical and Computer Engineering, McMaster University, Hamilton, Ontario, Canada.*

[5] *Department of Medical Physics and Applied Radiation Sciences, McMaster University, Hamilton, Ontario, Canada.*

*Corresponding Author:
Dr. Michael D. Noseworthy, PhD, PEng.
Imaging Research Center, Fontbonne Bldg, F-126-4
St. Joseph's Healthcare,
50 Charlton Ave. East.
Hamilton, Ontario L8N 4A6, Canada.
VOICE: (905) 522-1155 x35218
EMAIL: nosewor@mcmaster.ca

5.3.1 ABSTRACT

Purpose: To explore the effect of diffusion tensor imaging (DTI) acquisition parameters on principal and minor eigenvector stability within human lower leg skeletal muscles.

Materials and Methods: Lower leg muscles were evaluated in 7 healthy subjects at 3T using an 8-channel transmit/receive coil. Diffusion-encoding was performed with 9 signal averages (NSA) using 6, 15, and 25 directions (NDD). Individual DTI volumes were combined into aggregate volumes of 3, 2, and 1 NSA according to number of directions. Tensor eigenvalues ($\lambda_1, \lambda_2, \lambda_3$), eigenvectors ($\varepsilon_1, \varepsilon_2, \varepsilon_3$), and DTI metrics (fractional anisotropy, FA, and mean diffusivity, MD) were calculated for each combination of NSA and NDD. Spatial maps of SNR, λ_3:λ_2 ratio, and zenith angle were also calculated for ROI analysis of vector orientation consistency.

Results: ε_1 variability was only moderately related to ε_2 variability (r=0.4045). Variation of ε_1 was affected by NDD, not NSA ($p<0.0002$), while variation of ε_2 affected by NSA, not NDD ($p<0.0003$). In terms of tensor shape, vector variability was weakly related to FA (ε_1:r=-0.1854, ε_2:ns), but had a stronger relation to λ_3:λ_2 ratio (ε_1:r=-0.5221, ε_2:r=-0.1771). Vector variability was also weakly related to SNR (ε_1:r=-0.2873, ε_2:r=-0.3483). Zenith angle was found to be strongly associated with variability of ε_1 (r=0.8048) but only weakly with that of ε_2 (r=0.2135).

Conclusions: The second eigenvector(ε_2) displayed higher directional variability relative to ε_1, and was only marginally affected by experimental conditions which impacted ε_1 variability.

Keywords: diffusion tensor imaging (DTI), eigenvector, skeletal muscle, calf, reliability

5.3.2 INTRODUCTION

Diffusion tensor imaging (DTI) is a magnetic resonance technique sensitive to thermally driven mobility of water molecules in vivo. The efficiency of random water proton diffusion through muscle tissue is slowed or restricted by fascia, collagen lattices, cellular membranes, as well as the intracellular and extracellular biophysical matrix [1]. DTI utilizes bipolar magnetic field gradients along multiple directions [2] resulting in an array of micromotion-sensitized images that in turn are used to calculate 3-dimensional diffusion properties for each voxel location [3]. The simplest form of DTI results in a diffusion ellipsoid, calculated as a rank-2 diffusion tensor, and gives three eigenvectors ($\varepsilon_1, \varepsilon_2, \varepsilon_3$), representing the vectors of axis orientation, and corresponding eigenvalues ($\lambda_1, \lambda_2, \lambda_3$) representing the magnitude along each of the principal axes. Typically, the eigenvalues are further combined into scalar measures such as fractional anisotropy (FA), a measure of ellipsoid shape, and mean diffusivity (MD), an average of the three eigenvalues.

The stability of ε_1 has been addressed in simulations catering to brain tissue [4-6], although the models typically only consider anisotropy greater than that found in skeletal muscle [7]. Nonetheless, these simulations demonstrated that vector consistency diminishes with decreasing anisotropy [4]. Computer simulations of DTI specific to characteristics of skeletal muscle (e.g. parallel fiber arrangement, presence of lipids, low SNR, and low anisotropy) have modelled gradations in SNR requirements for ε_1 magnitude and angular accuracy [7,8], as well as numbers of diffusion-encoding directions (NDD) required for levels of variability in ε_1 [7]. The validity of ε_1 as representative of human skeletal muscle has been explored through visual comparison of vector fields with anatomy [9], success of fiber-tracking [10], positional changes [11,12] and reproducibility studies [13-15].

The minor eigenvalues (λ_2, λ_3) are of particular note in DTI studies of calf skeletal muscle, as they offer the potential for insight into the nature of cross-fiber tissue architecture. DTI studies of skeletal muscle have noted significant asymmetry between the two minor eigenvalues, assumed to represent diffusion in the plane orthogonal to the muscle fiber [11,16,17], although there is debate as to the structural origin of this asymmetry [18]. For example, Galban and colleagues studied muscles in the calf [16], and suggested that the asymmetry between λ_2 and λ_3 reflects water movement across the endomysium and through the fiber radius, respectively. Karampinos *et al.* [17] have further suggested that this asymmetry reflects the actual cross-sectional shape of the fibers, and is related to strain fields during contraction. However, there exists a potential for sorting bias of the eigenvalues [7], whereby the classification of each depends simply on magnitude. While the asymmetry between second and third eigenvalue has been noted in studies with high SNR (e.g. [13]), the corresponding eigenvectors were not investigated.

The minor eigenvalues have been shown to increase during passive muscle contraction and decrease with passive elongation [9,12]. Studies of active muscle contraction have reported differing results regarding changes in minor eigenvalues, possibly due to differences in muscle loading [11,18]. Despite the expected changes in gross muscle shape, orientations of the corresponding minor eigenvectors were not considered. Furthermore, only a few DTI studies of calf skeletal muscle have actually considered the orientation of the minor eigenvectors (ε_2, ε_3), but only qualitatively so [17,19]. Simulations of the effect of SNR on DTI indices indicated that stability of the minor eigenvalues require far higher SNR than that of the principal eigenvalue [8], and that

ε_2 has more angular error than ε_1 for a given level of SNR [7].

In order to more effectively utilize and interpret the three-dimensional nature of DTI in the quantitative study of human skeletal muscle, a better spatial and musculocentric understanding of the eigenvector behaviour of tensors calculated using empirical data is needed. If vector directions truly represent structural components of immobilized human muscle tissue, then the 2^{nd} and 3^{rd} eigenvectors should be consistent with repeated scanning of static muscle. Thus, the purpose of this study was to explore the effect of acquisition parameters on in vivo eigenvector stability within human lower leg skeletal muscles. The objectives were to (i) create spatial representations of the consistency of each eigenvector, (ii) evaluate the regional relationship between primary and minor eigenvector consistency, (iii) determine the impact of number of diffusion encoding directions and number of signal averages (NSA) on vector stability, and (iv) to understand the impact of SNR spatial variation on vector stability.

5.3.3 MATERIALS and METHODS

Subjects

Seven healthy volunteers (2 females, age 27.9±7.0) were recruited for this study. Body Mass Index (BMI) of subjects was calculated to be 21.9±3.2 kg/m^2, indicating normal weight status (BMI 18.5-24.9). All subjects engaged in regular physical activity and reported no past or present clinical issues related to skeletal muscle. Furthermore, a registered MRI technologist with 20 years of clinical MRI experience ascertained that the involved anatomical regions were devoid of cysts, hematomas, or unspecified pathology associated with edema. Subjects were asked to refrain from unnecessary physical activity for at least four hours preceding scanning. Our study was approved by the local ethics review board, and informed consent was obtained from all subjects prior to their participation.

Imaging

MRI data was collected at 3T (MR750, GE Healthcare, Milwaukee WI) using an 8-channel transmit/receive knee coil (Invivo, Gainsville FL). Each volunteer lay supine for 30 minutes prior to acquisition to allow for the potential redistribution of body water [20] after which they were transferred to the MRI bed.

Subjects were placed supine on the MRI bed in a foot-first orientation. The RF coil was centered around the widest section of the right calf, approximately 10 cm distal to the patella. The right foot was placed in a wooden stand fixed to the MRI bed, and held to a footrest with straps around both the ankle and toes to prevent movement and potential changes in muscle length. The footrest was a pedal angled 10° from vertical, holding the foot in a slightly plantar flexed position. In order to prevent compression of the muscle by the rigid coil construction, and to minimize signal bias (higher loading when on the coil), the leg was centered throughout the length of the coil and allowed to suspend freely, with the tibia approximately horizontal and parallel to the main magnetic field. The body position of the subject was modified with padding under the buttocks and heel to accommodate this position as well as provide comfort throughout the scan duration. Further strapping was placed around the thigh in order to secure the leg. Strapping was made snug, keeping subject comfort and free circulation to the lower limb in mind. Subjects were asked to relax and refrain from moving.

Initial scanning included localization, calibration for parallel imaging (ASSET) and acquisition of a proton density scan with fat saturation (PD-FatSat), performed to rule out any underlying subclinical pathology.

DTI acquisition was centered upon the widest axial slice of the calf, with additional axial slices extending proximal and distal from this slice position. DTI was acquired using a dual echo spin echo EPI sequence (b=400 s/mm^2, TR/TE=6000/70ms, 16 slices 4mm thick, 16cm FOV, 64x64, ASSET factor = 2). Importantly, DTI scans were done separately using three numbers of diffusion-encoding directions (NDD) (6, 15, or 25 directions). Nine individual signal averages (NSA) were collected as separate volumes for each NDD condition, per subject, in a randomized order. Scanning time for each NDD was 24m18s (25dir), 15m18s (15dir), and 7m12s (6dir). The experimental design is shown in **Figure 5.1**.

All scans were visually assessed for overt signs of muscle movement using a movie utility (FSLVIEW [21]). With dynamic viewing of multiple volumes, this tool made clear any signal dropouts or positional changes of the calf (greater than 1 voxel) that occurred during an individual DTI-NDD acquisition, either within the multiple diffusion-weighted volumes required for each DTI acquisition, or across the 9 repeats needed for a complete NDD set. It was vital that minimal motion took place within an NDD set, as no inter-volume motion correction was done to avoid the influence of interpolation on the results, and to mimic the output of a multi-NSA DTI scan. Typically an MRI system will add all the individual NSA together without motion or eddy current correction, which then would be done afterwards. We wanted to avoid interpolation schemes but yet still have the ability to potentially reject data if motion was an issue.

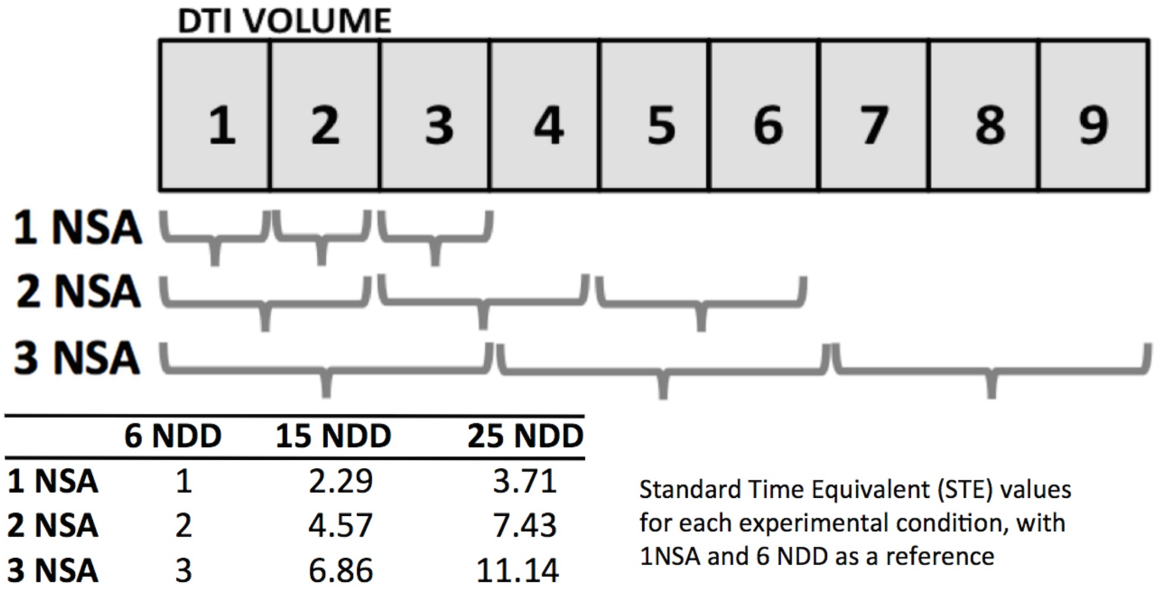

	6 NDD	15 NDD	25 NDD
1 NSA	1	2.29	3.71
2 NSA	2	4.57	7.43
3 NSA	3	6.86	11.14

Standard Time Equivalent (STE) values for each experimental condition, with 1NSA and 6 NDD as a reference

Figure 5.1: Overview of experimental design. In total, 9 individual signal average volumes (NSA) were acquired per experimental condition (6, 15 and 25 diffusion encoding directions (NDD)) for each subject. Individual volumes (1NSA) were combined to create the 2NSA and 3NSA volumes as indicated by the grey parentheses. The table (lower left) indicates the standard time equivalency (STE) of each experimental condition relative to the 6NDD/1NSA condition (assigned a value of 1).

Analysis

Following acquisition, raw individual DTI volumes were combined into aggregate volumes of 3, 2, and 1 NSA according to number of directions (**Fig. 5.1**). Once combined, the majority of skin and subcutaneous fat was removed from each individual or composite volume using an automated algorithm (BET) [22] followed by manual editing. Tensors and DTI indices (fractional anisotropy (FA), mean diffusivity (MD), eigenvalues ($\lambda_1, \lambda_2, \lambda_3$) and eigenvectors ($\varepsilon_1, \varepsilon_2, \varepsilon_3$)) were then calculated for each experimental combination of NSA and NDD using a constrained least-squares algorithm (FSL) [23]. Spatial maps of the λ_3:λ_2 ratio were calculated for comparison with vector variability to determine the extent to which the asymmetry of the minor eigenvalues plays a role in vector variability. All spatial maps calculated for this study were produced using custom scripts written in Matlab (version R2009b, Mathworks, Natick MA).

The nine combinations of NSA and NDD implies that total scan time varies between experimental conditions. Therefore, a measure of standard time equivalency (STE) was calculated for each experimental condition [6]. For all DTI acquisitions, the repetition time (TR) was 6000ms. An STE unit of 1 was allotted for each directional (or non-) diffusion-weighted image, and summed for each experimental condition. An STE value was thus calculated for each experimental condition, considering both NDD and NSA (**Fig. 5.1**).

In the absence of external validation of vector orientation, and to avoid simply comparing deviations from a potentially-flawed mean vector orientation of all volumes, it was decided to instead compare vector variability between volumes, and obtain a mean value of deviation of these fluctuations between two individual volumes in degrees. In order to determine the spatial arrangement of vector variability between volumes, sets of 3 volumes or composite volumes were compared. Voxel-wise differences in eigenvector orientation (θ) were calculated in degrees between each pair of volumes (**A** and **B**):

$$\theta = cos^{-1}\left(\frac{\mathbf{A} \bullet \mathbf{B}}{\mid \mathbf{A} \mid\mid \mathbf{B} \mid}\right) \tag{5.1}$$

and subsequently averaged between each set of volume pairs [5,24]. It should be noted that the maximum mean vector variation between 3 volumes is 120 degrees, while the maximum vector difference between two volumes is 180 degrees. In either case, a distribution not exhibiting any vector variability would have all measured volumes with a zero degree variation between their combinations. Vector differences greater than 90° were left uncorrected in order to determine the spatial location of these occurrences. Spatial maps of mean vector variation were generated for all three eigenvectors per subject for each combination of number of directions and NSA.

Because inter-subject longitudinal positioning and anatomical variability made direct overlay of MRI volumes of human calf difficult, histograms of the spatial vector variation maps were generated to allow initial qualitative visualization of variation distribution in degrees between each experimental condition and eigenvector. Prior to histogram calculation, each DTI volume was further masked to include only the five central slices. This was performed in order to reduce histogram contamination by peripheral regions along the longitudinal axis of the receive coil, thus restricting the analysis to the region of best signal and homogeneous magnetic field.

Signal-to-noise ratio (SNR) maps spatially corresponding to the vector variation maps were calculated representing each voxel of the b=0s/mm^2 image for each experimental condition per subject, allowing for voxel-wise SNR quantification for different locations within a single volume, as well as between subjects or experimental conditions (**Fig. 5.2**).

As parallel imaging was used, SNR was calculated by comparing two consecutive volumes according to Dietrich [25] and Rogers [26]. In calculating SNR of different NSA conditions, the consecutive volumes were chosen in the following manner (based on 9 separate volumes, **Fig. 5.1**): 1NSA = volume 1 vs. 2; 2NSA = (volume 1+2) vs. (volume 3+4); and 3NSA = (volume 1+2+3) vs. (volume 4+5+6).

The zenith angle between ε_1 (representing fiber orientation) and the main magnetic field (vector [0,0,1]) [17] was calculated using **Equation 5.1** so as to assess the potential impact of fiber pennation obliqueness on measures of minor eigenvector

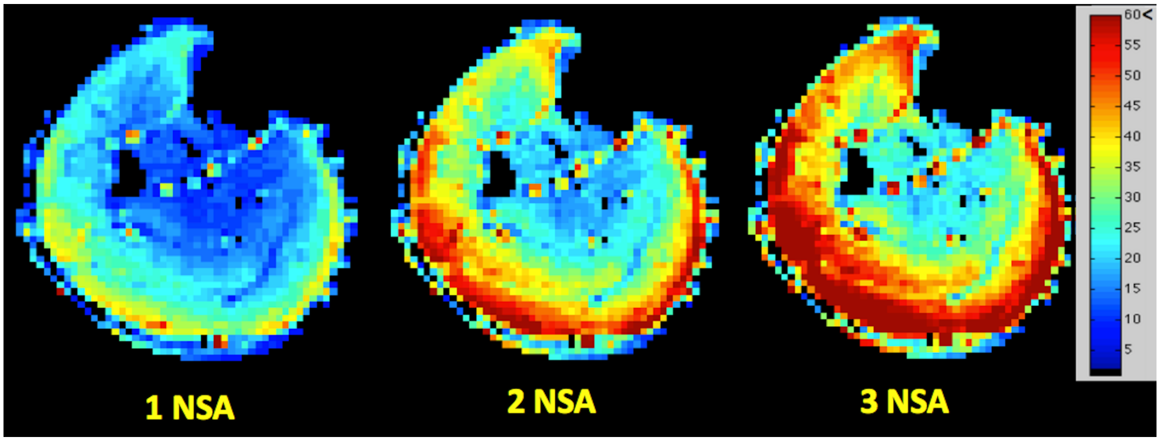

Figure 5.2: Examples of signal-to-noise spatial maps in one volunteer. Left to right is calculated SNR for the 1NSA, 2NSA and 3NSA conditions. The SNR increased with increased NSA, particularly within peripheral regions of the calf, such as gastrocnemius. Central regions display far less SNR than peripheral regions.

variability. The maps of the zenith angle were generated for each of three volumes within each experimental condition (**Fig. 5.1**) per subject. Voxels containing degrees of difference >90° were corrected by subtracting the value from 180. These maps were subsequently averaged to give an overall estimate of fiber obliqueness for each voxel.

In order to quantify regionally-specific interactions between each experimental condition, SNR, zenith angle, and eigenvector behaviour, and to reduce contamination from masking or non-muscle artifacts, a series of regions-of-interest (ROIs) were manually drawn on a composite image of all 9 b=0s/mm^2 volumes within an NDD set for each subject using FSLVIEW [21]. ROIs were dispersed throughout the image determined by muscle boundaries. Targeted muscle units for analysis were anterior tibialis (exterior), anterior tibialis (interior), extensor digitorum longus, peroneus longus, posterior tibialis, soleus (lateral), soleus (central), soleus (anterior), lateral gastrocnemius, medial gastrocnemius (posterior), and medial gastrocnemius (anterior) (**Fig. 5.3a**). ROIs were placed by an experienced DTI researcher with over 13 years of experience in diffusion ROI analysis (CR).

The ROIs consisted of two 2x2-voxel squares across 5 central contiguous axial slices within each muscle group, equaling 40 voxels per ROI, representing 1 cm^3. If 2x2 squares could not be used due to small muscle area, an equivalent number of single-voxel squares were used instead. Care was taken to avoid fascia, blood vessels, chemical shift artifacts, and mask borders, as well as to place ROIs in approximately

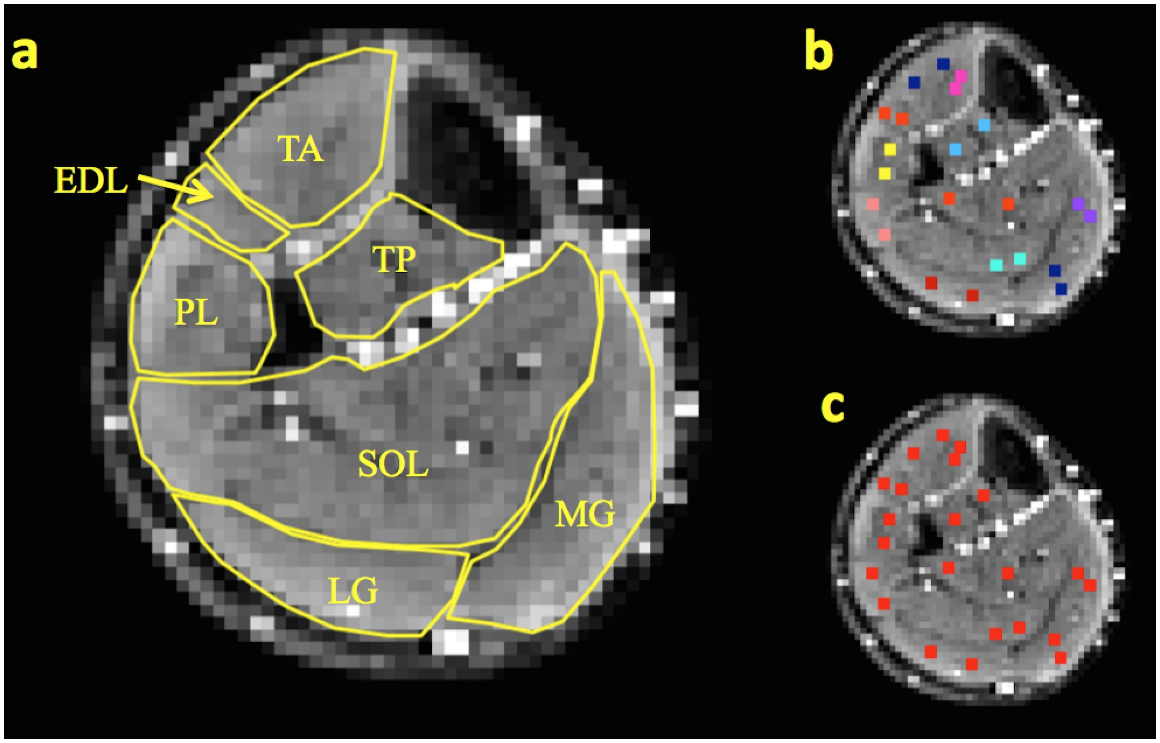

Figure 5.3: Calf regions used in analyses. **(a)** Outlined are muscles of the lower leg under investigation (TA: Tibialis Anterior, TP: Tibialis Posterior, EDL: Extensor Digitorum Longus, PL: Peroneus Longus, SOL: Soleus, LG: Lateral Gastrocnemius, MG: Medial Gastrocnemius). **(b)** Placement of regions-of-interest (ROIs) used to determine relative DTI values of individual muscles or muscle subsections, each ROI distinguished by separate colours. **(c)** Aggregate ROI created by amalgamation of individual ROIs in order to represent similar anatomy across multiple experimental conditions.

the same position across subjects (**Fig. 5.3b**). These ROIs were subsequently applied to each individual volume per NDD set and NSA combination. Despite all scans having been checked for movement, each ROI was visually inspected on every volume to ensure they remained within muscle boundaries and avoided non-muscle tissue such as fascia or blood vessels.

All eleven muscle ROIs were subsequently combined into an aggregate ROI consisting of 440 voxels (11 cm^3) (**Fig. 5.3c**). This aggregate ROI was used to evaluate differences in overall DTI measures between experimental conditions while accommodating assumed similar heterogeneity of diffusion between individual muscle composition, fiber angulation, and position relative to the RF coil. MD, FA, and eigenvalues ($\lambda_1, \lambda_2, \lambda_3$) were calculated using the aggregate ROI for each subject within each experimental condition.

Individual and aggregate muscle ROIs were used to analyze ε_1 and ε_2 vector variability spatial maps as well as maps of SNR, λ_3:λ_2, ratio and zenith angle for each experimental condition per subject. Due to orthogonality of ε_3 to both ε_1 and ε_2, maps of ε_3 were not deemed to provide any extra information, thus were not considered for ROI analysis.

Statistical Analysis

Statistical analysis was done for each eigenvector metric (ε_1 and ε_2 variability), SNR and zenith angle using a 3-way Analysis of Variance (ANOVA), with factors being NDD, NSA, and replicate of measurement within a muscle. Furthermore, each scalar measure (MD, FA and eigenvalues) was similarly assessed. For each statistical analysis interaction terms between all three factors was investigated, and a Kruskal-Wallis test for normality was also performed. When the ANOVA showed significance (i.e. $p>0.05$), multiple comparisons analysis was performed using Scheffes test. All statistical analysis was done using the statistics toolbox of Matlab (ver. R2014a, Mathworks, Natick MA).

The individual muscle ROI measures of ε_1 and ε_2 vector variability under each experimental condition were entered as data points into a series of Spearman correlations (two-tailed). Variables such as FA, MD, λ_3:λ_2 ratio, SNR, zenith angle, and STE were each assessed as to their relationship with ε_1 and ε_2 variability. Additionally, possible correlates between ε_1 and ε_2 variability were investigated. Finally, correlation analyses were further sub-divided into sets by NDD or NSA for comparisons between SNR and eigenvector variability, as well as relationships between ε_1 and ε_2 variability. All correlations were performed using Prism 5.0 (GraphPad Software Inc, La Jolla, CA).

5.3.4 RESULTS

Subjects

Despite the measures taken to immobilize subjects, two subjects were removed from analysis due to excessive positional shifting and/or movement during acquisition within at least one NDD DTI set. Thus the resultant acceptable data used in subsequent analysis was from 5 subjects (1 female, age 27.6±8.5, BMI 23.2±2.7).

Spatial Maps and Histograms

Spatial maps revealed that ε_1 varied in a coherent gradual manner, with minimal variation in peripheral muscles of the calf (gastrocnemius, anterior tibialis) (**Fig. 5.4a**). In contrast, central muscles (posterior tibialis, soleus) displayed higher ε_1 variability. Interestingly, the soleus demonstrated increased variation in comparison to other muscles, extending into its periphery. The variability of ε_2 had a similar spatial distribution to ε_1 per experimental condition, although overall displayed higher values of vector variability, as well as a speckled incoherent pattern of high-variability voxels (**Fig. 5.4b**).

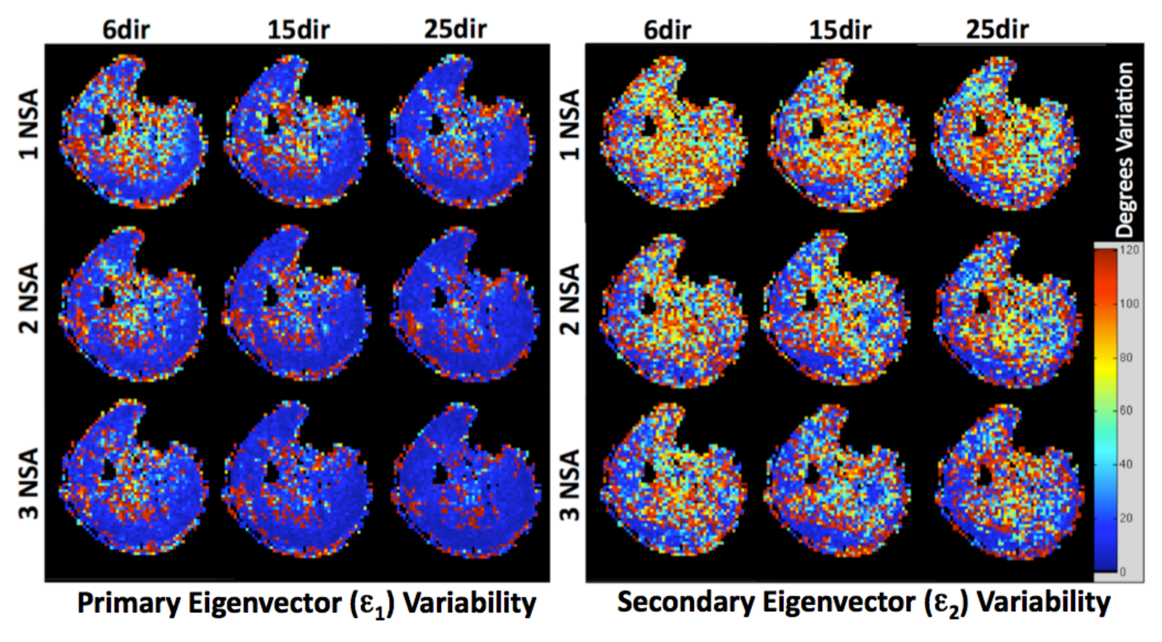

Figure 5.4: Spatial maps of vector variability within one volunteer across all experimental conditions. **(a)** Variation of the primary eigenvector (ε_1). **(b)** Variation of the secondary eigenvector (ε_2).

Qualitative examination of histograms revealed differences in the volumetric distribution of vector variation in spatial maps between eigenvectors, as well as experimental conditions. Histograms of vector variation showed the majority of ε_1 per volume varied less than 10° (**Fig. 5.5**). The histograms further demonstrate there is little tissue volume where ε_1 varies between 20° and 100°. However, a secondary peak was noted between 100-120°. Inspection of spatial maps (**Figs. 5.4a** and **5.4b**) showed this secondary peak originated predominantly in the central calf region, soleus, as well as mask edges and large blood vessels. In contrast to ε_1, the vector variability of both ε_2 and ε_3 was widespread, as shown by the reduced amplitude and increased width of the dominant histogram peak between 0 and 20°, as well as visually-evident increased area under the curve between 20° and 100° (**Fig. 5.5**).

For both ε_2 and ε_3, increasing NDD and NSA increased the height of the low variability peak, narrowed the peak width, and brought the peak closer to zero (in terms of degrees variability). Furthermore, less area under the curve was noted in the middle region (20° to 100° vector difference) with increasing NDD and NSA (**Fig. 5.5**).

Aggregate ROI: Scalar Values

The aggregate ROI was used to examine the effect of NDD and NSA on values of MD and FA. The mean MD, depending on experimental condition, ranged from 1.55 to 1.58 x10^{-3} mm^2/s, and no statistical differences were found between experimental conditions, nor did replicates contribute to any significant sources of variability for

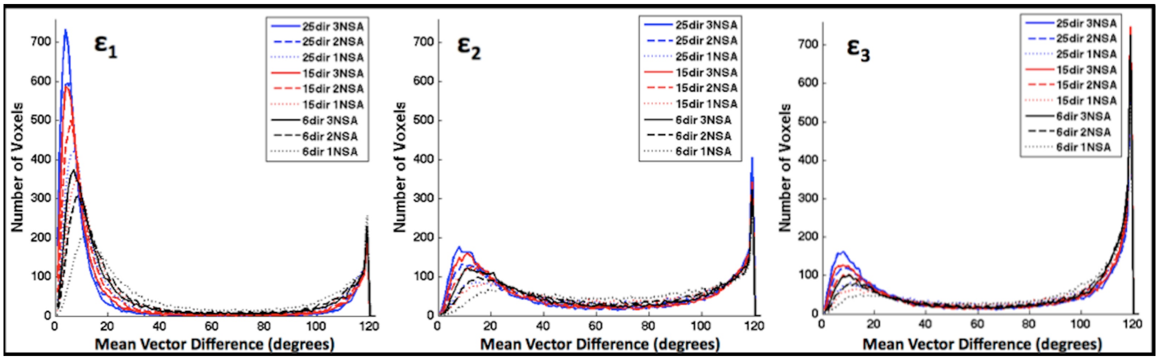

Figure 5.5: Histograms of vector variability per experimental condition. Left to right: ε_1, ε_2, and ε_3. The bulk of ε_1 variability, over the aggregate ROI was less than 20°, peaking at 10°. Both ε_2 and ε_3 variability were nearly identical also with a peak in variability around 10°, however, with much greater variability over the range between 0 and 120°. Furthermore a larger secondary peak at 120° was notably visible for both radial eigenvectors.

any of the parameters measured (**Fig. 5.6a**). The FA values, noted to be non-parametric, ranged from 0.23 to 0.28, and using Kruskal-Wallis tests significantly decreased with increasing NDD ($p<0.0001$) and increasing NSA ($p<0.0014$) (**Fig. 5.6b**). A significant interaction term between NSA and NDD was noted ($p<0.0055$).

Individual eigenvalues were also assessed with the aggregate ROI (**Figs. 5.6c-e**). The λ_1 of the 6 NDD condition was found to be significantly larger than both the 15- and 25-direction conditions and was also found to be non-parametric (Kruskal-Wallis, $p<0.000005$). NSA was not significant in determining λ_1 ($p<0.1968$). Replicate ROIs within muscle groups were not a significant source of variability ($p<0.7995$), nor were there any contributing sources of interaction as a result of ROI with NDD ($p<0.9983$) or NSA ($p<0.9678$).

The second eigenvalue (λ_2) was significantly greater using the 6 NDD condition ($p<0.0045$). Similar to λ_1, the value of λ_2 was noted to be non-parametric and was significantly affected by NDD ($p<0.000003$). Neither NSA ($p<0.6259$) nor ROI replicate ($p<0.8427$), nor combination of interaction of terms, were significant factors in determining λ_2.

The third eigenvalue, λ_3 was significantly lower with both the 6 NDD acquisition ($p<0.000002$) and the 1 NSA condition ($p<0.0248$). Both were found to be non-parametric and as such significance was through Kruskal-Wallis testing. Again, ROI replicates did not contribute to a significant source of variability ($p<0.9336$). No interactions between factors were significant in determining λ_3.

The ratio of λ_3:λ_2 (**Fig. 5.6f**) was significantly lower for the 6 NDD ($p<0.000001$) and 1 NSA conditions ($p<0.000001$). Both NDD and NSA were found to be significant and non-parametric (Kruskal-Wallis test) in their contribution to the λ_3:λ_2 ratio.

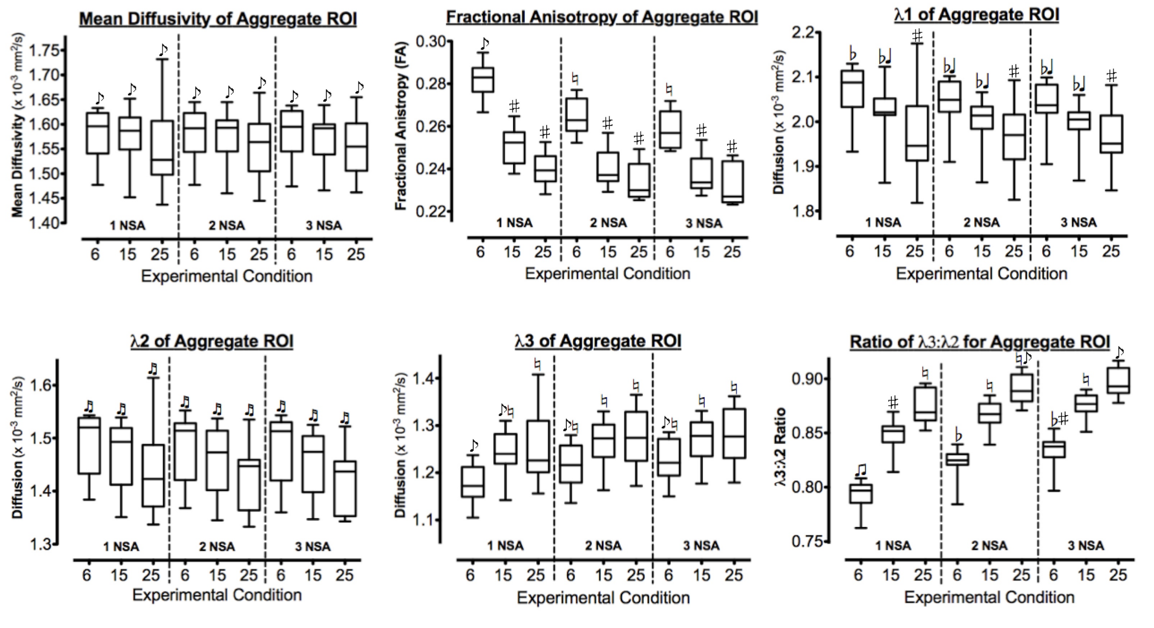

Figure 5.6: Box and whisker plots indicating scalar results of DTI analysis (Aggregate ROI) for each experimental condition. **(a)** Mean Diffusivity (MD). **(b)** Fractional Anisotropy (FA). **(c)-(e)** First (λ_1), second (λ_2), and third (λ_3) eigenvalues, respectively. **(f)** Ratio of the third (λ_3) to second (λ_2) eigenvalues where a value of 1.0 indicates parity. All distributions were noted to be non-normal, based on Kruskal-Wallis tests, except MD (NDD and NSA), λ_1 (NSA) and λ_2 (NSA). Differing symbols above bars indicate significance ($p<0.05$) from other experimental conditions.

Aggregate ROI: Eigenvector Variation

Aggregate ROI eigenvector variation showed the most ε_1 variation with the NDD 6 direction scan, decreasing for 15, and then 25 NDD (**Fig. 5.7a**). The NDD was a significant factor in determining ε_1 variability and it was noted to be non-parametric (Kruskal-Wallis, $p<0.0008$). NSA did not have a significant effect on ε_1 variation.

The ε_2 variation was always much greater than ε_1 (**Fig. 5.7a-b**). Decreased ε_2 variation was observed with increasing NSA (Kruskal-Wallis, $p<0.0005$). NDD was not a significant contributor to ε_2 variation.

The SNR was not affected by NDD. However SNR was noted to be significantly

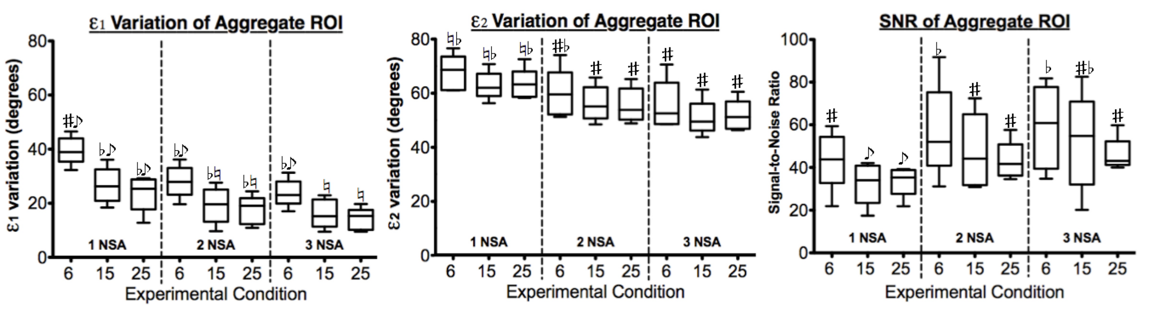

Figure 5.7: Results of DTI-derived spatial maps for each condition, measured using aggregate ROI. **(a)** ε_1 variation; **(b)** ε_2 variation; **(c)** Signal-to-noise ratio. All distributions were noted to be non-normal, based on Kruskal-Wallis tests, except ε_1 (NSA), ε_2 (NDD), and SNR (NDD). Differing symbols above bars indicate significance ($p<0.05$) from other experimental conditions.

affected by NSA (Kruskal-Wallis, $p<0.0036$). In terms of zenith angle, both NDD (parametric statistics $p<0.0186$) and NSA (Kruskal-Wallis $p<0.0098$) played significant roles.

Eigenvector Variation of Individual Muscle Regions

The amount of eigenvector variation (in degrees) for each muscle ROI (see **Fig. 5.3b**) is summarized as a comparison between the lowest STE condition (6dir, 1 NSA, STE=1) and highest (25dir, 3NSA, STE=11.14) in **Table 5.1**.

Correlation Analysis: DTI Scalar Indices and Eigenvector Variation

FA showed a significant but very weak correlation with ε_1 ($r=-0.185$; $p<0.0001$) but not ε_2 ($r=0.018$; $p>0.05$). MD showed significant very weak correlations with ε_1 ($r=0.181$; $p<0.0001$) and ε_2 ($r=-0.177$; $p<0.0001$). The ratio of λ_3:λ_2 ranged from 0.699 to 0.946, with mean of 0.860. Correlations of λ_3:λ_2 with ε_1 and ε_2 were both negative and significant, but the relationship between λ_3:λ_2 and ε_1 ($r=-0.522$; $p<0.0001$) proved to be much stronger than that of ε_2 ($r=-0.177$; $p<0.0001$).

ROI	**Condition**	**ε_1 Variation**		**ε_2 Variation**		**SNR**		**Zenith**	
		Mean	***SD***	**Mean**	***SD***	**Mean**	***SD***	**Mean**	***SD***
ATib_out	6d 1nsa	13.7	*16.9*	44.9	*8.0*	38.1	*17.9*	17.2	*10.3*
	25d 3nsa	7.6	*5.3*	33.4	*7.6*	52.6	*15.8*	15.9	*2.9*
ATib_in	6d 1nsa	13.6	*9.7*	64.4	*9.7*	33.3	*15.4*	9.5	*8.5*
	25d 3nsa	7.7	*3.8*	55.9	*9.9*	45.6	*7.9*	7.0	*0.3*
PTib	6d 1nsa	62.1	*16.3*	76.3	*8.1*	30.2	*10.9*	37.5	*17.2*
	25d 3nsa	16.1	*12.2*	63.6	*13.7*	32.2	*6.0*	27.6	*7.2*
EDL	6d 1nsa	10.1	*7.7*	65.1	*16.5*	34.0	*14.9*	10.2	*4.3*
	25d 3nsa	5.9	*0.9*	58.1	*14.9*	46.6	*12.3*	8.3	*2.2*
PER	6d 1nsa	9.3	*7.2*	51.5	*15.8*	34.6	*14.2*	14.2	*3.9*
	25d 3nsa	5.3	*1.0*	38.9	*17.2*	47.0	*10.6*	13.6	*1.6*
SOLlat	6d 1nsa	56.5	*17.0*	68.4	*6.5*	41.1	*14.9*	39.0	*17.1*
	25d 3nsa	38.9	*16.9*	55.6	*12.6*	56.6	*7.8*	39.0	*5.0*
SOLcent	6d 1nsa	55.4	*11.6*	70.0	*8.4*	28.7	*9.8*	37.9	*7.4*
	25d 3nsa	39.9	*20.4*	59.2	*6.9*	39.7	*8.2*	37.1	*5.8*
SOLant	6d 1nsa	39.1	*14.8*	74.1	*4.8*	22.6	*9.1*	23.5	*13.7*
	25d 3nsa	18.6	*10.2*	60.3	*7.9*	31.0	*7.4*	20.3	*5.3*
LG	6d 1nsa	6.0	*4.2*	58.9	*13.5*	42.9	*16.5*	10.2	*3.0*
	25d 3nsa	3.7	*0.5*	45.0	*25.0*	58.8	*8.6*	9.7	*2.0*
MGpost	6d 1nsa	7.5	*5.8*	65.1	*15.3*	37.9	*14.2*	12.6	*3.1*
	25d 3nsa	4.3	*0.7*	51.8	*13.1*	51.5	*8.0*	12.0	*2.5*
MGlat	6d 1nsa	13.2	*11.1*	57.0	*15.2*	33.6	*18.5*	16.5	*3.8*
	25d 3nsa	7.1	*5.9*	47.5	*8.4*	44.7	*4.0*	15.5	*5.2*

Table 5.1: Measurements from individual muscle ROIs, based on n=5. Condition indicates whether measurement is from experimental condition of minimum STE (NDD=6, NSA=1) or maximum STE (NDD=25, NSA=3). Values for ε_1 variation, ε_2 variation, and Zenith (zenith angle) are in degrees, while SNR is unitless.

Correlation Analysis: SNR and Eigenvector Variability

When combining all experimental conditions per subject, SNR was found to significantly negatively correlate with ε_1 (r=-0.287; p<0.0001) and ε_2 variation (r=-0.348; p<0.0001). Correlating ε_1 variability with ε_2 variability showed moderate association (r=0.405; p<0.0001), indicating that consistency of ε_2 decreases when ε_1 orientation becomes unstable. However, the region of highest ε_1 stability (i.e. from 0 to 20°, representing 37% of data points) also showed the widest range and density of ε_2

variability (**Fig. 5.8a**). It should be noted that only 3 of 495 data points displayed values greater than 90°, indicating that ROI placement independently excluded voxels contributing to the upper variability peak (100 to 120°) observed in the histograms.

When varying NDD, all correlations between SNR and ε_1 and ε_2 variability were significant and negative, yet ranged from weak to moderate in strength (r=-0.333 to -0.498) (**Table 5.2**). The relationship between ε_1 and ε_2 variability was moderate and positive (r = 0.348 to 0.441), and appeared greatest for the NDD=25 condition, and weakest for the NDD=15 condition.

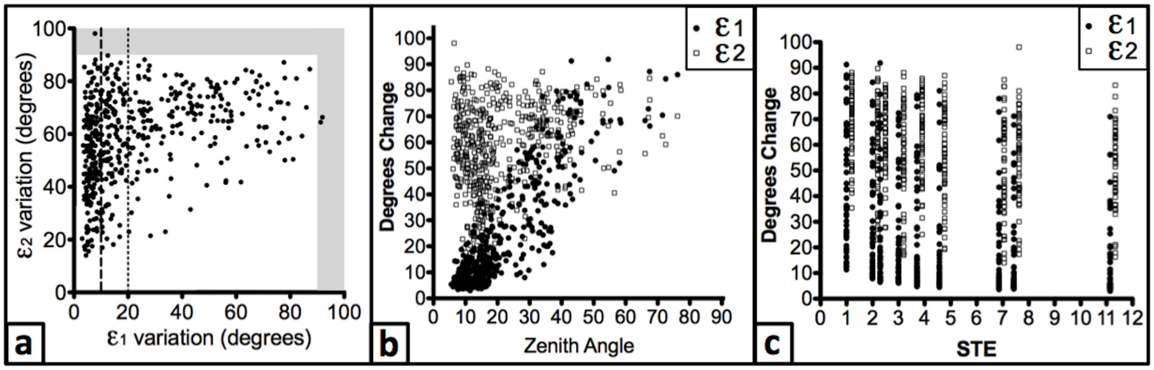

Figure 5.8: Scatterplots of data from individual muscle ROIs. **(a)** Relationship between ε_1 and ε_2 variation. Out of 495 included data points, 190 points (38%) fall between 0 and 10° of ε_1 variation (dashed line), while 306 points (62%) fall between 0 and 20° (dotted line). Note that of 495 ROIs, only 3 (2 for ε_1, 1 for ε_2) produced variability values greater than 90 degrees (shaded area). **(b)** Effect of zenith angle upon ε_1 variability (closed circles) and ε_2 variability (open circles). Note that ε_1 variation was strongly correlated with zenith angle (r=0.8048; p<0.0001) while ε_2 variation was only correlated weakly (r=0.2135; p<0.0001) as calculated using Spearman rank correlations. **(c)** Relationship between Standard Time equivalency (STE) and vector variability. (ε_1 variation = closed circles, ε_2 variation = open circles, nudged slightly right for clarity).

When grouped by NSA, correlations between SNR and ε_1 variability were again

Correlation Summary by NDD			
	NDD = 6	**NDD = 15**	**NDD = 25**
SNR vs ε_1	-0.463****	-0.373****	-0.498****
SNR vs ε_2	-0.333****	-0.457****	-0.409****
ε_1 **vs** ε_2	0.390****	0.348****	0.441****
Correlation Summary by NSA			
	NSA = 1	**NSA = 2**	**NSA = 3**
SNR vs ε_1	-0.180*	-0.250***	-0.194**
SNR vs ε_2	-0.181*	-0.324****	-0.334****
ε_1 **vs** ε_2	0.399****	0.362****	0.304***

Table 5.2: Summary of correlation values between signal to noise ratio (SNR) and eigenvector ε_1 and ε_2 variability, as influenced by number of diffusion encoding directions (NDD) and number of signal averages (NSA). (*p<0.05, **p<0.01, ***p<0.001, ****p<0.0001).

negative but weak (**Table 5.2**). Examination of ε_2 variability with SNR showed that within the 3NSA and 2NSA conditions, the correlations were moderately stronger than that of ε_1. The correlations between ε_1 and ε_2 variability were positive and highly significant across all NSA conditions (**Table 5.2**). Furthermore, increased ε_2 variability was weakly related to ε_1 variability, and this relationship increased with decreasing NSA.

Correlation Analysis: Zenith Angle and Eigenvector Variability

Zenith angle was found to be quite strongly correlated with ε_1 variation (r=0.8048; p<0.0001), which contrasts with the weak correlation between zenith angle and ε_2 variation (r=0.2135; p<0.0001) (**Fig. 5.8b**). Curiously, when the soleus ROIs (representing 135 data points) were removed the correlation between zenith angle and ε_1 variation dropped to moderate strength (r=0.5870; p<0.0001), while the relationship between zenith angle and ε_2 variation was not significant.

Correlation Analysis: Standard Time Equivalence and Eigenvector Variability

The STE (**Fig. 5.1**) had a moderate negative correlation with ε_1 variation (r=-0.4419; p<0.0001) (**Fig. 5.8c**). However, the correlation between STE and ε_2 variation was found to be weak (r= -0.2595; p<0.0001) (**Fig. 5.8c**).

5.3.5 DISCUSSION

As DTI becomes more commonplace in the study of human skeletal muscle, it is important to consider the precision of *in vivo* measures obtained by this method using clinical-strength MRI scanners within appropriate exam times. Using the immobilized lower leg as an accessible model of skeletal muscle, we have empirically demonstrated that the directional variability of minor eigenvectors (represented by ε_2) is substantially high in experimental conditions capable of producing minimal directional variation in the principal eigenvector (ε_1) of the calf. Furthermore, this study has demonstrated that experimental efforts to improve vector stability were far more effective in improving ε_1 than ε_2. The findings of the present study appear to replicate the simulation work of Froeling [7], who calculated greater degrees of directional error and variability in ε_2 than ε_1 for a given level of SNR. However, our study expands on that work by using real subjects, as well as localizing the regions and conditions under which these errors occur.

Variation in vector direction beyond 45°, such as that observed within ε_2, indicates a risk that the eigenvalue representing this eigenvector is being misclassified according to the ranking system used in tensor calculation [3], bringing into question the validity of reporting minor eigenvalues, especially when reporting experimental effects. Therefore, this study seeks to impress upon the reader that caution should be taken in interpreting the values of individual minor eigenvalues in skeletal muscle research, particularly in studies involving comparison between muscles or states of flexion, or comparing muscles of different composition and architecture.

The use of DTI in the study of skeletal muscle was initiated by findings that the anisotropic movement of water within the elongated and parallel tissue of skeletal muscle could be detected using diffusion imaging [27,28], as well as evidence that the principal eigenvector (ε_1) of the DTI ellipsoid corresponded with muscle fiber direction in high-field experiments using animal models [29,30]. As such, numerous *in vivo* human DTI experiments of skeletal muscle at clinical field strengths have been performed, using the thigh [31,32] or calf [16,19] in particular. DTI studies of human calf muscle have found differences in both diffusivity [11,19], and fiber orientation (ε_1) [12,17,19] between individual muscles.

The notion that DTI indices reflect muscle shape and function have prompted further studies into the biomechanics of muscles within the lower leg, with findings of relationships between individual eigenvalues and standing-to-supine positioning [20], passive angulation of the foot between dorsiflexed, neutral, and plantar positions [9,12], as well as effects of active isometric calf contraction [11,18]. While interpretations of the meaning of the minor eigenvalues were asserted in these studies, rarely were orientations of their respective eigenvectors actually reported, much less assessed.

By reporting individual eigenvalues, or comparing these eigenvalues between conditions, it is implicitly assumed that individual eigenvectors are stable metrics that reflect anatomical structures and thus warrant comparison. The results of the present study of eigenvector stability suggest that while this may be appropriate for the principal eigenvector and eigenvalue, these assumptions may not be valid with regard to the minor eigenvalues due to their high directional variability.

Studies using computer simulation have modeled experimental conditions such as SNR and NDD and their impact upon DTI indices of skeletal muscle. For example, Damon [8] noted that increasing levels of SNR are needed for accurate FA estimation (SNR>30), accurate MD estimation and prevention of λ_2 underestimation (SNR>40), and prevention of λ_3 underestimation and reduction of ε_1 variability to $\pm 9^\circ$ (SNR>60). Damon [8] further asserted that SNR levels required to reduce the variability of ε_2 to acceptable levels would be unrealistically high for human studies. Simulations by Froeling *et al.* [7] suggested that diffusion gradient schemes use greater than 12 directions, as schemes with low NDD resulted in directional bias for fibers coinciding with one of the gradient directions. Our experimental results unquestionably supported these findings as NDD of 6 resulted in the greatest degree of variability. However, it has been acknowledged that simulated results may differ from experimentally-acquired data [5,7], as simulations often do not account for factors such as subtle movement or physiological noise which occur during data acquisition. Furthermore, simulations tend to consider muscle a homogeneous material, when in fact tissue composition, architecture, and vascularity are quite different between individual muscles [33,34]. The present study was therefore undertaken within the human calf to investigate the complex relationships between muscle location and architecture, experimental condition, SNR, and eigenvector variability when using standard DTI protocols, as well as to better anticipate the potential errors of scanning in realistic settings.

Spatial mapping of eigenvector variation visibly indicated that ε_2 direction was much less consistent between consecutive volumes than that of ε_2 across all NDD and NSA conditions, which in turn could be observed in volume of high-variation voxels observed in the histograms. Visual inspection of the spatial variation maps indicated that variation was lowest in the outer regions of the calf, becoming increasingly variable towards the central muscle areas. This effect appeared to coincide with the concentrically-decreasing SNR with distance away from the RF coil, an effect that was anticipated based on the work of Damon [8]. However, the statistical results of the present study found only a weak although significant negative relationship between SNR and vector variability when considering all muscle regions, indicating that SNR cannot be the sole determinant of vector stability. This agrees with the findings of Landman *et al.* [6], who found that increasing SNR does not necessarily relate to improvements in consistency of DTI results.

Further inspection of the vector variability maps revealed the soleus contrasted with the concentrically-increasing variation pattern in comparison to adjacent muscles. As such, it displayed increased variation of ε_1 and ε_2 in both its central and peripheral regions. The soleus consists of fibers oriented far more obliquely to the tibia than other muscles, as observed in the results of the present study as well as previous studies [17]. Furthermore, it contains smaller and more highly-capillarized fibers [33,34], and has been cited in past studies as being troublesome for DTI analysis [35]. These differences in vector variation according to anatomical boundaries further suggest that vector variability is not simply due to heterogeneous SNR within an image, but of muscle geometry and composition as well.

Efforts to improve SNR within skeletal muscle, and thus DTI accuracy, often utilize time-consuming strategies such as increased numbers of signal averages (NSA) or numbers of gradient directions (NDD) [7,13,17], although extra acquisition time increases the risk of artifacts due to bulk motion, physiological pulsation, or equipment noise. Accordingly, our results show that increasing NSA resulted in overall increases of SNR, while increases in NDD did not.

The effect of increasing the time spent on scan acquisition (STE) showed a modest impact on improving ε_1 variability, an effect noted in previous studies of the brain [5,6]. However, the present study found that increases in STE were only weakly related to improved ε_2 stability, an effect that can also be observed within the histograms of vector variation maps. Our results also indicate that increasing the NDD decreased the overall ε_1 variability, while increasing the NSA served to reduce the overall ε_2 variability. Interestingly, however, decreasing NSA served to increase the correlation between ε_1 and ε_2 variability, indicating that factors affecting directional stability are shared between eigenvectors in conditions of low NSA.

The present study also investigated the relationships between various DTI scalar outputs and their directional variability, given the intrinsic relationship between eigenvectors and their respective eigenvalues. Mean diffusivity (MD) did not significantly change according to experimental condition, indicating the utility of a DTI acquisition scheme with minimal STE (e.g. 6 NDD and 1NSA) is adequate if this is the only intended measure. This effect has been previously observed in the brain [5,6]. Shape-based measures such FA and ratio of λ_3:λ_2 were assessed with the expectation that as eigenvalue relationships approached sphericity or radial equality, the variability in calculated vector direction or classification would increase [4]. The FA of skeletal muscle is typically quite low (0.18 to 0.40) [11,12,16,19], meaning that the three eigenvalues that contribute to this measure are approaching equality. While the present study was able to replicate the low FA measures of prior studies, correlations between FA and vector variability were quite weak or not significant. The ratio of λ_3:λ_2, assessed to investigate relationships between radial parity and eigenvector variability, displayed an extremely weak correlation with ε_2 variability, indicating that similarity between the two minor eigenvalues had little to do with the stability of their respective eigenvectors. Curiously, λ_3:λ_2 showed a stronger correlation with ε_1 variability than that of ε_2. This finding could perhaps be due to the underestimation of λ_3 in low SNR situations [5,8], with low SNR also contributing to instability of the ε_1 direction.

Calculations of zenith angle, representing angulation of fiber orientation relative to the main magnetic field, provided the strongest results of this study. Increased variability of ε_1 was strongly correlated with increases in the obliqueness of the calculated fiber orientation, an effect which has been previously noted [35]. This effect was downgraded to moderate when the soleus, known to contain fibers more oblique than adjacent muscles [17,19], was removed from the analysis. In contrast, the relationship between zenith angle and ε_2 variability was found to be weak and no more prominent than any of the other experimental variables assessed. However, we approach these findings regarding zenith angle with caution, as the measure with which we used to determine zenith angle (namely, ε_1) also demonstrated the most variability due to obliqueness.

It was hypothesized that increases in ε_1 variability would impact the variability of ε_2, however correlation analysis found only a minor relationship between the two.

The widest range and highest levels of ε_2 variability occurred in regions of least ε_1 variability. This seems to indicate that while increased ε_1 variability is related to increased ε_2 variability, ε_1 stability does not ensure stability in ε_2. This result, in addition to the other observations and analyses used in the present study, leads us to conclude that while the behaviour of ε_1 variation within human calf muscle is fairly stable and can be influenced by experimental conditions in a moderately predictable fashion, the direction of ε_2 remains quite variable regardless of condition.

There are several limitations regarding this study. First, our choice to not perform eddy current and gross motion corrections may seem a detriment given the availability of correction algorithms available today. However, the purpose of the present study was to illustrate the variability present under different experimental conditions, and identify how well individual and collective muscle regions may perform without the need for processing. Given the variety of correction algorithms available, and the fact that they are tailored to studies of the brain, it was thought best to evaluate the vector variation without post processing, lest the present study become a comparison of algorithm efficacy and errors in interpolation. Additionally, by not using post-processing, this study mimics the output of clinical scans utilizing multi-NSA acquisition. Finally, these measures of vector precision perhaps serve as a baseline with which to assess the efficacy of post-processing algorithms.

A second potential limitation of the present study is that the voxel dimensions were not isotropic. This could potentially bias assessment of vector variability, as spatial information is thus better represented across an axial slice than through it. Structures not aligned with the main axis of anisotropic voxels risk having spatial and angular information obscured due to partial voluming [36]. Indeed, the present study found that the calculated obliqueness of fiber direction had a strong relationship with the variability of the first eigenvector, and it is possible that voxel anisotropy played a role in this finding. However, there is no current evidence that voxel anisotropy plays a role in the stability of eigenvectors within skeletal muscle, therefore future empirical work examining the nature of voxel shape and ability to represent muscle structure is warranted.

The present study is also limited by the lack of external validation regarding the orientation of calculated eigenvectors. This limitation is most notable regarding our assessment of zenith angle, where the present study found a high relationship between fiber obliqueness and principal eigenvector variability, with the principal eigenvector direction being the measure by which we calculated zenith angle. As noted by Jones [4], precision can be assessed, but accuracy requires a gold standard. A temptation in designing the present study was to assess vector variability by deviation from an aggregate of all 9 volumes within each NDD scheme. However, it was felt that using such a standard would merely demonstrate that increasing NSA approaches a mean, rather than whether the data was accurate and representative of anatomy. Future work into assessing the validity of DTI eigenvectors, particularly the radial eigenvectors, would benefit from the use of complementary methods to visualize muscle fiber arrangement, such as ultrasound [35].

Finally, the present study is limited by the small sample size. While we were able to demonstrate differential variation in the stability of principal versus minor eigenvectors as well as statistical relationships between many of the variables assessed, it is believed that a larger cohort would aid in determining the influence of experimental conditions upon vector variability, especially given the non-normal behaviour of our data.

In conclusion, this study demonstrates that the minor eigenvectors are prone to high directional variability despite stability of the principal eigenvector, and that experimental efforts which improve ε_1 stability may not be nearly as effective in improving the stability of the minor eigenvectors. Thus, we recommend caution in allotting anatomical meaning to the individual minor eigenvalues unless the stability of their respective eigenvectors can be ascertained. Indeed, it is perhaps the better strategy to consider the mean of the second and third eigenvalues (Radial Diffusivity, RD) as used in studies of the brain [37].

5.3.6 REFERENCES

[1]Cleveland GG, Chang DC, Hazlewood CF, Rorschach HE. Nuclear Magnetic Resonance Measurement of Skeletal Muscle. Biophys J 1976; 16:1043-1053.

[2]Stejskal EO, Tanner JE. Spin diffusion measurements: spin echoes in the presence of time-dependent field gradient. Journal of Chemical Physics 1965; 42(1):288-292.

[3]Basser PJ, Mattiello J, Le Bihan D. MR diffusion tensor spectroscopy and imaging. Biophys J 1994; 66:259-267.

[4]Jones DK. Determining and visualizing uncertainty in estimates of fiber orientation from diffusion tensor MRI. Magn Reson Imaging 2003; 49:7-12.

[5]Farrell JAD, Landman BA, Jones CK. et al. Effects of Signal-to-Noise Ratio on the Accuracy and Reproducibility of Diffusion Tensor Imaging-Derived Fractional Anisotropy, Mean Diffusivity, and Principal Eigenvector Measurements at 1.5T. J Magn Reson Imaging 2007; 26:756-767.

[6]Landman BA, Farrell JAD, Jones CK, Smith SA, Prince JL, Mori S. Effects of diffusion weighting schemes on the reproducibility of DTI-derived fractional anisotropy, mean diffusivity, and principal eigenvector measurements at 1.5T. NeuroImage 2007; 36:1123-38.

[7]Froeling M, Nederveen AJ, Nicolay K, Strijkers GJ. DTI of human skeletal muscle: the effects of diffusion encoding parameters, signal-to-noise ratio and T2 on tensor indices and fiber tracts. NMR Biomed 2013; 26:1339-1352.

[8]Damon, BM. Effects of Image Noise in Muscle DT-MRI Assessed Using Numerical Simulations. Magn Reson Med 2008;60(4):934-944.

[9]Hatakenaka M, Yabuuchi H, Sunami S. et al. Joint Position Affects Muscle Proton Diffusion: Evaluation With a 3-T MR System. Am J Roent 2010; 194: W208-W211.

[10]Heemskerk AM, Strijkers GJ, Vilanova A, Drost MR, Nicolay K. Determination of Mouse Skeletal Muscle Architecture Using Three-Dimensional Diffusion Tensor Imaging. Magn Reson Med 2005; 53:1333-1340.

[11]Deux JF, Malzy P, Paragios N. et al. Assessment of calf muscle contraction by diffusion tensor imaging. Eur Radiol 2008; 18:2303-2310.

[12] Schwenzer NF, Steidle G, Martirosian P. et al. Diffusion tensor imaging of the human calf muscle: distinct changes in fractional anisotropy and mean diffusion due to passive muscle shortening and stretching. NMR Biomed 2009; 22:1047-53.

[13] Heemskirk AM, Sinha TK, Wilson KJ, Ding Z, Damon DM. Repeatability of DTI-based skeletal muscle fiber tracking. NMR Biomed 2010; 23:294-303.

[14] Sinha S, Sinha U. Reproducibility Analysis of Diffusion Tensor Indices and Fiber Architecture of Human Calf Muscles In Vivo at 1.5 Tesla in Neutral and Plantarflexed Ankle Positions at Rest. J Magn Reson Imaging 2011; 34:107-119.

[15] Froeling M, Oudeman J, van den Berg S, et al. Reproducibility of Diffusion Tensor Imaging in Human Forearm Muscles at 3.0 T in a Clinical Setting. Magn Reson Med 2010; 64:1182-1190.

[16] Galban CJ, Maderwald S, Uffman K, de Greiff A, Ladd ME. Diffusive sensitivity to muscle architecture: a magnetic resonance diffusion tensor imaging study of the human calf. Eur J Appl Physiol 2004; 93(3):256-62.

[17] Karampinos DC, King KF, Sutton BP, Georgiadis JG. Myofiber Ellipticity as an Explanation for Transverse Asymmetry of Skeletal Muscle Diffusion MRI In Vivo Signal. Ann Biomed Eng 2009; 37:2532-2546.

[18] Okamoto Y, Kunimatsu A, Kono T, Nasu K, Sonobe J, Minami M. Changes in MR Diffusion Properties during Active Muscle Contraction in the Calf. Magn Reson Med Sci 2010; 9(1):1-8.

[19] Sinha S, Sinha U, Edgerton VR. In vivo Diffusion Tensor Imaging of the Human Calf Muscle. J Magn Reson Imaging 2006; 24: 182-190.

[20] Elzibak AH, Noseworthy MD. Assessment of diffusion tensor imaging indices in calf muscles following postural change from standing to supine position. MAGMA 2014; 27(5):387-95.

[21] Smith SM, Jenkinson M, Woolrich MW et al. et al, 2004. Advances in functional and structural MR image analysis and implementation as FSL. Neuroimage 2004; 23:S208-S219.

[22] Smith SM. Fast robust automated brain extraction. Hum Brain Mapp 2002; 17(3):143-155.

[23] Behrens TE, Woolrich MW, Jenkinson M, et al. Characterization and propagation of uncertainty in diffusion-weighted MR imaging. Magn Reson Med 2003; 50(5):1077-88.

[24] Fleisch DA. A Students Guide to Vectors and Tensors. New York: Cambridge University Press; 2012. 175 p.

[25] Dietrich O, Raya JG, Reeder SB, Reiser MF, Schoenberg SO. Measurement of Signal-to-Noise Ratios in MR Images: Influence of Multichannel Coils, Parallel Imaging, and Reconstruction Filters. J Magn Reson Imaging 2007; 26:375-85.

[26] Rogers, J. J. NEMA Standards Publication MS 6-1991, 119. Rosslyn: National Electrical Manufacturers Association, 2008.

[27] Cleveland GG, Chang DC, Hazlewood CF, Rorschach HE. Nuclear Magnetic Resonance Measurement of Skeletal Muscle. Biophys J 1976; 16:1043-1053.

[28] Van Doorn A, Bovendeerd PHM, Nicolay K, Drost MR, Janssen. Determination of Muscle Fibre Orientation using Diffusion-Weighted MRI. Eur J Morphol 1996; 34(1):5-10.

[29] Van Donkelaar CC, Kretzers LJG, Bovendeerd PHM et al. Diffusion tensor imaging in biomechanical studies of skeletal muscle function. J Anat 1999; 194:79-88.

[30] Damon BM, Ding Z, Anderson AW, Freyer AS, Gore JC. Validation of diffusion tensor MRI-based muscle fiber tracking. Magn Reson Med 2002; 48:97-104.

[31] Budzik JF, Le Thuc V, Demondion X, Morel M, Chechin D, Cotton A. In vivo MR tractography of thigh muscles using diffusion imaging: initial results. Eur Radiol 2007; 17:3079-3085.

[32] Kermarrec E, Budzik JF, Khalil C, Le Thuc V, Hancart-Destee C, Cotton A. In Vivo Diffusion Tensor Imaging and Tractography of Human Thigh Muscles in Healthy Subjects. Am J Roentgenol 2010; 195(5):W352-6.

[33] Andersen P, Kroese AJ. Capillary Supply in Soleus and Gastrocnemius Muscles of Man. Pflugers Arch 1978; 375:245-249.

[34] Polgar J, Johnson MA, Weightman D, Appleton D. Data on Fibre Size in Thirty Six Human Muscles: An Autopsy Study. J Neurol Sci 1973; 19:307-318.

[35] Okamoto Y, Okamoto T, Kujiraoka Y, Hirano Y, Isobe T, Minami M. Correlation between pennation angle and image quality of skeletal muscle fibre tractography using deterministic diffusion tensor imaging. J Med Imag Rad Oncol 2012; 56:622-626.

[36] Oouchi H, Yamada K, Sakai K, et al. Diffusion Anisotropy Measurement of Brain White Matter is Affected by Voxel Size: Underestimation Occurs in Areas with Crossing Fibers. Am J Neuroradiol 2007; 29:1102-1106.

[37] Song SK, Sun SW, Ramsbottom MJ, Chang C, Russel J, Cross AH. Dysmyelination revealed through MRI as increased radial (but unchanged axial) diffusion of water. Neuroimage 2002; 17(3): 1429-36.

Chapter 6

Dynamic DTI (dDTI) Shows Differing Temporal Activation Patterns in Post-Exercise Skeletal Muscles

Conrad P. Rockel, B.A., Alireza Akbari, Ph.D., Dinesh Kumbhare, M.D., Michael D. Noseworthy Ph.D., P.Eng.

6.1 Context of Paper

The following experiment was performed in order to expand on the initial findings of post-exercise temporal diffusion described in Chapter 4. This study utilized a timecourse DTI acquisition strategy designed to enhance the temporal resolution in comparison to that of the pilot study. The time needed for acquisition of a single DTI volume (aka timepoint) was reduced from 108 to 35 seconds by limiting the number of diffusion gradients to N=6, as well as reducing the repetition time (TR) from 6000 to 4000 ms (see **Appendix A**).

In addition to TR optimization, this experiment targeted a different grouping of calf muscles than that described in Chapter 4, as the exercise task involving repetitive dorsiflexion-eversion of the foot was expected to involve antero-lateral muscles of the calf rather than muscles posterior to the tibia <Basmajian and de Luca, 1985>. Furthermore, a minimal level of resistance to the exercise motion was utilized in order to test the sensitivity of this DTI technique to exercise-derived temporal changes in diffusion. Concurrent temporal signal changes in the reference T2-weighted image (S_0) were also examined with respect to the DTI findings in order to determine the interpretive value of this measure in comparison to diffusion data. Finally, post-exercise temporal diffusion behaviour of individual muscles for both active and inactive muscles were measured in this study, and the tissue composition of each muscle was considered in the interpretation of the results.

It should also be noted that the present study was performed following a substantial hardware upgrade of the MRI scanner and related equipment in relation to that used in the preliminary study. The scanner was upgrade from a GE HD (software v.12) to a MR750 Discovery system (software v.22).

6.2 Declaration

Conrad P Rockel, in collaboration with Alireza Akbari, designed and performed the experiment. Conrad P Rockel performed data and statistical analyses, and wrote the initial manuscript, as well as proofread and edited further manuscript incarnations.

Dinesh Kumbhare provided some equipment, offered clinical and physiological perspective, as well as proofreading. Michael D Noseworthy provided funding, statistical advice, substantial proofreading, editing, reformatting, and tirelessness in the role of corresponding author.

This paper was published in *Magnetic Resonance Materials in Physics, Biology and Medicine (MAGMA)*:
Rockel C, Akbari A, Kumbhare DA, Noseworthy MD. Dynamic DTI (dDTI) shows differing temporal activation patterns in post-exercise skeletal muscles. MAGMA 2016; Sep 13 [Epub ahead of print]. doi: 10.1007/s10334-016-0587-7

6.3 Paper

Dynamic DTI (dDTI) Shows Differing Temporal Activation Patterns in Post-Exercise Skeletal Muscles

Conrad Rockel[1,2], Alireza Akbari[1,2], Dinesh A. Kumbhare[1,5],

and *Michael D. Noseworthy[1,2,3,4,6]

[1] *McMaster School of Biomedical Engineering, McMaster University, Hamilton, Ontario, Canada.*
[2] *Imaging Research Centre, St. Josephs Healthcare, Hamilton, Ontario, Canada.*
[3] *Department of Radiology, McMaster University, Hamilton, Ontario, Canada.*
[4] *Department of Electrical and Computer Engineering, McMaster University, Hamilton, Ontario, Canada.*
[5] *Department of Medicine, Division of Physical Medicine and Rehabilitation, University of Toronto, Toronto, Ontario, Canada.*
[6] *Department of Medical Physics and Applied Radiation Sciences, McMaster University, Hamilton, Ontario, Canada.*

*Corresponding Author:
Dr. Michael D. Noseworthy, PhD, PEng.
Department of Electrical and Computer Engineering
McMaster University
Engineering Technology Building, ETB-406
1280 Main St. West, Hamilton, Ontario. Canada L8S 4K1
VOICE: (905) 525-9140 x23727
EMAIL: nosewor@mcmaster.ca

Acknowledgements Funding provided to CR through a Natural Sciences and Engineering Research Council (NSERC) of Canada CGS-D PhD scholarship. The research was funded through an NSERC Discovery grant to MDN

Running Title: Post-Exercise Muscle DTI

6.3.1 ABSTRACT

Object: To assess post-exercise recovery of human calf muscles using dynamic diffusion tensor imaging (dDTI).

Materials and Methods: DTI data (6 directions, b=400s/mm^2) were acquired every 35 seconds from 7 healthy males using a 3T MRI, prior to (4 volumes) and immediately following exercise (13 volumes, ~7.5 minutes). Exercise consisted of 5 minutes in-bore repetitive dorsiflexion-eversion foot motion with 0.78kg resistance. Diffusion tensors calculated at each time point produced maps of mean diffusivity (MD), fractional anisotropy (FA), radial diffusivity (RD), and signal at b=0s/mm^2 (S_0). Region-of-interest (ROI) analysis was performed on 5 calf muscles: tibialis anterior (ATIB), extensor digitorum longus (EDL), peroneus longus (PER), soleus (SOL) and lateral gastrocnemius (LG).

Results: Active muscles (ATIB, EDL, PER) showed significantly-elevated initial MD post-exercise, while predicted inactive muscles (SOL, LG) did not ($p<0.0001$). The EDL showed greater initial MD increase (1.90 x10^{-4}mm^2/s) than ATIB (1.03x10^{-4}mm^2/s) or PER (8.79x10^{-5}mm^2/s) ($p=7.40x10^{-10}$), and remained significantly-elevated across more timepoints than ATIB or PER. Significant increases were observed in post-exercise EDL S_0 relative to other muscles across the majority of timepoints ($p<0.01$ to $p<0.001$).

Conclusions: dDTI can be used to differentiate exercise-induced changes between muscles. The differences are suggested to be related to differing fiber composition.

Keywords: DTI, skeletal muscle, exercise, recovery, time course, human

6.3.2 INTRODUCTION

Diffusion weighted imaging (DWI) and its more directionally-resolved offspring, diffusion tensor imaging (DTI), are magnetic resonance imaging (MRI) techniques that probe water proton mobility and restriction within tissues to assess tissue microstructure. DTI caters well to skeletal muscle, as it is able to represent diffusion as a three-dimensional rotationally-invariant ellipsoid, from which measures of diffusivity, shape, and orientation are obtained.

The anisotropic nature of diffusion within skeletal muscle has been detected using DWI [1], and the principal ellipsoidal axis from DTI shown to align with muscle fiber direction [2]. Studies of human skeletal muscle have used DTI to investigate tissue microstructure in the thigh [3] and calf [4-7], and the impact of exercise training on muscle structure [8, 9]. MRI diffusion techniques have also been used to study human skeletal muscle following a single session of exercise. Typically, post-exercise muscles have displayed increased diffusivity [10-18] and a fattening of shape (i.e. reduced fractional anisotropy) [15-18]. A small group of studies have investigated the acute time course of post-exercise diffusion change by acquiring repeated diffusion volumes across time [10-12, 19], a technique that may provide further insight about muscle dynamics beyond the simple ”snapshot” approach. These studies, which often consider only one diffusion-encoding direction, have observed diffusion is initially elevated following exercise cessation, then subsequently decreases back to baseline across time. However, these studies either focused on a single muscle [10, 12] or measured a group of muscles as a single unit [11, 19].

It is known that skeletal muscle is not a homogeneous tissue, but instead composed of fibers that belong to two broad classes: Type-I (slow-twitch) and Type-II (fast-twitch). These fiber types have different sizes [20], metabolism (aerobic versus anaerobic) [21] and densities of supporting vasculature [22]. Each muscle contains a mixture of both fiber types, although in differing proportions between individual muscles.

To take the lower leg as an example, the soleus and anterior tibialis are composed of largely slow-twitch fibers (87.7±9.6% and 73.5±7.8% Type-I, respectively) while the lateral gastrocnemius is largely composed of fast-twitch fibers (46.9±6.9% Type-I) [23]. It is therefore conceivable that muscles of differing composition and physiology would show differing temporal patterns in diffusion values following a session of exercise. Furthermore, the level of exertion is important in that it determines the metabolism used by the muscle as a whole, with increasing levels of exertion resorting to more anaerobic means of metabolism [24].

The time evolution of acute exercise-induced diffusion changes within muscles of differing fiber content has not been thoroughly studied with directionally-resolved diffusion techniques such as DTI. In a previously-reported pilot study [25], consecutive DTI acquisitions were used to investigate temporal changes in human calf muscles before and immediately following a 2.5 minute session of in-bore load-bearing plantar flexion. The authors showed how the gastrocnemius (containing a lower percentage of slow-twitch fibers) demonstrated a temporal pattern of mean diffusivity (MD) involving delayed increase, a peak 4 minutes following exercise cessation, then gradual decline, which is a pattern inconsistent with some previous time course studies [10-12] but similar to others [19]. In contrast, the soleus (mostly composed of slow-twitch fibers) showed a minor increase from baseline, and remained slightly elevated across all time points. These differential patterns warranted further investigation using this temporal DTI approach to evaluate leg muscles of different fiber composition.

The purpose of the present study was to use DTI in order to evaluate the temporal post-exercise characteristics of muscles in the antero-lateral compartment of the leg, consisting of muscles known to be predominantly composed of slow-twitch fibers (anterior tibialis and peroneus longus) and those presumed to have more equal ratios of fast- and slow-twitch fibers (extensor digitorum longus). A mild exercise paradigm was utilized to test the sensitivity of the DTI measures, as well preserve the default metabolism of each muscle.

6.3.3 MATERIALS and METHODS

Subjects

Seven male volunteers (mean age 28.8±5.4 yrs; BMI 24.2±3.1kg/m^2) participated in this study. All subjects participate in exercise or sport at least one day a week, with no subjects performing at an elite level. Subjects self-reported whether they had ever received any important leg injury or had been diagnosed with any disorder that could affect skeletal muscle health. Furthermore, the MRI technologist who performed the scanning, having more than 20 years of musculoskeletal imaging experience, did not note any abnormalities in any scans. Subjects were asked to refrain from exercise for at least 12 hours before the study. The work was approved by our institutional ethics review board and informed consent was obtained from each volunteer.

Prior to scanning, each volunteer lay supine on a bed, during which they were instructed on how to perform the exercise task (dorsiflexion-eversion of the foot) **(Fig. 6.1)**.

They continued to lie supine with relaxed legs and feet for 30 minutes prior to

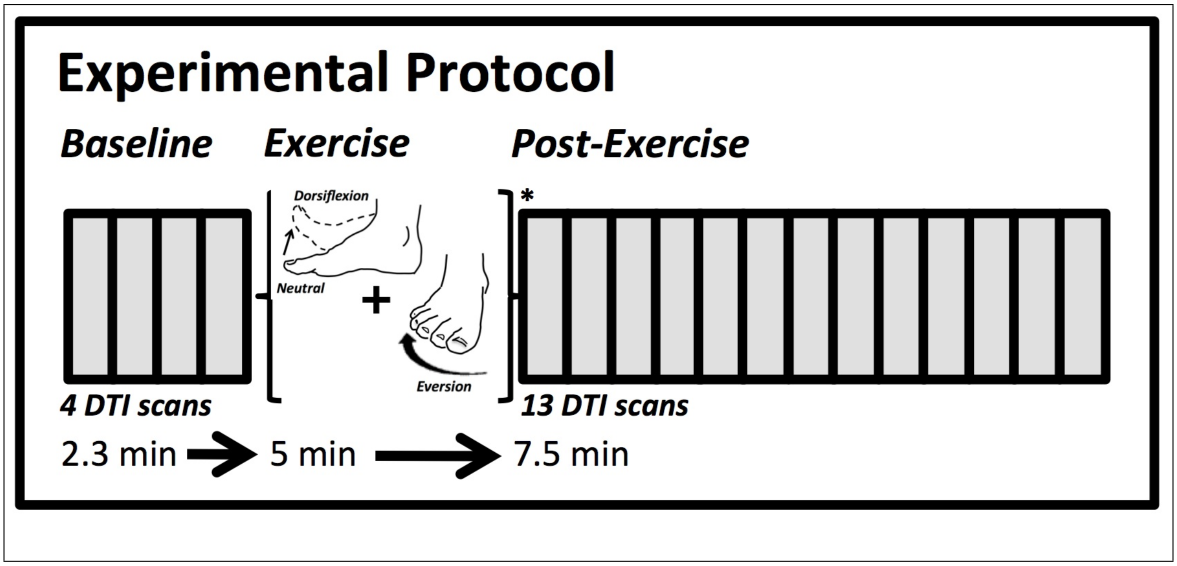

Figure 6.1: Experimental set up, including time required for each section. Four baseline DTI volumes were acquired. Exercise (repeated dorsiflexion-eversion performed at 1 Hz) is immediately (*) followed by 13 post-exercise DTI volumes (i.e. 13 timepoints).

scanning to allow for potential body water redistribution and to ensure muscle rest for the experiment [26]. Subjects were then transferred to the MRI table, lying supine and entering the bore feet-first, positioned with the distal end of the calf (proximal to the Achilles tendon) propped in a home-built wooden stand identical to that designed and built by others [26]. The leg was positioned to allow calf muscles to hang suspended through the MRI RF coil, avoiding compression on anterior or posterior muscles. The leg was then secured to the MRI table to prevent gross movement, using a strap about the thigh with enough tension to prevent gross movement without compromising subject comfort or blood flow, while still allowing the foot freedom to pivot about the ankle with the heel. A 3cm-wide strip of rubber exercise band (Blue Theraband; Pro HeathCare Products, www.prohealthcareproducts.com) was placed around the foot and the stand to provide 0.78kg resistance and assist the foot in returning to baseline position post-contraction. All scans were acquired with the foot relaxed at approximately 5° from right angle to the tibia (neutral position).

MRI Scanning and Exercise

MRI data was acquired using a GE 3T Discovery MR750 (General Electric Healthcare, Milwaukee WI) and an 8-channel transmit-receive knee coil (Invivo Corporation, Gainsville, FL), targeting the widest cross section of the calf (approximately 10 cm distal to the patella). DTI data was acquired using a single-shot dual echo spin echo EPI sequence (b=0 and 400s/mm^2, TR/TE=4000/70ms, 6 directions, 16 contiguous slices 4mm thick, 16cm FOV, 64x64 matrix, ASSET factor =2 and spectral-spatial RF excitation pulses). Each DTI volume took 32 seconds to acquire, followed by a 3-second dead time between successive acquisitions (i.e. 35s per temporal volume) **(Fig. 6.1)**. All DTI data were acquired with the same prescan values (i.e. shim, centre frequency, RF transmit gain), obtained for the first rest volume.

Following resting baseline acquisition (4 volumes), subjects were instructed to move their foot in a dorsiflexion-eversion motion (i.e. toes up and laterally) at 1Hz for a period of 5 minutes **(Fig. 6.1)**. The muscles targeted with this movement were the tibialis anterior (ATIB), extensor digitorum longus (EDL), and peroneus longus (PER) [21]. Subjects were instructed to let their foot relax to the neutral position between contractions and following cessation of the exercise task. This voluntary movement was self-paced using the timer on the front of the MRI scanner. Post-exercise DTI acquisition (13 consecutive volumes) began immediately following cessation of the in-bore exercise task, with pre-scan preparation having been completed prior to commencement of foot motion. Post-exercise scanning lasted for 7 minutes and 32 seconds.

DTI Analysis

Post-processing of DTI data involved affine registration and sinc interpolation of all 6 direction diffusion-weighted images to the T2-weighted zero diffusion image (b=0s/mm^2), for each time-based volume, using the FLIRT utility in FSL [27]. The diffusion tensor was calculated for each timepoint, after which mean diffusivity (MD), fractional anisotropy (FA), and eigenvalues (λ_1-λ_3) were calculated using FSL [27]. Radial diffusivity (RD) was calculated as the mean of λ_2 and λ_3. The T$_2$-weighted signal intensity (S$_0$) of the b=0s/mm^2 volume (acquired for diffusion calculations) was also assessed at each timepoint. Although T$_2$-weighted contrast mechanisms may differ from that of diffusion [10,11,28], S$_0$ was considered a DTI output (though only semi-quantitative) for the purposes of this study. Each DTI volume was measured in native space to minimize the effect of interpolation on tensor calculations.

Registration matrices were calculated between b=0s/mm^2 volumes across all time points within each pre-exercise and post-exercise dataset, and a composite volume was created for each dataset consisting of all time points. Regions of interest (ROIs) representing individual muscles were drawn on the composite volume for each DTI set and consisted of two 2x2 voxels across 5 slices (1 cm^3) **(Fig. 6.2)**. Muscle analysis is often performed by including the entire muscle as the ROI. However, the 2x2-voxel approach allows repeated measures analysis (to identify sources of variance), and there is a dramatic reduction in measurement error because the ROIs can be placed to avoid fascia, blood vessels, and artifacts from chemical shift across volumes [29]. The muscles investigated were tibialis anterior (ATIB), extensor digitorum longus (EDL), peroneus longus (PER), soleus (SOL), and gastrocnemius lateralis (LG). ROIs were

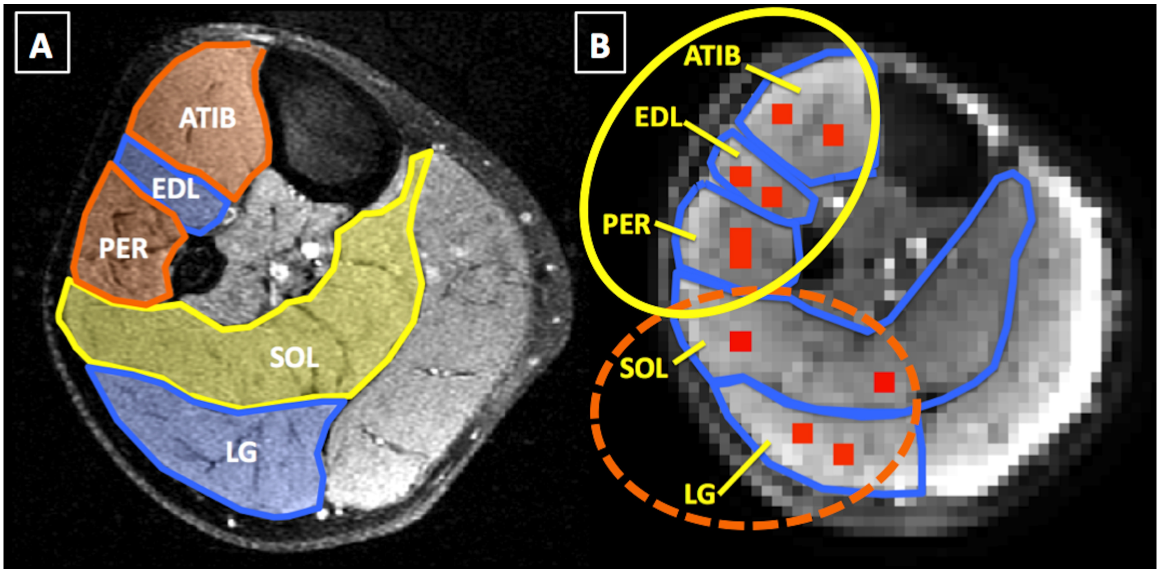

Figure 6.2: Axial view of human calf. **(A)** Outlines of muscles under study. ATIB = Anterior Tibialis, EDL = Extensor Digitorum Longus, PER = Peroneus Longus, SOL = Soleus, LG = Lateral Gastrocnemius. **(B)** Red squares denote region-of-interest size and placement. Yellow oval represents muscles expected to be active during exercise protocol, while orange oval represents muscles not expected to be active.).

drawn separately for pre- and post-exercise datasets to prevent mis-registration due to bulk movement resulting from exercise. All ROIs were drawn by a researcher with 12 years of MRI-based anatomical and DTI analysis. Subsequent inversion of the b=0s/mm^2 registration matrices allowed ROIs to be spatially adjusted, using nearest-neighbour interpolation, to each DTI time point for calculation of indices.

Pre-Exercise Baseline Calculation

Baseline DTI measures (MD, FA, λ_1, RD, and S_0) were calculated for each muscle ROI as a mean value across 4 time point volumes prior to the onset of exercise.

Spatial maps of signal-to-noise ratio (SNR) were calculated using the baseline b=0s/mm^2 images (i.e. S_0), and since parallel imaging was used in DTI acquisition, SNR was calculated according to the two-volume method of Dietrich [30, 31]. The two volumes necessary for this method of SNR calculation were collected in three pairs from the 4 baseline volumes (i.e. 1-2, 2-3, 3-4), with separate maps being produced for each pair. Measures of SNR from each ROI, per pair, per subject were subsequently combined to provide overall observed SNR for each muscle.

Post-Exercise Calculation

The magnitude of post-exercise change for each muscle DTI metric (MD, FA, λ_1, RD, and S_0) was calculated as the respective measurement unit difference from baseline. Percent change from baseline was also calculated to relate our present results to previous literature.

Statistical Analysis

Pre-exercise baseline data was assessed for each muscle ROI across 4 replicates for each subject for each of the experimental measures (MD, FA, λ_1, RD, S_0, and SNR). These measures were compared using a 3-way analysis of variance (ANOVA; Type III, constrained sums of squares) with subject, muscle and replicate as factors. Post-exercise data was analyzed by applying a 1-way ANOVA to the magnitude change values, per individual muscle, for each time point across all subjects. Both skewness and kurtosis were assessed to validate normality for each dataset. When the ANOVA test showed significance (i.e. $p<0.05$), *post hoc* multiple comparisons was performed using Scheffé's test. All statistical analysis was performed using the Statistics Toolbox of Matlab (v7.9; Mathworks, Natick MA). Following statistical analysis, data was visually presented as means ± standard error, generated using Prism (v5.0; GraphPad Software, La Jolla, CA).

6.3.4 RESULTS

Pre-Exercise Baselines

Significant differences were found between subjects, and between muscles, for each of the DTI metrics (MD, FA, λ_1, RD) ($p<0.0001$) **(Figs. 6.3a-d)**, while no significant results were found between the 4 pre-exercise baseline volumes for any of these measures ($p=0.1119$ to 0.7470).

Significant differences in baseline T_2-weighted b=0s/mm^2 image intensity (S_0)

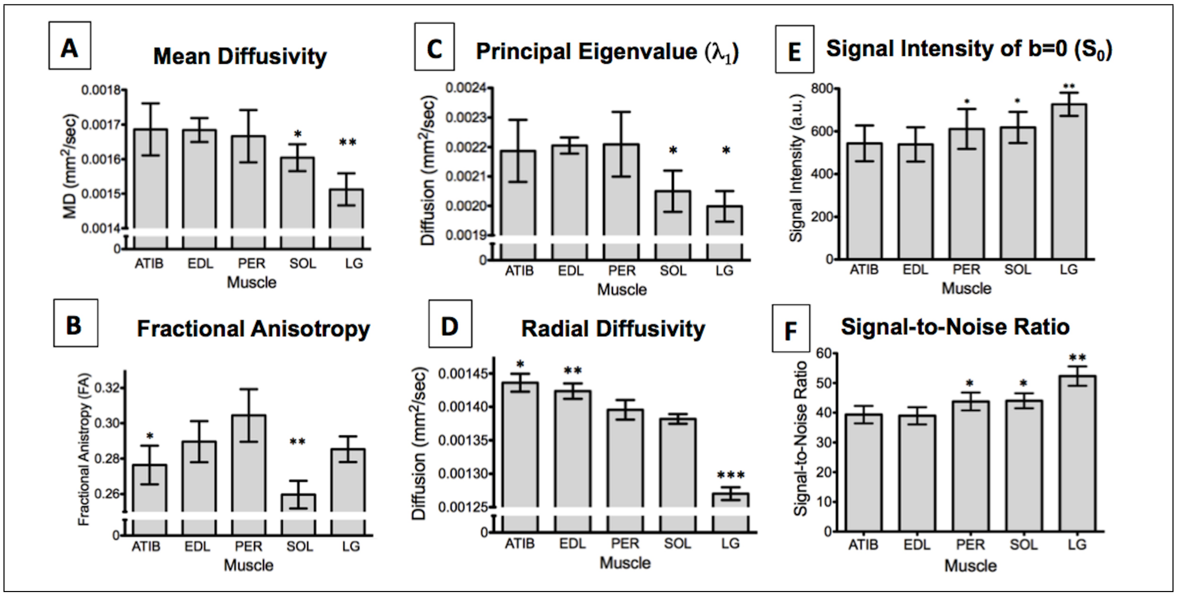

Figure 6.3: Baseline measures of individual muscles for each DTI measure. **(A)** Mean diffusivity (MD; * = significantly less than ATIB, EDL, and PER; ** = significantly less than all other measured muscles; $p<0.0001$). **(B)** Fractional anisotropy (FA; * = significantly less than PER; ** = significantly less than all other measured muscles; $p<0.0001$). **(C)** Principal eigenvalue (λ_1; * = significantly less than ATIB, EDL and PER; $p<0.0001$). **(D)** Radial diffusivity (RD; * = significantly greater than PER, SOL and LG; ** = greater than SOL and LG; *** = significantly less than all other measured muscles; $p<0.0001$). **(E)** Baseline signal intensity of zero-diffusion image (S_0 ; * = greater than ATIB and EDL; ** = greater than all other muscles, $p<0.0001$). **(F)** Signal-to-noise ratio (SNR; * = significantly greater ATIB and EDL; ** = significantly greater than all other measured muscles; $p<0.0001$).

were observed between subjects (*$p<0.0001$*), as well as between individual muscles (*$p<0.0001$*). Furthermore there was also a significant muscle-by-subject interaction (*$p<0.0003$*), but no muscle-by-replicate interaction effect (*$p=0.4373$*). Notably the LG had significantly higher S_0, likely due to proximity to the receiver coil. Also, PER and SOL each had significantly greater baseline S_0 than both ATIB and EDL (*$p<0.0001$*) **(Fig. 6.3e)**.

The SNR recorded from all ROIs across all subjects and volume pairs ranged from 20.6 to 72.9 with the mean individual muscle SNR being 40 or greater **(Fig. 6.3f)**. The LG showed significantly higher SNR than other measured muscles (*$p<0.0001$*). The SNR of PER and SOL were each significantly greater than both ATIB and EDL (*$p<0.0001$*) **(Fig. 6.3f)**.

Post Exercise

Immediately following exercise, the muscles predicted to be involved in the foot dorsiflexion/eversion motion (ATIB, EDL, PER) [21] showed a notable MD magnitude increase, ranging from 0.88 to $1.90\text{x}10^{-4}$ mm^2/s (~6-12% increase) across muscles at the first timepoint, while the MD of muscles predicted to be minimally-involved (SOL, LG) only changed +0.79 to -1.14 $\text{x}10^{-5}$ mm^2/s (~±2%) from baseline values **(Fig. 6.4a)**. The EDL showed the largest difference of MD in response to the exercise protocol, with a significant increase of $1.90\pm0.30\text{x}10^{-4}$ mm^2/s (12%) from baseline at the first DTI timepoint (35 seconds) (*$p=7.40x10^{-4}$*). The amount of MD change from baseline then decreased over the next 4 timepoints (70-175 seconds), while remaining significantly different from baseline **(Fig. 6.4a** and **Table 6.1)**.

ATIB and PER also showed a significant mean increase of $1.03\pm0.17\text{x}10^{-4}$ mm^2/s

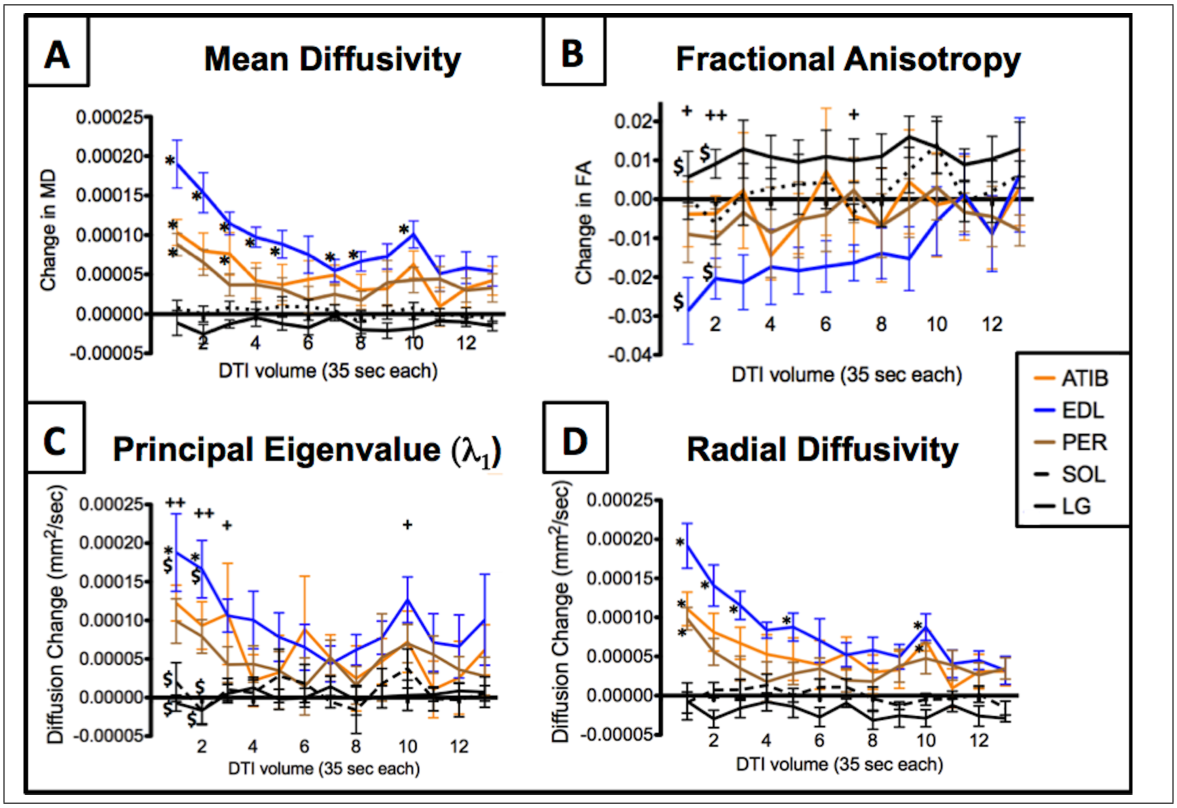

Figure 6.4: Temporal measures of post-exercise magnitude change in individual muscles for each DTI measure. **(A)** Mean diffusivity (MD) (* represents significant difference from baseline. Asterisks (*) represent significant difference from baseline. See **Table 6.1** for significance values and between-muscle differences. All error bars represent standard error of the mean. **(B)** Fractional anisotropy (FA). Symbols indicate timepoints with significant differences (+ $p<0.05$, ++ $p<0.01$; $ indicates significance between EDL and LG). **(C)** Principal eigenvalue (λ_1). Symbols indicate timepoints with significant differences (+ $p<0.05$, ++ $p<0.0001$; * indicates difference from baseline; $ indicates significance between EDL and LG or SOL. **(D)** Radial diffusivity. Asterisks (*) represent significant difference from baseline. See **Table 6.1** for significance values and between-muscle differences. All error bars represent standard error of the mean.

(7%) and 8.79±1.41x10^{-5} mm^2/s (6%) respectively from baseline at the first DTI timepoint ($p=7.40x10^{-4}$), after which the difference of MD from baseline decreased. The MD of LG, which was predicted to be less active during exercise, is worth noting for comparison since mean LG MD change is slightly decreased from baseline for every timepoint following exercise (ranging -0.31x10^{-5} to -2.56x10^{-5} mm^2/s across timepoints), though not significantly so. However, significant differences between the post-exercise LG MD and the predicted highly-active muscles (EDL, ATIB, PER) were found for 11 of 13 post-exercise timepoints **(Fig. 6.4a** and **Table 6.1)**.

The temporal progression of mean FA deviation from baseline demonstrated statistical significance at only 3 of 13 post-exercise timepoints (1 ($p<0.05$), 2 ($p<0.01$), and 7 ($p<0.05$)) **(Fig. 6.4b)**. No individual muscles demonstrated significant difference from baseline. However, at the first 2 post-exercise timepoints, the EDL FA showed a notable decrease (-0.028±0.008 and -0.020±0.005; -10% and -7%) that was significantly different from the slight increase in LG FA (0.0057±0.007 and 0.0091±0.004; 2% and 3%) ($p=0.0176$ and $p=0.0051$, respectively) **(Fig. 6.4b)**. The EDL FA then appeared to increase back towards baseline across subsequent timepoints, while the non-significant increase of LG FA from baseline persisted at a seemingly stable level.

Post-exercise changes of λ_1 were only significant between muscles or from baseline for 4 of 13 post-exercise timepoints (timepoints 1 ($p<0.0001$), 2 ($p<0.0001$), 3 ($p<0.05$), and 10 ($p<0.05$)) **(Fig. 6.4c)**. Of these, only the first two timepoints demonstrated any differences between muscles or baseline following testing for multiple comparisons, namely the increases in EDL λ_1 at timepoint 1 (1.88±0.50 x10^{-4} mm^2/s; 8.5%) and timepoint 2 (1.66±0.37 x10^{-4} mm^2/sec; 7.5%) were found to be significantly different from baseline, SOL and LG ($p=3.85x10^{-5}$ and $p=6.33x10^{-6}$,

MD	**Timepoint**	**P-value**	**ATIB**	**EDL**	**PER**	**SOL**	**LG**
	1	7.41x10^{-10}	X, XX, XXX	X, +, ++		XX, +	XXX, ++
	2	2.47x10^{-08}	X	+, ++, +++	+, $	++	X, +++, $
	3	6.60x10^{-07}	X	+, ++, +++	+	++	X, ++
	4	2.00x10^{-04}		+, ++		+	++
	5	7.00x10^{-04}		+, ++		+	++
	6	4.20x10^{-03}		+			+
	7	2.00x10^{-04}	X	+, ++		+	X, ++
	8	3.00x10^{-04}		+, ++		+	++
	9	4.90x10^{-03}		+			+
	10	9.15x10^{-07}	X	+, ++		+	X, ++
	11	3.60x10^{-02}					
	12	1.80x10^{-02}					
	13	2.50x10^{-03}		+			+
RD	**Timepoint**	**P-value**	**ATIB**	**EDL**	**PER**	**SOL**	**LG**
	1	4.96x10^{-09}	X, XX	+, ++	$, $$	X, +, $	XX, ++, $$
	2	2.61x10^{-06}	X	+, ++		+	X, ++
	3	1.79x10^{-06}	X	+, ++, +++	+	++	X, +++
	4	3.60x10^{-03}		+			+
	5	6.00x10^{-04}		+, ++		+	++
	6	1.72x10^{-02}		+			+
	7	5.10x10^{-03}					
	8	3.70x10^{-02}		+			+
	9	7.40x10^{-03}					
	10	3.73x10^{-07}	X, XX	+, ++	$	X, +	XX, ++, $
	11	***ns***					
	12	1.17x10^{-02}		+			+
	13	1.70x10^{-03}			$		$
S_0	**Timepoint**	**P-value**	**ATIB**	**EDL**	**PER**	**SOL**	**LG**
	1	1.70x10^{-03}		+, ++, +++	+	++	+++
	2	3.70x10^{-03}		+, ++	+		++
	3	2.20x10^{-03}		+, ++, +++	+	++	+++
	4	8.98x10^{-04}		+, ++, +++	+	++	+++
	5	1.50x10^{-03}		+, ++	+		++
	6	2.10x10^{-03}		+, ++	+		++
	7	1.00x10^{-03}		+, ++, +++	+	++	+++
	8	4.00x10^{-04}		+, ++, +++	+	++	+++
	9	9.10x10^{-03}		+			+
	10	1.70x10^{-03}		+, ++	+		++
	11	3.00x10^{-03}		+, ++, +++	+	++	+++
	12	2.30x10^{-03}		+, ++, +++	+	++	+++
	13	5.00x10^{-03}		+, ++	+		++

Table 6.1: Between-muscle differences for each post-exercise timepoint (MD, RD, S_0 only; FA and λ_1 are excluded due to fewer significant timepoints. Symbols indicate pairs of muscles found to be significantly different from one another per timepoint (see P-value column for significance). For each timepoint (following multiple comparisons), X, XX, and XXX pairs reflect those muscles significantly different from ATIB; +, ++, and +++ pairs the muscles significantly different from EDL; and $, $$ pairs the muscles significantly different from PER.

respectively).

The radial diffusivity (RD) of individual muscles immediately following exercise showed a similar temporal pattern to that of MD, as 12 of 13 timepoints showed significant differences between muscles or from baseline **(Fig. 6.4d** and **Table 6.1)**. At timepoint 1, the muscles hypothesized to be highly active (ATIB, EDL, and PER) showed a significant increase in RD from baseline (*p=*4.96×10^{-4}), while muscles expected to be less active (e.g. SOL, LG) did not **(Table 6.1)**. Furthermore, all muscles predicted to be highly-active were found to be significantly different from the less-involved muscles at this timepoint **(Table 6.1)**. Within the active muscles, the mean change in EDL RD at timepoint 1 ($1.92 \pm 0.29 \times 10^{-4}$ mm^2/s; 13.5%) appeared to be greater than that of ATIB ($1.11 \pm 0.22 \times 10^{-4}$ mm^2/s; 7.7%) or PER ($9.83 \pm 1.44 \times 10^{-5}$ mm^2/s; 7.0%), but this difference was found to be non-significant **(Fig. 6.4d** and **Table 6.1)**. After timepoint 1, EDL, ATIB, and PER all exhibit decreasing RD towards baseline across subsequent timepoints, with EDL alone maintaining significance from baseline at timepoints 2, 3 and 5 (*p=*2.61×10^{-4}, *p=*1.79×10^{-4}, and *p=0.0006*) **(Fig. 6.4d** and **Table 6.1)**. To contrast these results, the temporal behaviour of post-exercise LG RD showed a slight but non-significant decrease from baseline across all timepoints ($-0.73 \pm 2.36 \times 10^{-5}$ to $-3.15 \pm 1.4 \times 10^{-5}$ mm^2/s; -0.6 to -2.5%) **(Fig. 6.4d** and **Table 6.1)**. This slight decrease in LG RD was found to be significant from the predicted highly-active muscles in 10 of 13 timepoints (more notably the EDL) **(Fig. 6.4d** and **Table 6.1)**.

In assessing post-exercise S_0 magnitude change, only the EDL displayed significant differences from baseline, showing increased signal intensity of 62.2±25.2 a.u. (12%) and 64.4±32.4 a.u. (13%) at the first two timepoints (*p=*1.70×10^{-3}), after which

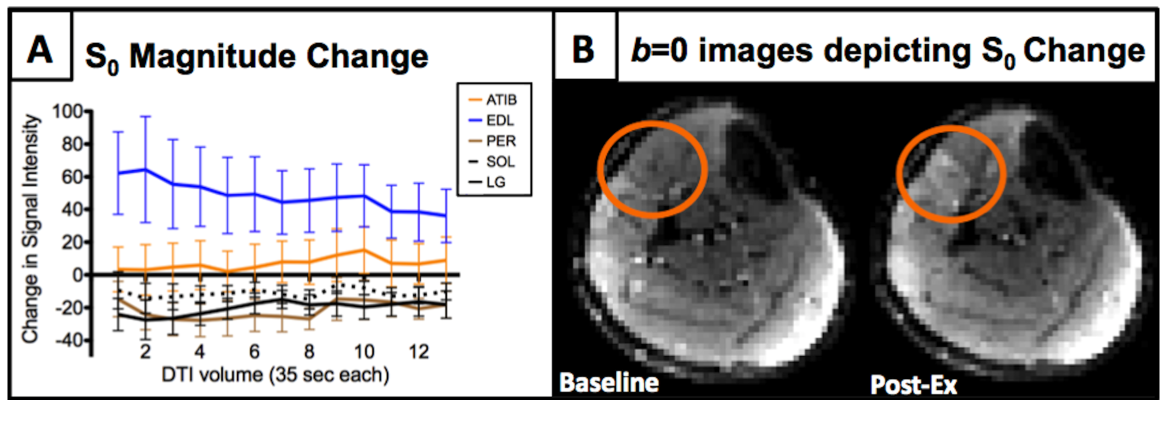

Figure 6.5: Effect of exercise upon signal intensity of b=0 s/mm^2 (S$_0$). **(A)** Temporal measure of post-exercise S$_0$ magnitude change. No measurements were significantly different from baseline, although EDL S$_0$ change was different from other measured muscles for all timepoints. See **Table 6.1** for significance values and between-muscle differences. **(B)** Pre- and post-exercise S$_0$ images of one subject demonstrating specific increased signal in EDL following exercise (orange oval). All error bars represent standard error of the mean.

the amount of change from baseline slightly receded **(Fig. 6.5a** and **Table 6.1)**. Furthermore, this increase in EDL S$_0$ was significantly different from all other muscles, across most timepoints (p=*0.0091* to p=*0.0009*) **(Table 6.1)**. Aside from EDL, the remaining muscles displayed stable although non-significant offsets from baseline **(Fig. 6.5a** and **Table 6.1)**. In this sense, the inter-muscular pattern of change from baseline was different between S$_0$ and that seen for DTI (e.g. MD or RD). The conspicuous increase in post-exercise EDL S$_0$ relative to adjacent muscles can be seen in **Fig. 6.5b**.

6.3.5 DISCUSSION

Although diffusion tensor imaging (DTI) is commonly used as a tool to assess static tissue structure, the present study demonstrates the utility of this technique to observe dynamic physiological activity within individual human muscles following mild exertion. Furthermore, this work provides insight into how individual muscles differ in terms of their post-exercise temporal patterns of response and recovery. The most noteworthy findings of the present study regarding post-exercise temporal DTI were: (i) the increased mean diffusivity (MD) in muscles expected to be involved with the exercise protocol (ATIB, EDL, and PER) [21]; (ii) the conspicuous increase in EDL MD, both initially and across timepoints, relative to ATIB and PER; (iii) the distinct S_0 increase observed only in EDL, both initially and across time; and (iv) the inter-muscular pattern of post-exercise MD change being different from that of S_0.

The effects within skeletal muscle related to a single episode of physical activity have previously been studied in humans with diffusion imaging, with increases of MD (i.e. apparent diffusion coefficient (ADC)) observed following periods of hand gripping [10, 13], calf plantar flexion [11, 17, 19, 25], dorsiflexion [12], or strenuous running tasks [14, 16, 18], with post-exercise diffusion increasing approximately 5 to 20 percent from baseline. The MD increases of 6 to 12 percent seen in the active muscles at the first timepoint fall within this range. In the one study assessing dorsiflexion exercise [12], the initial increase in diffusivity of the anterior tibialis was approximately 13 percent, while our results indicate an increase of 7 percent for this muscle. This may be due to factors such as (i) the level of exertion, where the cited study [12] utilized dorsiflexion to exhaustive levels, while the present study used a mild dorsiflexion-eversion exercise; and (ii) the cited study used a one-dimensional linescan diffusion protocol, while the present study used DTI.

The time course of acute post-exertion skeletal muscle diffusion using consecutive diffusion volumes has been measured in the human arm [10] and lower leg [11, 12, 19]. In these studies, a typical pattern within active muscles involves increased diffusivity in the scan acquisitions subsequent to exercise, followed by a decrease towards baseline, although this pattern is not universally found [19]. The results of the present study seem to echo this overall pattern, although direct comparisons are difficult because of the nature of the exercise and the individual muscles under investigation. This could also be why the results of the present study display different temporal patterns than the previous pilot study [25], which used a greater resistive load upon the posterior calf compartment.

The time course of MD change in the present study reveals that, upon cessation of mild exercise, ATIB and PER lose significance from baseline by timepoint 4 (2min 20s) while EDL finally loses significance from baseline at timepoint 11 (6min 25s). This time length for restitution from post-exercise diffusion increase is similar to a previous study using a similar resistive device [19], while another study using a foam ball observed approximation to baseline after 20 minutes [10]. The intensity of exertion appears to play a role in return to baseline values, as diffusion increases have been shown to last for hours [16], days [17], or weeks [18] following sessions of strenuous or exhaustive exercise.

The immediate post-exercise increases in MD have been attributed to a combination of increases in muscle water or blood volume [10-12], shifts of water from vascular compartments to interstitial spaces [11, 32] or from macromolecular-bound to free states [11, 33]. Post-exercise membrane damage, allowing more freedom of diffusion, has also been considered [17, 18]. Finally, temperature can also contribute to diffusion increases measured following exercise [10, 12, 34].

While these explanations may help to explain the general increases of post-exercise diffusion within activated skeletal muscle, our study also found differences between individual human calf muscles. Specifically, while EDL, ATIB, and PER all showed a significant increase from baseline at the first post-exercise timepoint (35s), the EDL MD increase was also found to be significantly different from that of ATIB. Furthermore, the EDL MD remained elevated from baseline across more time points than did that of ATIB or PER, suggesting that different recovery mechanisms must exist between EDL and ATIB or PER. We hypothesize that these inter-muscular diffusion differences are attributed (at least in part) to the physiology associated with the differing fiber composition of EDL versus that of ATIB and PER.

Skeletal muscles are composed of different proportions of two overarching classes of myofiber, namely Type-I (slow-twitch) and Type-II (fast-twitch). These fiber classes are differentiated by their respective metabolism for regeneration of adenosine triphosphate (ATP), the molecule that provides energy to the muscle for contraction and physiological function. Briefly, Type-I fibers utilize oxygen to regenerate ATP in a slow metabolic reaction that ultimately produces greater amounts of energy. These fibers are smaller and heavily capillarized in order to maintain a steady supply and efficient distribution of blood-borne oxygen [22], making them less prone to fatigue. In contrast, Type-II fibers rely on anaerobic metabolism of stored high-energy phosphates and glycogen. These large fibers are capable of strong, rapid contractions, yet are faster to fatigue and more prone to damage [17, 24]. Replenishment of ATP and removal of metabolic waste products within predominantly Type-II muscle tissue demands increased blood flow upon relaxation of the contracted muscle, a process known as reactive hyperemia.

Human muscles contain a combination of both fiber types, ranging from roughly an equal distribution of each fiber class, to those with an increased percentage of Type-I fibers [23]. With regards to muscles measured in this study, the lateral head of the gastrocnemius has previously shown a mean of 46.9±6.9% Type-I fibers, indicating a roughly equal fiber type ratio, while the anterior tibialis has 73.5±7.8% Type-I, peroneus longus 62.5±9.6% Type-I, and soleus 87.7±9.6% Type-I, establishing these muscles as predominantly slow-twitch [23, 35].

The scientific literature is remarkably sparse as to the fiber content of the human EDL, the muscle showing the greatest post-exercise diffusion change in the present study. The function of the EDL is not stabilizing or supportive, but assistive to the anterior tibialis in dorsiflexion and eversion of the foot about the ankle [21]. Muscles local to the EDL that play similar secondary roles (e.g. extensor digitorum brevis or flexor digitorum brevis) were found to be composed of a roughly equal fiber ratio (e.g. 45.3±15.2% and 44.5±11.6% Type-I content, respectively) [23]. Furthermore, the EDL is routinely used as a model of fast-twitch muscle in animal studies [36], although extrapolation between quadruped and biped fiber content is not necessarily accurate [37]. That said, we presume that EDL is made up of roughly equivalent percentages of fast- and slow-twitch fibers, rather than a predominance of slow-twitch fibers.

The baseline DTI results did not reflect the diversity in fiber composition. Our MD results appeared to be within range of values from a survey of existing literature [4-7, 17, 26, 34], although no consistent pattern of inter-muscular MD seemed to exist within this survey. Furthermore, our baseline MD data did not appear to be conspicuously associated with published values of muscle fiber percentages [23, 37], as the ranking of our muscle MD results did not match the ordering of mean fiber content values.

Unlike the MD results, a slight consistency of FA relationships between muscles emerged with our literature survey, in that the soleus displays the lowest FA of measured muscles [4, 5, 7, 17, 26], and the peroneus longus displays higher FA than most other muscles [4], a pattern echoed in the results of the present study. The soleus contains the highest concentration of Type-I fibers, so it is possible that smaller fiber size and accompanying capillarization contribute to the low FA value for this muscle. However, this interpretation fails to explain why the peroneus longus, another slow-twitch-dominant muscle, would have the highest FA.

The baseline results indicate that DTI measures of resting muscle are not related to fiber composition in an obvious manner, and that a multitude of other factors should be considered, such as fiber size, cross-sectional area, packing of fibers, fluid volume in interstitial and intracellular compartments, as well as heterogeneity in fiber composition between individual human subjects [23, 37, 38]. Numerous models have been proposed to address this complexity (e.g. the random permeable barrier model (RPBM) as per reference 14), but the relationship between tissue composition of resting skeletal muscle and DTI remains unclear.

Assessment of the activation and recovery states of skeletal muscle can reveal details beyond those of the muscle at rest. As mentioned, the present study observed differences in the magnitude of temporal diffusion increase between the individual active muscles following the mild exercise task, with EDL showing greater and sustained increases across time relative to ATIB and PER. Furthermore, EDL was the only muscle to display a post-exercise increase in S_0, while all other muscles showed only minimal offsets from baselines across time. We theorize that these between-muscle differences in post-exercise diffusivity measures are associated with fiber-related physiology. For example, the large capillary density of slow-twitch-dominant muscles [22] may be able to better maintain ATP and cellular metabolism during exercise, thus demonstrating lesser flow changes from baseline upon cessation of exertion. In contrast, muscles with a greater proportion of fast-twitch fibers would likely require increased blood flow for replenishment of ATP and disposal of anaerobic waste products.

These changes in vascular flow would alter DTI measures in a number of ways. First, an increase in perfusion would confound our measures because only two b-values were used, one of which was b=0 s/mm^2. Studies using more than two b-values have found diffusion within tissue to be at least bi-exponential, with a fast-diffusing compartment attributed to perfusion, and a slower compartment attributed to tissue water [39]. However, these non-tensor diffusion studies have observed increased diffusion even when perfusion has been accounted for [13]. An additional consequence of perfusion could be that the pulsatile nature of blood flow causes subtle motion disturbance in the infused tissue, contributing to signal attenuation, and thus greater estimates of diffusion [11]. Second, an influx of blood will increase the water content within the tissue, both interstitially and intracellularly, allowing more freedom for water to diffuse without encountering obstacles or restrictions [10, 11, 13].

Our measurement of the zero-diffusion image signal intensity (S_0) offers additional information into the recovery dynamics of individual calf muscles following mild exertion. As mentioned, the EDL demonstrated increased S_0 from baseline following the cessation of exercise, and did not begin to decrease until timepoint 3. This temporal S_0 behaviour contrasted with that of the adjacent muscles, which demonstrated only slight offsets from baseline across time.

The S_0 is a T_2-weighted image, the image signal being governed predominantly by the state of transverse relaxation (T_2) within the muscle tissue at the time of echo acquisition. While true quantification of T_2 requires several data points [33], increases in S_0 following exercise, as seen for EDL in contrast to adjacent muscles, can be suggestive in the underlying T_2 of the measured muscle tissue. A more complete model for the S_0 signal change would require both diffusion and multi-echo T_2 measures, but since post-exercise muscle changes happen quickly, the time required for acquisition of a multi-echo T_2 map (CPMG) [33, 40], precluded the use of this technique in the present study.

It is known that exercise induces increased tissue T_2 and thus T_2-weighted signal intensity with active human muscles [12, 41, 42] that can last days in the case of damaging eccentric exercise [17]. Additionally, it has been demonstrated that there are correlations between workload levels of individual muscles and increases observed in multi-echo T_2 measurements [11, 42-44]. The cause of these T_2 increases following exercise remains unclear, although they have been attributed to the release of intracellular tissue water from bound to free compartments [11, 12, 33]. inflammation [17], or osmotic water shifts induced by the accumulation of acidic metabolic byproducts of anaerobic glycolytic metabolism [28, 42, 45]. Acidic byproducts are more likely to increase in muscles with a greater proportion of Type-II (fast-twitch) fibers, and thus induce greater compartmental shifts than in Type-I (slow-twitch) dominant muscles [45].

Interestingly, studies reporting increases in slow-twitch-dominant muscle T_2 values, such as soleus [44] and anterior tibialis [12, 42], utilized strenuous or exhaustive exercise prior to T_2 measurement, meaning these muscles may have needed to utilize glycolytic as well as aerobic metabolism. In contrast, our exercise protocol was quite mild, allowing for the slow-twitch-dominant muscles (e.g. ATIB) to function aerobically and not demonstrate the increase in S_0 observed for the EDL, which likely has a more equal ratio of fiber types.

Several studies of post-exercise skeletal muscle have investigated the relationship between diffusion and multi-echo T_2 measurements, particularly regarding their corresponding temporal patterns. While similarities have been reported regarding the time course of these measures [12], differences have been found in their respective return to baseline, with T_2 demonstrating a faster rate of return than diffusion [10, 11], indicating these measures represent different recovery processes. These findings appear to differ from those of the present study, as mean S_0 (single-echo) of EDL was still considerably elevated from baseline at the final timepoint (7min 32s), by which time the mean MD had decreased to baseline proximity. Furthermore, the present study observed increases in the MD and RD of ATIB and PER which were not reflected in S_0, indicating that assessment of S_0 may provide complementary information to the standard outputs of DTI in studies of post-exercise skeletal muscle.

In fairness, we raise the possibility that these inter-muscular diffusion differences could be due to factors aside from those related to fiber physiology. One alternate explanation could be that individual muscles experienced different levels of workload during the exercise, with the notable increase of EDL MD indicating that this muscle performed greater work than other muscles during the exercise task. In fact, a major criticism of previous pilot work [25] was that the minimal increase observed for post-exercise soleus could be accounted for by its lack of involvement in the supine plantar flexion exercise task [21]. However, with regards to the present experiment, there is literature to support that ATIB, EDL, and PER are all involved in the dorsiflexion-eversion exercise [21]. Attributing our present results solely to workload would then beg questions as to the workload threshold needed to induce EDL S_0 increase relative to ATIB and PER within the mild exercise task, given that MD increases imply that all three muscles were involved. We feel that differing physiology of the underlying muscle composition is a better explanation of our results, although the workload upon individual muscles may contribute to their diffusion and S_0 results.

There are several potential limitations to our study. First, muscle fiber content for each subject, and for each muscle, were not histologically assessed due the invasiveness and impracticality of performing biopsies on so many lower leg muscles. Thus, fiber composition was instead based on published values from previous studies. Other researchers have acknowledged heterogeneity in fiber composition within muscles between human subjects [23, 37, 38], and potentially affected by training regimen [46]. It would be beneficial for future studies relating post-exercise diffusion behaviour to tissue content to acquire subject-specific measurements of fiber composition, either by biopsy, or perhaps with by non-invasive approaches such as T_1 mapping [38].

The second limitation was lack of subject monitoring. Although instructions were given to volunteers, their behaviour was not strictly controlled, either prior to scan acquisition or during the exercise task. Subjects were asked not to drink caffeinated beverages, eat, or exercise before the experiment, but no detailed assessment of pre-experiment activity or diet was obtained. Also, although subjects had learned the exercise task prior to MRI acquisition, and the imaged leg was firmly secured, during the actual exercise period subjects were self-paced. There was no regulation or quantification of exertion with which to assess subject compliance with the task.

The third limitation was that we did not utilize corroborative MRI sequences or other forms of external validation aside from scientific literature to substantiate the presented hypothesis of post-exercise muscle diffusion change according to fiber composition and physiology. Corroborative MRI sequences were not performed because they would have needed to be performed in series. Ideally, we would have added multiple b-value diffusion measurements, magnetization transfer (MT) and CPMG measures of T_2 to fully understand the behaviour of water within multiple tissue pools. However, this would have been impractical due to the poorer temporal resolution and added scan length necessitated by each. It has been shown that the effects of prior exercise can have a lasting effect on T_2-mapping measurements and diffusion values [11], and thus the addition of further sequences to a scanning session would introduce complications due to order effect. Performing corroborative MRI scans on an alternate day is possible, but factors such as water and food intake or muscle usage are difficult to control. Thus, future studies would benefit from using MRI-compatible modalities concurrent with exercise and MRI acquisition, such as electromyography (EMG) to assess level of muscle activation [43, 44], fiber-optic temperature readings, near infrared spectroscopy (NIRS), or perhaps Doppler ultrasound to provide temporally-matched information of blood flow. While the interaction of some of these devices with MRI acquisition is still under investigation, any additional data could perhaps enhance the interpretation of temporal diffusion results from this current study.

Finally, we acknowledge that our study used a small and somewhat homogeneous subject pool. Future studies would benefit from greater numbers of subjects, and perhaps inclusion of groups with different sex, training, or clinical status, to get a better sense of how these results apply to the population, and to perhaps provide more statistical power between muscles per timepoint.

Conclusion

In conclusion, mild exercise was shown to elicit differing temporal patterns in DTI between inactive and active muscles, as well as within the active muscle group. The differences in post-exercise temporal diffusion patterns between active muscles can potentially be explained by their relative fiber composition and associated physiology. Therefore, consecutive DTI acquisition immediately following exercise cessation shows promise in the characterization of dynamic processes within muscles of the lower leg.

Acknowledgements

Funding provided to CR through a Natural Sciences and Engineering Research Council (NSERC) of Canada CGS-D PhD scholarship. The research was funded through an NSERC Discovery grant to MDN.

6.3.6 REFERENCES

[1] Cleveland GG, Chang DC, Hazlewood CF, Rorschach HE. Nuclear Magnetic Resonance measurement of skeletal muscle. Biophys J 1976; 16:1043-1053.

[2] Van Donkelaar CC, Kretzers LJG, Bovendeerd PHM et al. Diffusion tensor imaging in biomechanical studies of skeletal muscle function. J Anat 1999; 194:79-88.

[3] Kermarrec E, Budzik JF, Khalil C, Le Thuc V, Hancart-Destee C, Cotton A. In vivo diffusion tensor imaging and tractography of human thigh muscles in healthy subjects. Am J Roentgenol 2010; 195:W352-W356.

[4] Galban CJ, Maderwald S, Uffman K, de Greiff A, Ladd ME. Diffusive sensitivity to muscle architecture: a magnetic resonance diffusion tensor imaging study of the human calf. Eur J Appl Physiol 2004; 93:253-262.

[5] Sinha S, Sinha U, Edgerton VR. In vivo diffusion tensor imaging of the human calf muscle. J Magn Reson Imaging 2006; 24:182-190.

[6] Deux JF, Malzy P, Paragios N. et al. Assessment of calf muscle contraction by diffusion tensor imaging. Eur Radiol 2008; 18:23032310.

[7] Hatakenaka M, Yabuuchi H, Sunami S. et al. Joint position affects muscle proton diffusion: evaluation with a 3-T MR system. Am J Roent 2010; 194:W208-W211.

[8] Okamoto Y, Mori S, Kujiraoka Y, Katsuhiro N, Hirano Y, Minami M. Diffusion property differences of the lower leg musculature between athletes and non-athletes using 1.5T MRI. Magn Reson Mater Phys (MAGMA) 2012; 25:277-284.

[9] Nakai R, Azuma T, Sudo M, Urayama S, Takizawa O, Tsutsumi S. MRI analysis of structural changes in skeletal muscles and surrounding tissues following long-term walking exercise with training equipment. J Appl Physiol 2008; 105:958-963.

[10] Morvan D, Leroy-Willig A. Simultaneous measurements of diffusion and transverse relaxation in exercising skeletal muscle. Magn Reson Imaging 1995; 13:943-948.

[11] Nygren AT, Kaijser L. Water exchange induced by unilateral exercise in active and in active skeletal muscles. J Appl Physiol 2002; 93:1716-1722.

[12] Ababneh ZQ, Ababneh R, Maier SE, et al. On the correlation between T2 and tissue diffusion coefficients in exercised muscle: quantitative measurements at 3T within the tibialis anterior. Magn Reson Mater Phy 2008; 21:273-278.

[13] Morvan D. In Vivo Measurement of diffusion and pseudo-diffusion in skeletal muscle at rest and after exercise. Magn Reson Imaging 1995; 13:193-199.

[14] Sigmund EE, Novikov DS, Sui D, et al. Time-dependent diffusion in skeletal muscle with the random permeable barrier model (RPBM): application to normal controls and chronic exertional compartment syndrome patients. NMR Biomed 2014; 27:519-528.

[15] Okamoto Y, Kunimatsu A, Miki S, Shindo M, Niitsu M, Minami M. Fraction anisotropy values of calf muscles in normative state after exercise: Preliminary results. Magn Reson Med Sci 2008; 7:157-162.

[16] Cermak NM, Noseworthy MD, Bourgeois JM, Tarnopolsky MA, Gibala MJ. Diffusion tensor MRI to assess skeletal muscle disruption following eccentric exercise. Muscle Nerve 2012; 46:42-50.

[17] Yangisawa 0, Kurihara T, Koayashi N, Fukubayashi T. Strenuous resistance exercise effects on magnetic resonance diffusion parameters and muscle-tendon function in human skeletal muscle. J Magn Reson Imaging 2011; 34:887-894.

[18] Froeling M, Oudeman J, Strijkers GJ, et al. Muscle changes detected with diffusion-tensor imaging after long distance running. Radiology 2015; 274:548-562.

[19] Baete SH, Cho GY, Sigmund EE. Dynamic diffusion-tensor measurements in muscle tissue using the single-line multiple-echo diffusion-tensor acquisition technique at 3T. NMR Biomed 2015; 28:667-678.

[20] Polgar J, Johnson MA, Weightman D, Appleton D. Data on fibre size in thirty six human muscles: An autopsy study. J Neurol Sci 1973; 19:307-318.

[21] Basmajian JV, De Luca CJ. Muscles Alive: Their Functions Revealed by Electromyography Hardcover, 5th Revised edition. New York: Williams & Wilkins; 1985. 561p.

[22] Andersen P, Kroese AJ. Capillary supply in soleus and gastrocnemius muscles of man. Pflugers Arch 1978; 375:245-249.

[23]Johnson MA, Polgar J, Weightman D, Appleton D. Data on the distribution of fibre types in thirty-six human muscles: An autopsy study. J Neurol Sci 1973; 18:111-129.

[24]Snell RS. Clinical Anatomy by Regions. 9th ed. Philadelphia: Lippincott Williams & Wilkens, 2012.

[25]Rockel C, Davis A, Wells G, Noseworthy MD. Monitoring exercise-induced muscle changes using diffusion tensor imaging. Proc Intl Soc Magn Reson Med 20, 2012, (abstract 1425).

[26]Elzibak AH, Noseworthy MD. Assessment of diffusion tensor imaging indices in calf muscles following postural change from standing to supine position. Magn Reson Mater Phy (MAGMA) 2014; 27:387-395.

[27]Jenkinson M, Beckmann CF, Behrens TE, Woolrich MW, Smith SM. FSL. NeuroImage 2012; 62:782-790.

[28]Damon BM, Gregory CD, Hall KL, Stark HJ, Gulani V, Dawson MJ. Intracellular acidification and volume increases explain R2 decreases in exercising muscle. Magn Reson Med 2002; 47:14-23.

[29]Rockel C, Noseworthy MD. An exploration of diffusion tensor eigenvector variability within human calf muscles. J Magn Reson Imaging 2016; 43:190-202.

[30]Dietrich O, Raya JG, Reeder SB, Reiser MF, Schoenberg SO. Measurement of signal-to-noise ratios in MR images: Influence of multichannel coils, parallel imaging, and reconstruction filters. J Magn Reson Imaging 2007; 26:375-85.

[31]Rockel C, Noseworthy MD. Modification of signal-to-noise calculation for use in spatial mapping. Magn Reson Mater Phy (MAGMA) 2015; 29 (Suppl 1:abstract 646).

[32]Lundvall J, Mellander S, Westling H, and White T. Fluid transfers between blood and tissues during exercise. Acta Physiol Scand 1972; 85:258269.

[33]Saab G, Thompson RT, Marsh GD. Effects of exercise on muscle transverse relaxation determined by MR imaging and in vivo relaxometry. J Appl Physiol 2000; 88:226-233.

[34]Okamoto Y, Kunimatsu A, Kono T, Nasu K, Sonobe J, Minami M. Changes in MR

diffusion properties during active muscle contraction in the calf. Magn Reson Med Sci 2010; 9:1-8.

[35]Scheel M, von Roth P, Winkler T, et al. Fiber type characterization in skeletal muscle by diffusion tensor imaging. NMR Biomed 2013; 26:1220-1224.

[36]Fitts RH, Widrick JJ. Muscle mechanics: adaptations with exercise-training. Exerc Sport Sci Rev 1995; 24:427-474.

[37]Edgarton VR, Smith JL, Simpson DR. Muscle fibre type populations of human leg muscles. Histochem J 1975; 7:259-66.

[38]Houmard JA, Smith R, Jenrasiak GL. Relationship between MRI relaxation time and muscle fiber composition. J Appl Physiol 1995; 78:807-809.

[39]Le Bihan D, Breton E, Lallemand D, Aubin ML, Vignaud J, Laval-Jeantet M. Separation of diffusion and perfusion in intravoxel incoherent motion MR imaging. Radiology 1988; 168:497-505.

[40]Noseworthy MD, Kim JK, Stainsby JA, Stanisz GJ, Wright GA. Tracking oxygen effects on MR signal in blood and skeletal muscle during hyperoxia exposure. J Magn Reson Imaging. 9:814-820.

[41]Fleckenstein JL, Canby RC, Parkey RW, Peshock RM. Acute effects of exercise on MR imaging of skeletal muscle in normal volunteers. Am J Radiol 1988; 151:231-237.

[42]Fisher MJ, Meyer RA, Adams GR, Foley JM, Potchen EJ. Direct relationship between proton T2 and exercise intensity in skeletal muscle MR images. Invest Radiol 1990; 25:480-485.

[43]Adams GR, Duvoisin MR, Dudlet GA. Magnetic resonance imaging and electromyography as indexes of muscle function. J Appl Physiol 1992; 73:1578-1583.

[44]Price TB, Kamen G, Damon BM, et al. Comparison of MRI with EMG to study muscle activity associated with dynamic plantar flexion. Magn Reson Imaging 2003; 21:853-861.

[45]Prior BM, Ploutz-Snyder L, Cooper TG, Meyer RA. Fiber type and metabolic dependence of T2 increases in stimulated rat muscles. J Appl Physiol 2001; 90:615-623.

[46]Tesch PA, Karlsson J. Muscle fiber types and size in trained and untrained muscles of elite athletes. J Appl Physiol 1985; 59:1716-1720.

Chapter 7

A Sliding-Window Diffusion Tensor Technique for Temporal Study of Post-Exercise Skeletal Muscle Dynamics

Conrad P. Rockel, B.A., Michael D. Noseworthy Ph.D., P.Eng.

7.1 Context

After performing several experiments using DTI to investigate skeletal muscle, some of which are included in this dissertation, it appeared that the measure of mean diffusivity (MD) was being preferentially used to assess post-exercise effects, rather than the other outputs of which DTI is capable. Given this, it was tempting to simply use an approach based on clinical Diffusion Weighted Imaging (DWI), which combines diffusion information from three orthogonal gradient directions to produce the measure of Apparent Diffusion Coefficient (ADC). While this would allow the temporal resolution to be further increased, it would mean sacrificing the potential to use the additional structural detail provided by DTI.

After further consideration, along with a small dose of inspiration, a concept was devised whereby repeated sets of 3 orthogonal directions could be acquired to allow for ADC calculation, but by orienting each of these sets, the diffusion information could be combined into larger groupings to allow for DTI calculation. Furthermore, by limiting the number of 3-direction positions, a ”sliding window” analysis could be performed to allow for ongoing DTI measurements. In theory, this would allow for higher temporal resolution without the sacrifice of spatial information, and provide further insight into both the timing and structural changes involved in skeletal muscle dynamics following exercise.

The following chapter and related appendix describe the development of this conceptual diffusion acquisition scheme, the efficacy of combining the 3-orthogonal-direction sets into larger groupings for DTI calculation, as well as the feasibility of this technique in monitoring *in vivo* skeletal muscle post-exercise. In that regard, a plantarflexion exercise task was used at four different intensities to investigate the utility of this technique in assessment of individual muscle recovery.

7.2 Declaration

Conrad P. Rockel conceptualized the technique outlined in the present study, performed all methodological development, experimentation, and data analysis, wrote the initial manuscript, created figures and performed subsequent editing. Michael

D. Noseworthy provided funding, oversaw the evolution of study methodology, and provided feedback and editing with regards to the manuscript.

The authors also wish to thank Dr. Maxime Descoteaux (University of Sherbrooke) and Dr. Emmanuel Caruyer (Universite de Rennes) for their feedback regarding the study methods in this paper.

The manuscript in its current form will be submitted as a paper at a later date. The data and conclusions contained in this chapter were presented at the *24th Annual Meeting of the International Society of Magnetic Resonance in Medicine (ISMRM)*, Presentation #14 in Singapore, Malaysia on May 9th, 2016.

7.3 Paper

A Sliding-Window Diffusion Tensor Technique for Temporal Study of Post-Exercise Skeletal Muscle Dynamics

Conrad Rockel[1,2] and *Michael D. Noseworthy[1,2,3,4,5]

[1] *McMaster School of Biomedical Engineering, McMaster University, Hamilton, Ontario, Canada.*

[2] *Imaging Research Centre, St. Josephs Healthcare, Hamilton, Ontario, Canada.*

[3] *Department of Radiology, McMaster University, Hamilton, Ontario, Canada.*

[4] *Department of Electrical and Computer Engineering, McMaster University, Hamilton, Ontario, Canada.*

[5] *Department of Medical Physics and Applied Radiation Sciences, McMaster University, Hamilton, Ontario, Canada.*

*Corresponding Author:
Dr. Michael D. Noseworthy, PhD, PEng.
Imaging Research Center, Fontbonne Bldg, F-126-4
St. Joseph's Healthcare,
50 Charlton Ave. East.
Hamilton, Ontario L8N 4A6, Canada.
VOICE: (905) 522-1155 x35218
EMAIL: nosewor@mcmaster.ca

7.3.1 ABSTRACT

Purpose: to develop and test a multiple timescale diffusion acquisition strategy allowing for higher temporal resolution while retaining the structural representation for functional assessment of skeletal muscle

Materials and Methods: The calfs of 4 healthy volunteers (3♂:29.9±3.7yrs,1♁:30.5yrs) were evaluated using temporal DTI method (b=0/450 s/mm^2, 15-dir, and custom gradient table. Volumes were grouped into 3-direction sets to produce measures of Apparent Diffusion Coefficient (ADC) and b=0 signal intensity (S$_0$), and 15-direction sets to produce DTI measures of Mean Diffusivity (MD), Fractional Anisotropy (FA), principal eigenvalue (λ_1), and Radial Diffusivity (RD; mean of λ_2,λ_3) using a 'sliding window' approach. Diffusion volumes were acquired before and immediately following in-bore exercise (plantarflexion @0.5 Hz for 20sec or 2min) using an MRI-compatible ergometer. Baselines consisted of 40 volumes (10 timepoints), while post-exercise consisted of 60-120 volumes (15-30 timepoints, ~4-8 min). Experiment duration (scanning, exercise, rest) was 90 min. Five plantarflexion exercises were performed, each separated by 5 or 10min rest, and varied by load (10% and 40% of subject max) and duration (10 or 60 flexes), with the 10% 10-flex condition performed twice. Regions-of-interest (ROIs) were drawn for anterior tibialis (ATIB), peroneus longus (PER), lateral soleus (SOLlat), lateral gastrocnemius (LG), and medial gastrocnemius (MG), each consisting of three 2x2-voxel squares across 5 axial slices and applied to all timepoints of each measure (ADC, S$_0$, MD, FA, λ_1, RD). Subject-wise post-exercise magnitude change was calculated for each timepoint per DTI measure by subtracting baseline mean from timepoint value. Comparisons were made between each of the four exercise conditions, as well as between the two 10% 10-flex conditions.

Results:

Four different post-exercise temporal patterns were observed in the ADC, S_0, and MD amongst the measured muscles: 'elevated-decline' (initial increase of measure followed by decrease towards baseline); 'latent peak' (initial values proximal to baseline, followed by a peak); 'sub-to-peak', (initial values below baseline, followed by a peak); and 'horizontal' (values proximal to baseline for all timepoints). The 10-flex 10% condition elicited 'elevated-decline' in muscles particularly SOLlat, a muscle not expected to be active in plantarflexion. Exercise of greater intensity produced 'latent peak' and 'sub-to-peak' patterns, with peak height associated with greater workload, particularly in PER. The 'sub-to-peak' pattern was only observed for the 10-flex 40%, and only within LG and MG. The 60-flex 40% condition induced a large 'latent peak' in MG. Repeat analysis of the 10-flex 10% condition demonstrated that SOLlat activation is repeatable, with Time 2 of this analysis producing a slight increase in S_0 temporal measures.

Conclusions: A novel sliding window DTI approach shows promise in measuring post-exercise dynamics within individual skeletal muscle dynamics. The approach appears robust although more validation is required.

.

7.3.2 INTRODUCTION

Diffusion imaging is a magnetic resonance imaging (MRI) technique increasingly employed in the study of skeletal muscle, due its ability to probe tissue anisotropy. On modern clinical MRI scanners, diffusion can be assessed using Diffusion Weighted Imaging (DWI), a technique that encodes diffusion as images from three orthogonal directions, and subsequently combines these volumes to produce an estimate of overall diffusion, known as the Apparent Diffusion Coefficient (ADC). Diffusion can also be assessed using Diffusion Tensor Imaging (DTI), which incorporates at least 6 non-collinear diffusion directions, and has been found to produce better spatial assessments of anisotropic tissue structure than single or 3-direction ADC estimates [1]. However, greater numbers of gradient directions and/or signal acquisitions are needed for reasonable spatial representation [2-4].

Diffusivity is known to increase in skeletal muscle following exercise [5], and more recently, DTI measures of mean diffusivity (MD) have been shown to increase in post-exercise skeletal muscles [6-8]. However, the DTI studies often acquire a single volume ”snapshot” to represent diffusion immediately following exercise, and also have used an exercise protocol consisting of high intensity tasks known to be damaging to skeletal muscle (e.g. exercise to exhaustion, downhill or marathon running), allowing for exercise-based changes in DTI measurements to be observed via the ”snapshot” approach over the course of days or weeks.

An alternate approach to the assessment of post-exercise muscle diffusion is to create an acute timecourse of diffusion change. This is achieved by collecting a series of consecutive diffusion volumes within a single scan immediate to exercise, and then observing the measures of diffusion within specified locations for each volume ("timepoint"). Early studies that employed this technique to study sub-maximal exercise observed that diffusion is initially high in activated muscles following exercise, and subsequently decreases across time [9, 10]. These studies also collected concurrent T_2 information, and observed that the rate of return to baseline was different between these two measures, suggesting that diffusion and T_2 have different origins within the muscle [9, 10]. Although pioneering in their approach, these timecourse studies have become somewhat antiquated, as diffusion data was collected using either a single diffusion direction or outdated acquisition strategies (e.g. tetrahedral gradient strategies). Many advancements have been made in the field of MRI since these studies were performed, such as higher field strengths, faster acquisitions, better RF coils (e.g. phased array), not to mention the advent of techniques such as DTI.

Few studies have been performed which investigate acute post-exercise temporal skeletal muscle using DTI, although this field is emerging [11, 12]. When performing a timecourse analysis using DTI, as described in *Chapters 4* and *6* of this dissertation, it appears that increased temporal resolution has the potential to reveal more intricate information about post-exercise muscle temporal behaviour. However, temporal information comes at the expense of diminished representation of accurate structure. Thus, in order to assess muscle behaviour following a single episode of exercise using current diffusion MRI methods, one must opt for either temporal resolution or accurate structural representation, but not both, and thus a second episode of exercise must be performed either within the same scan session or on an alternate day. Unfortunately, there is no guarantee that both episodes of exercise would be identical, due the influence of previous exercise, or perhaps differing amounts of daily muscle usage, diet, water consumption, sleep, and overall wellness, not to mention experimental factors such as subject or coil positioning.

The **purpose** of the present study was to develop and test a novel diffusion acquisition/analysis strategy capable of producing diffusivity measures of dynamic tissue with high temporal resolution while also allowing for ongoing accurate structural representation. In essence, this strategy involves acquiring a series of 3-orthogonal-direction (”triplet”) sets, each preceded by a b=0 s/mm^2 image, in order to calculate an estimate of diffusion according to current DWI methods, thus providing diffusion measures that are more time-resolved than DTI. The triplet sets would be oriented in five different positions, allowing the resultant diffusion data to be combined into greater numbers of directions sufficient to calculate the diffusion tensor. Finally, a ’sliding window’ analysis would allow ongoing inclusion of the triplets, providing temporally progressive DTI measures of skeletal muscle following exercise.

7.3.3 MATERIALS and METHODS

Stage 1: Development of the Gradient Table

DTI, irrespective of MRI vendor, uses a ”gradient table” which is a N-by-3 table that defines the X-, Y-, and Z-encoding gradients used by the scanner to produce each of N diffusion vector directions. The default gradient table used by our local MRI scanner (GE 3T Discovery MR750, General Electric Healthcare, Milwaukee, WI) includes a single volume of b=0 s/mm^2 prior to N non-collinear vectors with greater diffusion weighting (e.g. b=450 s/mm^2), with N determined by the user. The individual vectors for each value of N from 6 to 75 diffusion directions are evenly distributed throughout a sphere, based on an electrostatic repulsion algorithm. Previous work has shown that N=15 provides reasonable spatial representation of the skeletal muscle diffusion tensor [3], and thus N=15 was used in the present study. However, the proposed N=15 gradient table would need to differ from the default table in three essential ways:

(1) Additional b=0 s/mm^2 volumes would need to be inserted into the gradient table every three vector directions in order to allow timepoint-based calculation of 3-dir ADC estimates, as well as provide a measure of S_0 (b=0 signal intensity) for that timepoint (**Fig. 7.1a**).

(2) Within each 3-dir set, the three vector directions would need to be orthogonal to provide the least directional bias possible with three vectors, thus conforming with clinical measures of ADC. The default N=15 gradient table uses vector directions based on electrostatically-dispersed charge distributions over a sphere, and thus none are orthogonal, especially within 3-dir sets. Furthermore, five distinct positions of 3-dir orthogonal vector sets would be needed to produce a 15-dir non-collinear vector set.

(3) The acquisition ordering of diffusion directions would need to be addressed, since default 15-dir vector sets are acquired with the intention of calculating a single DTI volume, rather than consideration of temporal acquisition of sub-units within the main 15-direction set. In order to generate diffusion measures from sub-units (i.e. 3- or potentially 6- or 9-directions), it was essential that the temporal distribution of

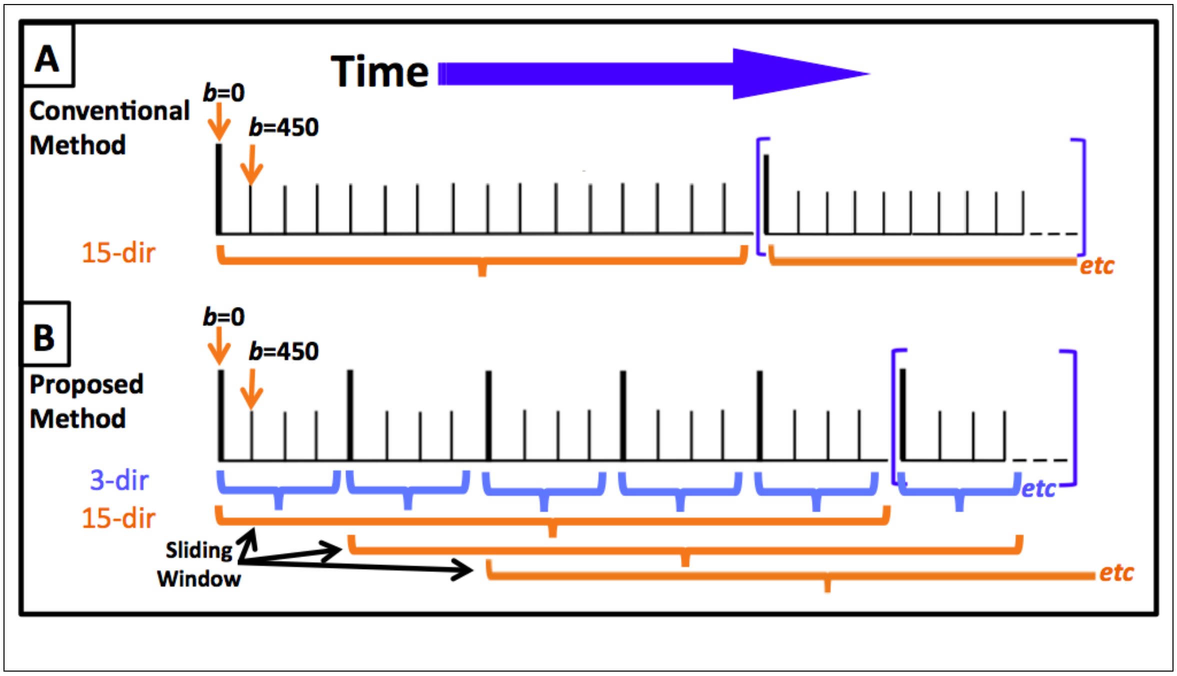

Figure 7.1: Comparison of DTI acquisition strategies. **(A)** Conventional method, consisting of an initial b=0 volume, followed by N=15 DW volumes, the directions of which are dispersed throughout a sphere. **(B)** Proposed sliding window method. An additional b=0 image is acquired prior to every 3-DW-image "triplet". The gradient-encoded diffusion directions within a triplet are orthogonal to one another, but the 5 triplets have different orientations within space. The grouping of the acquisition into 3- and 15-dir sub-units during post-processing is shown, as well as how the "sliding window" incorporates progressing groups of triplets for temporal measures of N=15 DTI.

all 3-dir sets be as equally distributed as possible to maintain equivalency between each consecutive timepoint. It was also important that the wrap-around sets of vector ordering be considered, such that 3-dir sets occurring at the end of the 15-dir gradient table have the same spatial relationships to those at the start of the gradient table as that found between consecutive sets found within the 15-dir table. As the proposed diffusion acquisition strategy was to involve a series of consecutive 15-dir datasets, this would allow better continuity in the timecourse generated by 3-dir sets, better equivalency between sub-units of <15 directions, and less potential temporal bias in progressing across time when using 15-direction groupings in a sliding-window manner (**Fig. 7.1b**).

Summary of Gradient Table Testing

*(NOTE: Details of these experiments can be found in **Appendix B**)*

Many potential gradient tables were generated by different strategies, and then assessed based on dispersion of the five triplets, similarity of between-triplet angles, and stability of DTI measure across time within phantom studies. Eventually, one candidate table (test name ”02_s7”) was found to perform better than the other test tables in meeting the three requirements listed above (**Fig. 7.2**).

Sub-divisions of 6- and 9-dir (of the N=15 table) were found to produce improbable values (e.g. FA>1.0) or less than satisfactory temporal stability. Therefore, the next stage of this preliminary experiment (*in vivo* with exercise) only included 3- and 15-dir sliding window analysis.

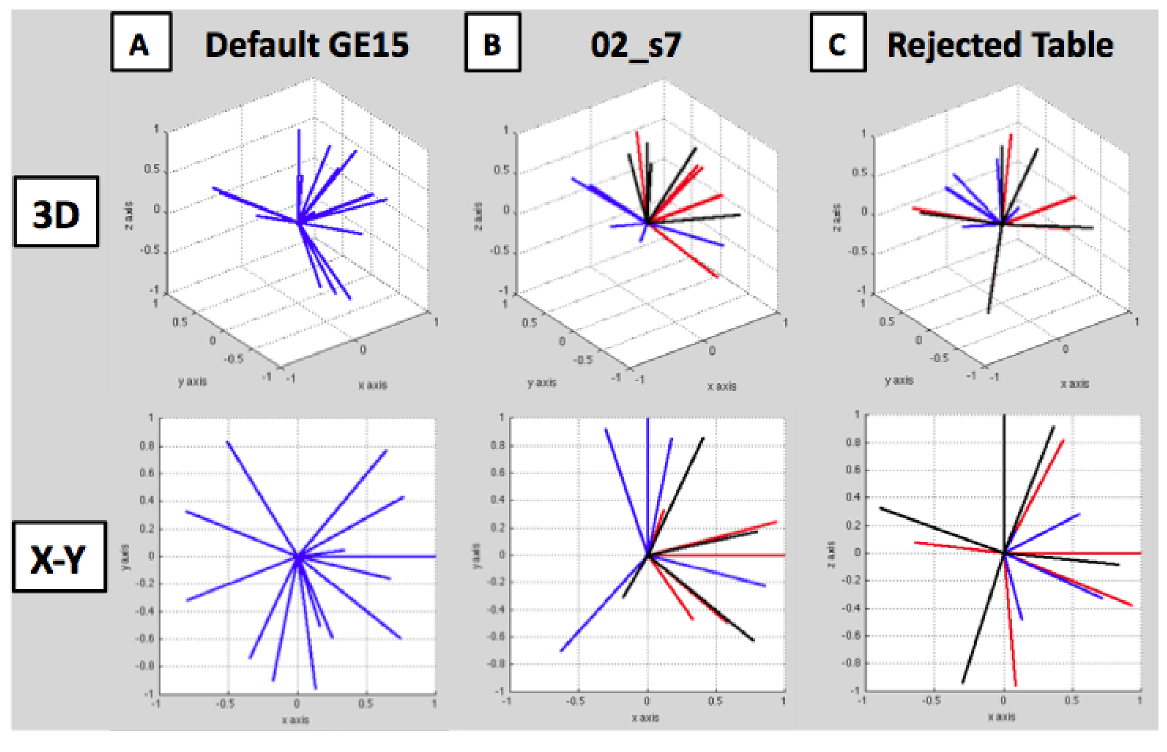

Figure 7.2: Dispersion of gradient table vectors from three-dimensional (3D) and X-Y perspectives. **(A)** Default N=15 table found on GE 3T 750 MRI. **(B)** Best candidate table for present multi-timescale analysis (test name "02_s7"). **(C)** Example of table rejected due to poor vector dispersion.

Stage 2: In vivo Testing of Sliding Window Strategy

Having settled upon a satisfactory gradient table ("02_s7"), the next stage of experimentation was to use the 'sliding window' strategy to acquire diffusion data from human volunteers following exercise performed inside the MRI scanner bore.

The **objectives** of the following experiment were to (i) assess the sensitivity of this diffusion acquisition technique in detecting post-exercise changes within individual muscles; (ii) assess the specificity of this technique by having subjects perform different levels of exercise intensity; (iii) compare the results between diffusion measurements based on different sub-unit length; and (iv) to compare the post-exercise measures of diffusion with signal changes of b=0 s/mm^2 (S_0) for individual muscles across conditions of exercise intensity.

METHODS:

Subjects: Three male volunteers (age 29.9±3.7 years; BMI 23.6±2.1 kg/m^2) participated in the main exercise intensity experiment, which involved a series of in-bore exercise tasks of increasing intensity within a single scanning session. A second experiment, investigating repeatability of the lightest exercise condition (described below), utilized the data from two of these subjects, plus an additional female (age 30.5 years; BMI 23.0 kg/m^2). Subjects were asked to refrain from exercise for at least 12 hours before the scan. The study was approved by our institutional ethics review board, and each subject gave informed consent prior to participating.

MRI Scanning: The field of view was centered in the sagittal plane around the widest axial cross section of the calf. DTI data was acquired using a dual echo spin echo EPI sequence (b=0 and 450 s/mm^2, TR/TE=4000/69.6ms, custom 15-dir gradient scheme ("02_s7"), 16 slices 4mm thick, 16cm FOV, 64x64 matrix, ASSET = 2).

Diffusion volumes were acquired prior to and immediately following each of five exercise sessions (**Fig. 7.3**). A single diffusion acquisition triplet set consists of one b=0 s/mm^2 volume, and 3 diffusion-weighted volumes (b=450 s/mm^2), each with an orthogonal gradient direction relative to the other two directions within the set (**Fig. 7.1b**). One triplet set produces a single timepoint representative of the preceding 16 seconds of time. Baseline DTI acquisitions consisted of 10 sets while post-exercise acquisitions consisted of 15 (lightest exercise condition) or 30 sets (remainder of exercise conditions; utilizing spinescan once to trigger acquisition of the latter 15 sets), accounting for ∼4 or 8 minutes of post-exercise diffusion. Post-exercise scanning commenced immediately following cessation of the exercise task. The experiment duration, including multiple sessions of scanning, exercise, and rest, was approximately 90 minutes.

Exercise Protocol: Exercise consisted of repeated plantar flexion using a custom MRI-compatible ergometer (**Fig. 7.3 (inset)**). Exercises were varied by the weight

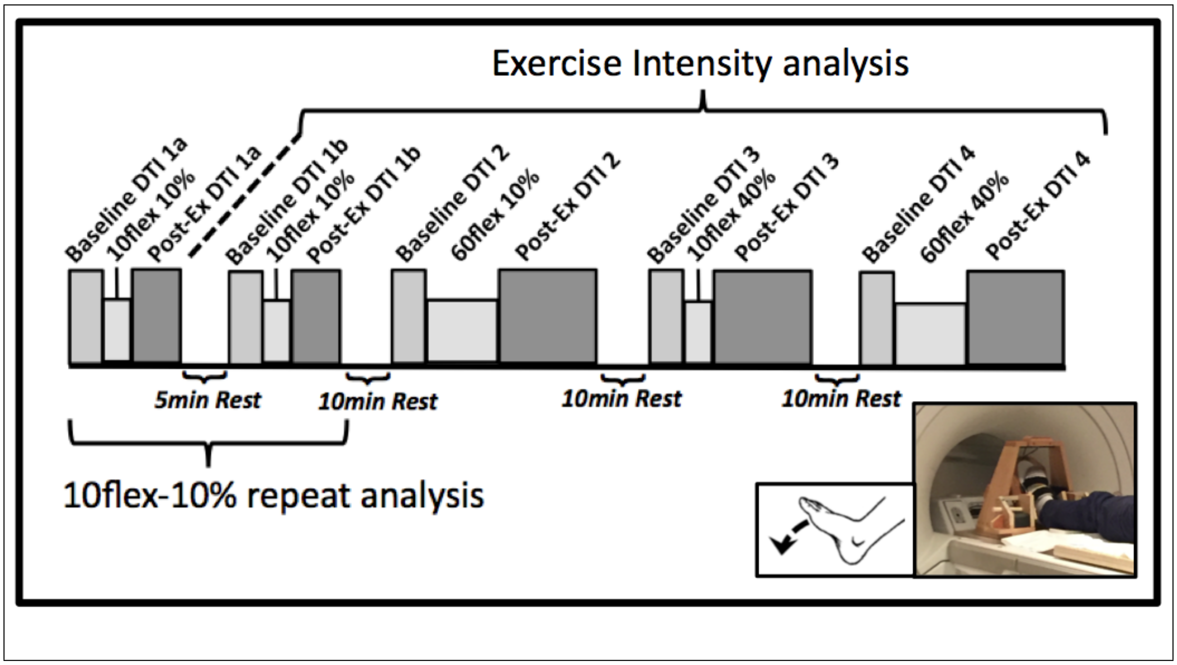

Figure 7.3: Experimental set up, depicting the ordering of MRI scanning, exercise, and rest periods. The clusters of scanning and exercise included in each of the two overall analyses (”Exercise Intensity” and ”10-flex 10% Repeat”) are indicated with horizontal parentheses. Inset shows a picture of foot positioning within the MRI-compatible ergometer (pictured out of bore) as well as a diagram of the plantarflexion motion used as an exercise model.

pressed by the foot pedal (based on a previously-measured maximum weight, single flex (MWSF) per individual volunteer), as well as the number of flexions at 0.5 Hz. The mean 10% MWSF was 4.0±0.8 kg, while the mean 40% MWSF was 14.3±2.6 kg. Each flex consisted of the weight moving vertically by 7 cm via a single pulley attached to the ergometer foot pedal.

Five sessions of exercise were performed, each separated by a rest gap of 5-10 minutes during which no scans were acquired (**Fig. 7.3**). The first two exercise sessions (1a and 1b) each consisted of 10 flexes at 10% MWSF (10flex10%), acquired in duplicate due to pilot studies showing unpredicted diffusion increases for this particular exercise condition. The intensity of exercise was then altered for each subsequent exercise set by manipulation the number of flexes and the weight pressed: (2) 60 flexes at 10% MWSF (60flex10%); (3) 10 flexes at 40% MWSF (10flex40%); and (4) 60 flexes at 40% MWSF (60flex40%). Note that 2 of the 3 male subjects participated in all 5 exercise conditions, while the third participated in only conditions 1a, 2, 3, and 4. An additional female subject participated in exercise session 1a and 1b that was not preceded by other exercise. It is therefore expected that the results of the main exercise intensity condition may differ slightly from the repeatability analysis of the 10flex10% condition.

It was expected that lateral gastrocnemius (LG), medial gastrocnemius (MG), and peroneus longus (PER) would be actively involved in the exercise, that soleus (SOLlat) would not be involved due to the supine nature of the exercise, and that anterior tibialis (ATIB) would only be passively elongated [13-15].

In this preliminary study, we acknowledge that an ordering effect may be present

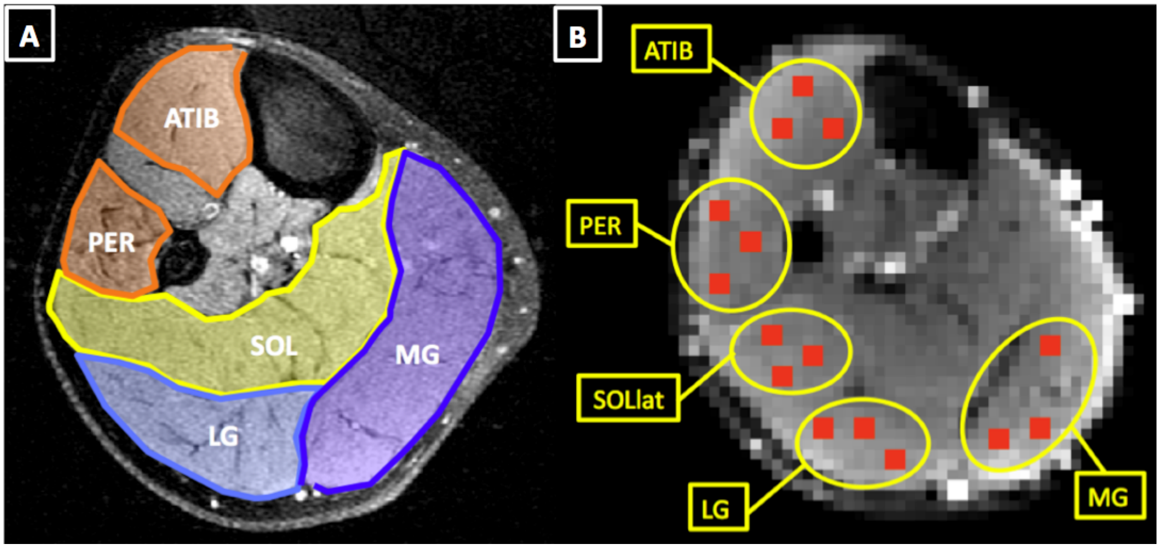

Figure 7.4: Cross section of the human calf, depicting anatomy under investigation. **(A)** Boundaries of investigated muscles as shown on a T_1-weighted MR image. ATIB: Anterior Tibialis, PER: Peroneus Longus, SOL: Soleus, SOLlat: lateral Soleus, LG: Lateral Gastrocnemius, MG: Medial Gastrocnemius. **(B)** Examples of ROIs used for measurement of each muscle, overlaid on a T_2-weighted b=0 image.

by our use of identical task ordering for each subject. It is possible that the diffusion results for an exercise task in this experiment are systematically influenced by the task preceding it. However, randomization of ordering would mean that the expected post-exercise effects of the most intense exercise condition (60flex40%) would confound subsequent diffusion measurements if placed anywhere but the end of the scanning session, especially given the small number of subjects. Therefore, task ordering was kept constant between subjects for this round of experimentation. In order to minimize the effects of previous exercise tasks within the scanning session, a rest period of 5 (post-10flex10%) to 10 minutes (remainder of tasks) was observed following each post-exercise DTI acquisition, itself a a period of ∼4-8-minutes. Hence, the total rest time between tasks was ∼10 minutes following the 10flex10% condition, and ∼20 minutes following the remainder of tasks.

Post-Processing: For each pre- and post-exercise acquisition, the individual DICOM output files were compiled into a single 4-dimensional (4D) volume. Each 4D volume was then registered to a common space, typically the first pre-exercise volume per individual subject, using FLIRT with sinc reconstruction [16, 17]. The 4D volumes were then broken into 3- and 15-direction subunits subsequent to each b=0 s/mm^2 image, allowing for a sliding-window of 4D volumes to representing ongoing diffusion across all timepoints (**Fig. 7.1b**). Intermittent b=0 s/mm^2 images within a 15-dir set were omitted when calculating diffusion for that particular 4D volume.

Apparent Diffusion Coefficients (ADCs) [18] were calculated for each 3-dir subunit using a custom script within Matlab (v7.9; Mathworks, Natick MA). The signal intensity (S_0) of each b=0 s/mm^2 image was measured to provide comparative information relating to changes in muscle T_2 as well as insight into calculation of the diffusion measures. The diffusion tensor was calculated for each 15-dir subunit using FSL [17, 19]. The diffusion tensor calculations produced maps of the three eigenvalues (λ_1-λ_3) representing the shape of the tensor ellipsoid, from which maps of mean diffusivity (MD), and radial diffusivity (RD, representing the mean of λ_2 and λ_3) were generated. Data from the 3- and 15-dir subunit time scales were temporally aligned according to the final diffusion-weighted image contributing to the 3- or 15-dir set, meaning that 15-dir measures did not commence until Timepoint 5 (**Fig. 7.5**).

Regions-of-Interest (ROIs): Muscle ROIs were drawn for anterior tibialis (ATIB),

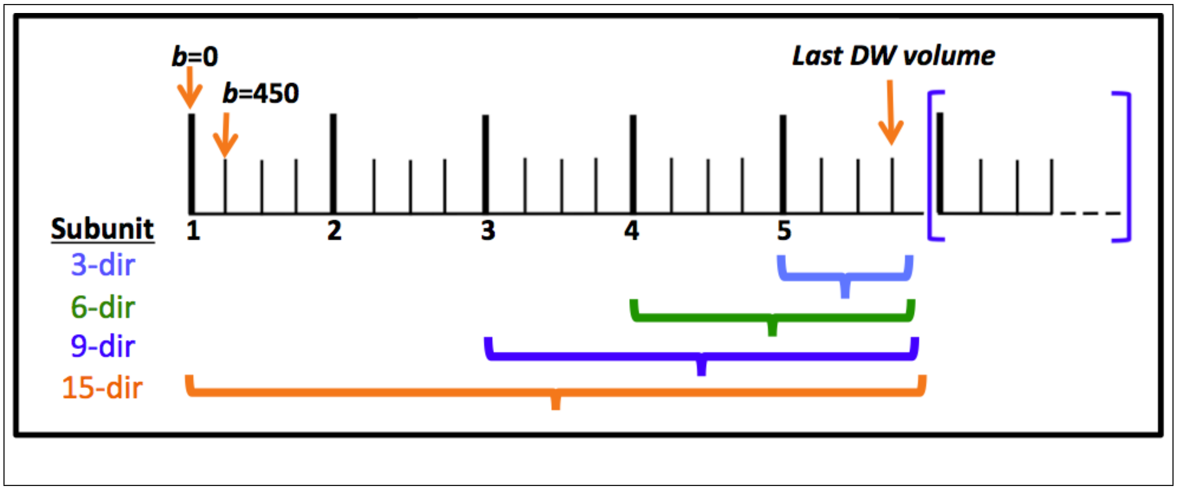

Figure 7.5: Example of inter-timescale alignment for comparison of diffusion measures. Depicted are the b=0 and 450 s/mm^2 volumes needed to produce Timepoint 5 at each of the tested time scales. Inter-timescale subunits were aligned according the last diffusion weighted (b=450 within the set.

peroneus longus (PER), lateral soleus (SOLlat), lateral gastrocnemius (LG), and medial gastrocnemius (MG) (**Fig. 7.4**). Each ROI consisted of three 2x2-voxel squares on each of 5 contiguous axial slices. ROIs were applied to each subunit to create a timecourse of diffusion for each measure (3-dir ADC, S_0, 15-dir MD, λ_1, RD).

ANALYSES

Baseline Assessments: The temporal diffusion measures (3-dir ADC, S_0, 15-dir MD, λ_1, RD) were acquired for each muscle per subject prior to each exercise session, and then averaged across timepoints (10 timepoints for 3-dir, 6 timepoints for 15-dir) to provide baseline values. The individual baseline measures were then averaged across subjects (n=3) to produce an overall mean baseline for each exercise. This was performed in order to assess possible changes in diffusion values due to multiple exercise periods within a single scanning session.

Post-Exercise Assessments: In order to assess the effect of exercise on diffusion measures, the magnitude change for each DTI output was obtained by subtracting the mean baseline measure from each post-exercise timepoint on a subject-wise basis per exercise condition and ROI. Post-exercise magnitude change data from each subject was subsequently combined into a mean of all subjects for each timepoint per exercise condition.

The main ”Exercise Intensity” analysis consisted of comparing the post-exercise temporal diffusion patterns following the four differing intensities of plantarflexion (**Fig. 7.3**). Note that the second 10flex10% condition (Post-Ex 1b) was used for this analysis if present. Post-exercise diffusion was assessed per individual muscle across each of the four exercise conditions. Although this experiment provided quantitative data, the described preliminary comparisons between muscles or diffusion measures (ADC, S_0, MD) muscles are largely qualitative descriptions due to low statistical power. Additionally, the relative temporal patterns of magnitude change in 15-dir λ_1 and RD were compared within each muscle per exercise in order to determine whether diffusion changes were preferentially occurring along or across the tensor ellipsoid.

A second analysis involved comparison of the two 10flex10% conditions acquired at the beginning of each scan (”10-flex 10% Repeat”; **Fig. 7.3**). This was undertaken to assess the repeatability of post-exercise muscle diffusion changes found to occur for this particular exercise condition, based on pilot tests of this experiment. Essentially, the pilot data demonstrated large increases of S_0 within SOLlat, a muscle not expected to be involved in this exercise, and thus this experiment was performed to determine whether the pilot results were related to the particular exercise task, or perhaps due to the task being performed first after the pre-exercise 30-minute rest period. For the sake of expediency, only ADC and S_0 of PER, SOLlat, and LG were assessed for this second analysis.

7.3.4 RESULTS

Baseline Assessments

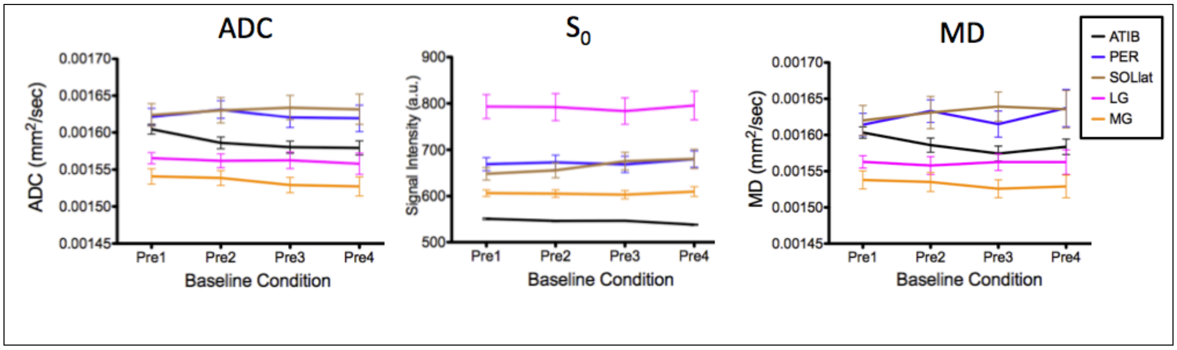

Figure 7.6: Baseline data for individual measured muscles obtained prior to each of the tasks in the "Exercise Intensity" analysis. 'Pre1' is prior to 10flex10%, 'Pre2' prior to 60flex10%, 'Pre3' prior to 10flex40%, and 'Pre4' prior to 60Flex40%. 'ATIB': Anterior Tibialis, 'PER': Peroneus Longus, 'SOLlat': lateral Soleus, 'LG': Lateral Gastrocnemius, 'MG': Lateral Gastrocnemius.

In examination of the baseline measures acquired prior to each exercise condition, it appears that 3-dir ADC and 15-dir MD are roughly equivalent for LG and MG (**Fig. 7.6**) across exercise sessions. The ADC and MD of ATIB appears to slightly decrease with additional exercise sessions. Furthermore, SOLlat appears to slightly increase with additional exercise sets, and PER appears to slightly increase after 10-flex conditions and decrease after 60-flex conditions. However, the range of values (standard error of the mean (SEM)) for each muscle across conditions indicate that ADC and MD measures are not substantially different prior to each exercise across conditions. Additionally, measures of S_0 appear to be equivalent prior to each exercise condition for all assessed muscles.

Post-Exercise: Patterns

With one exception (MG at 60flex 40% MWSF), the mean temporal measures return to baseline during the post-exercise scanning period (∼8 minutes). Several notable patterns of change from baseline are evident in the timecourse of post-exercise diffusion measures (**Fig. 7.7**). In order to better describe the following results, these patterns will be used as nomenclature and thus are described below:

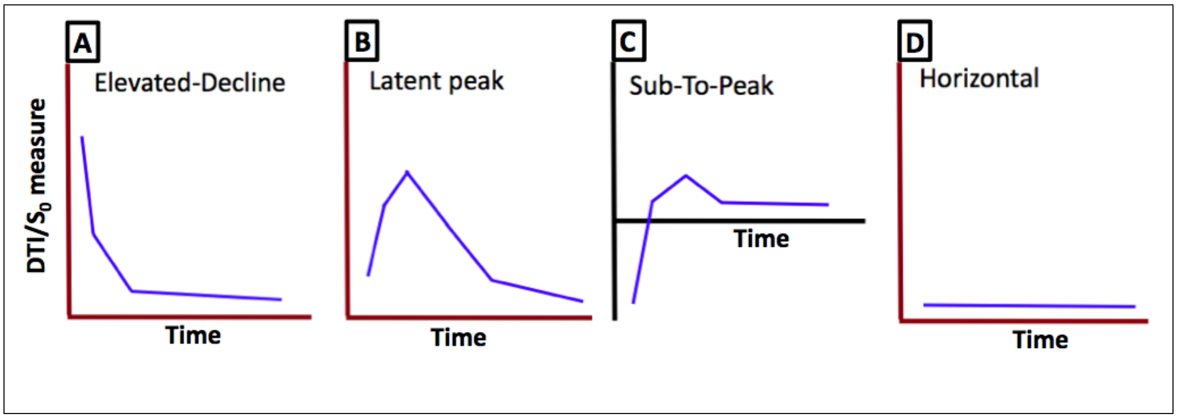

Figure 7.7: Depictions of four general patterns observed in the post-exercise data. See text for full description.

- 'Elevated-Decline' (***Fig. 7.7a***): This pattern displays increased diffusion measures immediately following exercise cessation. The magnitude change values then return to baseline across timepoints, although the slope of this decline varies between muscles and exercise conditions.
- 'Latent Peak' (***Fig. 7.7b***): Diffusion values are proximal or slightly elevated from baseline following exercise cessation, and then display increasing change from baseline measures across subsequent timepoints, before peaking and declining.
- 'Sub-to-Peak' (***Fig. 7.7c***): This pattern displays diffusion values that are distinctly below baseline values immediately following exercise cessation. Then, as with

the Latent Peak pattern, the diffusion values increase to a peak before returning to baseline.

- 'Horizontal' (***Fig. 7.7d***): This pattern displays a horizontal trajectory across time-points and little change from baseline values, although slight fluctuations may occur.

Post-Exercise: EXERCISE INTENSITY Analysis

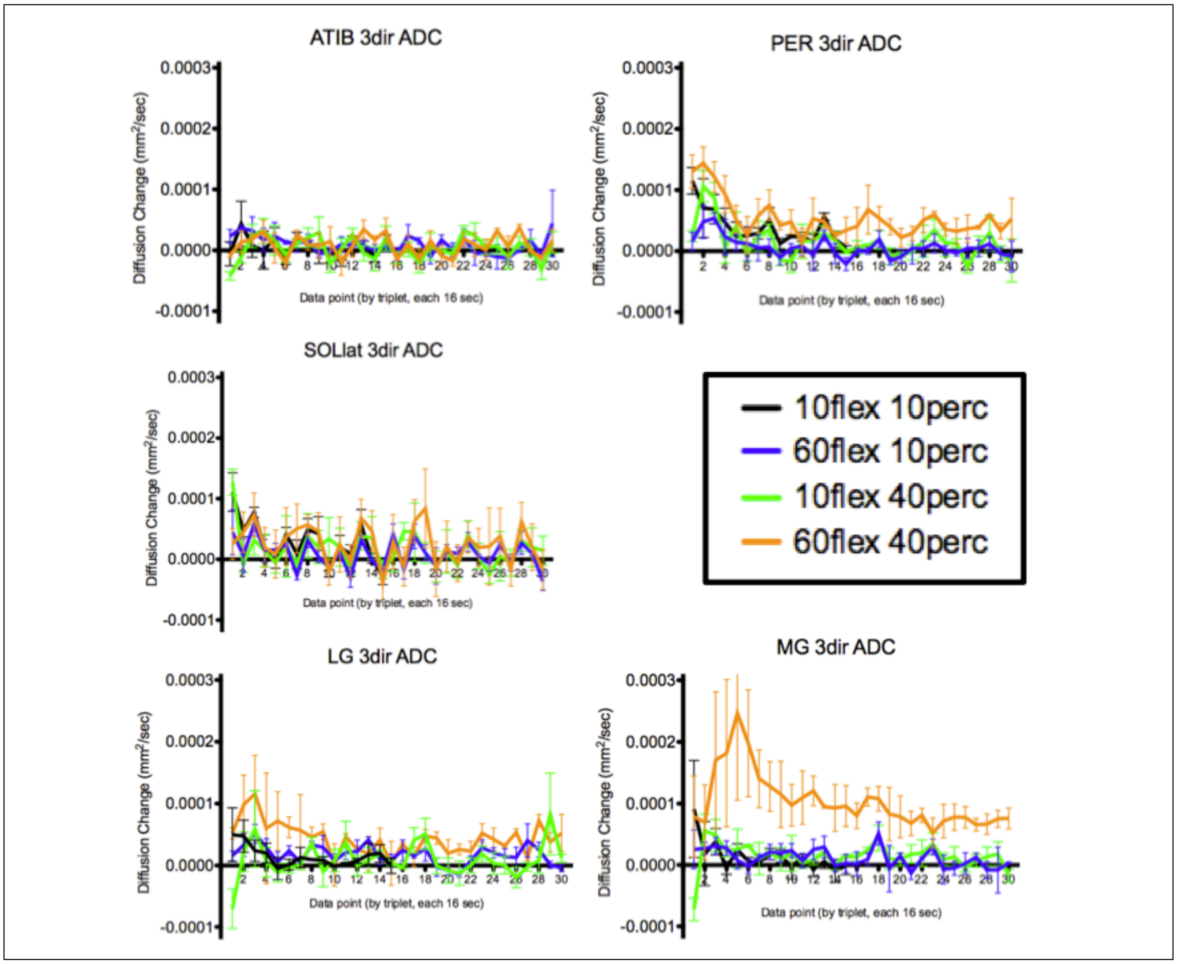

Figure 7.8: Post-Exercise temporal measures of 3-dir ADC for individual muscles according to exercise task. 'ATIB': Anterior Tibialis, 'PER': Peroneus Longus, 'SOL-lat': Lateral Soleus, 'LG': Lateral Gastrocnemius, 'MG': Lateral Gastrocnemius.

3-direction ADC (**Fig. 7.8**) The ATIB appeared to show little departure ('horizontal' pattern) from baseline following any of the four exercise conditions.

The PER shows an 'elevated-decline' pattern following the 10flex10% condition, but produces 'latent peak' patterns for the 60flex10%, 10flex40%, and 60flex40% conditions, with greater peak magnitudes, representing change from baseline, associated with increasing exercise intensity. It is possible that 60flex40% PER results could be also suggestive of an elevated-decline pattern. Furthermore, the PER 60flex10% peaks at timepoint 2, while both the 10flex40% and 60flex40% conditions peak at timepoint 1.

The SOLlat displays an 'elevated-decline' pattern for both 10-flex conditions, while a 'horizontal' pattern is observed for the 60-flex conditions, however the results are somewhat noisy for this muscle.

For LG, both of the 10% MWSF conditions (i.e. 10flex10% and 60flex10%) produce a horizontal pattern that is proximal to baseline, however the exercises using 40% MWSF (i.e. 10flex40% and 60flex40%) invoke distinct post-exercise change from baseline, although in unique ways. The 10flex40% condition produces a 'sub-to-peak' pattern that is consistent across subjects, while the 60flex40% condition produces a 'latent peak' pattern with values remaining elevated from baseline until approximately timepoint 10. Both the LG 10flex40% and 60flex40% conditions achieve their peak departure from baseline at timepoint 3.

Within MG, the 10flex10% condition appears to show a slight 'elevated-decline' pattern, while the 60flex10% condition shows a 'horizontal' pattern that is proximal to baseline. However, like LG, the 40% MWSF conditions invoke notable but distinct responses. The 10flex10% condition displays a 'sub-to-peak' pattern that peaks at timepoint 2, while the 60flex10% condition elicits a substantial 'latent peak' pattern that does not peak until timepoint 5, and maintains a sustained elevation from baseline across the remaining timepoints.

Signal Intensity of b=0 s/mm^2 (S$_0$) (Fig. 7.9)

The temporal results of ATIB S$_0$ indicate a slight 'elevated-decline' pattern following all exercise conditions, with the 10flex40% condition invoking the greatest magnitude of change.

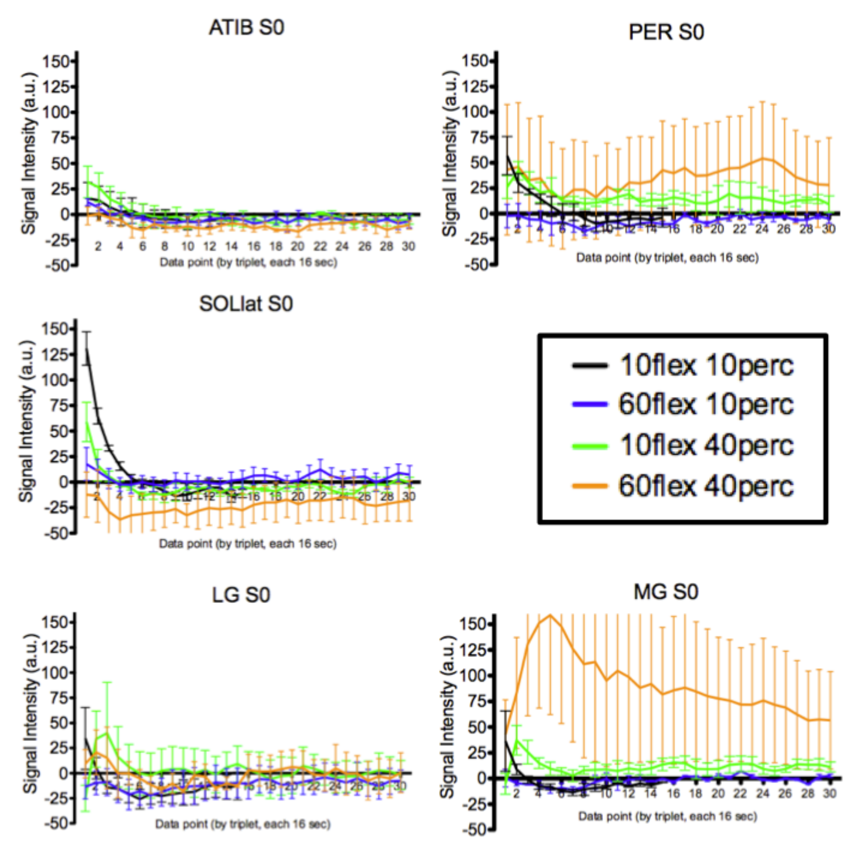

Figure 7.9: Post-Exercise temporal measures of b=0 s/mm^2 signal intensity (S$_0$) for individual muscles according to exercise task. 'ATIB': Anterior Tibialis, 'PER': Peroneus Longus, 'SOLlat': lateral Soleus, 'LG': Lateral Gastrocnemius, 'MG': Lateral Gastrocnemius.

In PER, the 10flex10% condition elicits an 'elevated-decline' pattern, while the 60flex10% results in a 'horizontal' pattern that is proximal to baseline. Both PER 40% MWSF conditions show indications of a 'latent peak' pattern, though some initial elevation is observed. Both 40% MWSF conditions have similar magnitude that peak at timepoint 2, although the 60flex40% condition elicits a second gradual increase that peaks at timepoint 24 but demonstrates an unusually wide range of error (upon investigation, driven by one subject).

Within SOLlat, both of the 10-flex conditions induce distinct 'elevated-decline' patterns, with a greater magnitude observed for 10flex10%. The 60flex10% condition shows a slight 'elevated-decline' pattern, while the 60flex40% condition appears to drop below baseline and remaining decreased for the remainder of timepoints, although the wide range of error makes interpretation difficult.

For LG, the 10flex10% produces a slight 'elevated-decline' pattern, while the 60flex10% produces a 'horizontal' pattern that demonstrates a decrease from baseline between timepoints 4 and 8. The 40% conditions are suggestive of a 'latent peak' pattern, with the 10flex40% showing a larger magnitude peak than the 60flex40% condition, although the wide error range of the first 6 timepoints makes interpretation difficult.

With regards to the MG, the 10flex10% condition produces an 'elevated-decline' pattern, while the 60flex10% condition produces a 'horizontal' pattern that remains proximal to baseline across all timepoints. Both of the 40% MWSF conditions induce 'latent peak' patterns in post-exercise MG S_0, although the number of flexes produce quite different results. The 10flex40% condition has a peak of moderate height at timepoint 2, while the 60flex40% condition invokes a considerable increase of S_0 that does not reach a peak until timepoint 5, a result that remains relevant despite the extremely wide range of error. The differing timelines of S_0 change between muscles and exercise conditions, as well as the restriction of these changes to muscle boundaries, can be seen in **Figure 7.10**.

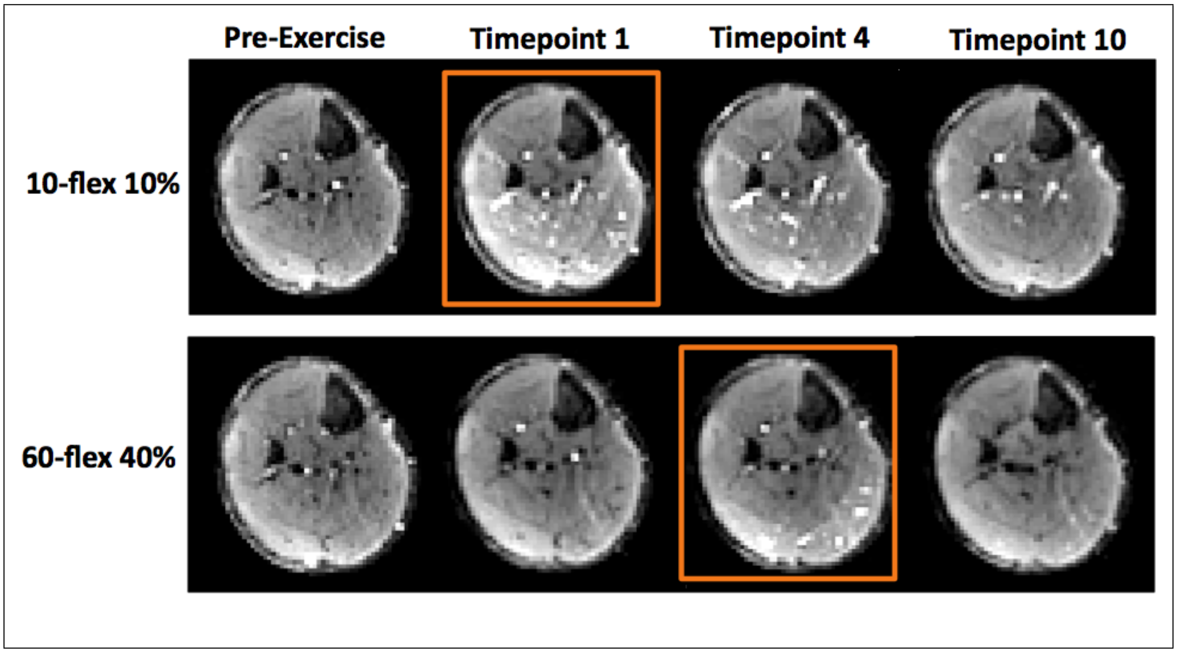

Figure 7.10: Comparisons of S_0 timepoint images following the lowest intensity (10flex10%) and highest intensity (60flex40%) tasks in the present study. S_0 increases according to muscle boundaries are apparent. The orange rectangle indicates the timepoint of peak S_0 signal following each task. The 10flex10% condition demonstrates S_0 increase in soleus, while the 60flex40% condition does not. Furthermore, the peak S_0 signal appears delayed in the 60flex40% condition relative to that seen for 10flex10%.

15-direction MD (Fig. 7.11)

The post-exercise MD of ATIB displays a slight 'elevated-decline' pattern for the 10% MWSF conditions, with the decline continuing until timepoint 10. Meanwhile, both of the ATIB 40% MWSF conditions suggest a 'latent peak' pattern, peaking at

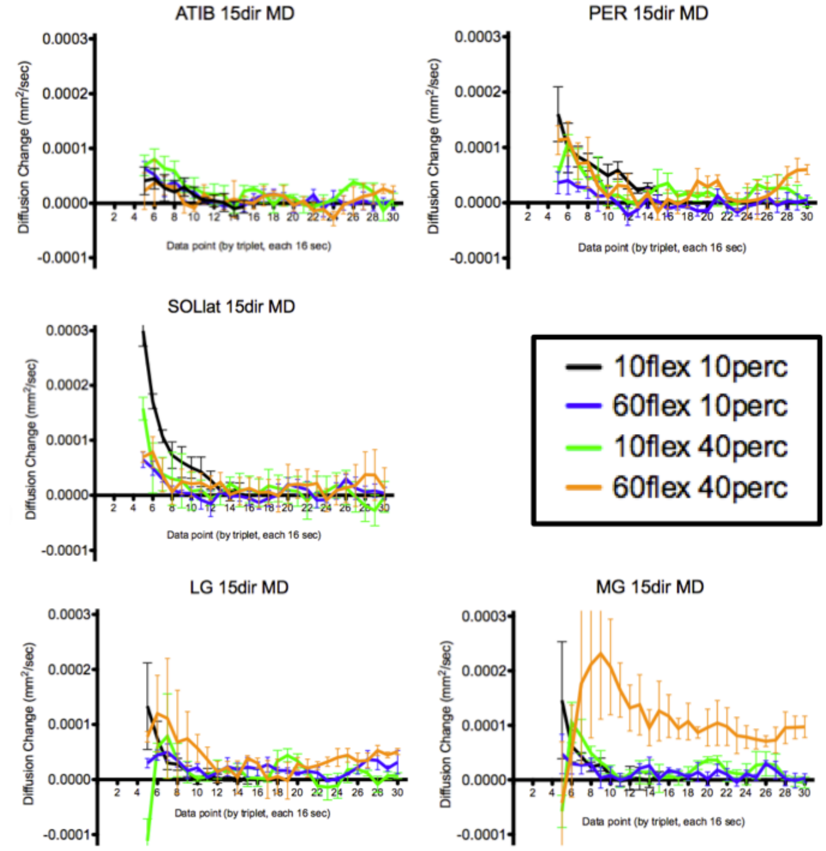

Figure 7.11: Post-Exercise temporal measures of 15-dir mean diffusivity (MD) for individual muscles according to exercise task. Note that 15-dir DTI data begins on Timepoint 5 (see **Figure 7.5**). 'ATIB': Anterior Tibialis, 'PER': Peroneus Longus, 'SOLlat': lateral Soleus, 'LG': Lateral Gastrocnemius, 'MG': Lateral Gastrocnemius.

timepoint 6. The 10flex40% condition appeared to show a greater increase in MD than the 60flex40%.

The PER 10flex10% condition produces an 'elevated-decline' pattern that demonstrates the greatest magnitude of MD change in this muscle of all exercise conditions, and does not reach baseline by timepoint 15. The 60flex10% condition produces a slight 'elevated-decline' pattern that becomes proximal and level with baseline at timepoint 11. Both 40% MWSF conditions produce a 'latent peak' pattern, peaking at timepoint 6 with roughly the same magnitude, although the 60flex40% condition shows a greater initial post-exercise increase at timepoint 5, almost suggestive of an 'elevated-decline' pattern.

Within SOLlat, all exercise conditions produce an 'elevated-decline' pattern, although the 60flex40% condition also suggests a 'latent peak' pattern that peaks at timepoint 6. Both 10-flex conditions, particularly 10flex10%, show a greater magnitude of initial increase than the 60-flex conditions, which show similar initial magnitude. Furthermore, the 10flex10% becomes proximal to baseline at timepoint 13, the 10flex40% at timepoints 9 to 12, and the 60-flex conditions at timepoint 8.

For LG MD, the 10flex10% condition produces an 'elevated-decline' pattern, while 60flex10% displays a 'latent peak' pattern showing a small peak at timepoint 7, and eventually both become proximal to baseline at timepoint 11. The 60flex10% MD then demonstrates a roughly horizontal pattern across remaining timepoints, although notable increases from baseline occur at timepoints 17 and 27. As for the 40% MWSF conditions, 10flex40% produces a distinct 'sub-to-peak' pattern within LG, with the peak occurring at timepoint 7, while the 60flex40% condition induces a 'latent peak' pattern that peaks at timepoint 6, although there is a wide range of error in this temporal vicinity. The peaks observed for LG at timepoints 6 to 7 seem to increase according to intensity of exercise condition.

The MG MD showed an 'elevated-decline' pattern for the 10flex10% exercise condition, with a notable initial elevation from baseline that was equivalent to LG and PER. The 60flex10% condition showed a 'elevated-decline' pattern with slight increase from baseline, and appeared to be proximal from baseline from timepoint 9 onwards. Both of the 40% MWSF conditions produce a 'latent peak' pattern, both of which are also suggestive of 'sub-to-peak' but for the wide SEM range at timepoint 5. However, the 10flex40% condition shows a moderate peak height that occurs at timepoint 6 and becomes proximal to baseline at timepoint 11, while the 60flex40% condition displays a huge peak magnitude that does not occur until timepoint 9. Furthermore, the 60flex40% condition remains elevated from baseline across all remaining timepoints.

*Post-Exercise: λ_1 vs RD Analysis (**Fig. 7.12**)*

The post-exercise changes of λ_1 and RD appeared quite similar to another across most muscles and exercise conditions, with their patterns akin to those found in their corresponding MD, and are thus not described further. However, it was found that within the 10flex10% condition, PER displays an increase in λ_1 greater than that of RD for Timepoints 7-10 and 14, while in the 10flex40% condition, PER displays an increase of RD greater than λ_1 for timepoints 12-14 and 16-20.

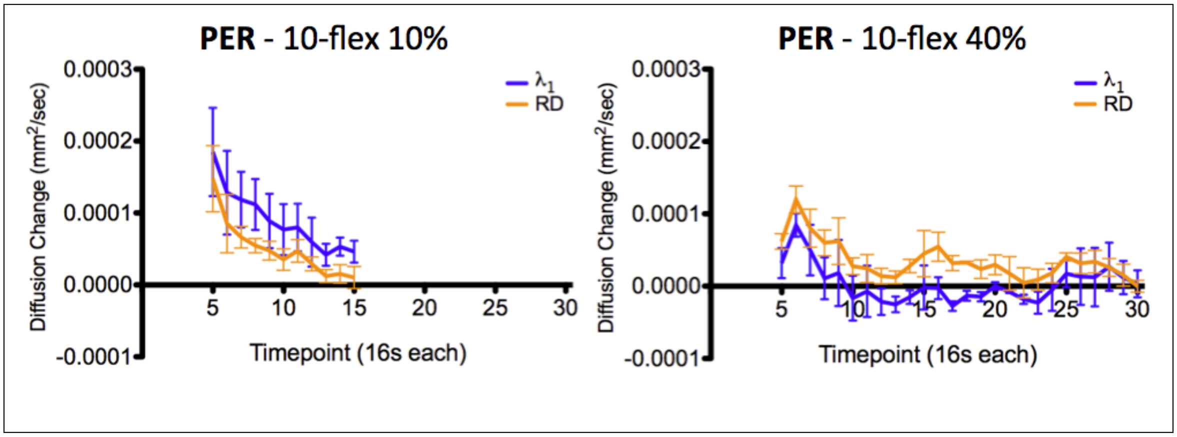

Figure 7.12: Comparison of post-Exercise λ_1 and RD measures in the peroneus longus. These examples are the only instances of differences between λ_1 and RD in the current study. Note that 15-dir DTI data begins on Timepoint 5 (see **Figure 7.5**). Also, only 15 timepoints were collected for the 10flex10% condition, but 30 timepoints collected for the 10flex40%.

Post-Exercise: 10-FLEX 10% MWSF REPEAT Analysis

The 10flex10% exercise condition was performed twice in three subjects to verify observations made for this condition in a pilot test. Note that the subject group used in this experiment is changed by one individual subject, therefore the 10flex10% results presented for this experiment differ slightly from those described for the main exercise intensity experiment. Only ADC and S_0 measures of PER, SOLlat and LG were assessed for this experiment.

3-direction ADC (**Fig. 7.13**)

PER and SOLlat demonstrate an 'elevated-decline' pattern of similar magnitude to one another for both Time 1 and Time 2, with the magnitude of change being quite similar for both trials, PER in particular. Time2 of SOLlat, while showing similar values of ADC increase to Time 1 for the first 5 timepoints, demonstrated a slight increase in ADC relative to Time1 for timepoints 6 to 14. The LG demonstrated a relatively horizontal pattern of ADC change across timepoints for both Time 1 and Time 2, although within Time 2, there is a slight peak that is distinct from baseline at timepoint 3. However, the level of this ADC 'horizontal' pattern differs between trials, as Time 1 displays values slightly decreased from baseline, while Time 2 shows values slightly increased from baseline. The Time 2 ADC of LG is thus suggestive of increase from Time 1, particularly across the first seven timepoints.

Signal Intensity of b=0 s/mm^2 (S_0) (**Fig. 7.13**)

Upon exercise cessation, PER displays a slight 'elevated-decline' pattern for both trials, with Time 2 displaying a slight increase from Time 1 for timepoints 2 to 5.

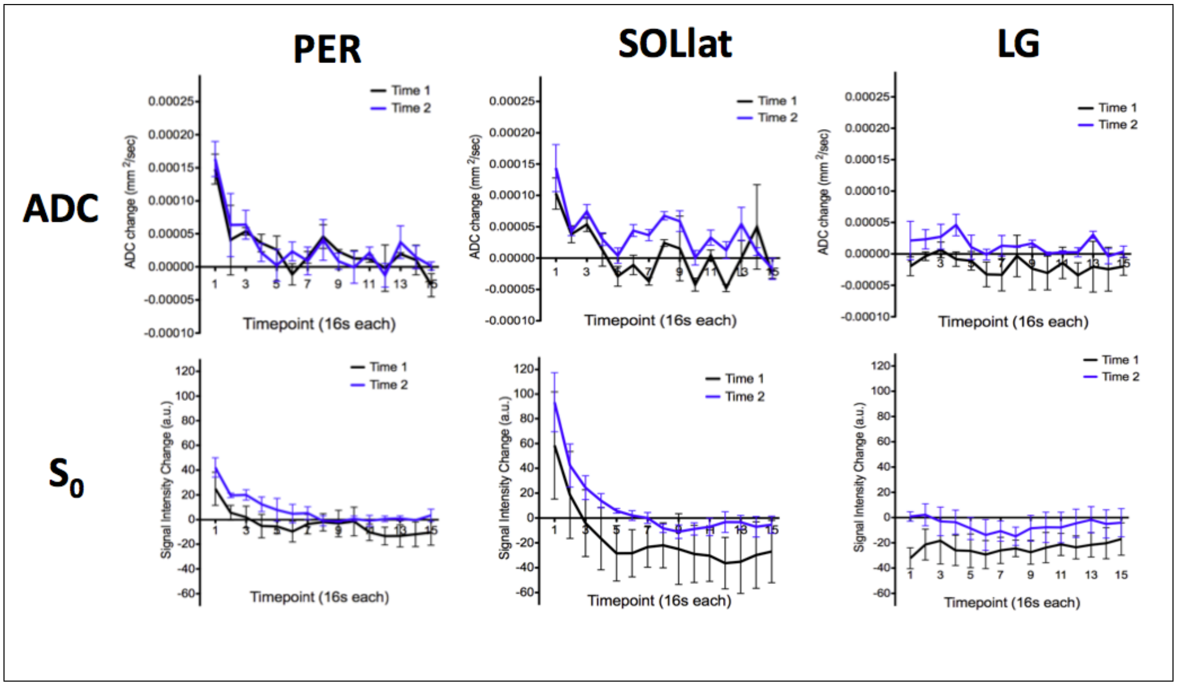

Figure 7.13: 10-flex 10% MWSF Repeat Analysis. Comparison of Time1 and Time2 trials of the 10flex10% exercise task. SOLlat shows an initial elevation of ADC and S_0 for both the first and second trials (Time 1 and Time 2). Time 2 displays a slight increase relative to baseline for ADC and S_0 in all muscles except for PER ADC. Exercise/scanning trials were separated by 5 minutes rest. 'PER': Peroneus Longus, 'SOLlat': lateral Soleus, 'LG': Lateral Gastrocnemius.

Both Time 1 and Time 2 of SOLlat display notable 'elevated-decline' patterns, with Time 1 showing a moderate S_0 increase at timepoint 1, and Time 2 showing a larger S_0 increase. Furthermore, later Time 1 timepoints appear to decrease to a level that is decreased from baseline values, while Time 2 appears to settle at a level that is proximal to baseline. For LG, both trials display a 'horizontal' pattern following exercise. However, Time 1 maintains a level of post-exercise S_0 that is decreased from baseline, whereas Time 2 displays S_0 values proximal to baseline, aside from a decrease seen in the vicinity of timepoint 8.

7.3.5 DISCUSSION

The *in vivo* results of the present study demonstrate that this diffusion technique is sensitive to changes in skeletal muscle following exercise paradigms of different load and duration. Furthermore, by measuring multiple muscles with increased temporal resolution, fresh insights are offered regarding muscle responses to each paradigm that are unique with respect to the current muscle diffusion MRI literature. However, these results also indicate challenges for continuing research, such as interpreting the complexity of human calf muscles and their individual reaction to different motor tasks, and determining the appropriate means of DTI calculation and quantification within a dynamic physiological medium.

The key findings of the present study were that (i) diffusion increases were observed in muscles expected to be involved in plantarflexion (PER, LG, MG) while those not expected to be involved did not (ATIB); (ii) the SOLlat, not expected to be involved in supine straight-legged plantarflexion [13-15], in fact showed strong changes across all subjects in the lightest and short duration exercise conditions; (iii) post-exercise temporal diffusion responses tended to differ between individual muscles, with SOLlat typically showing 'elevated-decline', LG and MG demonstrating a 'latent peak' (or 'sub-to-peak' for short duration exercise), and PER showing 'latent peak' in ADC but 'elevated-decline' for S_0; (iv) for muscles exhibiting "peaking" diffusion responses, the peak magnitude appears associated with exercise intensity; and (v) based on the post-exercise diffusion increases, muscle recruitment differs by exercise condition, with SOLlat active in short duration conditions, LG and MG active in conditions of heavier load, and MG particularly active in the heavy load condition with longer duration.

The increase in diffusion immediately following exercise has previously been observed, with this effect being associated with increased volume of free water and blood within the muscle [9, 10, 20-22]. Disruption of myocytic membranes has also been suggested as a cause of increased diffusion in cases of intensive exercise [6, 7]. Finally, temperature is known to increase within muscle tissue during exercise [23, 24], and it has been shown that this can significantly impact diffusion results [25].

The signal intensity (S_0) of the b=0 s/mm^2 volume used within the present study is governed in part by the transverse magnetization properties (T_2) of the calf muscle, with increases of T_2 indicating that protons within the tissue are taking longer for magnetization to relax to equilibrium (hence more signal). True measurement of T_2 within tissue requires a multi-echo acquisition approach [21] that is capable of distinguishing multiple water compartments. Although superior for assessing tissue water pools, this approach has very a poor temporal resolution (7-10 minutes). Therefore, while S_0 values are not themselves quantitative measures of underlying tissue T_2, changes in the S_0 following exercise are suggestive of alterations in the transverse magnetization relaxation time within the tissue.

A number of studies have investigated post-exercise skeletal muscle T_2 increases [9, 21, 26]. Some groups have observed differential increases between muscles following a common task, suggestive of muscle recruitment [27, 28], while other groups have demonstrated this inter-muscular pattern of T_2 increase can change depending on limb joint positioning during exercise [15]. Additionally, increases in T_2 within muscles have been correlated to gradations of workload intensity within an exercise task [10, 29, 30]. The causes of this post-exercise T_2 increase are not well understood, although many explanations have been proposed. For example, increased muscle T_2 has been associated with tissue water increases [25, 30] due to post-exercise hyperemia [10, 21], although it has been shown that water volume is not the sole cause of T_2 increase [29, 31], nor is the amount of perfusion [10]. Other explanations for post-exercise T_2 increase involve intracellular processes, such as the mobilization of bound water from macromolecules [21, 22, 30] or the accumulation of acidic byproducts of metabolism [28, 29, 31, 32].

Regardless of the underlying causes of the changes in S_0, axial visualization of the temporal volumes acquired by this diffusion technique undeniably indicate that these changes are invoked by different sets of muscles at different timepoints by the same exercise task under different intensities. Furthermore, as **Figure 7.10** shows, these changes are confined by muscle boundaries, indicating that these S_0 measures are endemic to the measured muscles rather than extraneous factors such as proximity to the RF coil.

Interpretation of the Temporal Patterns

The temporal diffusion acquisition used in the present study reveals that not only do muscles active in an exercise task display elevated diffusion, but also that the time course of these increases have differing patterns of temporal trajectory depending on the exercise intensity and muscle measured. Increases in diffusion indicate increased mobility of water molecules, which can result due to increased volume of water, fewer subcellular obstacles (i.e. lipid bilayers), fluid flow, or increased temperature. While this experiment was not designed to parse the contributions of these factors, we speculate that temporal diffusion changes are related to the changes in blood flow to individual muscles, as well as metabolic activity. With this in mind, we attempt to interpret what is occurring during each of the observed temporal diffusion patterns (**Fig. 7.7**).

The 'elevated-decline' pattern indicates the processes affecting diffusion have increased from baseline values during the exercise, and subside following exercise cessation. Both the initial elevation and subsequent decline to baseline are potential components of interest in this pattern. The initial increase in diffusion indicates that diffusion has been elevated during the exercise task. Curiously, this pattern tended to occur within the short duration (10-flex) exercise tasks, and so it does not seem to be associated with exercise intensity per se. It is possible that the initial elevation is related more to metabolic activity involving available nutrients (e.g. ATP, phospcreatine, glucose) rather than blood flow, or alternatively, the lightest condition (10-flex 10% MWSF) presented the least hindered blood flow during the task due to muscle contraction. The rate at which the initial elevation returns to baseline may be of relevance, as it indicates the time needed for a muscle to return to equilibrium, with a steeper slope indicating more regulatory mechanisms to maintain homeostasis at that exercise level.

The 'latent peak' pattern suggests that factors affecting diffusion are minimal during exercise, but increase upon cessation of exercise. This pattern occurred in PER, LG, and MG, and the height of the peak seemed to be associated with exercise intensity. It is possible that this pattern is a result of blood influx and perfusion that occurs following exercise cessation, and is proportionate to the task. Based on the results of the present study, this suggests that PER is more involved in the lighter intensity exercise, while LG and especially MG become active in the heavier exercise tasks. The delay in peak could be due to the time needed for the muscle to relax and cease compression on local capillaries, or perhaps for the processes of vasoconstriction and vasodilation to take effect and direct blood to the recently-active muscles.

The 'sub-to-peak' pattern is a special circumstance, as it only appeared in LG and MG within the task of short duration with heavier load (10-flex 40% MWSF). This pattern, which was found in all subjects, indicates that diffusion has actually decreased from baseline measures during the exercise task, but then increases to a small peak 16-32 seconds later. It is possible this is due to muscle compression on local capillaries during the stronger contractions needed by the gastrocnemius to move the heavier load. We also propose that the reason this pattern is not seen in the 60-flex 40% MWSF condition is because the longer duration and repetitive muscle contraction of this task have induced venous pumping and thus some blood flow through the muscle during the exercise [33].

The 'horizontal' pattern tends to be proximal to baseline, and occasionally at values decreased from baseline. This indicates that the factors dictating diffusion measures have not been affected by the preceding exercise condition beyond the range of noise in calculation. This suggests that the muscles displaying this temporal pattern have not played an active role in the exercise task.

Very few studies have measured the temporal nature of acute diffusion changes within skeletal muscle following exercise, and of these, either only a single muscle was measured [9, 22], or multiple muscles (e.g. soleus and gastrocnemius) were assessed as a single unit [10, 12]. Although this makes direct comparison of temporal patterns of individual muscles to previous studies difficult, some common patterns were observed. For example, measurement of the forearm following hand gripping displayed an 'elevated-decline' pattern [9], as did the anterior tibialis following exhaustive dorsiflexion [22]. The two studies studying soleus and gastrocnemius as a collective measure following plantar flexion appeared to display differing post-exercise patterns, with one experiment displaying an 'elevated-decline' pattern [10], but a more recent study displaying a 'sub-to-peak' pattern [12].

It should also be noted that early work related to the present study describes the then-novel 'latent peak' pattern in post-exercise gastrocnemius [11] and peroneus longus (*Section 4.1.4*), although the latter shows a greater initial elevation, shorter and more delayed peak, and faster return to baseline. Furthermore, earlier work related to this study (*Chapter 6*) proposed that the differing temporal patterns between muscles is due to their differing capillarization [34] and metabolic activity based on fiber content [28, 31, 35].

Effect of previous exercise on present measures

The effect of a single exercise episode on diffusion response to subsequent exercise sessions should not be overlooked. For practical reasons, multiple exercise tasks were performed within a single scanning session for each subject. These tasks were performed in the same order for each subject, progressing from the task of least intensity to most intensive, rather than in a randomized order. This was purposefully done to minimize the possible contamination effect of a high intensity exercise on a subsequent light intensity exercise, since only a few subjects were planned for this pilot study. Efforts were taken to provide rest periods of at least 10 minutes between the end of post-exercise diffusion acquisition for one task and the onset of baseline acquisition for the next task, with the exception of the '10-flex 10% Repeat Analysis', which were separated by only 5 minutes due to the negligible lasting effects this exercise condition was thought to incur at time of experiment design. However, as demonstrated by the results of the '10-flex 10 Repeat Analysis', this exercise task is not negligible, as greater increases in diffusion and S_0 were observed for the second trial (Time 2), and therefore a 10-minute rest period should have been performed following this task as well.

Baseline measures preceding each exercise task were compared across conditions, in anticipation that multiple exercises within a single scanning session may increment the pre-exercise diffusion values. However, we found that all active muscles displayed relatively stable baseline values preceding each exercise condition, although the results for SOLlat suggest a slight increase across subsequent exercise tasks. Surprisingly, the ATIB, which displayed minimal response during any of the post-exercise measurements, demonstrated a notable decrease in ADC and MD values across time, although this finding is not echoed in the measures of S_0.

Despite baseline stability, the identical ordering of these exercise tasks means that we cannot rule out how muscle priming impacts subsequent exercise tasks, nor how the time the subject had been continuously lying in the MR scanner may have affected performance of the task, particularly regarding the later more intensive exercise conditions. That said, the ordering of exercise tasks used in the present study also provide evidence that the observed results are not strictly cumulative, but perhaps task-based as well. The most notable example of this are findings within SOLlat, which demonstrate moderate 'elevated-decline' ADC and then moderate-to-large 'elevated-decline' for the short duration 10-flex conditions, but minimal response from the longer duration 60flex10% condition that separates them, as well as a similar minimal response the longer duration 60flex40% condition that follows all three of the previous tasks.

3-dir ADC vs S_0

When comparing the temporal changes between ADC and S_0, we observed that post-exercise increases in ADC tended to occur at timepoints where S_0 had also shown increases from baseline, with notable examples being all muscles (aside from ATIB) within the 10flex10% condition, as well as for MG within the 60flex40% condition. This would make sense, as calculation of diffusion uses the b=0 s/mm^2 volume as a reference, meaning that the measures of ADC and S_0 are not truly independent from one another. However, the temporal measures of ADC and S_0 were found not to be strictly linked, as some increases in S_0 were not accompanied by increases in ADC, and vice versa. For example, the conspicuous 'elevated-decline' pattern observed for SOLlat in 10-flex conditions did not show a similar magnitude of change within the corresponding ADC measures. Another set of examples are in cases where S_0 shows a decrease from baseline but ADC does not, such as in SOLlat following the 60flex40% condition, and LG after 60flex10%. In turn, the 'sub-to-peak' diffusion responses observed in LG and MG following 10flex40% do not show the same sub-measures in S_0. Finally, the large increase in the later timepoints of PER S_0 following the 60flex40% condition are not matched with equivalent increases in ADC.

Previous temporal studies of post-exercise skeletal muscle using diffusion and multi-echo T_2 measurement have observed that while both of these measures increase following exercise [22], they are found to recede at different rates, with longer times observed for the diffusion values to return to baseline [9, 10].

MD Calculation, relationship to ADC and S_0

When reviewing the MD results across muscles and exercise conditions, it appeared as though they bore a strong resemblance to the temporal patterns of S_0 rather than to ADC. A notable example of this was comparison of the post-exercise changes of 3-dir ADC, 15-dir MD, and S_0 observed for SOLlat (**Fig. 7.14**).

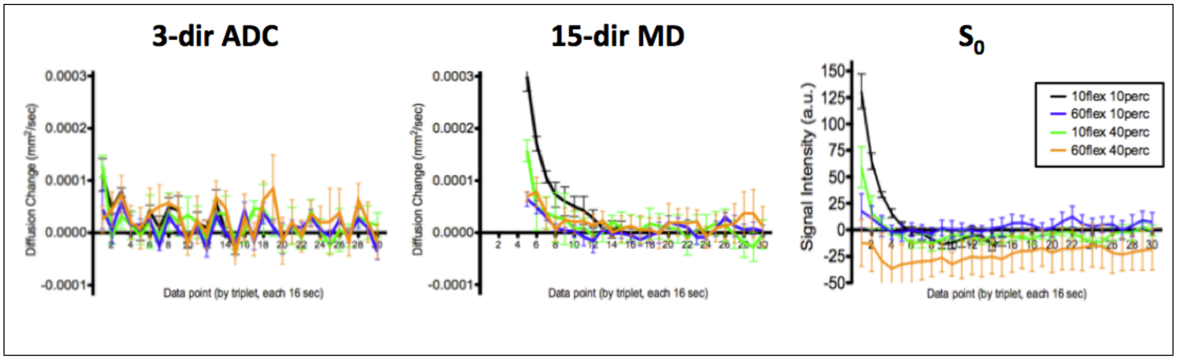

Figure 7.14: Comparison of 3-dir ADC, 15-dir MD, and S_0 temporal measures for lateral soleus (SOLlat) following four exercise conditions of differing intensity. 15-dir MD timepoint values appear more strongly associated with S_0 than with ADC measures. Note that 15-dir DTI data begins on Timepoint 5 (see **Figure 7.5**).

One possibility for this is the manner in which the diffusion tensor was calculated. Recall that DTI was calculated using a single b=0 s/mm^2 volume as a reference, while subsequent b=0 s/mm^2 volumes found among the diffusion-weighted images per 15-dir subset were omitted. The purpose of the b=0 s/mm^2 reference is to account for the T_2 value of the tissue in calculating diffusion measures, which use signal decreases within diffusion-weighted volumes to quantify greater diffusion along that particular direction. However, if the signal intensity of the reference volume is dynamically changing in signal intensity, and the diffusion-weighted volume with which it is compared is separated by a considerable length of time (up to 76 seconds in the

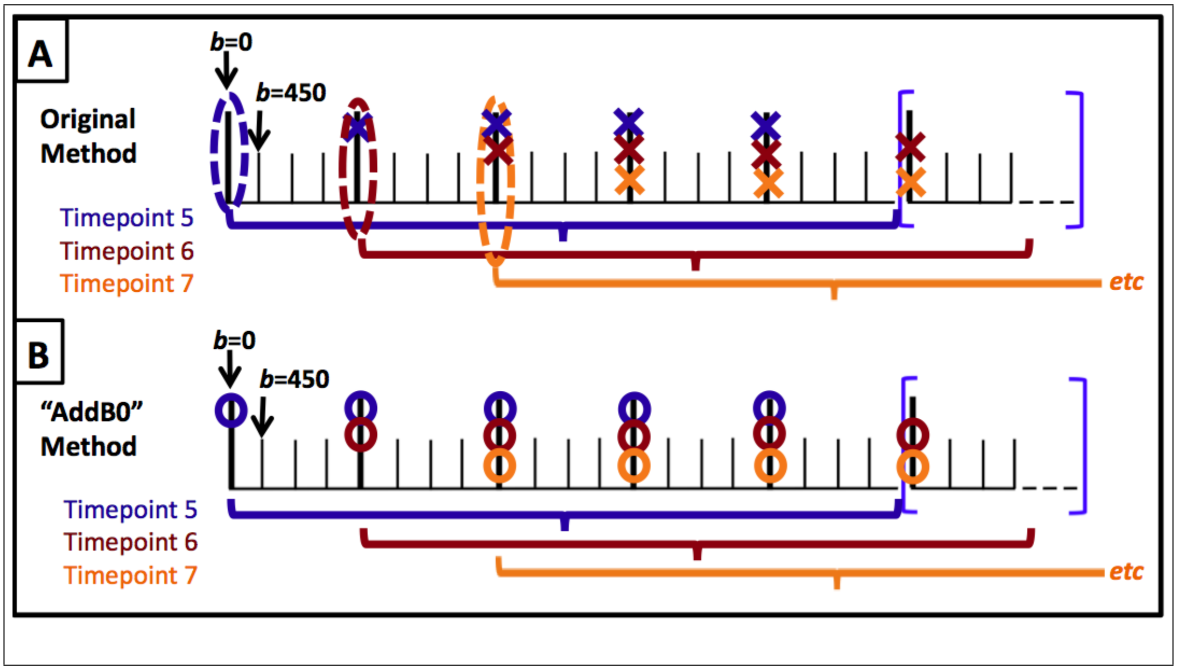

Figure 7.15: Utilization of b=0 volume in DTI calculation. **(A)** Method originally used for calculation of N=15 DTI sliding window. Coloured ellipses indicate b=0 s/mm^2 volume used for DTI calculation, while corresponding 'X' colour indicates volumes omitted during N=15 sliding window aggregation. **(B)** Proposed method of b=0 s/mm^2 volume incorporation ("AddB0"). Coloured circles correspond with b=0 s/mm^2 volumes used for N=15 sliding window aggregation.

present study), the diffusion calculation has the potential to exaggerate the amount of diffusion observed.

One solution to this confounding element would be to include the intermittent b=0 s/mm^2 reference volumes that were omitted in the original calculation of each 15-dir volume (the "AddB0" strategy; **Fig. 7.15**). Ideally, each b=0 s/mm^2 volume would only be used to calculate diffusion for the triplet set that succeeds it, and then subsequently combined into the 15-dir subunits for tensor calculation. On the other hand, if all the b=0 s/mm^2 volumes are merely averaged together, this may under-represent the magnitude of temporal diffusion changes, as there would be less relative signal loss in the diffusion weighted images.

Although the FSL software was not designed for dynamic assessment of diffusion, a rudimentary test was nonetheless performed to examine how temporal measures using the "AddB0" analysis with FSL would compare to the original DTI calculations. Baseline and post-exercise MD magnitude change data from a single subject were recalculated according to the "AddB0" method for SOLlat 10flex10%, as well as all exercise conditions of LG and MG. Upon recalculation, the mean test baseline for the "AddB0" method appears to demonstrate similar values to previous ADC and MD calculations for the selected muscles and exercise conditions in this subject (**Fig. 7.16a**).

In fact, it appears that the "AddB0" method is more stable in value across timepoints than the original method. The post-exercise "AddB0" temporal results for

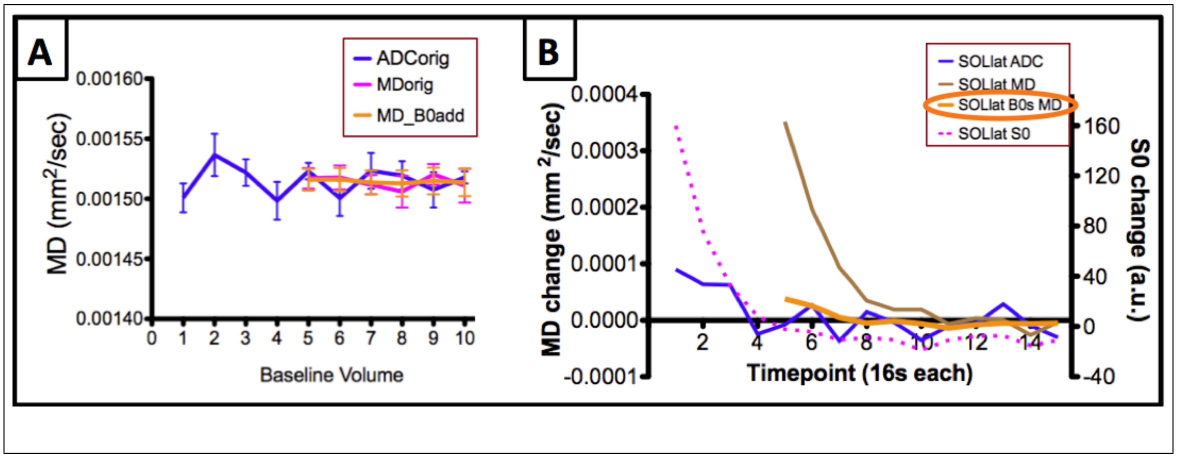

Figure 7.16: Comparison of b=0 s/mm^2 volume utilization methods. Note that 15-dir MD measures begin at Timepoint 5 (see **Figure 7.5**). **(A)** Baseline comparison. ADCorig and MDorig are based on an ROI that includes lateral soleus (SOLlat), lateral gastrocnemius (LG), and medial gastrocnemius (MG), and were calculated according to the original timecourse method used in the described experiment. MD_B0add represents the values generated by this ROI following DTI calculated by inclusion of all b=0 s/mm^2 volumes ("addB0"). **(B)** Post-exercise calculations of SOLlat ROI for ADC, MD, S_0, and the experimental "AddB0" DTI calculation.

SOLlat 10flex10% display a slight 'elevated-decline' which is much diminished from the temporal pattern of the original calculation (**Fig. 7.16b**). Furthermore, the "AddB0" result resembles the pattern and trajectory seen in the ADC results, and now bears slight resemblance to the large changes observed for S_0. Measurement of LG and MG (assessing only the first 15 timepoints) across all exercise conditions using the "AddB0" strategy appeared to blunt many of the original findings for this subject (**Fig. 7.17**).

The 'elevated-decline' pattern is still present for the 10flex10% condition, particularly in LG, and still contrasts with the temporal pattern found for other exercise

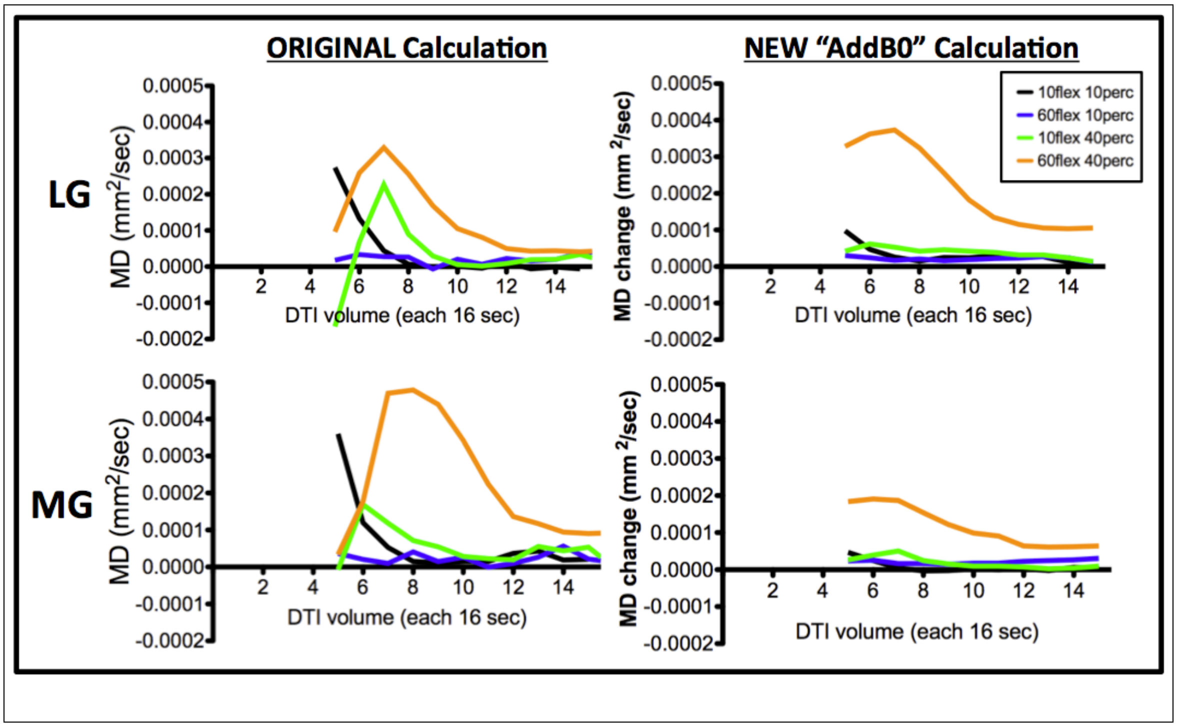

Figure 7.17: Comparison of b=0 volume s/mm^2 utilization methods in measurement of the lateral (LG) and medial gastrocnemius (MG) following all four exercise conditions. "ORIGINAL" indicates the results described in the present study (single b=0 s/mm^2 per N=15 DTI), while "AddB0" indicates the alternative method whereby all 5 b=0 s/mm^2 volumes within an N=15 subunit are considered in DTI calculation. Note that 15-dir MD measures begin at Timepoint 5 (see **Figure 7.5**).

conditions, however its initial elevation is much smaller. The 10flex40% condition no longer produces a notable peak, nor 'sub-to-peak' pattern, in either LG or MG. Both LG and MG continue to demonstrate a distinct increase for the 60flex40% condition. However, the initial value at timepoint 5 is increased when analyzed using the "AddB0" method, and the MG peak is substantially reduced from the initial calculation.

LIMITATIONS

There are a number of limitations to the present preliminary study which can be potentially addressed and improved with further experimentation. First, and perhaps most important, is that dynamic measures of muscle using DTI appear dependent upon the analysis strategy. This was not predicted in the static phantom work leading up to the present method, although this is the precise reason that the present preliminary *in vivo* experiment was performed. The FSL software package is an "off-the-shelf" analysis tool that widely-used in traditional anatomical studies using DTI. However, this tool may not offer the flexibility in calculation required for the temporal analysis of the present study, and thus further exploration into other means of DTI calculation (e.g. diPy [36]) is warranted. Despite this issue of DTI calculation, the gradient table and analysis method used in the present study have demonstrated their capability in producing useful ADC data regarding muscle diffusion differences between exercises. This allows fruitful data collection to continue while the issue of how best to calculate DTI is investigated. Despite the challenges of DTI calculations encountered in the present study, and the wealth of temporal information regarding exercise in different skeletal muscles provided by the simple 3-dir ADC method, we contend that further investigation into finding an acceptable dynamic DTI analysis technique is still worthwhile.

Secondly, the heterogeneity between individual subjects regarding performance of the exercise task would need to be examined in more detail. Although height, weight, and MWSF were obtained from each subject, as well a verbal agreement not to perform exercise for 12 hours prior to scanning, little quantitative information as to their exercise habits was gathered. Furthermore, outside measurements of habitual muscle preference may help explain the variation in diffusion response observed between subjects in the present study. An anecdotal example was that one subject demonstrated little change in either LG or MG following plantarflexion in any of the exercise conditions, while demonstrating increasing changes in PER according to exercise intensity. Furthermore, these results were duplicated upon a repeat of the experiment (undertaken because the initial session had produced results contrary to those expected.) Qualitative observation of this subject indicates a bow-legged stance and mode of walking appearing to place weight laterally rather than anteriorly upon the foot, and could be related to the preference for PER vs LG or MG in the diffusion results. Therefore, future experiments involving temporal diffusion and plantarflexion would benefit from performing gait analysis of each subject in order to provide quantitative measures of their natural weight distribution and muscle preference.

Third, it is important that future studies using temporal DTI methods consider external validation in order to substantiate the results. Modalities such as electromyography (EMG), ultrasound or near infrared spectroscopy (NIRS) could potentially provide measures of electrical activity, muscle fiber movement and oxygenation concurrent with the exercise eliciting diffusion change. Of course, incorporation of these modalities into the MR environment and targeting each of the desired tissues would present their own challenges.

Finally, as with any preliminary study, more data needs to be collected in order to better interpret the results obtained in the experiment. Additional subjects would be helpful to better assess the ubiquity or variation in post-exercise temporal diffusion patterns. Repeated scanning of subjects on different days could solidify anecdotal observations that inter-muscular temporal patterns are consistent within individual people. Enrolment of more subjects would also allow group analyses to be performed, such as investigation of differences between genders, age groups, athletes of different disciplines, or health status. Additional exercise tasks requiring the same muscle group, such as alternate task ordering, additional workload options or alterations in limb angulation could be performed in order to study how diffusion patterns would vary depending on predicted recruitment. Furthermore, this diffusion approach could be tested in other muscle groups, such the arm, shoulder, or neck, provided that their motion can be controlled and regulated within the constraints of the MRI environment.

CONCLUSIONS

Although some methodological issues remain to be solved, the proposed sliding window multi-scale diffusion approach shows promise in the detection and characterization of temporal changes within and between skeletal muscles following exercises of differing intensity. Future work is needed regarding DTI calculation method, as well as additional data collection and independent validation in order for better interpretation of these temporal patterns.

Acknowledgements:

Thanks to Dr. Maxime Descoteaux and Dr. Emmanuel Caruyer for their input regarding creation of gradient tables. Funding for this study was provided a National Sciences and Engineering Research Council of Canada (NSERC) Discovery grant (MDN), as well as TD Canada Trust, who have yet to unleash the hounds (CPR).

7.3.6 REFERENCES

[1]Basser PJ, Mattiello J, Le Bihan D. MR diffusion tensor spectroscopy and imaging. Biophys J 1994; 66:259-267.

[2]Damon BM. Effects of Image Noise in Muscle DT-MRI Assessed Using Numerical Simulations. Magn Reson Med 2008; 60(4):934-944.

[3]Froeling M, Nederveen AJ, Nicolay K, Strijkers GJ. DTI of human skeletal muscle: the effects of diffusion encoding parameters, signal-to-noise ratio and T2 on tensor indices and fiber tracts. NMR Biomed 2013; 26:1339-1352.

[4]Rockel C, Noseworthy MD. An Exploration of Diffusion Tensor Eigenvector Variability Within Human Calf Muscles. J Magn Reson Imaging 2016; 43(1):190-202.

[5]Morvan D. In Vivo Measurement of diffusion and pseudo-diffusion in skeletal muscle at rest and after exercise. Magn Reson Imaging 1995; 13:193-199.

[6]Yangisawa 0, Kurihara T, Koayashi N, Fukubayashi T. Strenuous resistance exercise effects on magnetic resonance diffusion parameters and muscle-tendon function in human skeletal muscle. J Magn Reson Imaging 2011; 34:887-894.

[7]Cermak NM, Noseworthy MD, Bourgeois JM, Tarnopolsky MA, Gibala MJ. Diffusion tensor MRI to assess skeletal muscle disruption following eccentric exercise. Muscle Nerve 2012; 46:42-50.

[8]Froeling M, Oudeman J, Strijkers GJ, et al. Muscle changes detected with diffusion-tensor imaging after long distance running. Radiology 2015; 274:548-562.

[9]Morvan D, Leroy-Willig A. Simultaneous Measurements of Diffusion and Transverse Relaxation in Exercising Skeletal Muscle. Magn Reson Imaging 1995; 13(7):943-948.

[10]Nygren AT, Kaijser L. Water exchange induced by unilateral exercise in active and in active skeletal muscles. J Appl Physiol 2002; 93:1716-1722.

[11]Rockel C, Davis A, Wells G, Noseworthy MD. Monitoring exercise-induced muscle changes using Diffusion Tensor Imaging, with and without caffeine. Proceedings of the International Society of Magnetic Resonance in Medicine, Melbourne Australia, 2012. Poster 1425.

[12]Baete SH, Cho GY, Sigmund EE. Dynamic diffusion-tensor measurements in muscle tissue using the single-line multiple-echo diffusion-tensor acquisition technique at 3T. NMR Biomed 2015; 28:667-678.

[13]Basmajian JV, De Luca CJ. Muscles Alive: Their Functions Revealed by Electromyography Hardcover, 5th Revised edition. New York: Williams & Wilkins; 1985. 561p.

[14]Miaki H, Someya F, Tachino K. A comparison of electrical activity in the triceps surae at maximum isometric contraction with the knee and ankle at various angles. Eur J Appl Physiol 1999; 80:18591.

[15]Price TB, Kamen G, Damon BM, et al. Comparison of MRI with EMG to study muscle activity associated with dynamic plantar flexion. Magn Reson Imaging 2003; 21:853-861.

[16]Jenkinson M, Bannister P, Brady M, Smith S. Improved optimization for the robust and accurate linear registration and motion correction of brain images. Neuroimage 2002; 17(2):825-841.

[17]Jenkinson M, Beckmann CF, Behrens TE, Woolrich MW, Smith SM. FSL. NeuroImage 2012; 62:782-790.

[18]Le Bihan D, Breton E, Lallemand D et al. MR Imaging of intravoxel incoherent motions: application to diffusion and perfusion in neurologic disorders. Radiology 1986; 161(2):401-407.

[19]Behrens TE, Woolrich MW, Jenkinson M, et al. Characterization and propagation of uncertainty in diffusion-weighted MR imaging. Magn Reson Med 2003; 50(5):1077-1088.

[20]Lundvall J, Mellander S, Westling H, and White T. Fluid transfers between blood and tissues during exercise. Acta Physiol Scand 1972; 85:258269.

[21]Saab G, Thompson RT, Marsh GD. Effects of exercise on muscle transverse relaxation determined by MR imaging and in vivo relaxometry. J Appl Physiol 2000; 88:226-233.

[22]Ababneh ZQ, Ababneh R, Maier SE, et al. On the correlation between T2 and tissue diffusion coefficients in exercised muscle: quantitative measurements at 3T within

the tibialis anterior. Magn Reson Mater Phy 2008; 21:273-278.

[23]Saltin B, Gagge AP, Stolwijk JAJ. Muscle temperature during submaximal exercise in man. J Appl Physiol 1968; 25:679-688.

[24]Simonis FFJ, Petersen ET, Lagendijk JJW, van den Berg CAT. Feasibility of Measuring Thermoregulation during RF Heating of the Human Calf Muscle Using MR Based Methods. Magn Reson Med 2016; 75:1743-1751.

[25]Morvan D, Leroy-Willig A, Malgouyres A, Cuenod CA, Jehenson P Syrota A. Simultaneous temperature and regional blood volume measurements in human muscle using an MRI fast diffusion technique. Magn Reson Med 1993; 29:371-377.

[26]Fleckenstein JL, Canby RC, Parkey RW, Peshock RM. Acute effects of exercise on MR imaging of skeletal muscle in normal volunteers. Am J Radiol 1988; 151:231-237.

[27]Green R, Wilson D. A pilot study using magnetic resonance imaging to determine the pattern of muscle group recruitment by rowers with different levels of experience. Skeletal Radiol 2000; 29:196-203.

[28]Yangisawa O, Niitsu M, Yoshioka H, Goto K, and Itai Y. (2003). MRI Determination of Muscle Recruitment Variations in Dynamic Ankle Plantar Flexion Exercise. Am J Phys Med Rehabil 2003; 82:760765.

[29]Fisher MJ, Meyer RA, Adams GR, Foley JM, Potchen EJ. Direct relationship between proton T2 and exercise intensity in skeletal muscle MR images. Invest Radiol 1990; 25:480-485.

[30]Adams GR, Duvoisin MR, Dudlet GA. Magnetic resonance imaging and electromyography as indexes of muscle function. J Appl Physiol 1992; 73:1578-1583.

[31]Prior BM, Ploutz-Snyder, Cooper TG, Meyer RA. Fiber type and metabolic dependence of T2 increases in stimulated rat muscles. J Appl Physiol 2001; 90:615-623.

[32]Damon BM, Gregory CD, Hall KL, Stark HJ, Gulani V, Dawson MJ. Intracellular acidification and volume increases explain R2 decreases in exercising muscle. Magn Reson Med 2002; 47:14-23.

[33]Guyton A, Hall J. Textbook of Medical Physiology, 11th ed. Philadelphia: Elselvier Inc., 2006.

[34] Andersen P, Kroese AJ. Capillary supply in soleus and gastrocnemius muscles of man. Pflugers Arch 1978; 375:245-249.

[35] Johnson MA, Polgar J, Weightman D, Appleton D. Data on the distribution of fibre types in thirty-six human muscles: An autopsy study. J Neurol Sci 1973; 18:111-129.

[36] Garyfallidis E, Brett M, Amirbekian B, Rokem A, van der Walt S, Descoteaux M, Nimmo-Smith I and Dipy Contributors. Dipy, a library for the analysis of diffusion MRI data. Front Neuroinform 2014; 8(8). doi: 10.3389/fninf.2014.00008.

Chapter 8

Conclusions and Future Directions

Diffusion Tensor Imaging (DTI) has gained much attention in recent years, largely driven by advancements and tool development aimed at the brain and nervous system. The study of skeletal muscle has benefited greatly by the availability of these DTI methods and tools. However, the composition and functional behaviour of skeletal muscle differs from that of the brain, meaning that neuro-derived analytical tools may need to be adapted from their original purpose in order to quantify muscle appropriately.

As described in the preceding chapters, multiple studies have investigated the architecture of resting muscle using DTI techniques, while post-exercise temporal diffusion changes have been observed using diffusion MRI techniques of lower directional resolution. The work described in this dissertation sought to apply modern DTI acquisition in a temporal context in order to characterize timelines of muscle change following exercise. Of particular interest was the demonstration of differing post-exercise temporal diffusion behaviours between individual muscles in the human calf, and discussing the possible connection to tissue composition and related physiology.

8.1 Main Findings and Contributions

(1) The secondary eigenvector (ε_2) was found to display much less directional stability than the principal eigenvector (ε_1) within resting muscle tissue. Furthermore, time-expensive methods to improve signal appeared to improve principal eigenvector stability much more than that of the minor eigenvectors. This study served to accentuate the limits of DTI in skeletal muscle, in that the minor eigenvalues (λ_2 and λ_3) should not be regarded as separate entities for investigation, but instead combined into the mean measure of radial diffusivity (RD). Furthermore, this study employed novel mapping techniques to visualize and quantify the heterogeneity of eigenvector variability and SNR across an image and between muscles. These findings served the overall project in that the expectations of DTI measure reliability from *in vivo* human muscle were better understood, as well as providing the scientific community with empirical evidence that complements previous benchmark simulation studies.

(2) Individual muscles within a muscle group displayed differing temporal patterns of mean diffusivity (MD) following exercise tasks. Furthermore, the signal intensity (S_0) of the b=0 s/mm^2 displayed a notable increase within the extensor digitorum longus (EDL) following a mild dorsiflexion-eversion task, a result that was distinct from the other measured muscles. It is possible that inter-muscle post-exercise differences are related to their differing tissue composition and related physiology. The diffusion and S_0 changes elicited in this study also demonstrate that mild exercise intensity can be used to induce detectable post-exercise diffusion changes, indicating that intense exercise tasks are not requisite in the assessment of muscle function. This may be useful in the investigation of fragile or pathological muscle tissues.

(3) The feasibility of a gradient table allowing for stable measures of temporal muscle diffusion at multiple timescales was demonstrated, allowing for diffusion assessments with 16 second resolution that could be subsequently combined to produce ongoing DTI indices of structure. *In vivo* utilization of this technique in the human calf indicated four temporal diffusion patterns that frequently occurred amongst individual calf muscles following different intensities of a plantarflexion exercise task: an initial elevation, a delayed peak originating at baseline, a delayed peak originating below baseline, and a horizontal pattern proximal to baseline. For the patterns with peaks, the peak magnitude appeared to be related to exercise intensity. The varied exercise conditions, consisting of four combinations of short and long duration, and light and moderate weight load, appeared to demonstrate differing muscle recruitment as evidenced by post-exercise diffusion and S_0 increases. In brief, the soleus and peroneus longus appeared to be involved in exercise of lighter intensity, while heavier weight loads elicited more diffusion response from first the lateral gastrocnemius, and then the medial gastrocnemius with long duration. Furthermore, the activation of soleus was notable, as this muscle showed unanimous increases in diffusion and S_0 following exercise of short durations, a result that counters the existing literature regarding subjects performing supine straight-legged plantarflexion.

8.2 Future Work

The results of this preliminary study demonstrate that this novel method of DTI acquisition and temporal analysis has the sensitivity to detect dynamic differences in post-exercise recovery between muscles and exercise conditions. There are several ways by which to continue the work described in this dissertation, both in terms of methodological improvements as well as additional experimentation into post-exercise muscle dynamics.

To begin with, the method by which DTI is calculated could be explored more thoroughly. As described in *Chapter 7*, the 'sliding window' N=15 DTI technique requires further investigation regarding how best to incorporate the b=0 s/mm^2 volume into ongoing tensor calculations. Additionally, DTI calculation has become more sophisticated over the duration of this project, with denoising algorithms becoming more common, and other tensor models (e.g. weighted linear least squares) developed to handle outliers, possibly allowing for better eigenvector stability. While developed for the purposes of fiber tracking in the brain, these techniques could be explored within the realm of skeletal muscle and temporal analysis. Another manipulation of DTI methodology could be the use of low but >0 b-values rather than b=0, as this is thought to reduce the infiltration of perfusion on diffusion measures <LeBihan *et al.*, 1986; Morvan, 1995>. While this methodological change could provide an explanation as to the source of diffusion changes, the impact of such a strategy on temporal resolution would need to be investigated more thoroughly.

Another methodological improvement would be to develop a more quantitative way of representing the temporal diffusion data. The preceding work described the temporal diffusion patterns using qualitative descriptions of relative peak height and timepoints of pattern landmarks. However, a quantitative standardization of the diffusion changes induced within muscle by exercise would allow better comparison between subjects and exercise conditions, as well as interpretation of temporal patterns and potentially long-term therapeutic monitoring within a single subject.

Despite these technical considerations, the temporal diffusion methods described in *Chapters 6* and *7* were able to produce intriguing data in their current form, which could launch several directions of further investigation into post-exercise muscle dynamics.

Repeatability studies would determine the consistency with which temporal diffusion measures are able to characterize the skeletal muscles within individual subjects. Anecdotal evidence during the course of the described experiments has suggested that individual subjects differ in terms of muscle recruitment for plantarflexion exercises, and that these differences can be consistently detected using temporal dMRI methods. Experimentation based on this anecdotal finding could perhaps be used to explain variation in post-exercise diffusion measures, as well as lead to techniques for therapeutic assessment or monitoring.

Recruitment of more subjects would be of benefit in determining the utility of temporal DTI in the study of muscle activation and recovery. The group size of the described studies has been small and relatively homogeneous (young adults). Future studies could include recruitment into subject groupings such as athletes vs non-athletes, muscle pathology vs healthy, or divisions of gait preference.

Exercises targeting other muscle groups could be explored to test the ubiquity of temporal DTI analysis and characterization of temporal patterns per muscle. Of course, the immediacy of the diffusion effects following exercise cessation necessitates that exercise must be performed within the magnet bore, which may limit exercise options. Furthermore, the supine nature of MRI acquisition may mean that in-bore exercises may not fully represent true full body exercise. However, *Chapter 7* demonstrated that temporal DTI was able to detect changes elicited by mild exercise consisting of little more than repetitive voluntary movement, so it is possible that other muscle groups can be studied with consideration of bore layout, subject comfort, joint positioning, and appropriate RF coils. Furthermore, studies of in-bore exercise using custom MRI-compatible ergonometric equipment would benefit from having subjects measured using out-of-bore dynamometric equipment to provide standardized context to the in-bore exercise tasks.

The temporal diffusion patterns described in this dissertation would benefit from additional measures to provide corroborative information regarding the changes observed within and between the individual muscles and exercise conditions. Ideally, such techniques would acquire data concurrent with the scanning session, pending their compatibility and functionality within the MR environment. Examples of such techniques are electromyography (EMG) to assess muscle electrical activity, cardiac monitoring and pulse oximeters or to assess pulse and heart rate, or perhaps fiber-optic temperature monitoring of skin temperature, although each of these modalities provide their own challenges. Corroborative MR sequences would also provide supportive evidence to the temporal diffusion results, but their application is more problematic.

Concurrent acquisition of two types of MRI data is difficult without advanced pulse sequence development, although some groups have developed experimental approaches to simultaneous acquisition of diffusion and T_2 data <Morvan, 1995>. Serial acquisition of additional MR sequences representing exercise-based muscle and blood flow changes risk such confounds as contamination by earlier exercise, exercise performed differently, or, if the scan is performed at an alternate time, differing diet and energy level. As an additional thought, the present body of work used the signal intensity of the b=0 volume (S_0) to provide additional perspective to the diffusion measures and suggestive of T_2 changes in the underlying tissue. Further work using S_0 to complement diffusion measures would benefit from explicit investigation as to how post-exercise S_0 relates to the quantitative multi-exponential measurements of T_2.

Finally, the work described in *Chapters 6* and *7* suggested that muscle composition and associated physiology played a role in the differential diffusion patterns observed between individual muscles. As the work within this thesis was dedicated to non-invasive means of muscle assessment, the interpretations regarding tissue composition were based on previous scientific studies of cadavers rather than samples from the subjects themselves. Additionally, these studies acknowledged variability in fiber content of a single muscle across individual subjects. Biopsies are the most reliable method of determining fiber content such as Type I and II fibers, yet they require an invasive tissue sample, a procedure that would be impractical to verify each muscle within the calf of volunteers. Nonetheless, biopsy data may be needed to further the hypothesis that fiber composition plays a role in the temporal diffusion changes within muscle following exercise. Perhaps a compromise in this matter could be reached, such as collaboration with kinesiological studies which are already collecting tissue samples from the muscles targeted by temporal DTI analysis.

8.3 Concluding Statement

Temporal patterns of water diffusivity differ between individual muscles following exercise, and are affected by the nature of exercise and potentially tissue composition. The presented approach for measurement of temporal diffusion shows promise in the investigation and characterization of muscle recovery dynamics following exercise.

Appendix A

Choice of TR for Temporally Optimized DTI Acquisition

Following the preliminary study described in *Chapter 4*, options were explored that would increase the temporal resolution of the DTI volumes. The easiest means of doing this were to reduce the number of diffusion directions from N=15 to N=6, and to reduce the repetition time (TR) between signal acquisitions.

A convention in the field of MRI is to set the acquisition TR to 5 x T_1 (the time needed for 67% recovery of longitudinal magnetization) in order to safely allow for full magnetic relaxation of the nuclei, which occurs at at negative exponential rate. By not allowing for full recovery, less net magnetization is available for subsequent excitation, resulting in reduced signal and signal-to-noise ratio (SNR). Previous studies have modelled the impact of SNR decreases in 3T DTI measures within skeletal muscle (e.g. <Damon, 2008; Froeling *et al.*, 2013>), and reported that low SNR can result in overestimation of FA values, as well as over-estimation of λ_1 and underestimation of λ_3. The MD, however, seems to be somewhat stable, although prone to underestimation in extremely low SNR conditions.

The T_1 within skeletal muscle at 3T has been found to be approximately 1412-1420 ms <Stanisz *et al.*, 2005; Gold *et al.*, 2004>, making 5 x T_1 equal to 7060-7100 ms. The initial study in this body of work (*Chapter 4.1*) was performed with a default value of TR=6000 ms (a TR value preceding the input of your humble author (CPR)). That said, the **purpose** of the present experiment was to determine how much TR could be reduced from 6000ms while maintaining proximal DTI and SNR.

Methods

The right calf of two human male volunteers (exams 162 and 167) was imaged using 6-dir DTI (b=0/400 s/mm^2) at TR values varying from 2000-10000 ms in increments of 1000 ms. Echo time (TE) remained constaint across b-values. The scans were acquired in randomized order. MRI parameters were otherwise equivalent to those described in *Chapter 6*.

DTI measures (MD and FA) for volumes representing each TR value were then were calculated using FSL. A large muscle ROI was drawn across two slices per subject, consisting of voxels belonging to LG, MG, and central-medial SOL that avoided blood vessels, aponeuroses, and chemical shift artifacts (see **Figure A.1**). A second large ROI was drawn for background (avoiding ghosting artifact).

These ROIs were applied to every TR condition to produce measures of MD, FA, and SNR. SNR for the b=0 volume of each TR value was calculated according to the equation:

$$SNR = \frac{Signal(Mean)}{Background(SD)} \tag{A.1}$$

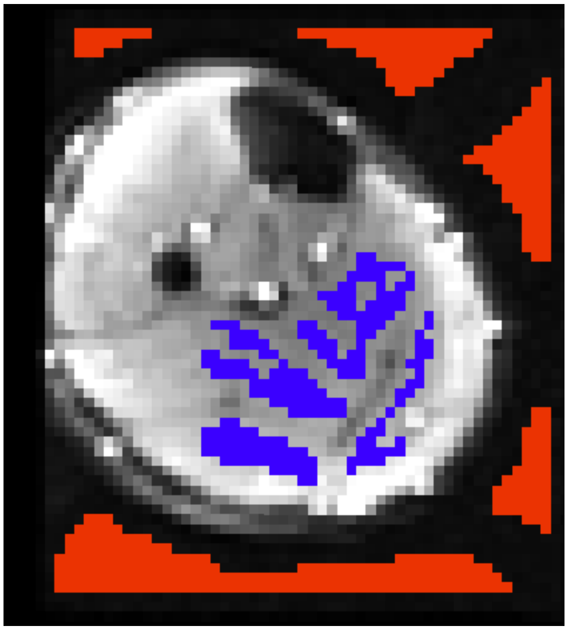

Figure A.1: Regions of interest (ROIs) used for this analysis of repetition time (TR). Blue ROI represents approximate location and size of muscle ROI, while red ROI represents that of Background signal.

Results (see Figure A.2)

MD appeared to initially increase with increasing TR, levelling off at TR=4000 and reaching an approximate asymptote at TR=6000. Less variation in measure was demonstrated for TR=5000 and greater. FA values decreased with increasing TR, although levelled off somewhat at TR=4000. The FA of TR=4000 was proximal to that of TR=6000. The FA showed a slight increase at TR=5000, but subsequently decreased at a slight rate until TR=9000. The SNR increased with increasing TR, although appeared to reach an asymptote at TR=6000.

Conclusion

Based on these results, it appeared that reducing the TR below 4000 ms would cause distortion in the measures of MD and FA. Furthermore, TR=4000 produced

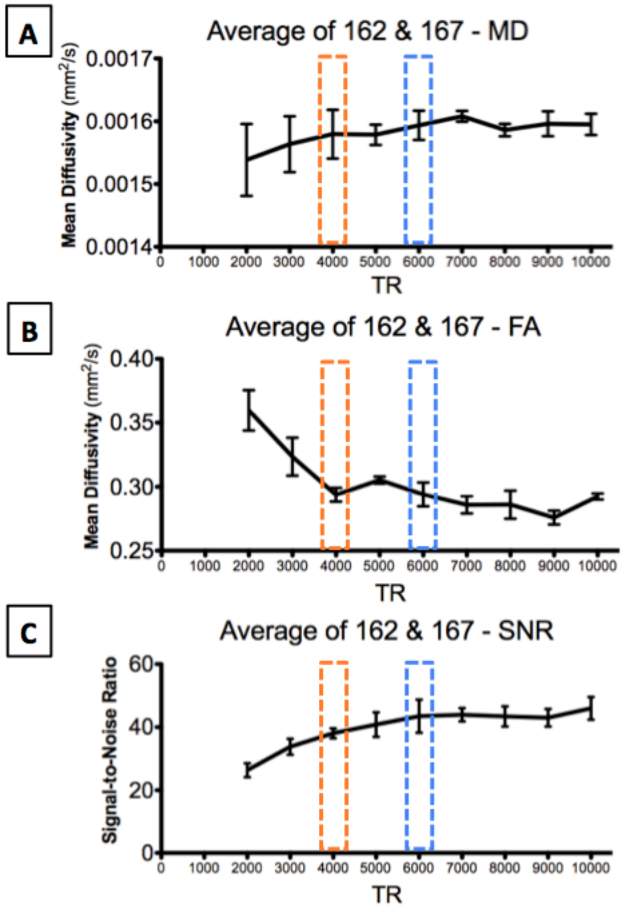

Figure A.2: DTI measures according to repetition time (TR). Blue rectangle depicts default TR used in preliminary study (TR=6000ms), orange rectangle depicts minimal TR needed to approximate default TR values (TR=4000ms). **(A)** Mean diffusivity (MD). **(B)** Fractional anisotropy (FA). **(C)** Signal-to-noise ratio (SNR).

DTI measures proximal to TR=6000, as was used in the preliminary study. The FA results were a particular factor in deciding upon TR, as this value indicated the relationship between the individual eigenvalues. Therefore, a TR of 4000 ms was utilized for subsequent temporal DTI studies of skeletal muscle in order to increase the temporal resolution, meaning that acquisition of a 6-direction 16-slice DTI volume could reduced from 48 to 32 seconds.

Appendix B

Methodological Development of Sliding-Window DTI

This appendix provides more detail regarding the generation and construction of diffusion gradient tables to be used in the multiple-timescale approach to diffusion acquisition proposed in *Chapter 7*. All vector distributions were calculated and represented in three dimensions using custom scripts within Matlab (v7.9; Mathworks, Natick MA).

B.1 Gradient Table Creation

The main problems in creating the intended gradient table were how best to distribute the five orthogonal 3-dir sets throughout three-dimensional space, while avoiding vector collinearity, and arranging the temporal acquisition of triplet sets to provide continuity using the sliding window approach, as well as to allow for DTI calculation using potential sub-units of 6 to <15 gradient directions (see **Figure B.1**).

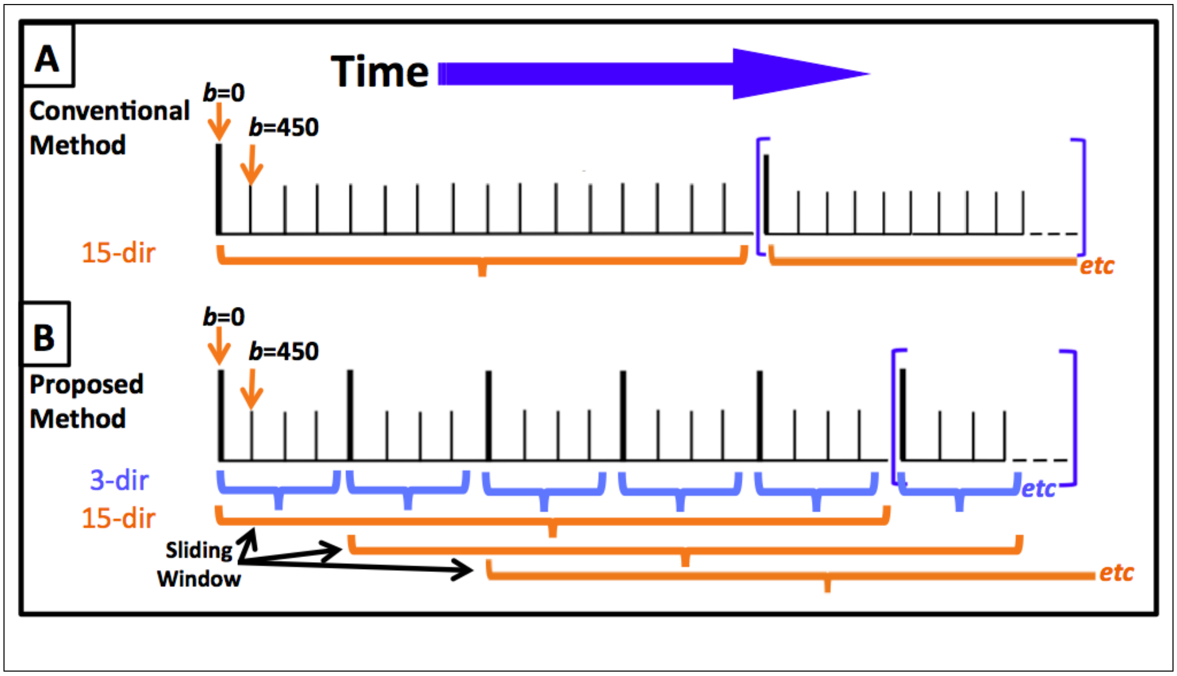

Figure B.1: Comparison of DTI acquisition strategies. **(A)** Conventional method, consisting of an initial b=0 volume, followed by N=15 DW volumes, the directions of which are dispersed throughout a sphere. **(B)** Proposed sliding window method. An additional b=0 image is acquired prior to every 3-DW-image ”triplet”. The gradient-encoded diffusion directions within a triplet are orthogonal to one another, but the 5 triplets have different orientations within space. The grouping of the acquisition into 3- and 15-dir sub-units during post-processing is shown, as well as how the ”sliding window” incorporates progressing groups of triplets for temporal measures of N=15 DTI.

Several strategies were considered regarding how to produce the 15-direction table while abiding by the constraints. An early strategy was to force dispersion of five vectors throughout a sphere using an electrostatic-repulsion algorithm (’ParticleSampleSphere’ by A. Semechko; Matlab v7.9; Mathworks, Natick MA). Each of these vectors could represent either (i) one of the vectors within the orthogonal 3-direction set; or (ii) the mean vector of the 3 orthogonal directions. This idea was soon abandoned, as a minimum of 9 directions was needed to operate this algorithm, while the present study sought to disperse 5 vectors. Furthermore, this route to generating the five central dispersed directions would likely have produced additional problems, such as how best to orient the remaining 2 (or 3) vectors around each of the 5 main dispersed vectors.

Gradient table creation using triplets of orthogonal vectors

The second strategy was to start with one 3-direction (triplet) set of orthogonal vectors, aligned with the main X ([1, 0, 0]), Y ([0, 1, 0]), and Z ([0, 0, 1]) axes, and progressively reorient this triplet by angle *theta* to four additional positions throughout the sphere by rotation and tilting. A hypothetical fifth position in these calculations was intended to be equivalent or collinear to the initial 3-direction vector set, allowing for cyclical triplet combination for ongoing generation of DTI using a 'sliding window'. This strategy would also ideally allow equivalent spatial distribution between triplets to ensure that there would be no bias in positions of 15-direction groupings, as well as groupings of <15-directions. A variety of *theta* angles and methods of vector reorientation were explored to generate the additional positions of the orthogonal triplet sets, including:

– fractions of 90°, 180° and 360° with a denominator of 5

– addition of 1° to the "/5" fractions described above to account for curvature

– iterative *theta* increase (*theta* x *PositionNumber*) rather than iterative rotation of a single *theta*

– the lower component of the Golden Ratio for a circle (111.25°) as well as division of this value by 2 and 4

– adding a 180° flip to each of the rotation iterations for values of *theta* described above

Three-dimensional representations of each vector distribution produced by these calculations, as well as their cardinal planes (X-Z, Y-Z, X-Y), were then visualized using Matlab (v7.9; Mathworks, Natick MA). Using the vector depictions of the default 15-direction gradient table (Jones15) as an example of functional dispersion, each vector distribution was visually inspected to eliminate distribution strategies that appeared to under-represent a sphere or contained vectors that appeared too closely aligned (see **Figure B.2**).

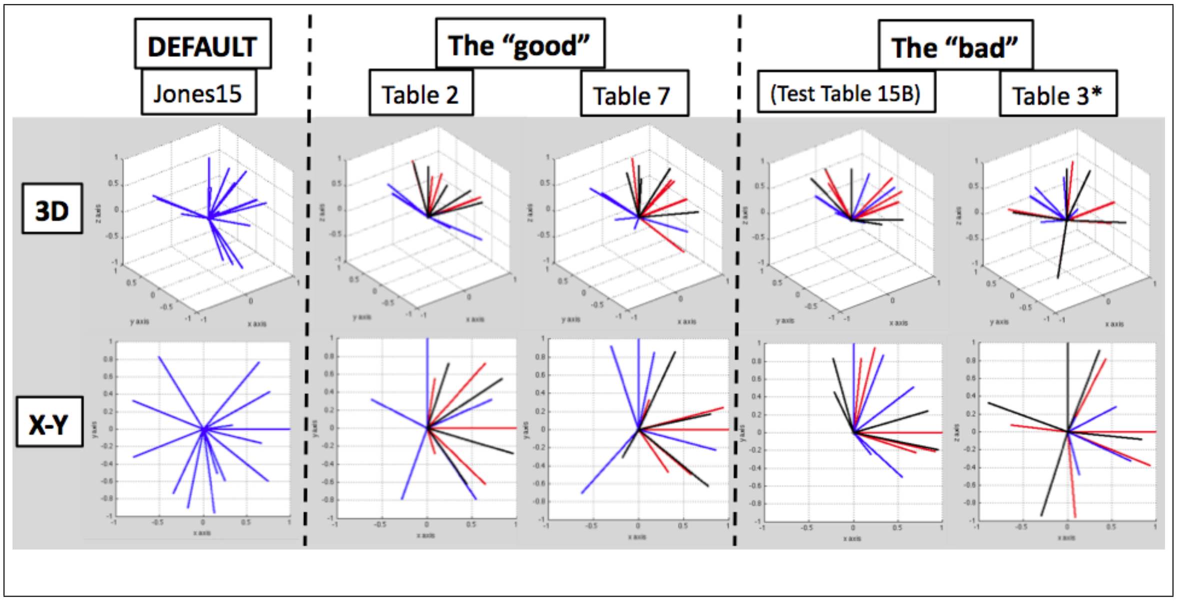

Figure B.2: Dispersion of gradient table vectors from three-dimensional (3D) and X-Y perspectives. "Jones15" represents the vectors for the default N=15 gradient table of our local MRI scanner (GE 3T 750). Tables '2' and '7' ("The good") are examples of vector arrangements showing dispersion comparable "Jones15" based on visual inspection in three dimensions. Tables depicted as "The bad" displayed vector arrangements that appeared to underrepresent the sphere. Table '3*' was selected for future testing to investigate how a "bad" table would perform in temporal diffusion calculations.

Based on this visual analysis, seven potential gradient tables were identified as candidates for the next stage of testing (**Table B.1**).

Table#	Theta(°)	Calculation Details
1	72	4/5 of 90°
2	73	4/5 of 90° + 1 (curvature)
3*	73	4/5 of 90° + 1 with iterative 180° flip
4	73	4/5 of 90° + 1, increment *theta*
5	54	3/5 of 90°, increment *theta*
6	111.25	Golden Ratio, increment *theta*
7	55.125	Golden Ratio/2, increment *theta*

Table B.1: Summary of final candidate gradient table dispersion strategies for dispersion of orthogonal 3-direction triplets. ”*” indicates a table that performed poorly in visible inspection, but intentionally selected for further testing to assess validity of the visual test.

Non-orthogonal gradient table creation

Two additional 15-dir gradient tables were generated for temporal comparison with the previous orthogonally-based gradient tables, with a particular focus on the stability of measures generated from N<15 subunits, such as 3-, 6-. or 9-directions. These two tables were attempted in *Exam 4156* and tested more thoroughly in *Exam 4483* (described below).

The first of these non-orthogonal tables (test name: ”Jones15SD”) is the default N=15 table found on the local MRI scanner (GE 3T Discovery MR750, General Electric Healthcare, Milwaukee, WI). However, the ordering of gradient directions was reorganized so as to allow consistent angulation between individual vectors. This was achieved by calculating 100,000 combinations of the vector ordering (from a possible ~$1.31\text{x}10^{12}$ permutations). Each combination was assessed by calculating the angle between adjacent vectors, including the angulation between Vector#15 and Vector#1 to account for the ”wrap-around” desired by the ongoing temporal DTI strategy using a 'sliding window'. The standard deviation (SD) of these inter-vector angulations was calculated for each ordering of gradients, with the permutation providing the lowest SD (now dubbed "JonesSD") selected for further investigation.

The second non-orthogonal table (test name: "multRANDSD") was generated with a custom Matlab script that produced 1000 random permutations of an electrostatically repulsed 15-vector distribution throughout a sphere (using ParticleSampleSphere by A. Semechko; Matlab v7.9; Mathworks, Natick MA). For each of these vector distributions, 100,000 combinations were assessed to determine the ordering that provided the least SD. These orderings of least SD were then compared between the 1000 random distributions, with the overall minimum SD to determine the "best" table generated by this method. However, the distribution generating the actual minimum SD was found to contain collinear vectors, therefore the second-to-minimum SD distribution was selected for further investigation, and thus dubbed "multRANDSD".

B.2 Testing of Prospective Gradient Tables

The following is a chronological summary of experimentation that identified the best-performing DTI gradient table ("02_s7") and shaped the methodology used in subsequent *in vivo* studies (see *Chapter 7*).

All described tests were performed using a GE 3T Discovery MR750 (General Electric Healthcare, Milwaukee, WI). DTI data was acquired according to each tested gradient table using a dual echo spin echo EPI sequence (b=0 and 450 s/mm^2, TR/TE=4000/69.6ms, 16 slices 4mm thick, 16cm FOV, 64x64, ASSET = 2). All post-processing of DTI data utilized tools within FSL <Jenkinson *et al.*, 2012> unless otherwise noted.

B.2.1 Exam 4156 - Initial test of acquisition

This experiment was the first attempt to collect and analyze DTI data using the seven orthogonally-based gradient tables generated in *Appendix B.1* (see **Table B.1**). DTI measures of Mean Diffusivity (MD) and Fractional Anisotropy within isotropic media were compared amongst generated candidate tables, and between candidates and values produced by the default N=15 and N=6 tables found on the local MRI scanner. This test was performed to assess whether candidate vector tables produced DTI values proximal to those of the default table.

Each of the candidate 15-direction gradient tables were prepared by inserting a b=0 s/mm^2 volume after every three diffusion-weighted acquisitions. While this brought the total number of volumes acquired per table to 19, these tables are referred to as N=15.

A phantom (consisting of a gel block, bottle of tap water, and semi-thawed ice pack) was used to acquire DTI data (see **Figure B.3**). (Unfortunately, temperature was not monitored during this experiment, as the primary concern was creating a phantom that filled the space within the RF coil).

Three repeated N=15 scans were initially acquired for each candidate table to test for consistency of measure, although the repetitions were eventually reduced to two and then one DTI volume as scanning commenced due the practicality of MRI scheduling. DTI measures of MD and FA were calculated for each volume, and signal intensity measures (S_0) of the initial and interspersed b=0 volumes were acquired. Values of MD and FA were calculated with and without eddy-current correction (EC/noEC; a common step in tensor calculation; calculated with FSL) to determine the impact of this procedure on temporal stability of DTI measures.

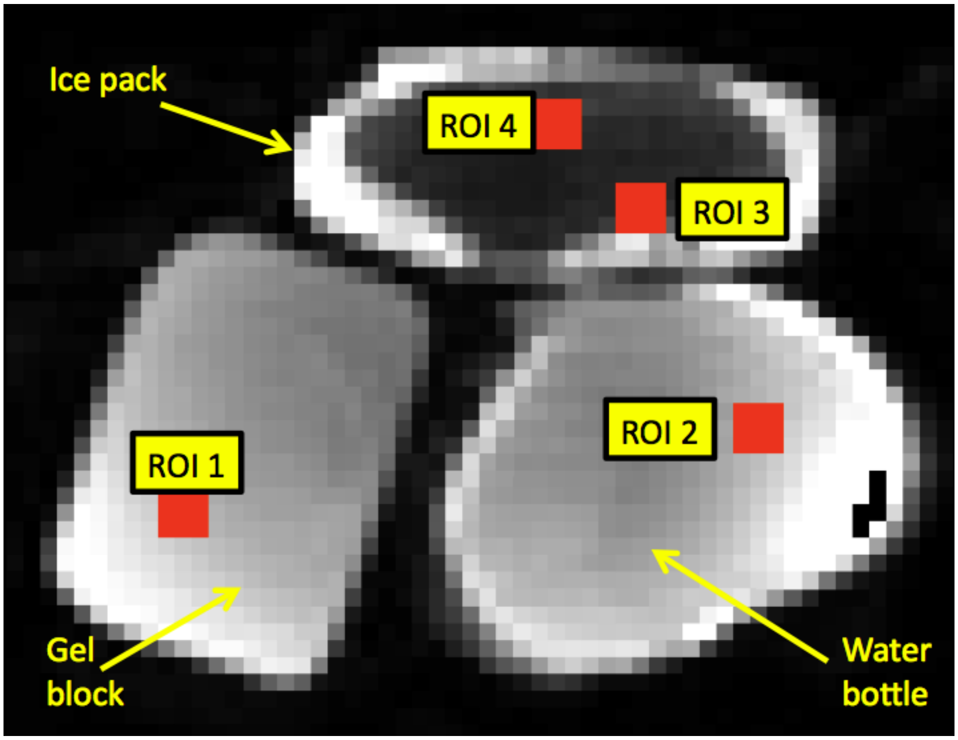

Figure B.3: Zero-diffusion (b=0) image of phantom composed of various isotropic media. Four regions-of-interest were used for DTI measurement (red squares).

Each N=15 acquisition was then sub-divided into three sets of N=9 consecutive diffusion directions to calculate the consistency of <15 subunits across time. The assumption of this test was that measures of a static medium should produce stable measures across time, and that erratic measures would indicate less than adequate vector combinations to represent ongoing in vivo diffusion changes.

Four regions-of-interest (ROIs) were drawn to assess the diffusion in the various phantom media (see **Figure B.3**).

Exam 4156 RESULTS and CONCLUSIONS

It became quickly apparent that having the semi-thawed icepack as part of the

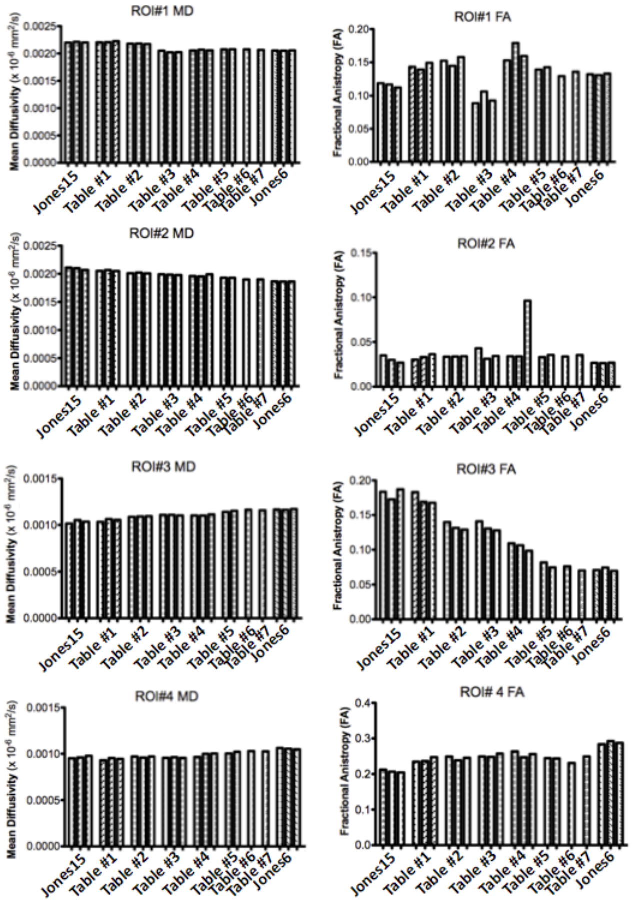

Figure B.4: Graph showing the MD and FA collected for each DTI volume. Represented are the default N=15 (Jones15) and N=6 (Jones6) gradient tables found on the local GE MRI, as well as the seven candidate gradient tables (#1-#7).

phantom was an unwise decision, as the changing temperature had a noticeable effect on the diffusion results (see **Figure B.4**). Notably, the MD of ROI#2 (water bottle) steadily declined across repeated scans of the phantom, while ROIs#3 and #4 (thawing ice pack) showed a slight increase with consecutive scanning. This made it difficult to compare the MD produced by the seven candidate tables with that collected by the default gradient table. However, as this pattern of MD differences with consecutive scans is somewhat linear, it should be noted that no table produces values that drastically deviate from these progressions of diffusion increase or decrease, indicating the likelihood of the candidate tables producing MD values proximal to default.

The FA values calculated for ROI#1 showed Table#3 produced measures lower than both default and candidate tables, although the FA from Table#3 was closer to that of N=15 than that produced by other tables. ROI#2 showed a spike in FA value for Table#4. ROI#3 shows a notable decrease in FA across acquisitions, while ROI#4 shows a slight increase, although neither of these has the same linearity across consecutive acquisitions as that observed in MD. It was interesting to observe that the FA decline of ROI#3 appeared to level out during the acquisition of Table#5, perhaps indicating that the icepack had thawed.

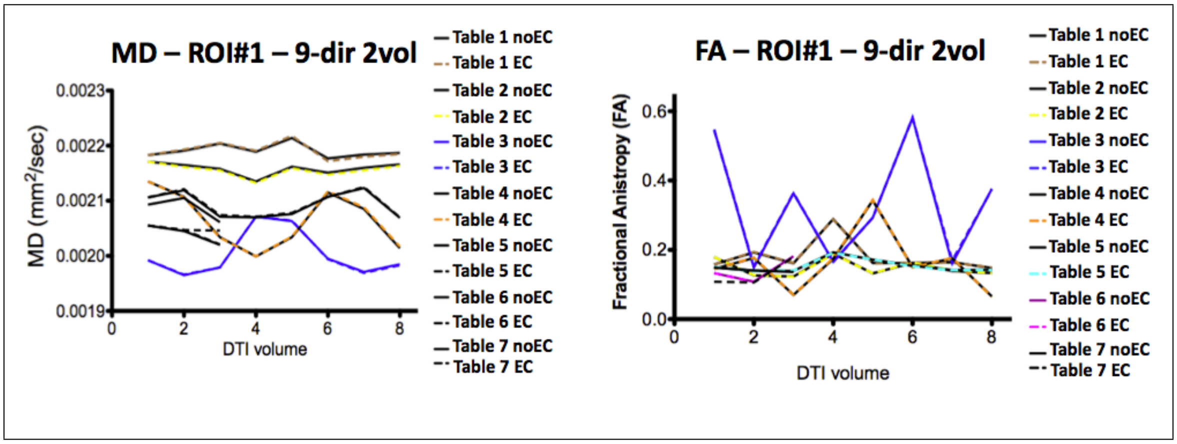

Figure B.5: MD and FA results for each of the seven candidate gradient tables using ROI#1 based on 9-direction subunits and sliding window analysis. Comparisons were made between raw (noEC) and eddy-corrected (EC) DTI calculations.

Upon division of the DTI data generated by each gradient table into 9-direction subunits, and review of each of the four ROIs, Table #'s 2, 5, and 7 seemed to have the most stable measures across time (**Figure B.5**), and were selected for further experimentation. Table#3 (intentionally selected to test the diffusion measures of a table identified as having poor vector dispersion (**Table B.1**) demonstrated wide fluctuations in both MD and FA measures across time.

Furthermore, the temporal stability of the measures did not seem to improve or even change with the use of eddy-correction.

B.2.2 Exam 4440 - Discovery of 'spinescan' issue

The intent of this experiment was to test the three top-performing candidate tables identified in *Exam 4156* (Table #'s 2, 5, 7) using a phantom with anisotropic media (asparagus and celery)and more careful control of temperature. These candidate tables were to be compared with non-orthogonal gradient tables ("JonesSD" and "multRANDSD") regarding the stability of measure across time. Additionally, a custom scanner-based script ('*spinescan*' by L. Ryner) was to be used to automatically trigger repeated acquisitions of each gradient table to provide temporal consistency.

Exam 4440 RESULTS and CONCLUSIONS

Upon analyzing the data, a curious artifact appeared in the b=0 volumes of DTI volumes triggered by 'spinescan'. Specifically, this artifact consisted of alternating high and low signal slices that in turn affected the DTI calculations (see **Figure B.6**). This artifact needed to be resolved before *in vivo* studies of skeletal muscle could commence. On a more positive note, this experiment observed that asparagus was a much better model of anisotropic media than celery, which actually appeared to be quite isotropic (see **Figure B.7**).

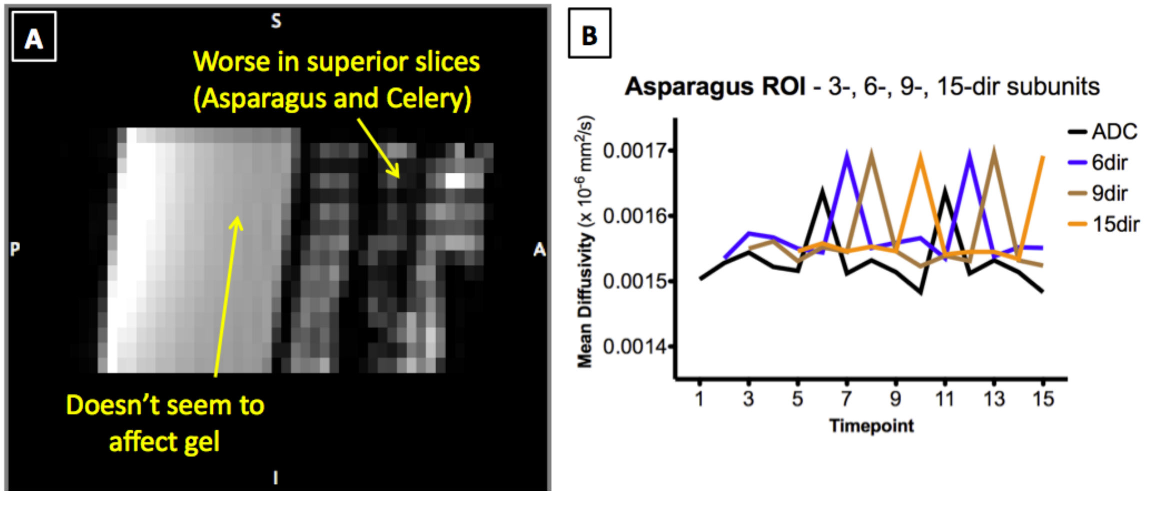

Figure B.6: Artifact resulting from 'spinescan'-triggered image acquisition. **(A)** Sagittal view of b=0 volume displaying inconsistent signal across slices. **(B)** Sliding window diffusion calculations from asparagus ROI for all subunits. Peaks in temporal diffusion measurements indicate the timepoints affected by the signal artifacts in 'spinescan'-triggered b=0 volumes.

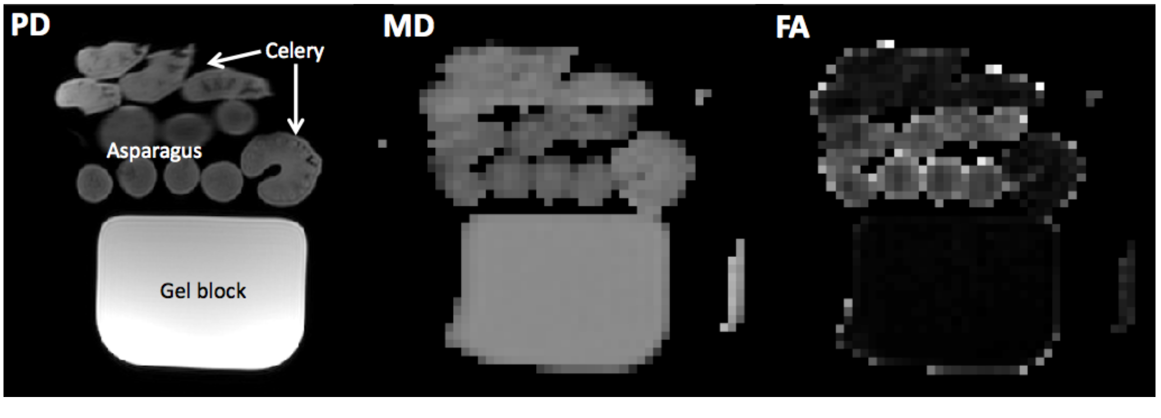

Figure B.7: Phantom comprised of gel block, asparagus and celery. The bright signal on the FA image indicates that the asparagus is anisotropic, while the celery displays isotropy akin to the gel block. PD: Proton Density-weighted image; MD: Mean Diffusivity; FA: Fractional Anisotropy.

B.2.3 Exam 4461 - Investigation into 'spinescan' issue

This experiment was conducted to determine the cause of the 'spinescan'-related artifacts observed in *Exam 4440*. Specifically, we investigated whether this artifact was a result of using too short of a "dead time" before the script triggered the next scan, and also whether the artifact was due to using too short of a repetition time (TR). As the artifact was not preferential to gradient table (see *Exam 4440*), a single gradient table was used in this experiment (Gradient Table #5, see **Table B.1**).

DTI data was collected using the 'spinescan' trigger with dead times of 2, 3, and 7 seconds for each of TR=4000, 6000, and 8000 ms. Three repetitions of each gradient table were acquired. Control DTI scans were acquired using the default trigger method for comparison of MD and FA values. An additional series was run with the intended parameters (dead time = 2 seconds, TR=4000ms), but with a second b=0s/mm^2 acquired prior to the diffusion-weighted volumes. This second b=0 volume was collected to determine whether it was affected by the artifact as well.

Exam 4461 RESULTS and CONCLUSIONS

The artifact persisted regardless of dead time and TR value. However, the series containing two b=0 volumes revealed that the second volume was intact, indicating that the artifact affected only the first volume acquired, and did not impact all b=0 volumes. Measures of MD and FA calculated using the second b=0 volume were consistent with those collected with the scans not initiated with 'spinescan'.

Ultimately, the source of this problem could not be determined, despite interviews with multiple local physicists, technologists, and field engineers. The 'spinescan' script has been available for many years as a "legacy" hack of the system, but no concrete answers were obtained as to how it functioned, nor the impact of the omitted prescan in auto-triggered acquisitions.

The results of this experiment, particularly the affirmation of integrity of the second b=0 volume, allowed for a restructuring of the strategy for acquisition ongoing DTI volumes for temporal measures.

Looping of the Gradient Table

The solution to this issue was implemented in two steps. First, rather than repeat the 15-dir gradient table using spinescan, three repetitions of the 15-dir table were embedded into the N=59 entry of the table to be used by the MR scanner, allowing for ongoing acquisition of the gradient table for a duration of 4 min 8 sec.

The logic behind 'Step 1': The default gradient table used on the local GE scanner (EPIC v.24 circa 2015) has entries for numbers of diffusion gradients ranging from N=6 to N=75. The 'TST7' 15-direction gradient table, when considering the intermittent b=0 volumes every 3 diffusion-weighted directions, totals 19 vector directions. Each set of 19 directions would then need to be preceded by an additional b=0 volume, meaning that the total of vector directions was now 20. Since one initial b=0 volume is automatically acquired prior to any diffusion acquisition, the maximum repetitions was 3, with a value of N=59. (Made up by [auto b=0] + [19 dir] + [20 dir] + [20 dir]). A shorter version consisting of two gradient table cycles was inserted at N=39 ([auto b=0] + [19 dir] + [20 dir]) for the purposes of acquiring pre-exercise baseline data.

The second step would use 'spinescan' to trigger a second round of three 15-dir gradient acquisitions, allowing for 8 min 13 sec of temporal diffusion data to be acquired, as well as allowing for further 4 minute increments if needed. This was deemed necessary, as previous studies of post-exercise diffusion changes have observed the potential to last at least as long as this timespan (<Morvan, 1995; Nygren and Kaijser, 2002>; *Chapter 6*).

In cases where use of 'spinescan' would be required for extending the duration of temporal diffusion acquisition, an accommodating gradient table entry at N=60 was created. The N=60 entry was identical to that of N=59, with the exception of an additional b=0 s/mm^2 volume placed in the initial position. Upon post-processing, the b=0 volume automatically placed by the scanner (auto-triggered by 'spinescan') would be treated as a 'dummy' and dropped from analysis, at the expense of 4 seconds (TR=4000 ms). The inserted b=0 volume would then be used for ongoing analysis of 3-dir ADC at that timepoint, or the overlapping DTI measures. Additional triggers and N=60 tables could be applied if deemed necessary for further time coverage.

B.2.4 Exam 4483 - Final sliding-window strategy test

The purpose of this experiment was to select the gradient table that provided the best temporal stability in measure from the pool of tables generated during this study (orthogonally-based Table #'s 2, 5, and 7; non-orthogonal "Jones15SD" and "multRANDSD") (**Figure B.8**).

The optimal table was that which demonstrated consistent measures of diffusivity in both isotropic and anisotropic media using the sliding window analysis, as well as demonstrating consistency in diffusion measures using <15-direction subunits (3-, 6-, and 9-directions). The measures of anisotropic media were of particular interest, as it is here that vector underrepresentation by <15-dir subunits would become most

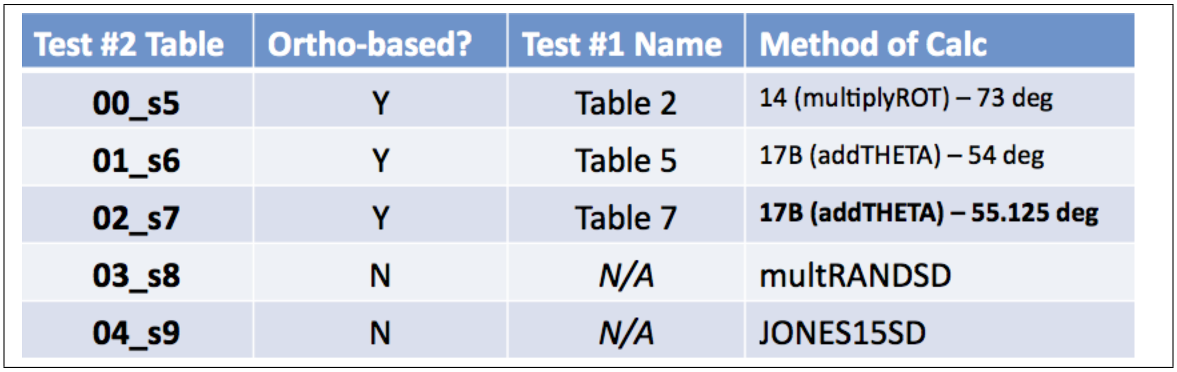

Test #2 Table	Ortho-based?	Test #1 Name	Method of Calc
00_s5	Y	Table 2	14 (multiplyROT) – 73 deg
01_s6	Y	Table 5	17B (addTHETA) – 54 deg
02_s7	Y	Table 7	17B (addTHETA) – 55.125 deg
03_s8	N	*N/A*	multRANDSD
04_s9	N	*N/A*	JONES15SD

Figure B.8: Details and nomenclature of gradient tables tested in *Exam 4483* (Test#2). Note that the table naming convention has changed from Test#1 (*Exam 4156*).

obvious and generate erratic temporal measures.

Each gradient table was prepared with b=0 volumes inserted every three diffusion-weighted (DW) volumes, as described previously (see **Figure B.1b**). Three repetitions of each 19-volume set (the latter two repeats preceded by an additional b=0 volume) were then incorporated into an N=59 table, as described in the ”Looping Strategy” section within *Exam 4461*.

A phantom consisting of gel and asparagus, representing isotropic and anisotropic media, was used for all tests (see **Figure B.9**). The phantom was placed in the MR scanner room for two hours prior to scan in order to stabilize the temperature of the different media to the cooler MR environment.

DTI data was collected for each of the five gradient tables using the N=59 gradient table entry. Following acquisition, the output data was compiled into 4-dimensional (4D) volumes which were in turn eddy-corrected, then registered to a space common to all acquisitions using sinc interpolation, both steps using tools within FSL. (While the common-space registration was likely unnecessary for a static phantom, it was anticipated that this step may be required for eventual *in vivo* subjects.)

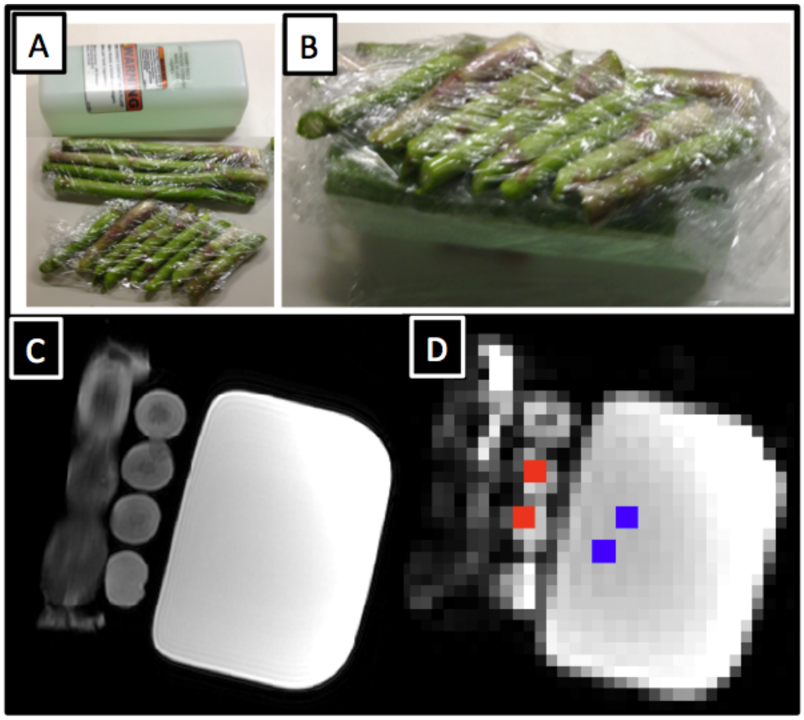

Figure B.9: Gel/asparagus phantom representing isotropic and anisotropic media. **(A)** Phantom components: gel block, asparagus aligned with magnetic field, asparagus oblique to magnetic field. **(B)** Completed phantom. **(C)** Proton Density-weighted image of the phantom, axial view. **(D)** Zero-diffusion (b=0) image of phantom displaying ROIs for asparagus (red squares) and gel (blue squares).

Each 4D volume was then parsed into sub-units of 3, 6, 9, and 15 consecutive DW volumes commencing from each b=0 volume (see **Figure B.1b**). Apparent Diffusion Coefficients (ADCs) were calculated for each 3-dir subunit using custom scripts within Matlab, while diffusion tensors were calculated for subunits of 6-, 9-, and 15-directions using FSL, producing maps of MD and FA for each subunit length across time. Temporal alignment of diffusion measures between subunits of different length was based on the last diffusion-weighted image contributing to the volume or subunit (see **Figure 7.5**). The signal intensity (S_0) of each b=0 volume was also measured to give insight into the stability of this value across time.

Regions-of-interest (ROIs) were drawn on both gel (isotropic media) and asparagus (anisotropic media), and consisted of two 2x2-voxel squares on each of five slices (see **Figure B.9**).

Exam 4483 RESULTS

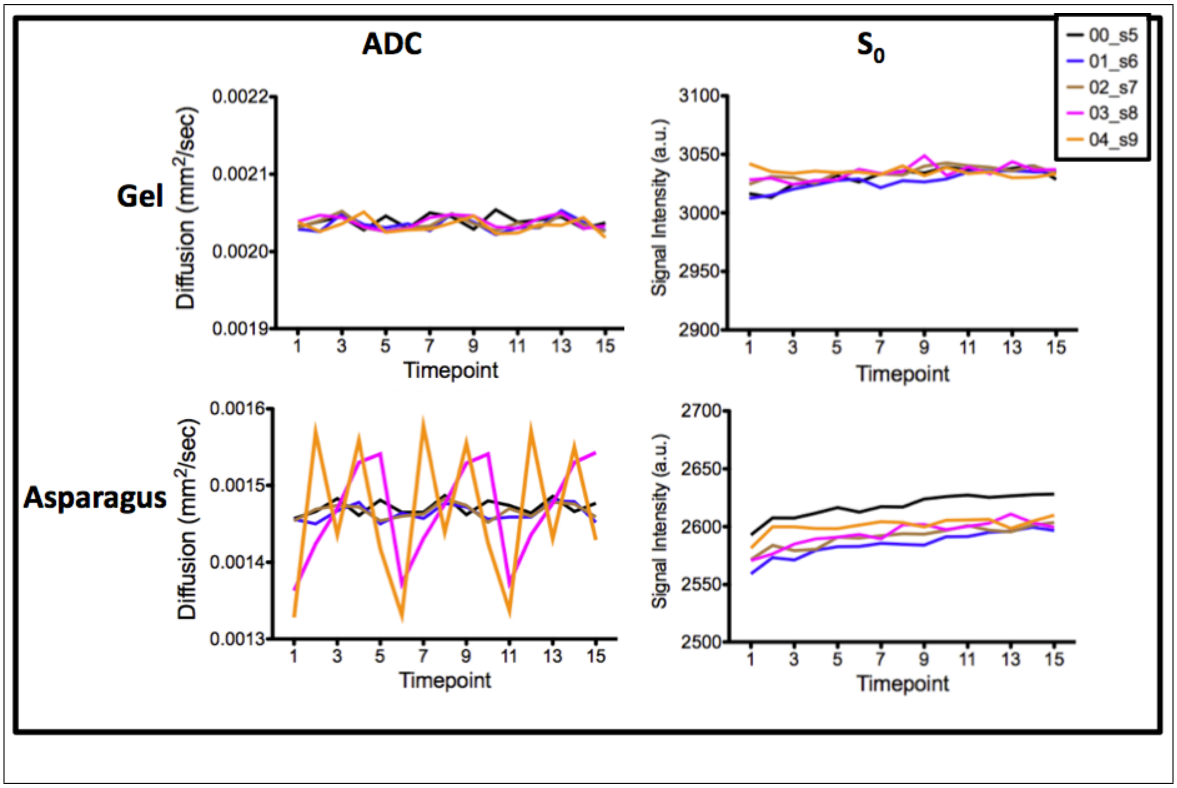

Figure B.10: Measures of 3-direction apparent diffusion coefficient (ADC) and b=0 signal intensity (S_0) for each candidate table for gel (isotropic) and asparagus (anisotropic) across time. Each timepoint represents 1 b=0 and 3 diffusion-weighted volumes (16 seconds).

ADC (3-dir): Within the isotropic media, all gradient tables demonstrated similar ADC values, as well as little variation in measure across time (see **Figure B.10**). Within the anisotropic media, the three orthogonally-derived tables (00_s5, 01_s6, 02_s7) appear relatively stable across time, with minimal range in fluctuation. However, the two non-orthogonal tables (03_s8, 04_s9) demonstrated a wide range of value and rapid fluctuation across timepoints.

Signal intensity of b=0 image (S_0): Within the gel, the S_0 appeared level across time, whereas the $S_0$0 of asparagus appeared to show a slight drift of increasing signal across timepoints for all collected series (see **Figure B.10**). All acquisitions appeared to ”reset” to lower signal, but signal value did not appear to be strongly linked to ordering of acquisition.

DTI: Mean Diffusivity (MD): Within the gel, the mean MD generated by each gradient table seems to be equivalent to the values found for 3-dir ADC across all subunit lengths. However, the 6-dir subunits show more variation in measure in comparison to their 9- and 15-dir counterparts (see **Figure B.11**).

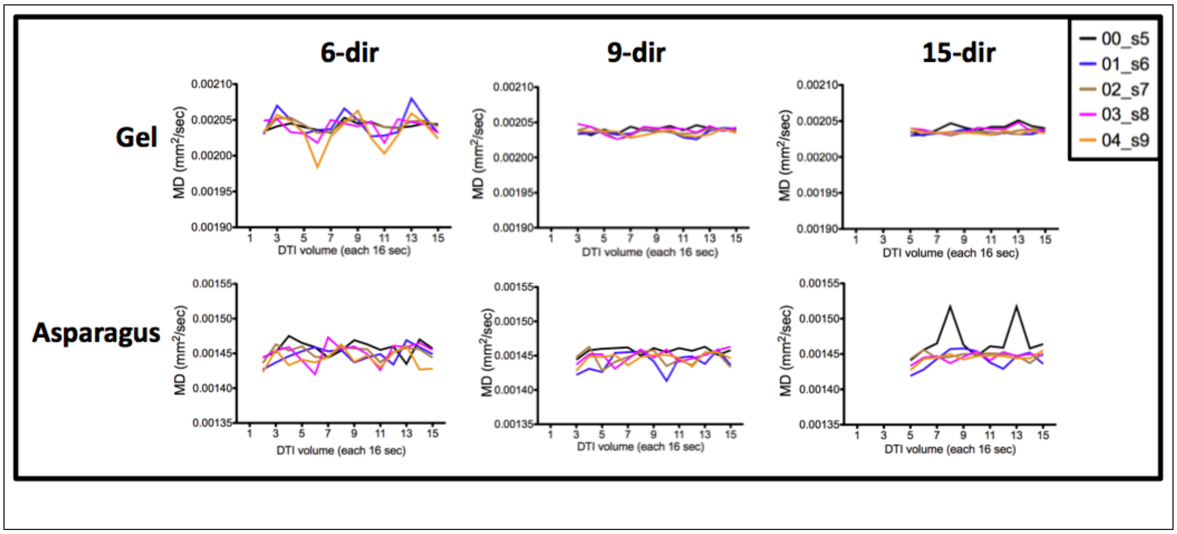

Figure B.11: Temporal measures of mean diffusivity (MD) for each of the candidate gradient tables within gel and asparagus using sliding window subunits of 6-, 9-, and 15-directions. Each timepoint represents 1 b=0 and 3 diffusion-weighted volumes (16 seconds).

At the 6-dir subunit length, gradient tables 01_s6 and 04_s9 show more notable extremes in range than the other three tables, while at the 15-dir length, table 00_s5 seems to show a repetitive elevation in MD that is not observed in other measures, aside from table 03_s8 at timepoints 12 and 13. Within the asparagus at 6-dir, all gradient tables seem to demonstrate variability in measures of asparagus across time, with table 03_s8 displaying notable rapid changes. The 9-dir and 15-dir measures of table 01_s6 show notable fluctuation relative to other gradient tables. The 15-dir measure of 00_s5 shows repetitive peaks that were not predicted based on analysis of smaller subunits for this table.

DTI: Mean Diffusivity (FA): As it has been demonstrated that MD can remain stable despite changes between eigenvalues <Damon, 2008; Froeling *et al.*, 2013>, three gradient tables were selected for further study using fractional anisotropy (FA) to measure the consistency of diffusion tensor shape at each subunit length across time. Tables investigated were 02_s7, as it demonstrated the most consistent temporal values of ADC and MD; 01_s6, as it was a less successful representative of orthogonal gradient table generation; and 03_s8, as it represented a table of non-orthogonal gradient dispersion for the following temporal comparisons of subunit length.

For the 6-direction subunits, both orthogonally-based gradient tables (01_s6 and 02_s7) produced FA values >1 across multiple timepoints, indicative of an error, as the maximum FA value should be 1 (see **Figure B.12**). In contrast, table 03_s8 (non-orthogonal) produced measures proximal to zero for the isotropic gel, and measures for asparagus that demonstrated increased anisotropy. These measures appeared stable across time relative to the orthogonally-based tables. However, a repeating pattern of increase was observed in both media at timepoints 2, 7, and 12, corresponding to the first 6-dir subunit within this 15-dir table.

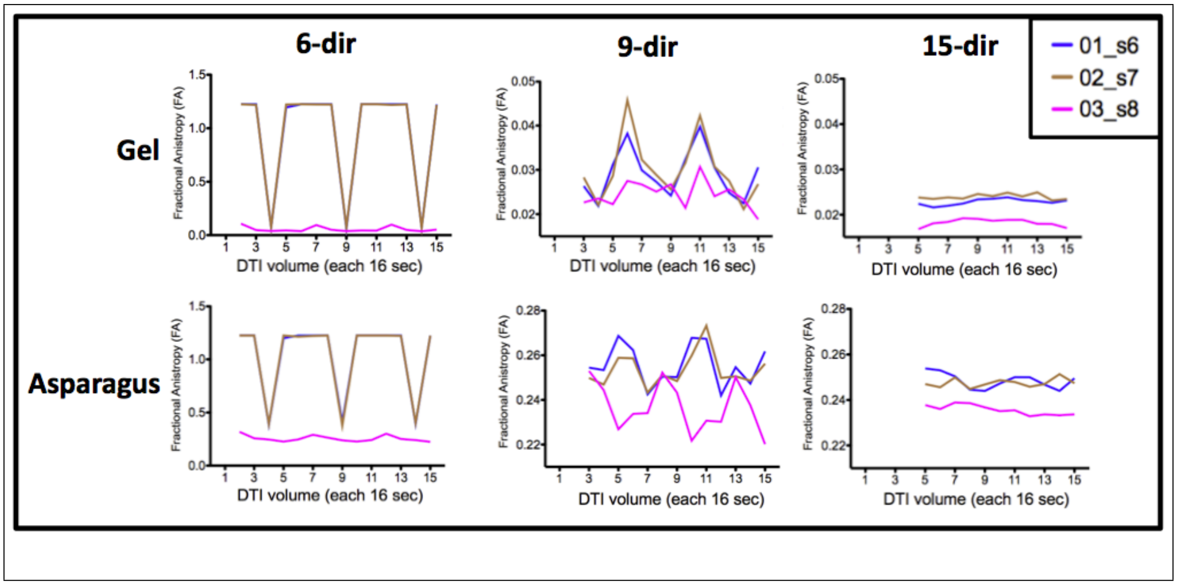

Figure B.12: Temporal measures of fractional anisotropy (FA) for 01_s6 and 02_s7 (orthogonally-based) and 03_s8 (non-orthogonal) within gel and asparagus using sliding window subunits of 6-, 9-, and 15-directions. Each timepoint represents 1 b=0 and 3 diffusion-weighted volumes (16 seconds).

For the 9-direction subunits, both of the orthogonally-based tables produced a repetitive pattern of peaks for both isotropic and anisotropic media (see **Figure B.12**). The measured FA would increase by 0.015-0.023 across two timepoints, then similarly decrease across time points. Peaks occurred for both orthogonally-based tables at timepoints 6 and 11, corresponding with the fourth 9-dir position of the gradient table. The 03_s8 table, for the isotropic media, displayed a stable though noisy level of FA across timepoints. However, in the anisotropic media, this table produced troughs at the same timepoints (6 and 11) that the orthogonally-based tables produced peaks.

For the 15-direction subunits, the FA within the isotropic media displays relatively level values across timepoints, with 03_s8 displaying a slightly lower level than those of the orthogonally-based tables. The same observations apply to the anisotropic media, although more variation is observed across time. The 03_08 table appears to have the most temporal stability, while the orthogonally-based tables display wave-like variation, with 02_s7 showing a shorter period with less magnitude range than 01_s6.

Exam 4483 CONCLUSIONS

The results of this experiment indicated two issues to consider in selecting the best gradient table from the pool of candidates. These tests revealed that orthogonally-derived tables produced more consistent 3-dir ADC results than those tables created through electrostatic repulsion. This was not unexpected, since diffusion measurement using only three non-orthogonal vectors have a large potiential for directional bias within anisotropic media. Of the orthogonally-based tables, 02_s7 demonstrated the most consistent measure of diffusion across time, and across subunits of different length.

However, the orthogonally-based tables demonstrated poor temporal FA stability relative to the multRANDSD (03_s8) table, especially for subunits of 6- and 9-dir. The repetitive patterns of major change suggest flaws in the ability of a gradient table subunit to produce reasonable measures of the investigated media. Although FA is not planned to be a primary measure used in future work, this measure is indicative of the relationship between the calculated eigenvalues, which are indeed planned for use in future investigation. After some deliberation, it was decided that the temporal resolution of the 3-dir ADC was more important than the tenuous ability of these tables to produce DTI results using <15-dir subunits. Therefore, table **02_s7** (see **Appendix B.3**) was selected for use in the next stage of this experiment (*in vivo* tests of post-exercise human muscle), but analysis of 6- and 9-dir subunits would be eliminated, limiting the sliding window analysis to 3-dir ADC and 15-dir DTI measures. It is possible that further gradient table development could produce reasonable DTI results with subunits of a 15-direction gradient table.

B.3 Final Gradient Table (”02_s7”)

(**NOTE:** this table describes 15 diffusion-encoding gradient directions, but contains 19 volumes due to $b=0$ volumes (”0.000000 0.000000 0.000000”) inserted every 3 diffusion-weighted volumes.)

1.000000	0.000000	0.000000
0.000000	1.000000	0.000000
0.000000	0.000000	1.000000
0.000000	0.000000	0.000000
0.326900	-0.469100	0.820400
0.853900	-0.225200	-0.469100
0.404800	0.853900	0.326900
0.000000	0.000000	0.000000
0.119800	0.324700	0.938200
-0.629400	-0.706000	0.324700
0.767800	-0.629400	0.119800
0.000000	0.000000	0.000000
0.936200	0.244300	0.252500
-0.306000	0.920200	0.244300
-0.172600	-0.306000	0.936200
0.000000	0.000000	0.000000
0.578200	-0.493800	-0.649400
0.173100	0.852100	-0.493800
0.797300	0.173100	0.578200

(**NOTE:** N=59 was generated by 3 repetitions of this N=19 table, with an entry of

”0.000000 0.000000 0.000000” between each table repetition for the purposes of acquiring a b=0 volume. In turn, the N=60 gradient table, used in ’spinescan’ repeated acquisition consisted of an additional ”0.000000 0.000000 0.000000” entry followed by the N=59 gradient table.)

Appendix C

Permissions for Use of Copyrighted Material

Figure 2.2a: This figure was published in Textbook of Medical Physiology, 11th ed., AC Guyton and JE Hall, p. 73. Copyright Elsevier Inc., 2006.

Figure 2.2b: This figure was published in Textbook of Medical Physiology, 11th ed., AC Guyton and JE Hall, p. 74. Copyright Elsevier Inc., 2006.

Figure 2.3b: This figure was published in Textbook of Medical Physiology, 11th ed., AC Guyton and JE Hall, p. 75. Copyright Elsevier Inc., 2006.

Appendix D

Rappalistic Ode to Dr Who

Out to my crew, from the 212
Anotha two-one that I need to stun
'Coz I I gotta do it better for my letter to the editor
So time to 'GET' a run
Onto Dr Whoooo!

(Background Singers):
2-1-Twooooo
212 is Dr Who-oooh
An-oth-er late night log on
To 212-oooh

It seems I'm brain a-lacking
Like a cracker whacka-lacking
While my deadlines keep on stacking
It's back to 212

So I ask a Persian for dispersion
Of confusion 'bout my physics version
And what I get from his assertion
Is a rendezvous with the 212

Resolution, reconstruction,
Signal noise from lead induction

Just at when you think you're through
You're logging into 212

(Background Singers):
 2-1-Twooooo
 212 is Dr Who-oooh
 An-oth-er late night log on
 To 212-oooh

Out to my crew, from the 212
Within the IRC, out my grey hairs grew
Oh you think you're clever 'coz your degree was not forever
But when you think you're through
You're back on 212

You get P-files and your spectra
SNR that you'd expect, ya?
But then the harddrive's wrecked, ya?
You're back at 212

Upon inspection, no detection
Of all that damn da-ta collection
So I ask a Persian for some diversion
And drain a beer of my selection

And won't think 'bout
2-1-2!
Yo, don't think 'bout
2-1-2!

(Background Singers):
 2-1-Twooooo
 212 is Dr Who-oooh
 An-oth-er late night log on
 To 212-oooh

Tryin'ta stop procrastination
To leave this situation
But I've got no destination
And no means of automation

Need more initiation
But first I'll try this station
Watch a doc on Dutch claymation
Or some ancient civilization

So many things to do, time for the 21-2!
Back to Dr Who, I need the 21-2!

(Background Singers):
2-1-Twooooo
212 is Dr Who-oooh
An-oth-er late night log on
To 212-oooh

Out to my crew from the 212
All roads are leading back again to Dr Who
I just might market those implants of poo
Then I'm logging back in to the 2-1-2!

(Repeat as needed to hype crowd)
Just when you think you're through
You're back on 2-1-2!
So many things to do
Time for 2-1-2!

Bibliography

Ababneh, Z., Ababneh, R., Maier, S., Winalski, C., Oshio, K., Ababneh, A., and Mulkern, R. (2008). On the correlation between T_2 and tissue diffusion coefficients in exercised muscle: quantitative measurements at 3T within the tibialis anterior. *Magn Reson Mater Phy*, **21**, 273–278.

Adams, G., Duvoisin, M., and Dudley, G. (1992). Magnetic resonance imaging and electromyography as indexes of muscle function. *J Appl Physiol*, **73**, 1578–1583.

Ai, T., Yu, K., Gao, L., Zhang, P., Goerner, F., Runge, V., and Li, X. (2014). Diffusion tensor imaging in evaluation of thigh muscles in patients with polymyositis and dermatomyositis. *Br J Radiol*, **87**.

Allen, D. and Westerblad, H. (2001). Role of phosphate and calcium stores in muscle fatigue. *J Physiol*, **536**, 657–665.

Allen, D., Lamb, G., and Westerblad, H. (2008). Impaired calcium release during fatigue. *J Appl Physiol*, **104**, 296–305.

Andersen, P. and Kroese, A. (1978). Capillary Supply in Soleus and Gastrocnemius Muscles of Man. *Pflugers Arch*, **375**, 245–249.

Basmajian, J. and de Luca, C. (1985). *Muscles Alive: Their Functions Revealed by Electromyography*. Williams & Wilkins, Baltimore, 5th edition.

Basser, P. and Pierpaoli, C. (1996). MR Diffusion Tensor Spectroscopy and Imaging. *J Magn Reson B*, **111**, 209–219.

Basser, P., Mattiello, J., and LeBihan, D. (1994). MR Diffusion Tensor Spectroscopy and Imaging. *Biophys J*, **66**, 259–267.

Beaulieu, C. (2002). The basis of anisotropic water diffusion in the nervous system - A technical review. *NMR Biomed*, **15**(7-8), 435–455.

Bergstrom, J., Hermansen, L., Hultman, E., and Saltin, B. (1967). Diet, muscle glycogen and physical performance. *Acta Physiol Scand*, **71**, 140–150.

Bonny, J. and Renou, J. (2002). Water diffusion features as indicators of muscle structure *ex vivo*. *Magn Reson Imaging*, **20**, 395–400.

Budzik, J., Thuc, V. L., Demondion, X., Morel, M., Chechin, D., and Cotton, A. (2002). In vivo MR tractography of thigh muscles using diffusion imaging: initial results. *Eur Radiol*, **17**, 3079–3085.

Campos, G., Lueke, T., Wendeln, H., Toma, K., Hagerman, F., Murray, T., Ragg, K., Ratamess, N., Kraemer, W., and Staron, R. (2002). Muscular adaptations in response to three different resistane-training regimens: specificity of repetition maximum training zones. *Eur J Appl Physiol*, **88**, 50–60.

Carr, H. and Purcell, E. (1954). Effects of diffusion on free precession in nuclear magnetic resonance experiments. *Phys Rev*, **94**, 630–638.

Cermak, N., Noseworthy, M., Bourgeois, J., Tarnopolsky, M., and Gibalah, M. (2012). Diffusion Tensor MRI to assess Skeletal Muscle Disruption following Eccentric Exercise. *Muscle Nerve*, **46**, 42–50.

Cleveland, G., Chang, D., Hazlewood, C., and Rorschach, H. (1966). Nuclear Magnetic Resonance Measurement of Skeletal Muscle. *Biophys J*, **16**, 1043–1053.

Damon, B. (2008). Effects of Image Noise in Muscle DT-MRI Assessed Using Numerical Simulations. *Magn Reson Med*, **60**, 934–944.

Damon, B., Gregory, C., Hall, K., Stark, H., Gulani, V., and Dawson, M. (2002a). Intracellular Acidification and Volume Increases Explain R_2 Decreases in Exercising Muscle. *Magn Reson Med*, **47**, 14–23.

Damon, B., Ding, Z., Anderson, A., Freyer, A., and Gore, J. (2002b). Validation of Diffusion Tensor MRI-Based Muscle Fiber Tracking. *Magn Reson Med*, **48**, 97–104.

Deux, J., Malzy, P., and et al, N. P. (2008). Assessment of calf muscle contraction by diffusion tensor imaging. *Eur Radiol*, **18**, 2303–2310.

Duner, H. and Penrow, B. (1958). Histamine and leukocytes in blood during muscular work. *Scand J Clin Lab Invest*, **10**, 394–396.

Edgarton, V., Smith, J., and Simpson, D. (1975). Muscle fibre populations of human leg muscles. *Histochem J*, **7**, 259–266.

Elzibak, A. and Noseworthy, M. (2014). Assessment of diffusion tensor imaging indices in calf muscles following postural change from standing to supine positioning. *MAGMA*, **27**, 387–395.

Elzibak, A., Kumbhare, D., Harish, S., and Noseworthy, M. (2014). Diffusion tensor imaging of the normal foot at 3T. *J Comput Assist Tomogr*, **38**, 329–334.

Fisher, M., Meyer, R., Adams, G., Foley, J., and Potchen, E. (1990). Direct Relationship Between Proton T2 and Exercise Intensity in Skeletal Muscle MR Images. *Invest Radiol*, **25**, 480–485.

Fitts, R. and Widrick, J. (1995). Muscle mechanics: adaptations with exercise-training. *Exerc Sport Sci Rev*, **24**, 427–474.

Fleckenstein, J., Canby, R., Parkey, R., and Peshock, R. (1988). Acute Effects of Exercise on MR Imaging of Skeletal Muscle in Normal Volunteers. *Am J Roent*, **151**, 231–237.

Froeling, M., Nederveen, A., Heijtel, D., Lataster, A., Bos, C., Nicolay, K., Maas, M., Drost, M., and Strijkers, G. (2012). Diffusion-Tensor MRI Reveals the Complex Muscle Architecture of the Human Forearm. *J Magn Reson Imaging*, **36**, 237–248.

Froeling, M., Nederveen, A., Nicolay, K., and Strijkers, G. (2013). DTI of human skeletal muscle: the effects of diffusion encoding parameters, signal-to-noise ratio and T_2 on tensor indices and fiber tracts. *NMR Biomed*, **26**, 1339–1352.

Froeling, M., Ouderman, J., Strijkers, G., Maas, M., amd K Nicolay, M. D., and Nederveen, A. (2015). Muscle Changes Detected with Diffusion-Tensor Imaging after Long-Distance Running. *Radiology*, **274**, 548–562.

Fung, B. and Puon, P. (1981). Nuclear magnetic resonance transverse relaxation in muscle water. *Biophys J*, **33**, 27–37.

Galban, C., Maderwald, S., Uffman, K., de Greiff, A., and Ladd, M. (2004). Diffusive sensitivity to muscle architecture: a magnetic resonance diffusion tensor imaging study of the human calf. *Eur J Appl Physiol*, **93**, 256–262.

Gold, G., Han, E., Stainsby, J., Wright, G., Brittain, J., and Beaulieu, C. (2004). Musculoskeletal MRI at 3.0 T: Relaxation Times and Image Contrast. *Am J Roent*, **183**, 343–351.

Graham, T. (2001). Caffeine and Exercise: Metabolism, Endurance and Performance. *Sports Med*, **31**, 785–807.

Green, R. and Wilson, D. (2000). A pilot study using magnetic resonance imaging to determine the pattern of muscle group recruitment by rowers with different levels of experience. *Skeletal Radiol*, **29**, 196–203.

Guyton, A. and Hall, J. (2006). *Textbook of Medical Physiology*. Elselvier Inc., Philadelphia, 11th edition.

Hata, J., Yagi, K., Hikishima, K., Komaki, Y., Goto, M., and Yano, K. (2012). Diffusion Fractional Anisotropy-based Transformation in Skeletal Muscle Cause by Pressure. *Magn Reson Med Sci*, **11**, 179–184.

Hatakenaka, M., Matsuo, Y., Setoguchi, T., Yabuuchi, H., Okafuji, T., Kamitani, T., Nishikawa, K., and Honda, H. (2008). Alteration of Proton Diffusivity Associated With Passive Muscle, Extension and Contraction. *J Magn Reson Imaging*, **27**, 932–937.

Hatakenaka, M., Yabuuchi, H., Sunami, S., Kamitani, T., Takayama, Y., Nishikawa, K., and Honda, H. (2010). Joint Position Affects Muscle Proton Diffusion: Evaluation with a 3-T MR System. *Am J Roent*, **194**, W208–W211.

Heemskirk, A., Strijkers, G., Vilanova, A., Drost, M., and Nicolay, K. (2005). Determination of Mouse Skeletal Muscle Architecture Using Three-Dimensional Diffusion Tensor Imaging. *J Magn Reson Imaging*, **53**, 1333–1340.

Heemskirk, A., Signha, T., Wilson, K., Ding, Z., and Damon, B. (2010). Repeatability of DTI-based skeletal muscle fiber tracking. *NMR Biomed*, **23**, 294–303.

Jenkinson, M., Beckmann, C., Behrens, T., Woolrich, M., and Smith, S. (2012). FSL. *NeuroImage*, **62**, 782–290.

Jiang, H., van Zijl, P., Kim, J., Pearlson, G., and Mori, S. (2006). DtiStudio: resource program for diffusion tensor computation and fiber bundle tracking. *Comput Methods Programs Biomed*, **81**, 106–116.

Johnson, M., Polgar, J., Weightman, D., and Appleton, D. (1973). Data on the Distribution of Fiber Types in Thirty-Six Human Muscles: An Autopsy Study. *J Neurol Sci*, **18**, 111–129.

Jones, G., Kumbhare, D., Harish, S., and Noseworthy, M. (2013). Quantitative DTI assessment in human lumbar stabilization muscles at 3T. *J Comput Assist Tomogr*, **37**, 98–104.

Kan, J., Heemskirk, A., Ding, Z., Gregory, A., Mencio, G., Spindler, K., and Damon, B. (2009). DTI-Based Muscle Fiber Tracking of the Quadriceps Mechanism in Lateral Patellar Dislocation. *J Magn Reson Imaging*, **29**, 663–670.

Karampinos, D., King, K., Sutton, B., and Georgiadis, J. (2009). Myofiber Ellipticity as an Explanation for Transverse Asymmetry of Skeletal Muscle Diffusion MRI *In Vivo* Signal. *Ann Biomed Eng*, **37**, 2532–2546.

Kermarrec, E., Budzik, J., Khalil, C., Thuc, V. L., Hancart-Destee, C., and Cotton, A. (2010). In Vivo Diffusion Tensor Imaging and Tractography of Human Thigh Muscles in Healthy Subjects. *Am J Roentgenol*, **195**, W352–W356.

Lansdown, D., Ding, Z., Wadington, M., Hornberger, J., and Damon, B. (2007). Quantitative diffusion tensor MRI-based fiber tracking of human skeletal muscle. *J Appl Physiol*, **103**, 673–681.

LeBihan, D., Breton, E., Lallemand, D., Grenier, P., and Laval-Jeantet, M. (1986). MR Imaging of of intravoxels incoherent motions: application to diffusion and perfusion in neurologic disorders. *Radiology*, **161**, 401–407.

LeBihan, D., Mangin, J., Poupon, C., Clark, C., Pappata, S., Molko, N., and Chabriat, H. (2001). Diffusion Tensor Imaging: Concepts and Applications. *J Magn Reson Imaging*, **13**, 534–546.

Li, G., Liang, Y., Xu, P., Ling, J., and Chen, Y. (2016). Diffusion-Tensor Imaging of Thigh Muscles in Duchenne Muscular Dystrophy: Correlation of Apparent Diffusion Coefficient and Fractional Anisotropy Values With Fatty Infiltration. *Am J Roentgenol*, **206**, 867–870.

Liu, S., Wang, M., Ai, T., Wang, Q., Wang, R., Chen, W., Pan, C., and Zhu, W. (2016). In vivo morphological and functional evaluation of the lateral pterygoid muscle: a diffusion tensor imaging study. *Br J Radiol*.

Mabbott, D., Noseworthy, M., Bouffet, E., Laughlin, S., and Rockel, C. (2006). White matter growth as a mechanism of cognitive development in children. *NeuroImage*, **33**, 936–946.

Marieb, E. and Hoehn, K. (2010). *Human Anatomy and Physiology*. Pearson Education, Inc., San Francisco, 8th edition.

McKenna, M. and Hargreaves, M. (2008). Resolving fatigue mechanisms determining exercise performance: integrative physiology at its finest! *J Appl Physiol*, **104**, 286–287.

McMillan, A., Shi, D., Pratt, S., and Lovering, R. (2011). Diffusion Tensor MRI to Assess Damage in Healthy and Dystrophic Skeletal Muscle after Lengthening Contractions. *J Biomed Biotechnol*.

McRobbie, D., Moore, E., Graves, M., and Prince, M. (2006). *MRI: From Picture to Proton*. Cambridge University Press, New York, 2nd edition.

Meiboom, S. and Gill, S. (1958). Modified spin-echo method for measuring nuclear relaxation times. *Rev Sci Instr*, **29**, 688–691.

Miaki, H., Someya, F., and Tachino, K. (1999). A comparison of electrical activity in the triceps surae at maximum isometric contraction with the knee and ankle at various angles. *Eur J Appl Physiol*, **80**, 185–191.

Mori, S., Crain, B., Chacko, V., and van Zijl, P. (1999). Three-dimensional tracking of axonal projections in the brain by magnetic resonance imaging. *Ann Neurol*, **45**, 265–269.

Morvan, D. (1995). In vivo measurement of diffusion and pseudo-diffusion in skeletal muscle at rest and after exercise. *Magn Reson Imaging*, **13**, 193–199.

Moseley, M., Cohen, Y., and Mintorovich, J. (1990). Early detection of regional cerebral ischemia in cats: comparison of diffusion- and T2-weighted MRI and spectroscopy. *Magn Reson Med*, **14**, 330–346.

Neumann-Haefelin, T., Wittsack, H., Wenserki, F., Siebler, M., Seitz, R., Modder, U., and Freund, H. (1999). Diffusion- and Perfusion-Weighted MRI: The DWI/PWI Mismatch Region in Acute Stroke. *Stroke*, **30**, 1591–1597.

Noseworthy, M., Kim, J., Stainsby, J., Stanisz, G., and Wright, G. (1999). Tracking Oxygen Effects on MR Signal in Blood and Skeletal Muscle During Hyperoxia Exposure. *J Magn Reson Imaging*, **9**, 814–820.

Nygren, A. and Kaijser, L. (2002). Water exchange induced by unilateral exercise in active and inactive muscles. *J Appl Physiol*, **93**, 1716–1722.

Okamoto, Y., Kunimatsu, A., Miki, S., Shindo, M., Niitsu, M., and Minami, M. (2008). Fractional Anisotropy Values of Calf Muscles in Normative State after Exercise: Preliminary Results. *Magn Reson Med Sci*, **7**, 157–162.

Okamoto, Y., Kunimatsu, A., Kono, T., and Nasu, K. (2010). Changes in MR Diffusion Properties during Active Muscle Contraction in the Calf. *Magn Reson Med Sci*, **9**, 1–8.

Okamoto, Y., Okamoto, T., Kujiraoka, Y., Hirano, Y., Isobe, T., and Minami, M. (2012). Correlation between pennation angle and image quality of skeletal muscle fibre tractography using deterministic diffusion tensor imaging. *J Med Imag Rad Oncoli*, **56**, 622–627.

Ploutz-Snyder, L., Nyren, S., Cooper, T., Potchen, E., and Meyer, R. (1997). Different Effects of Exercise and Edema on T_2 Relaxation in Skeletal Muscle. *Magn Reson Med*, **37**, 676–682.

Polgar, J., Johnson, M., Weightman, D., and Appleton, D. (1973). Data on Fibre Size in Thirty Six Human Muscles: An Autopsy Study. *J Neurol Sci*, **19**, 307–318.

Price, T., Kamen, G., Damon, B., Knight, C., Applegate, B., Gore, J., Eward, K., and Signorile, J. (2003). Comparison of MRI with EMG to study muscle activity associated with dynamic plantar flexion. *Magn Reson Imaging*, **21**, 853–861.

Prior, B., Ploutz-Snyder, L., Cooper, T., and Meyer, R. (2001). Fiber type and metabolic dependence of T_2 increases in stimulated rat muscles. *J Appl Physiol*, **90**, 615–623.

Saab, G., Thompson, R., and Marsh, G. (1999). Multicomponent T_2 Relaxation of In Vivo Skeletal Muscle. *Magn Reson Med*, **42**, 150–157.

Saab, G., Thompson, R., and Marsh, G. (2000). Effects of exercise on muscle transverse relaxation determined by MR imaging and in vivo relaxometry. *J Appl Physiol*, **88**, 226–233.

Sinha, S., Sinha, U., and Edgarton, V. (2006). In vivo Diffusion Tensor Imaging of the Human Calf Muscle. *J Magn Reson Imaging*, **24**, 182–190.

Snell, R. (2012). *Clinical Anatomy by Regions.* Lippincott Williams & Wilkens, Philidelphia, 9th edition.

Stanisz, G., Odrobina, E., Pun, J., Escaravage, M., Graham, S., Bronskill, M., and Henkelman, R. (2005). T1, T2 Relaxation and Magnetization Transfer in Tissue at 3T. *Magn Reson Med*, **54**, 507–512.

Stejkal, E. and Tanner, J. (1965). Spin diffusion measurements: Spin echoes in the presence of a time-dependent field gradient. *J Chem Phys*, **42**(1), 288–292.

van Donkelaar, C., Kretzers, L., and et al, P. B. (1999). Diffusion tensor imaging in biomechanical studies of skeletal muscle function. *J Anat*, **194**, 79–88.

van Doorn, A., Bovendeerd, P., Nicolay, K., Drost, M., and Janssen, J. (1996). Determination of Muscle Fibre Orientation using Difusion-Weighted MRI. *Eur J Morphol*, **34**, 5–10.

Westerblad, H., Allen, D., and Lannergren, J. (2002). Muscle fatigue: lactic acid or inorganic phosphate the major cause. *News Physiol Sci*, **17**, 17–21.

Yangisawa, O., Niitsu, M., Yoshioka, H., Goto, K., and Itai, Y. (2003). MRI Determination of Muscle Recruitment Variations in Dynamic Ankle Plantar Flexion Exercise. *Am J Phys Med Rehabil*, **82**, 760–765.

Yangisawa, O., Kurihara, T., Kobayashi, N., and Fukubayashi, T. (2011). Strenuous Resistance Exercise Effects on Magnetic Resonance Diffusion Parameters and Muscle-Tendon Function in Human Skeletal Muscle. *J Magn Reson Imaging*, **34**, 887–894.

Zaraiskaya, T., Kumbhare, D., and Noseworthy, M. (2006). Diffusion Tensor Imaging in Evaluation of Human Skeletal Muscle Injury. *J Magn Reson Imaging*, **24**, 402–408.

Zijta, F., Froeling, M., Nederveen, A., and Stoker, J. (2013). Diffusion tensor imaging and fiber tractography for the visualization of the female pelvic floor. *Clin Anat*, **26**, 110–114.